Universidade de Aveiro Departamento de Engenharia Cerâmica e do Vidro
2005

Oleksandr Tkach

Cerâmicos à base de $SrTiO_3$ para aplicações em dispositivos sintonizáveis

Strontium titanate based ceramics for tunable device applications

Universidade de Aveiro Departamento de Engenharia Cerâmica e do Vidro
2005

Oleksandr Tkach

Cerâmicos à base de $SrTiO_3$ para aplicações em dispositivos sintonizáveis

Strontium titanate based ceramics for tunable device applications

dissertação apresentada à Universidade de Aveiro para cumprimento dos requisitos necessários à obtenção do grau de Doutor em Engenharia e Ciência de Materiais, realizada sob a orientação científica da Dr. Paula M. L. S. Vilarinho, Professora Associada do Departamento de Engenharia Cerâmica e do Vidro da Universidade de Aveiro e do Dr. Andrei L. Kholkine, Investigador principal do Departamento de Engenharia Cerâmica e do Vidro da Universidade de Aveiro

Dissertation presented to the University of Aveiro to obtain the Doctor degree in Materials Science and Engineering, under the scientific guidance of Dr. Paula M. L. S. Vilarinho, Associate Professor of the Department of Ceramics and Glass Engineering of the University of Aveiro, and Dr. Andrei L. Kholkine, Principal Researcher of the Department of Ceramics and Glass Engineering of the University of Aveiro

o júri

presidente

Prof. Dr. Joaquim Borges Gouveia
professor catedrático da Universidade de Aveiro

Prof. Dr. Mário Maglione
professor catedrático da Universidade de Bordéus - França

Prof. Dr. Jorge Ribeiro Frade
professor catedrático da Universidade de Aveiro

Prof. Dr. Abílio de Jesus Monteiro Almeida
professor associado com agredação da Faculdade de Ciências da Universidade do Porto

Prof. Dr. Paula Maria Lousada Silveirinha Vilarinho
professora associada da Universidade de Aveiro

Prof. Dr. José Luís Pires Ribeiro
professor associado da Escola de Ciências da Universidade do Minho

Prof. Dr. Andrei Leonidovitch Kholkine
Investigador principal convidado da Universidade de Aveiro

acknowledgments

I am very grateful to my supervisor Paula Vilarinho for her guidance and constant encouragement. She was always open for discussions and ready to share her deep understanding of material science.

I am very grateful to my co-supervisor Andrei Kholkin for his wide knowledge, thorough analysis critical reading of the present manuscript which resulted in great improvement of the thesis.

Many thanks to Ian Reaney and Augusto Lopes, who introduced me to the powerful transmission electron microscopy technique. Maria Paula da Silva Seabra and Javier Perez de La Cruz are acknowledged for excellent companionship and help. A lot of help I received from other members of Department of Ceramics and Glass Engineering. This concerns not only scientific work but also friendly and cheerful atmosphere in the department. In order not to miss some of their names, I want to thank all of them.

My visits to Institute of Physics, Academy of Science of the Czech Republic in order to perform measurements on microwave, infrared, terahertz and Raman spectroscopy measurements were possible due to the kind invitation of Jan Petzelt, the head of the institute. I would like to thank him and Alexej Pashkin who introduced me to high frequency dielectric spectroscopy as well as to the whole group of Department of Dielectrics. The group is acknowledged for hospitality during my stays in Prague.

I would like to thank Ian Reaney and Jan Petzelt for useful discussions.

Many thanks to Viktor Bovtun for useful discussions and also for inviting me to the PhD study in Aveiro.

I acknowledge the FCT (Portuguese Foundation for Science and Technology) for financial support.

I am very grateful to my family and friends studied together with me in National Technical University of Ukraine “KPI” for their support over the years.

Last but not least, many thanks to Olena Okhay for her patience, her enthusiastic support and her continuous understanding.

palavras-chave

titanato de estrôncio, cerâmicos, caracterização da estrutura, propriedades dieléctricas, comportamento ferroeléctrico relaxor, sintonização.

resumo

O titanato de estrôncio (ST) é conhecido como um paraeléctrico quantum no qual a permitividade dieléctrica aumenta gradualmente após arrefecimento até cerca de 0 K e nenhuma anomalia do tipo ferroeléctrica é observada. A dependência acentuada da permitividade dieléctrica do campo eléctrico dc torna ST um material atractivo para aplicações em componentes electrónicos sintonizáveis, particularmente em dispositivos para operação à frequência das microondas, que incluem, por exemplo, filtros e modificadores de fase para antenas. Devido ao valor elevado de permitividade dieléctrica estes dispositivos podem ser miniaturizados e tornados economicamente viáveis. Contudo ST apresenta uma limitação em termos de aplicações para indústria electrónica de microondas, na medida em que a capacidade de sintonização (tunability) (definida como a variação da permitividade induzida por um campo dc) adequada é apenas atingida abaixo de ~80 K. A gama de temperaturas de sintonização elevada pode ser mudada para temperaturas mais altas através de substituições atómicas no local Sr da rede, por exemplo, por Ba. É conhecido que para esta substituição uma fase ferroeléctrica é induzida nas soluções sólidas de $Ba_xSr_{1-x}TiO_3$ (BST) numa gama de temperaturas entre temperaturas 0-400 K. Contudo, perdas (insertion loss) e instabilidade térmica elevadas para BST, que aumentam com o aumento da concentração de Ba, impõe sérias restrições à sua aplicação nas antenas. Desta forma são necessários sistemas alternativas à base de ST, nos quais uma anomalia da resposta dieléctrica seja induzida.

Neste trabalho foi efectuada uma investigação sistemática do efeito de substituições atómicas de Sr e Ti por Mg e Mn na estrutura, microestrutura e comportamento dieléctrico e ferroeléctrico de cerâmicos de ST. As propriedades dieléctricas foram estudadas numa gama alargada de temperaturas, frequências e campos eléctricos.

Os cerâmicos de ST e com substituições a nível dos locais A e B da estrutura de perovesquite por Mg e Mn foram preparados pelo método convencional de mistura de óxidos. A estrutura cristalográfica e microestrutura dos cerâmicos foi analisada por difracção de RX, espectroscopia de Raman, microscopia electrónica de varrimento (SEM) e de transmissão (TEM) e espectroscopias de energias dispersivas (EDS). Investigação detalhada da dinâmica de rede e o comportamento dieléctrico numa gama alargada de frequências for também efectuada.

A caracterização dieléctrica dos cerâmicos de $Sr_{1-x}Mg_xTiO_3$, $SrTi_{1-y}Mg_yO_{3-\delta}$, $Sr_{1-x}Mn_xTiO_3$ e $SrTi_{1-y}Mn_yO_3$ foi realizada em função da temperatura e frequência, incluindo a caracterização às frequências rádio (rf), microondas (MW), “time-domain terahertz” (TDT), e infravermelho (IR). A dependência da permitividade dieléctrica do campo eléctrico às frequências rádio foi explorada para uma possível aplicação como componente sintonizável. A comparação dos efeitos de dopantes observados é discutida com base no tamanho, local de ocupação catiónica, carga e estequiometria dos sistemas.

A solubilidade sólida de Mg em ST é restrita a $x \leq 1$ % para o caso da substituição nos locais A ($Sr_{1-x}Mg_xTiO_3$) e restrita a $y \leq 10$ % para a ocupação nos locais B ($SrTi_{1-y}Mg_yO_{3-\delta}$). Verificou-se que o parâmetro de rede aumenta com o aumento da concentração de Mg para $SrTi_{1-y}Mg_yO_{3-\delta}$ e é praticamente invariante para $Sr_{1-x}Mg_xTiO_3$. A dependência da ocupação do local da rede foi também verificada no crescimento de grão dos cerâmicos. Para $SrTi_{1-y}Mg_yO_{3-\delta}$ o tamanho de grão decresce acentuadamente com o aumento da concentração de Mg. Para $Sr_{1-x}Mg_xTiO_3$ é observada a dependência inversa. Os espectros de micro-Raman e da variação da permitividade dieléctrica com a frequência, numa gama alargada de frequências e as características de sintonização dos cerâmicos de $Sr_{1-x}Mg_xTiO_3$ não variam consideravelmente em relação aos cerâmicos de ST não dopados, confirmando a pequena inserção do Mg na rede perovesquítica de ST. Os resultados indicam que Mg não induz comportamento ferroeléctrico ou ferroeléctrico relaxor no titanato de estrôncio. Mais ainda, o ajustamento do comportamento dieléctrico observado à lei de Barrett demonstrou que a dopagem com Mg nos locais B da rede “afasta” o sistema da instabilidade ferroeléctrica. Os resultados mostraram para este sistema um endurecimento considerável do modo mole de vibração da rede observado nos espectros de IR. A permitividade e perda dieléctrica decrescem na região das frequências rádio e também para frequências mais elevadas (THz), acompanhados de um decréscimo da sintonização, de acordo com o endurecimento do modo ferroeléctrico mole. Estes resultados confirmam uma ocupação mais favorável do Mg nos locais Ti da rede de ST e mostram a possibilidade de utilizar $SrTi_{1-y}Mn_yO_3$ como guias de onda e ressonador às frequências das microondas.

Para ambas as formulações $Sr_{1-x}Mn_xTiO_3$ e $SrTi_{1-y}Mn_yO_3$ o parâmetro de rede, calculado dos perfis de difracção de raios X decresceu com o aumento da concentração de Mn, mas com diferentes taxas de decréscimo. As análises de TEM indicaram que a solubilidade de sólida de Mn em $Sr_{1-x}Mn_xTiO_3$ é limitada a $x < 3$ %, enquanto que as análises de SEM mostraram um decréscimo acentuado do tamanho de grão dos cerâmicos de $SrTi_{1-y}Mn_yO_3$. A temperatura da transição de fase estrutural aumentou consideravelmente (acima de 150 K) com a dopagem com Mn nos locais A da rede da perovesquite, enquanto que foi observada a diminuição desta transição para as amostras dopadas com Mn nos locais B.

A dopagem com Mn nos locais B reduz o valor da permitividade dieléctrica, variação esta que é também acompanhada pelo endurecimento do modo mole e diminuição da contribuição do modo mole para a resposta dieléctrica e afasta o sistema da instabilidade ferroeléctrica. Mai ainda foi observado um decréscimo da sintonização dieléctrica, seguida de uma redução da permitividade dieléctrica dos cerâmicos de $SrTi_{1-y}Mn_yO_3$.

Em oposição foi observado comportamento polar nos sistema $Sr_{1-x}Mn_xTiO_3$. As medidas dieléctricas às frequências rádio mostraram um máximo de permitividade difuso a 25-80 K, que se desloca para temperaturas mais elevadas com o aumento da frequência de medida e aumento da concentração de Mn. A anomalia dieléctrica é também observada na região das microondas e terahertz. A observação do comportamento histerético nas curvas de P versus E confirma a existência de um estado polar a baixas temperaturas. A resposta histerética degenera lentamente num comportamento não linearidade à medida que a temperatura aumenta. O comportamento relaxor observado foi atribuído à formação de dipolos eléctricos e correspondentes campos aleatórios devido às posições não centrais (off-centre position) dos iões Mn nos locais de Sr e à rede polarizável de $SrTiO_3$. A difusividade do máximo implica uma elevada estabilidade térmica do comportamento dieléctrico de $Sr_{1-x}Mn_xTiO_3$, fazendo com que ST dopado com Mn seja um possível candidato para aplicações como componente electrónico sintonizável. Ainda a gama de temperaturas na qual a constante dieléctrica é sintonizável foi alargada (~70%) e foi obtido o factor de qualidade sintonizável de cerca ~6000, às temperaturas de 75-100 K.

keywords

Strontium titanate, ceramics, structural characterisation, dielectric properties, ferroelectric relaxor behaviour, tunability.

abstract

Strontium titanate (ST) is known as a quantum paraelectric in which the dielectric permittivity monotonously increases upon cooling down to near 0 K and no ferroelectric-type anomaly is observed. A strong dc-electric-field dependence of the dielectric permittivity makes ST an attractive material for applications in tunable electronic components, particularly in several microwave devices including filters and phase shifting elements in phased array antennas. Due to the high dielectric permittivity, these devices may be miniaturized and cost-effective. However, ST has limited application in the microwave electronic industry, since adequate tunability (change in the permittivity induced by a dc field) is achieved only below ~80 K. The temperature range of high tunability can be shifted towards high temperature by means of Sr-site substitution by Ba, for example. Such shift corresponds to an induced ferroelectric phase transition in $Ba_xSr_{1-x}TiO_3$ (BST) solid solutions at temperatures in the range of 0-400 K. However, higher insertion loss and thermal instability of barium strontium titanate, continuously increasing with Ba concentration, impose serious restrictions to its application in phased array antennas. Hence, alternative ST-based systems, in which an anomaly of the dielectric response would be induced, are required.

In this work, systematic research of Sr- and Ti-site substitutions by Mg and Mn on structure, microstructure, dielectric and ferroelectric behaviour of ST ceramics is investigated. The dielectric properties are studied in wide temperature, frequency and electric field ranges.

ST ceramics with Sr- and Ti-site substitutions by Mg and Mn are synthesised by conventional mixed oxide method. The crystallographic and micro structures of the doped ceramics are analysed by X-ray diffraction (XRD), Raman spectroscopy, scanning and transmission electron microscopy (SEM and TEM) together with energy dispersive spectroscopy (EDS) techniques. Detailed investigation of the lattice dynamics and dielectric behaviour in a wide frequency range is undertaken also. The dielectric characterisation of $Sr_{1-x}Mg_xTiO_3$, $SrTi_{1-y}Mg_yO_{3-\delta}$, $Sr_{1-x}Mn_xTiO_3$ and $SrTi_{1-y}Mn_yO_3$ ceramics is performed as a function of temperature and frequency by the radio-frequency (rf), microwave (MW), time-domain terahertz (TDT), and infrared (IR) spectroscopy. The dc-electric-field dependence of permittivity in rf range was explored for possible application as tunable components. A comparison of the observed doping effects is discussed based on ion size, cation site occupancy, charge and chemical stoichiometry in the systems.

It was observed that, the solid solubility of Mg is restricted to $x \leq 1$ % for Sr-site occupancy ($Sr_{1-x}Mg_xTiO_3$) and to $y \leq 10$ % for Ti-site occupancy ($SrTi_{1-y}Mg_yO_{3-\delta}$). The lattice parameter is found to increase with Mg content for $SrTi_{1-y}Mg_yO_{3-\delta}$ system, while it is almost invariant in $Sr_{1-x}Mg_xTiO_3$ one. The dependence on the lattice site occupancy is also verified for the grain growth of ceramics. For $SrTi_{1-y}Mg_yO_{3-\delta}$ the average grain size markedly decreases with

increasing Mg content. For $Sr_{1-x}Mg_xTiO_3$ the inverse dependence is observed. The micro-Raman spectra and the wide frequency dielectric properties of $Sr_{1-x}Mg_xTiO_3$ including rf tunability do not differ considerably from the properties of undoped $SrTiO_3$, confirming only slight incorporation of Mg into the Sr site of ST perovskite lattice. Mg does not induce ferroelectricity or relaxor-like behaviour in strontium titanate, either located in A- or B-site of the $SrTiO_3$ lattice. Moreover, fitting the dielectric behaviour to Barrett's law demonstrates that B-site doping drives the system away from the ferroelectric instability. Ti-site Mg doping results in significant stiffening of the soft lattice mode observed in IR reflectivity spectra. Dielectric permittivity and dielectric loss decreases in the frequency range from radio to THz frequencies accompanied by the decrease of the tunability, in accordance with the stiffened ferroelectric soft mode. These results confirm more favourable occupation of Mg at the Ti site of the ST lattice and show the possibility of using Ti-site Mg-doped ST as an material for low-loss microwave waveguides and resonators.

For both $Sr_{1-x}Mn_xTiO_3$ and $SrTi_{1-y}Mn_yO_3$ formulations, the lattice parameter, calculated from XRD profiles, was found to decrease with increasing Mn content, but with different rates. TEM analysis indicated that the solid solubility of Mn for $Sr_{1-x}Mn_xTiO_3$ system is limited to $x < 3$ %, while SEM analysis revealed a marked decrease of the grain size for $SrTi_{1-y}Mn_yO_3$ ceramic samples. The temperature of the structural phase transition was found to increase considerably (above 150 K) with Mn doping at Sr site, while reduction of this transition was observed for Mn doping at Ti site.

Ti-site Mn doping reduces the dielectric permittivity value, associated with a soft mode stiffening and a lowering of the soft mode phonon contribution to the dielectric response, and drives the system away from ferroelectric instability. In addition, a decrease of the dielectric tunability, following a reduction of dielectric permittivity was observed in $SrTi_{1-y}Mn_yO_3$ ceramics.

On the contrary, polar behaviour was found in $Sr_{1-x}Mn_xTiO_3$ ceramic system. Radio-frequency dielectric measurements showed a diffuse maximum at 25-80 K shifting to higher temperatures with increasing measurement frequency and amount of Mn. The dielectric anomaly is observed in the microwave and terahertz ranges also. The observation of hysteretic behaviour in the P versus E curves shows the existence of a polar state at low temperatures. The hysteresis response slowly degenerates into just nonlinearity as the temperature increases. The observed relaxor-type dielectric behaviour is attributed to the formation of electric dipoles and corresponding random fields due to the off-centre position of Mn^{2+} ion at the Sr site of highly polarisable $SrTiO_3$ lattice. The diffusivity of the peak implies a higher thermal stability of the dielectric behaviour of $Sr_{1-x}Mn_xTiO_3$ compound, making Mn-doped ST system a possible candidate for the tunable electronic component applications. Moreover, the temperature range where the dielectric constant is tunable was enlarged for $Sr_{1-x}Mn_xTiO_3$ ceramics comparing with undoped $SrTiO_3$. A higher tunability (~70%) and quality factor for tunable components (~6000) around 75-100 K were obtained as well.

Table of Contents

List of Figures

List of Tables

List of Symbols

A - fitting parameter
A_{hs} - hyperfine splitting constant
a - cubic unit cell parameter
a, b, c - unit cell parameters
a', b', c' - thermodynamic potential coefficients
a_0 - constant of thermodynamic potential coefficient a'
B - magnetic field
C - Curie constant
D - density
D_r - relative density
D_t - theoretical density
d - distance between atomic layers
$\mathrm{d}_{\mathrm{air}}$ - density of air
$\mathrm{d}_{\mathrm{liq}}$ - density of liquid
d_s - sample thickness
E - dc bias electric field
E_0 - test signal amplitude
E_2-E_1 - energy difference
E_{max} - maximum applied bias electric field
e - elementary charge (1.6×10^{-19} C)
f - frequency
g factor - characteristic property of the paramagnetic species
ħ - reduced Plank constant (1.05458×10^{-34} Js)
I - current
I_C - capacitive current
I_R - ac conduction current
i - imaginary operator
K - quality factor of a tunable component
k - integer
k_B - Boltzmann constant ($1.38066 \cdot \times 10^{-23}$ J/K)
L_{dB} - insertion loss in dB
l - linear dimension

M - molar mass

m - mass

$\mathrm{m_e}$ - electron mass (9.1×10^{-28} g)

N_A - Avogadro number (6.022×10^{-23} mol^{-1})

N_c - coordination number

n - tunability

n_r - relative tunability

n_max - relative tunability at maximum applied bias electric field

P - polarization

P_r -remnant polarization

P_s - spontaneous polarization

p - isostatic pressure

p_C - critical isostatic pressure

Q - quality factor

$\mathbf{q}$ - wave-vector

r - ionic radius

r_A - average ionic radius of A-site cations

r_B - average ionic radius of B-site cations

S - area of electrodes

T - temperature

T_0 - Curie temperature

T_1 - temperature of crossover between classical and quantum behaviour

T_a - temperature of antiferrodistortive phase transition

T_C - temperature of ferroelectric phase transition

T_f - freezing temperature

T_m - temperature of the maximum dielectric constant

T_s - sintering temperature

t - tolerance factor

t_s - sintering time

$tan\delta$ - dielectric loss or dissipation factor

$tan\delta(0)$ - zero-field dissipation factor

$tan\delta(E_\mathrm{max})$ - dissipation factor under maximum applied bias electric field

U - activation energy

V - voltage

W_1 - weight of sample in air

W_2 - weight of sample in liquid

x - A-site dopant concentration

x_c - critical concentration

y - B-site dopant concentration

Z - impedance

α - angle of semicircular arc, describing diffuseness of dielectric spectrum

Γ, M, X, R - especial points of Brillouin zone

γ - effective exponent

γ_i - inverse dielectric susceptibilities

ΔE - energy uncertainty

ΔP - increment of polarisation

Δa - increment of unit cell parameter

$\Delta\varphi_{\text{degree}}$ - phase shift in degrees

Δq - uncertainty in the structural coordinate

Δp - impulse uncertainty

$\Delta\omega$ - Raman shift

δx - deviation of concentration

ε_0 - dielectric constant of vacuum (8.854×10^{-12} F/m)

ε^* - complex dielectric permittivity

ε' - real part of dielectric permittivity or dielectric constant

ε'' - imaginary part of dielectric permittivity

ε_{dc} - static dielectric permittivity

ε_∞ - dielectric permittivity at infinite frequency

$\varepsilon'(0)$ - zero-field dielectric constant

$\varepsilon'(E)$ - dielectric constant under bias electric field

ε'_m - maximum dielectric constant

μ_B - Bohr magneton (9.274×10^{-24} J/T)

η - order parameter

θ - diffraction angle

λ - wavelength

π – constant (3.1416)

σ - uniaxial stress

σ_{c1}, σ_{c2} - critical values of uniaxial stress

τ - relaxation time

τ_0- relaxation time pre-exponential factor

τ_ε - temperature coefficient of dielectric constant

Φ - thermodynamic potential

Φ_0 - thermodynamic potential for the case of zero spontaneous polarisation

φ - rotation angle of oxygen octahedra

χ' - real part of dielectric susceptibility

χ'' - imaginary part

ψ - angle $90°-\delta$

ω - angular frequency

ω_{LO} - long-wave longitudinal optical phonon frequency

ω_{TO} - long-wave transverse optical phonon frequency

ω_{in} - incident phonon frequency

ω_{sc} - scattering phonon frequency

ω_{s} - soft mode frequency

Ω - created phonon or annihilated phonon frequency

Abbreviations

ac - alternating current

a.u. - arbitrary units

BST - barium strontium titanate

BT - barium titanate

dc - direct current

DPT - diffused phase transition

ED - electron diffraction

EPR - electron paramagnetic resonance

ESR - electron spin resonance

EDS - energy dispersive spectroscopy

FC - field cooling

FOJT - first-order Jahn-Teller effect

GG - grain growth

HOMO - highest occupied molecular orbital

IR - infrared

LO - longitudinal optical

LUMO - lowest unoccupied molecular orbital

MW - microwave

QFTC - quality factor of a tunable component
PLZT - lead lanthanum zirconate titanate
PMN - lead magnesium niobate
PST - lead scandium titanate
PT - lead titanate
RT - room temperature
rf - radio-frequency
SBiT - strontium bismuth titanate
SCT - strontium calcium titanate
SMT - strontium magnesium titanate
SMnT - strontium manganese titanate
SPT - strontium lead titanate
ST - strontium titanate
STM - strontium magnasate titanate
STMn - strontium manganate titanate
SEM - scanning electron microscopy
SOJT - second-order Jahn-Teller effect
TDT - time-domain terahertz
TO - transversal optical
TEM - transmission electron microscopy
XRD - X-ray diffractometry
YBCO - yttrium barium cuprate
ZFC - zero-field cooling

Introduction

$SrTiO_3$-based compounds have been attracting a considerable interest from the fundamental point of view for more than fifty years (von Hippel, 1946). Significant fundamental properties of strontium titanate (ST) include: a structural phase transition (Lytle, 1964; Fleury et al., 1968; Shirane and Yamada, 1969), semiconductivity (Frederikse et al., 1964), superconductivity (Schooley et al., 1964) and quantum paraelectric behaviour (Müller and Burkhard, 1979, Viana et., 1994) among others.

On the other hand, strontium titanate, as a material with relatively high dielectric constant ε' and low loss tangent $tan\delta$, is of interest for a wide range of applications, particularly in electronic devices.

Currently, due to the extensive use of microwaves in radar and communication applications, including military, airport and police radars, satellite communication systems, mobile phones and wireless computer networks (Scott, 1993) and due to the approaching of the computer clock frequency to the GHz range, the most important applications for ST-based materials are related to microwave microelectronic elements. Thus, cylinders or cubes of dielectric single crystals or ceramics can be used as dielectric resonators or filters. Their linear dimension l is proportional to $1/\sqrt{\varepsilon'}$ (Sivasubramanian et al., 1997). Hence, a high dielectric constant of material is particularly important for mobile and satellite communication systems, allowing to reduce the dimensions and correspondingly mass of the dielectric resonators and filters. In addition, if the dielectric constant of the material reveals a dependence on an applied bias electric field E, these elements can be tunable (Vendik et al., 1995; Wooldridge et al., 1999; Gevorgian, 2001; Misra et al., 2003). This property, commonly called tunability, is characteristic of ferroelectric materials and is strengthened on approaching the paraelectric-ferroelectric phase transition, at which the dielectric constant has a maximum (Lines and Glass, 1977). Thus, applying bias electric field to the ferroelectric material of resonator of finite dimensions, it is possible to obtain the desirable resonance frequency proportional to $\varepsilon'(E)^{-1/2}$. Bulk ferroelectrics can also be used as parallel plate tunable capacitors or varactors at radio frequencies; as electroded slabs in stack of lens antennas (Tagantsev et al., 2003); and as small low cost microwave phase shifters for electronic scanning antennas with high reliability and low complexity (Varadan et al., 1992; Babbit et al., 1992). In other words, applying bias electric field, it is possible to obtain desirable capacitance [which is proportional to $\varepsilon'(E)$]; desirable steering of the electromagnetic beam, passing through the lens antenna; and desirable phase shift [proportional to $\varepsilon'(0)^{-1/2} - \varepsilon'(E)^{-1/2}$], respectively.

Along with the high dielectric constant and high tunability, low loss (or high quality factor $Q = 1/tan\delta$) and high temperature-stability of the material are also important for microwave elements. However, such microwave application requirements are quite contradictory, because the temperature-stable and low-loss materials (such as diamond or sapphire) have rather small ε' and tunability, whereas high dielectric constant and tunability (usually observed for ferroelectrics, such as $BaTiO_3$ (BT) and $PbTiO_3$ (PT), especially near the phase transition) is accompanied by high temperature coefficient $\tau_\varepsilon = d\varepsilon'/dT$ and loss (von Hippel, 1946).

In general, ferroelectrics both in polar and paraelectric phase may be used in tunable microwave devices provided they have low losses and sufficient dependency of the permittivity on the dc field (Gevorgian, 2001). However, the paraelectric phase seems to be preferable due to the absence of loss related to domain motion. In this respect, the pure incipient ferroelectrics / quantum paraelectrics $SrTiO_3$, $CaTiO_3$, $KTaO_3$ and TiO_2 (Lemanov et al., 1999) have an advantage. They possess only a paraelectric phase, displaying a quite high dielectric constant that continuously increases with decreasing temperature, and have much smaller dielectric loss than ferroelectrics. ST possesses the highest known dielectric permittivity among the incipient ferroelectrics, although substantial tunability is achieved in undoped strontium titanate only below ~80 K, limiting the practical application of ST in the past. However, the discovery of high temperature superconductivity in $YBa_2Cu_3O_7$ (YBCO) together with the chemical and structural compatibility of YBCO with ST renewed attempts to use ST in tunable microwave technology, resulting in ultra-high-quality-factor elements, operating below liquid nitrogen temperature (Vendik et al., 1995).

The temperature range of high tunability and high dielectric constant can be shifted towards room temperature by means of formation of solid solutions between incipient ferroelectric $SrTiO_3$ and classical ferroelectric $BaTiO_3$. Such shift corresponds to an induced ferroelectric phase transition in $Ba_xSr_{1-x}TiO_3$ (BST) solid solutions at temperatures in the range of 0-400 K (Lemanov et al., 1996), and found practical applications near room temperature (Varadan et al., 1992; Babbit et al., 1992; de Flaviis et al., 1997). However, it was observed that the higher Ba concentration the higher the microwave loss in BST solid solutions (Vendik, 1999). So, different kinds of doping, including Mg (Kim et al., 1998; Sengupta and Sengupta, 1999; Chang and Sengupta, 2002), Al (Wu et al., 1999; Wu et al., 2000), Cr, Fe and Mn (Newnham, 1983) were used to decrease the dielectric loss and/or to broaden the phase transition in such a way to increase the temperature stability of the dielectric constant of BST, i.e., $\tau_\varepsilon = d\varepsilon'/dT \rightarrow 0$. An additional disadvantage of BST is that for the same permittivity, the tuning ability decreases with increasing barium content (Tagantsev, 2003).

It is interesting to notice that the solid solutions between two incipient ferroelectrics such as $SrTiO_3$ and $CaTiO_3$ (Mitsui and Westphal, 1961; Bednorz and Müller, 1984; Ranjan et al., 2000; Kleemann et al., 2000) or $SrTiO_3$ and $KTaO_3$ (Lemanov et al., 1997b; Trepakov et al., 1997) also exhibited the phase transition shifting towards room temperature with increasing second member content until a certain limit. The $Sr_{1-x}Ca_xTiO_3$ system is one of the most interesting and extensively studied ST-based solid solution, where the transition temperature T_C rises up to ~30 K with Ca concentration (x) up to $x \approx 0.016$, obeying the relationship $T_C \sim (x - x_c)^{1/2}$ for quantum ferroelectrics (Bednorz and Müller, 1984). However, at $0.016 < x < 0.12$, the T_C appears to be nearly constant (Mitsui and Westphal, 1961; Bednorz and Müller, 1984). The ferroelectric phase produced by the small Ca introduction was ascribed to the enlarged ionic polarisability of Ca^{2+} in the ST lattice and to the occupation of off-centre positions at Sr sites (Mitsui and Westphal, 1961). Later, the overall dielectric behaviour of the $Sr_{1-x}Ca_xTiO_3$ system for $x < 0.12$ was studied in detail (Bednorz and Müller, 1984) and attributed to an impurity-induced second order phase transition disrupted by the random electric and strain fields (Zhang et al., 2002b).

In more general consideration, one can expect the ferroelectric phase to be produced in ST by the small divalent atoms, occupying off-centre positions at Sr sites. Such idea was confirmed by theoretical calculations (Kvyatkovskii, 2002), which predicted a dielectric relaxation mechanism, based on the displacement of ions smaller than Sr^{2+} (such as Mg^{2+} and Zn^{2+}) in a multi-well local potential.

Just as Mg^{2+}, Mn^{2+} may form off-centres and its random distribution among the A-lattice sites of perovskite ABO_3 system may lead to relaxor ferroelectric properties due to the large difference between the ionic size of Mn^{2+} and Sr^{2+} (Shannon, 1976). In addition, since magnesium titanate has a positive temperature coefficient of dielectric permittivity τ_ε

(von Hippel, 1946), mixtures of strontium titanate, whose τ_ε is negative, with this material may be used to produce a temperature-stable material. A similar idea is valid for $SrTiO_3$ - $MnTiO_3$ system, since both $MnTiO_3$ and $MgTiO_3$ are microwave dielectrics of ilmenite-type structure (Sohn, et al., 1994).

On the other hand, Mg^{2+} and Mn^{4+} ions may occupy also Ti site of ST perovskite lattice. For Mg^{2+} case, extra charges are expected to be compensated by oxygen vacancies, what can affect the dielectric properties. For Mn^{4+} case, no extra charges are expected due to multivalent nature of Mn. However, polar anomalies in the dielectric response of Ti-site Mn-doped ST due to displacement of small Mn^{4+} ions at large Ti sites are possible.

Currently, use of ST-based ceramics (bulk and thick films) in tunable microwave devices is considered for industrial applications due to considerable cost reduction, comparing with single crystals. On the other hand, thin films regardless of fabrication method and substrate type, have much lower dielectric permittivity and higher microwave loss, in spite of recent extensive efforts to improve them (Gevorgian, 2001).

Thus, ***the problems addressed in this work*** are:

- To establish processing-structure-dielectric property relationships for $Sr_{1-x}Mg_xTiO_3$, $Sr_{1-x}Mn_xTiO_3$, $SrTi_{1-y}Mg_yO_{3-\delta}$ and $SrTi_{1-y}Mn_yO_3$ ceramics, including influence of doping site occupation and processing conditions on ceramics morphology, dielectric permittivity and tunability behaviour.

- To verify the existence of polar anomalies in the dielectric response of Mg- and Mn-doped ST and to elucidate the nature of polar state (if any) induced by these dopants.

- To develop $SrTiO_3$-based ceramics with high tunability of the dielectric constant and low loss to be used as tunable components for electronic devices.

1. Overview

1.1. Crystal structure of $SrTiO_3$ and its phase transition

As one of the double oxides with a general formula ABO_3, strontium titanate, $SrTiO_3$ (ST) is a member of the perovskite family. The prototype perovskite structure is cubic, where A cations (in this case Sr atoms) are situated at the cube corners, small B cation (in this case Ti atom) at the body centre and oxygen ions at the face centres, as represented in Figure 1.1a. The structure can also be viewed as a three-dimensional framework of BO_6 octahedra, arranged in a simple cubic pattern (Fig 1.1b). In the octahedron unit, B atom is at the centre with the oxygen atoms at the corners shared for different octahedron and with A cations in the space between (Last, 1957). Thus, the coordination numbers of A and B cations are 12 and 6, respectively, and the ideal perovskite unit cell contains one formula unit, i.e., one A cation, one B cation and 3 oxygen ions.

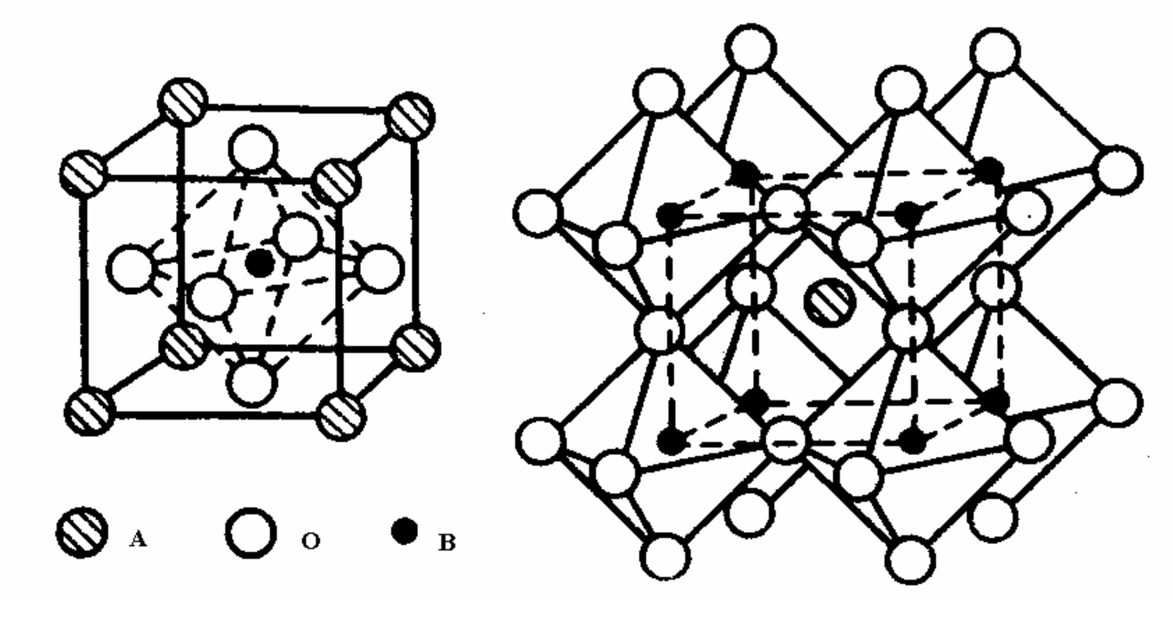

(a) (b)

FIGURE 1.1. Cubic perovskite structure with A-cation at origin (**a**) and with B-cation at origin (**b**).

The stability of the perovskite lattice is related to the high degree of ionic bonding and to the proper value of the Goldschmidt tolerance factor *t* that defines relation between the ionic radii in the perovskite lattice (Bhalla et al., 2000), as:

$$t = \frac{r_A + r_O}{\sqrt{2}\left(r_B + r_O\right)}, \tag{1.1}$$

where r_A and r_B stand for the average ionic radius at A and B-site respectively, and r_O stands for the ionic radius of the oxygen (equal to 1.40 Å (Shannon, 1976)). As can be seen from Eq. (1.1), when $t < 1$ the A ions fluctuate in their sites, whereas B ions are closely packed. And vice versa, when $t > 1$ the A ions are closely packed, while B ions fluctuate. The appropriate effective ionic radii for $SrTiO_3$ are: 1.44 Å for Sr^{2+} ion and 0.605 Å for Ti^{4+} ion (Shannon, 1976). Therefore, according to Eq. (1.1), the tolerance factor is very close to 1, confirming the very high packing density of $SrTiO_3$ for both A and B ions.

$SrTiO_3$ structure possesses two substitution sites for foreign cations: the Sr (or A) site and the Ti (or B) site. The incorporation of a foreign cation into the $SrTiO_3$ lattice depends on the ionic size and electronic structure of both the foreign ion and the substituted one.

At room temperature, strontium titanate has an undistorted cubic perovskite structure, which belongs to *Pm3m* space group, with a lattice parameter a = 3.905 Å (Mitsui and Westphal, 1961). $SrTiO_3$ undergoes an antiferrodistortive phase transition at a temperature T_a = 105-110 K. This close to second order structural phase transition from a high-temperature cubic to low-temperature tetragonal but centrosymmetric phase (Müller, 1959; Rimai and deMars, 1962; Lytle, 1967) with a doubling of the unit cell (Fleury et. al., 1968; Shirane and Yamada, 1969) is connected to an anti-phase tilting of the oxygen octahedra around one of the [100] axes, as presented in Figure 1.2a (Unoki and Sakudo, 1967). Hence no polarisation is induced in ST below T_a and the transition is a non-ferroelectric structural phase transition with almost no influence on the dielectric response. The order parameter of such transition is a rotation angle φ. The electron paramagnetic resonance (EPR) analysis of Fe-doped ST allowed Müller and Berlinger (1971) to measure the local symmetry and, consequently, φ, as shown in Figure 1.2b. Below the phase transition temperature, the structure is of the space group *I4/mcm* and has a unit cell of $\sqrt{2}\,a \times \sqrt{2}\,a \times 2c$, where a and c correspond to the tetragonal one-molecule unit (Shirane and Yamada, 1969).

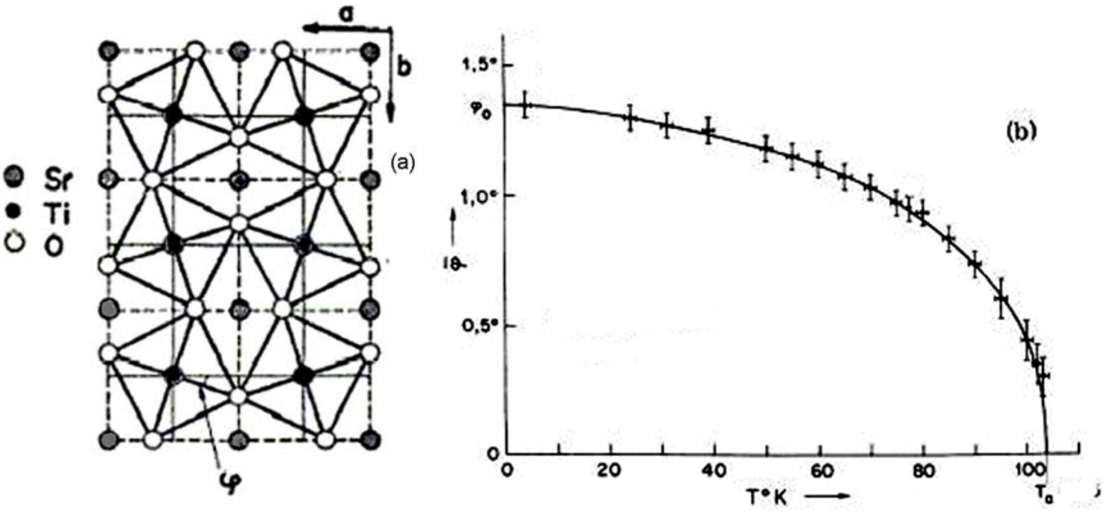

FIGURE 1.2. **a** - Oxygen octahedra tilting at antiferrodistortive phase transition of $SrTiO_3$ from cubic to tetragonal phase at 105-110 K (Unoki and Sakudo, 1967); **b** - tetragonal rotation angle φ of oxygen octahedra in $SrTiO_3$ as a function of temperature below T_a(Müller et al., 1968).

1.2. Dielectric behaviour of undoped $SrTiO_3$

1.2.1. Temperature dependence of permittivity and Landau-Ginsburg-Devonshire model

As mentioned before, strontium titanate belongs to the unique category of dielectric materials known as incipient ferroelectrics, along with $KTaO_3$, $CaTiO_3$ and TiO_2 (Lemanov et al., 1999). The dielectric constant of the incipient ferroelectrics gradually increases with the temperature decrease, reaching high values and remaining constant when the temperature approaches 0 K, but no peak is observed on the $\varepsilon' = f(T)$ curve and no ferroelectric phase transition occurred, as seen from Figure 1.3.

The paraelectric phase of incipient ferroelectrics is unstable and the application of a high enough electric field (Fleury et al., 1968), uniaxial stress (Uwe and Sakudo, 1976), oxygen isotope exchange (Itoh et al., 1999) or chemical substitutions in the lattice (Bednorz and Müller, 1984; Lemanov et al., 1996; Lemanov et al., 1997a; Ang et al., 1998, Guzhva et al., 2001) can easily induce the ferroelectric state in ST.

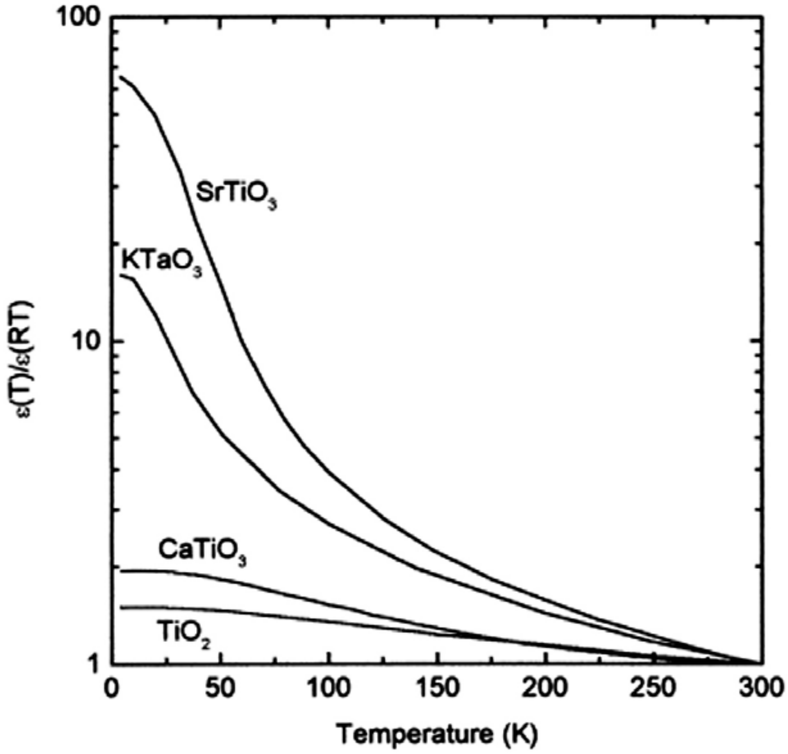

FIGURE 1.3. Temperature dependence of the relative dielectric constant *ε*(T)/*ε*(RT) in $SrTiO_3$, $KTaO_3$, $CaTiO_3$ and TiO_2. *ε*(RT) is the dielectric constant at room temperature (Lemanov et al., 1999).

By the definition, the ferroelectric state is characterised by a presence of spontaneous polarisation P_s of the material at the absence of external electric field, in a certain temperature and isotropic pressure range (Smolenskii, 1984), but the polarization can be switched by the application of an external electric field and, in some cases, by a mechanical stress. The phenomenological (or thermodynamic) approach proposed by Landau was used by Ginsburg and Devonshire for the macroscopic description of the phase transition in ferroelectric single crystals with a perovskite type structure, expanding the thermodynamic potential Φ of non-equilibrium state in power of the order parameter η identified as spontaneous polarization P_s:

$$\Phi = \Phi_0 + \frac{a'}{2}P_s^2 + \frac{b'}{4}P_s^4 + \frac{c'}{6}P_s^6 + \ldots, \tag{1.2}$$

where coefficients a', b', c' and so on are functions of temperature and pressure and Φ_0 is the thermodynamic potential for the case $P_s = 0$ (Venevtsev et al., 1985). Near the stability limit T_0, the last considered coefficient (b' or c' for second and first order phase transition, respectively) is assumed to be positive and practically temperature-independent, whereas the coefficient a' is supposed to show a critical temperature dependence $a'(T) = a_0(T-T_0)$, $a_0 > 0$ (Blinc and Zeks, 1974). Then, the dielectric constant (susceptibility $\chi' = \varepsilon'-1$, indeed) of these materials can be expressed as the second derivative of thermodynamic potential with respect to polarisation and its temperature dependence above the phase transition temperature can be expressed by the Curie-Weiss law:

$$\varepsilon' \approx \chi' = (\partial^2\Phi/\partial P_s^2)^{-1} = [a_0(T-T_0)]^{-1} = C/(T-T_0), \tag{1.3}$$

where $C = 1/a_0$ is the Curie constant and T_0 is the Curie temperature, above which ferroelectric material is in the paraelectric state. The transition temperature $T_C = T_0$ for second order phase transition, but $T_C > T_0$ for first order transition (see Figure 1.4). As also schematically shown in Figure 1.4, the second order transition is characterised by a smooth increase of P_s as temperature decreases starting from T_C, while for the first order transition the P_s jumps for some value at T_C with a further slight increase as temperature decreases (Smolenskii, 1984).

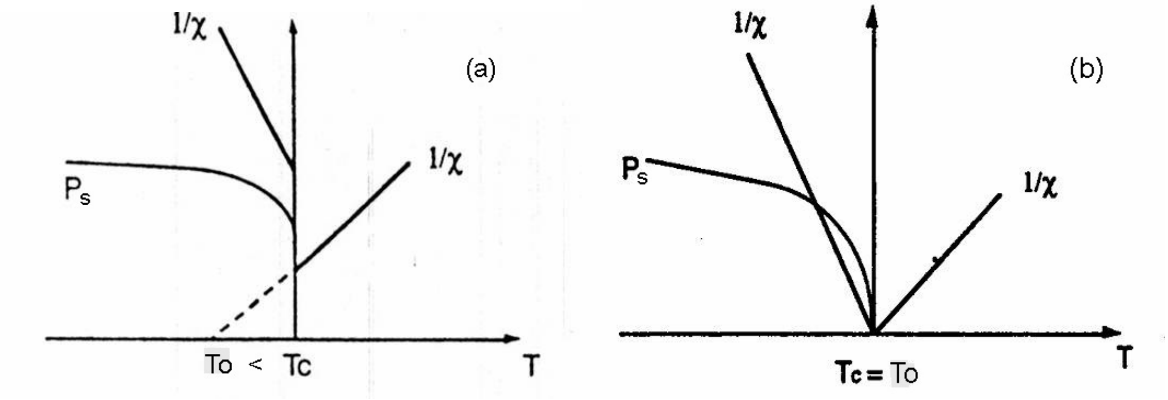

FIGURE 1.4. Temperature dependence of inverse dielectric susceptibility and spontaneous polarisation for first order (**a**) and second order (**b**) phase transitions.

From 300 K down to 70 K, the temperature dependence of permittivity of $SrTiO_3$ follows the Curie-Weiss law just as in an ordinary ferroelectric. Obvious deviation from the Curie-Weiss law begins below 50 K. The fitting to the Curie-Weiss law (Eq. 1.3) with the Curie constant of 8 × 10^4 K and Curie temperature of 35.5 K is shown in the inset of Figure 1.5 (Müller and Burkhard, 1979). However, no ferroelectric phase transition occurred and no peak of the $\varepsilon' = f(T)$ curve was observed at obtained value of T_C, both due to the quantum mechanical suppression of the ferroelectric fluctuations by the zero point motion of the ions (Müller and Burkhard, 1979; Zhong and Vanderbilt, 1996) and due to the antiferrodistortive cubic-to-tetragonal phase transition (Yamanaka et al., 2000; Kvyatkovskii, 2001; Zhong and Vanderbilt, 1995).

1.2.2. Low temperature quantum paraelectric behaviour of $SrTiO_3$ and Barrett relation

The temperature dependence of the real part of the complex-permittivity (ε') along the [110] direction of $SrTiO_3$ single crystal is shown in Figure 1.5. The low temperature permittivity of $SrTiO_3$ increases to about 2.4 × 10^4 upon cooling and remains constant below 4 K until 0.035 K rather than exhibits the dielectric discontinuity at T_C. This effect has been attributed by Müller and Burkhard (1979) to existence of a quantum paraelectric state at low temperature.

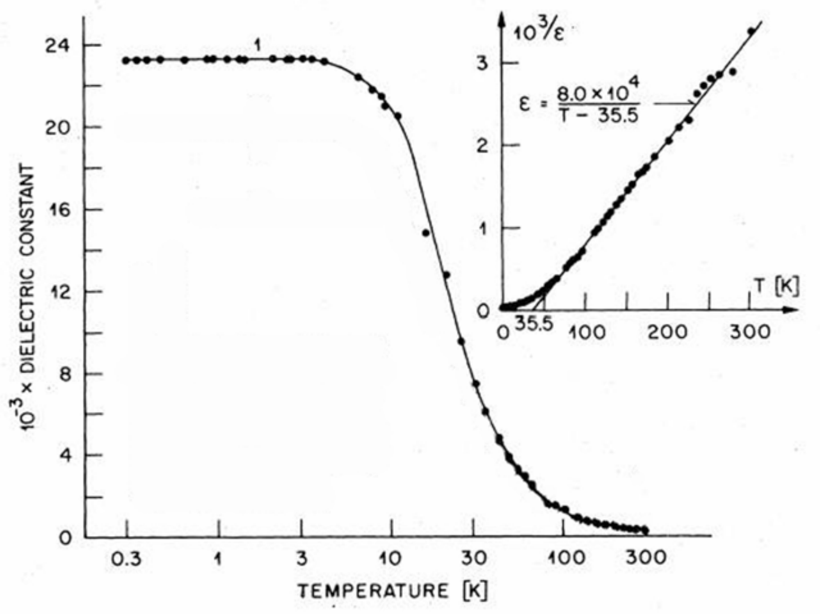

FIGURE 1.5. Temperature dependence of dielectric constant of the single-domain $SrTiO_3$ crystal along [110] direction [adapted from (Müller and Burkard, 1979)].

Thus, quantum effects are crucial for the understanding the dielectric properties of $SrTiO_3$ at low temperatures. The steep increase of the permittivity and its levelling-off at high values, as temperature approaches 0 K, was described by Barrett relation (Barrett, 1952), which is based on the mean-field theory taking quantum fluctuations into account:

$$\varepsilon' = C/[(T_1/2)\coth(T_1/2T) - T_0], \tag{1.4}$$

where C is the Curie-Weiss constant, T_1 is the temperature of the crossover between classical and quantum behaviour, and T_0 is the transition temperature at which the lattice instability would occur in the absence of quantum fluctuations. At $T >> T_1$ value $(T_1/2)\coth(T_1/2T)$ approximate to T and equation transforms into Curie-Weiss law.

Barrett theory is a quantum version of classical microscopic theory proposed by Slater to explain the dielectric behaviour of ferroelectric $BaTiO_3$ (Slater, 1950). Ti ion was supposed to be rather loosely bound in too large oxygen octahedron in $BaTiO_3$ and to act as independent harmonic oscillator with small additional anharmonic terms and the only interaction between these oscillators is through the electric field. Hence, the ferroelectric phase transition was supposed to be created by the displacement of anharmonicaly vibrating ions from the equilibrium, i.e., the displacement titanium ions with respect to oxygen ions. In such a way, the transition to the ferroelectric state is accompanied by a lowering of symmetry associated with the lowering of free energy. The Slater theory became the main theory of displacive-type phase transitions. According to Barrett, deviation from the Curie-Weiss law at low temperatures comes from the quantum effect on displacement of Ti ions (Barrett, 1952).

The quantum fluctuations, in rough approximation, originate from the Heisenberg uncertainty principle:

$$\Delta p \cdot \Delta q \geq \hbar/2, \text{ or equivalently } \Delta E \geq \hbar^2/(8m\Delta q^2). \tag{1.5}$$

Here, Δq denotes the uncertainty in the structural coordinate, which is related to the structural difference between the ferroelectric and paraelectric phases. ΔE is the energy uncertainty, or zero-point energy, which may prevent the occurrence of the distorted phase if it is larger than the reduction of classical free energy (Zhong and Vanderbilt, 1996). So, if the structural and energetic differences between the ferroelectric and paraelectric phases are small enough, quantum suppression may occur even for ions with fairly big mass *m*. The displacive ferroelectric transition in $SrTiO_3$ would be created by the shift of the titanium ions with respect to oxygen ions with displacement value of 0.045 Å, evaluated by Müller and Burkhard, 1979. At the same time, they have obtained a $\Delta q = 0.077$ Å > 0.045 Å, demonstrating that ferroelectric order is suppressed by quantum mechanical effects. Fitting of the experimental data to the Barrett relation yielded that quantum fluctuations are considerable below $T_1 = 80$ K (Müller and Burkhard, 1979).

1.2.3. Frequency dependence of dielectric permittivity and loss and Arrhenius law

The dielectric permittivity in general is a complex parameter, consisting of real part or dielectric constant ε' and imaginary part or loss factor ε'', although usually dielectric loss are described by $tan\delta = \varepsilon''/\varepsilon'$ (Jaffe et al., 1971). Both parts of the dielectric permittivity has been measured for $SrTiO_3$ single crystals (Linz, 1953; Sakudo and Unoki, 1971; Neville et al., 1972; Müller and Burkhard, 1979; Rupprecht and Bell, 1962; Viana et al., 1994; Mizaras and Loidl, 1997; Ang et al., 2000a) and ceramics (Neumann and Artl, 1986; Petzelt et al., 2001) in wide frequency and temperature range. No obvious frequency dispersion in dielectric constant of undoped $SrTiO_3$ was observed for temperatures of 10-300 K neither in single crystals (Neville et al., 1972) nor in ceramics (Petzelt et al., 2001). As shown in Figure 1.6a for ST ceramics, temperature dependences of the dielectric constant are coincident from radio frequency through microwave to terahertz range, implying that the static permittivity is essentially determined by the soft mode contribution (Petzelt et al., 2001). In all the frequency range of 10^2-10^{12} Hz, the maximum value of ε' in ST ceramics is reduced, compared to that of ST single crystals, conceivably due to a frozen dipole moment connected with the grain boundaries. On the other hand, high values of the dielectric constant reaching $\varepsilon' \sim 24000$ were observed for single-domain (i.e., without structural twins) ST single crystals below T_a (Dec et al., 1999) and just in [110] crystallographic direction (Sakudo and Unoki, 1971; Müller and Burkhard, 1979).

Neumann and Artl measured the dielectric permittivity of undoped $SrTiO_3$ ceramics in frequency range of 10^{-5}-10^3 Hz for temperatures of 373-523 K. A relaxation of the dielectric constant accompanied with pronounced dielectric loss peak was found in the ultra-low frequency range of 10^{-2}-10^{2} Hz, and was attributed to the Maxwell-Wagner relaxation at high temperatures (Neumann and Artl, 1986). The relaxation process was described by the Arrhenius phenomenological law:

$$\tau = \tau_0 \exp(U/k_B T) \qquad (1.6)$$

containing two temperature-independent parameters: activation energy $U = 0.7$ eV and pre-exponential factor $\tau_0 = (2\text{-}6) \times 10^{-2}$ s.

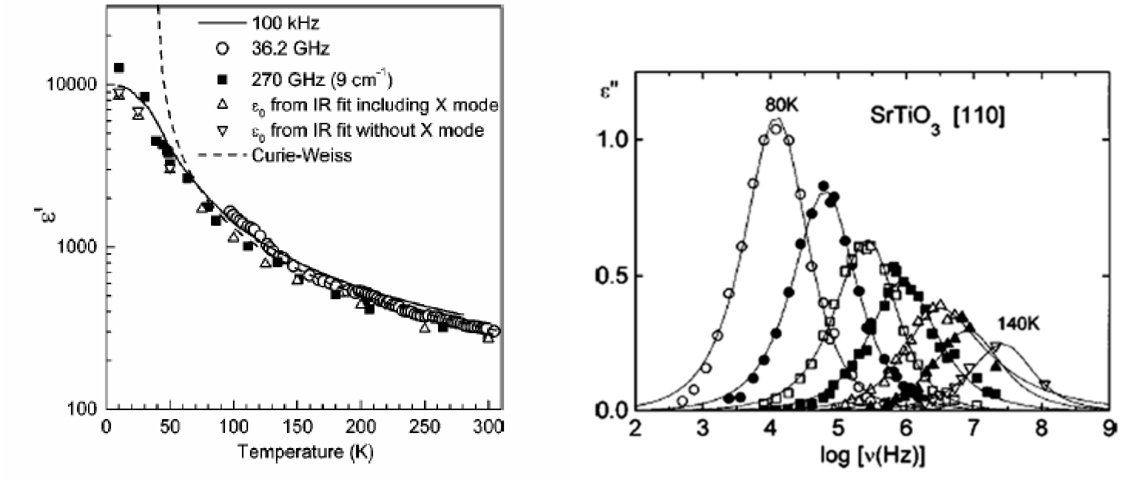

(a) (b)

FIGURE 1.6. Temperature dependence of ε' of $SrTiO_3$ ceramics at different frequencies (**a**) (Petzelt et al., 2001) and frequency dependence of ε'' of $SrTiO_3$ single crystal at different temperatures with electric field parallel to [110] (**b**) (Mizaras and Loidl, 1997).

Regarding a loss factor dependence on the frequency, *tanδ* linearly increasing with the frequency in microwave range (3-36 GHz) was observed in ceramic and single crystal $SrTiO_3$ in temperature range of 60-600 K (Rupprecht and Bell, 1962), while room-temperature loss tangent of 2.4×10^{-4}, independent on frequency in range between 10^{2} and 10^{7} Hz, has been reported earlier for $SrTiO_3$ single crystal (Linz, 1953). Later, a strong frequency dependent loss peak at 60-150 K for a frequency range of 10^{2}-10^{8} Hz, shown in Figure 1.6b, was observed for $SrTiO_3$ single crystals (Viana et al., 1994) and ceramics (Ang et al., 1999) and explained in terms of the dynamics of domain walls (Mizaras and Loidl, 1997). Elastic domains were supposed to appear at structural phase transition around

T_a = 105 K and domain-walls relaxation was found to be characterised by Arrhenius law with energy barrier U = 0.105 eV and pre-exponential factor $\tau_0 = 2 \times 10^{-11}$ s. The loss phenomena above T_a were connected with the precursor clusters and described with U = 0.143 eV and $\tau_0 = 3 \times 10^{-13}$ s (Mizaras and Loidl, 1997). On the other hand, the dielectric loss relaxation with similar Arrhenius law parameters was observed in ST by Ang et al. (2000a) and attributed to unavoidable defects or impurities (oxygen vacancies) interacting with the soft mode.

It is worth to mention that the loss peak under consideration was accompanied with rather small dielectric constant values [~10000-14000 in maximum (Viana et al., 1994; Ang et al., 2000a)], whereas no loss peak in this temperature range was observed for crystals in single-domain state with maximum ε' ~24000 (Dec et al., 1999). Thus, structural domain wall dynamics play an important role in the behaviour of both dielectric loss and dielectric constant of undoped ST.

Viana et al. (1994) found also that the loss relaxation near 10 K obeyed an Arrhenius law above ~9 K with U = 0.014 eV and $\tau_0 = 1.6 \times 10^{-11}$ s. The dynamics demonstrates a non-Arrhenius character at lower temperatures (Viana et al., 1994). This peak was observed in single-domain $SrTiO_3$ crystals also (Dec et al., 1999) and recent studies showed no detectable dependence of loss position on applied hydrostatic pressure (Venturini et al., 2004), implying that 10-K relaxation is simply due to an unknown impurity or defect.

1.2.4. Lattice dynamics of $SrTiO_3$ and Lyddane-Sachs-Teller relation

The small motion within the crystal may be described by normal mode vibrations. Ginsburg predicted the presence of dynamic lattice vibrations with frequency approximating to 0 as temperature approaches to T_C in ferroelectric crystals, whereupon Anderson and Cochran proposed more consistent microscopic approach (Venevtsev et al., 1985). Thus, Cochran has suggested that ferroelectricity in the perovskite titanates is connected with the lattice dynamics. Of central importance in his theory is the Lyddane-Sachs-Teller (LST) relation (Lyddane et al., 1941):

$$\omega_{LO}^2/\omega_{TO}^2 = \varepsilon_{dc}/\varepsilon_\infty \ , \tag{1.7}$$

written here for a diatomic lattice. ω_{LO} and ω_{TO} are the long-wave longitudinal and transversal optical phonon frequencies at Brillouin zone centre (Γ point), ε_{dc} is the static dielectric constant and ε_{∞} is the dielectric constant for frequencies well above all lattice modes, obtained by extrapolating the square of the index of refraction of the crystal. The rapid rise of ε_{dc} with decreasing temperature was associated with a mutual cancellation of the collective long-range forces, which cause the displacement of ions from the equilibrium state, and restoring forces resulting from the interaction with nearest neighbors. As a result of such compensation, the frequency of the transverse optical oscillation of the lattice reaches an anomalously small value, the crystal loses stability relative to the oscillation and a phase transition occurs. Thus, the dynamic theory of ferroelectricity, based on the idea of the soft mode near the phase transition, was created. In this theory, attention is focused on the active normal vibrations or active modes, rather than on active ions as in Slater theory (Smolenskii, 1984). Although, some authors calls the soft mode as a Slater mode.

The existence of the soft ferroelectric mode with the strong temperature dependence has been clearly demonstrated for $SrTiO_3$ by infrared reflectivity measurements (Barker and Tinkham, 1962; Spitzer et al., 1962) and by the inelastic neutron scattering technique, as shown in Figure 1.7a (Cowley, 1962).

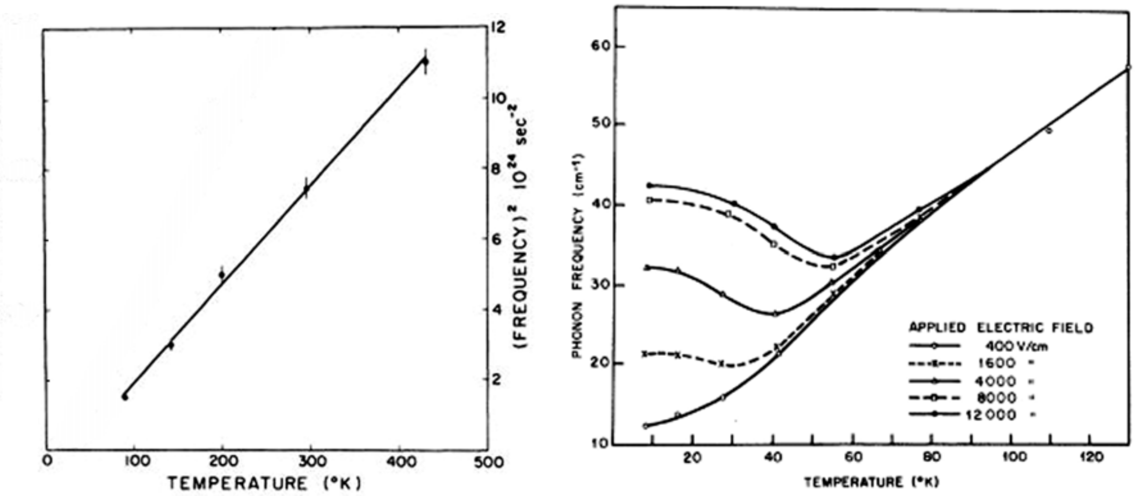

(a) (b)

FIGURE 1.7. Temperature dependence of the soft phonon mode obtained by inelastic scattering of slow neutrons (**a**) [adapted from (Cowley, 1962)] and by field induced Raman scattering for various values of applied electric field (**b**) (Worlock and Fleury, 1967).

In addition, the experimental results of field-induced Raman spectra of $SrTiO_3$, shown in Figure 1.7b, revealed that, with very small applied fields the soft-mode frequency varies with temperature from 85 cm^{-1} at 250 K to 10 cm^{-1} at 8 K (Worlock and Fleury, 1967, Fleury and Worlock, 1968). However, the soft-mode frequency shows no minima or zero value at attainable temperatures under small fields, confirming that a ferroelectric transition does not take place in $SrTiO_3$.Thus, the validity of the soft-mode theory has been proved and this concept has been widely applied to the more general field of structural transitions.

As an example, Fleury et al. (1968) observed the appearance of several sharp lines in the Raman spectra of ST below 110 K and a definite softening of two of these phonon frequencies as the temperature increases approaching T_a (see Figure 1.8a). Based on these facts a model was proposed, according to which: a) there is a soft mode at the antiferrodistortive transition in $SrTiO_3$, which frequency approaches zero as the temperature decreases to T_a, but at the Brilloin zone boundary (R point); b) the doubling of lattice constant at T_a leads to folding of Brilloin zone so that R point is in the zone centre and hence the number of zone-centre excitations increases and c) two new zone-centre phonons (R-modes), whose progenitor was the zone-boundary phonon, increase in frequency or harden as T is lowered from T_a (Unoki and Sakudo, 1967; Fleury et al., 1968).

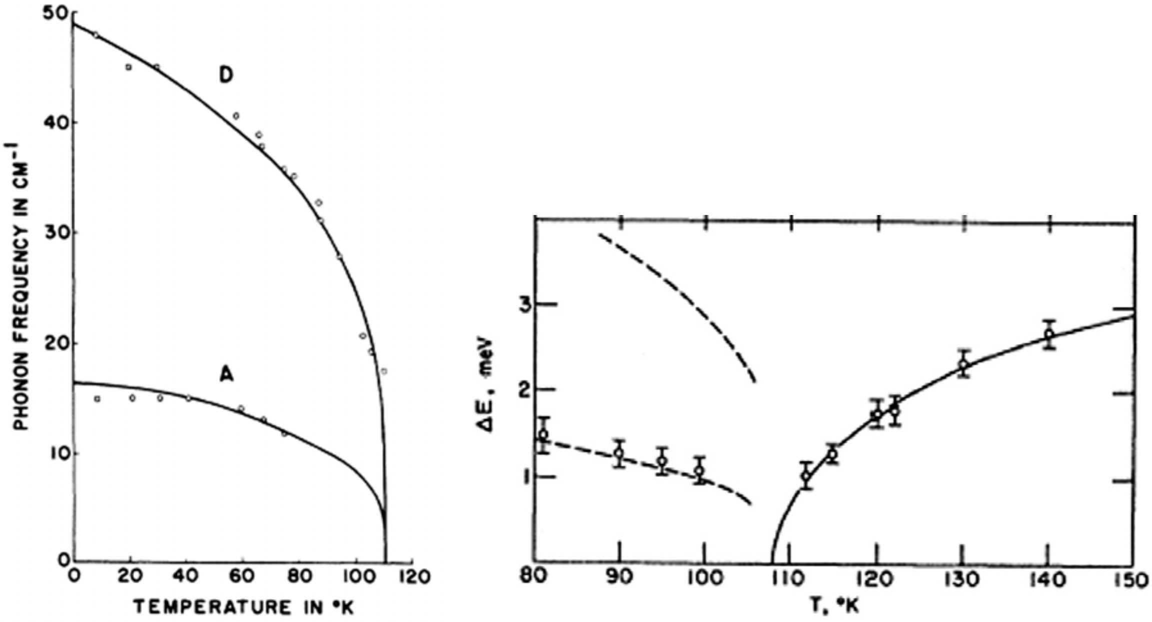

(a) (b)

FIGURE 1.8. Temperature dependence of the phonon modes obtained by Raman scattering (**a**) (Fleury et al., 1968) and by inelastic neutron scattering (**b**) (Shirane and Yamada, 1969).

The correctness of this model was supported by the shift of the sound velocity at T_a (Bell and Rupprecht, 1963; Rupprecht and Winter, 1967) and confirmed by EPR measurements (Müller et al., 1968; Thomas and Müller, 1968). Shirane and Yamada (1969) obtained a temperature dependence of the progenitor zone-boundary phonon mode above T_a along with one of the R-modes below T_a by inelastic neutron scattering measurements. Thus, the picture of the modes around structural phase transition in ST was completed in full agreement with the model discussed above, as shown in Figure 1.8b.

1.2.5. Field-induced permittivity peak and tunability

The spectrum of the field induced Raman scattering of $SrTiO_3$ exhibited a field-dependent structure at low temperatures (<55 K) revealing also a broad minimum in the temperature dependence of the soft phonon mode frequency under bias field $E \geq 1.6$ kV/cm and shift of this minimum with increasing field to higher temperature, as shown in Figure 1.7b (Worlock and Fleury, 1967). Consequently, according LST relation, a peak in temperature dependence of the dielectric constant of ST should be expected under strong enough bias electric field.

Figure 1.9a presents a temperature dependence of the dielectric constant of ST single crystal at different bias fields obtained by Saifi and Cross (1970). No peak but a reducing of low-temperature dielectric constant was observed in the $\varepsilon'(T)$ under dc bias increasing from 0 to 0.648 kV/cm. However, at further increase of an electric field, a broad peak in the $\varepsilon'(T)$ appear with the peak temperature shifting towards higher values with increasing fields (Saifi and Cross, 1970), as was expected.

As was shown by Müller and Burkhard (1979), in strontium titanate as in typical example of incipient ferroelectrics / quantum paraelectrics, Ti ions tend to displace from the centre position of oxygen octahedra for 0.045 Å, but cannot do it due to the quantum fluctuations of larger value. In other words, there are off-centre local potential minima, but they are not deep enough to fix the titanium ions. The application of a bias electric field stabilises the local potential of a dipolar entity, making one of its potential minima deeper and other shallower, what is schematically shown for one-dimensional case in the top inset of Figure 1.9a. Thus, at certain bias value, the zero-point energy is not enough to overcome the deeper barrier and thermal energy is necessary, what corresponds to the appearance of the peak in the $\varepsilon'(T)$. As higher bias electric field, as bigger thermal energy is necessary to overcome the deeper barrier, leading to higher peak temperature. Additionally, the field aligns and clamps the polarisation of the sample, suppressing ε'.

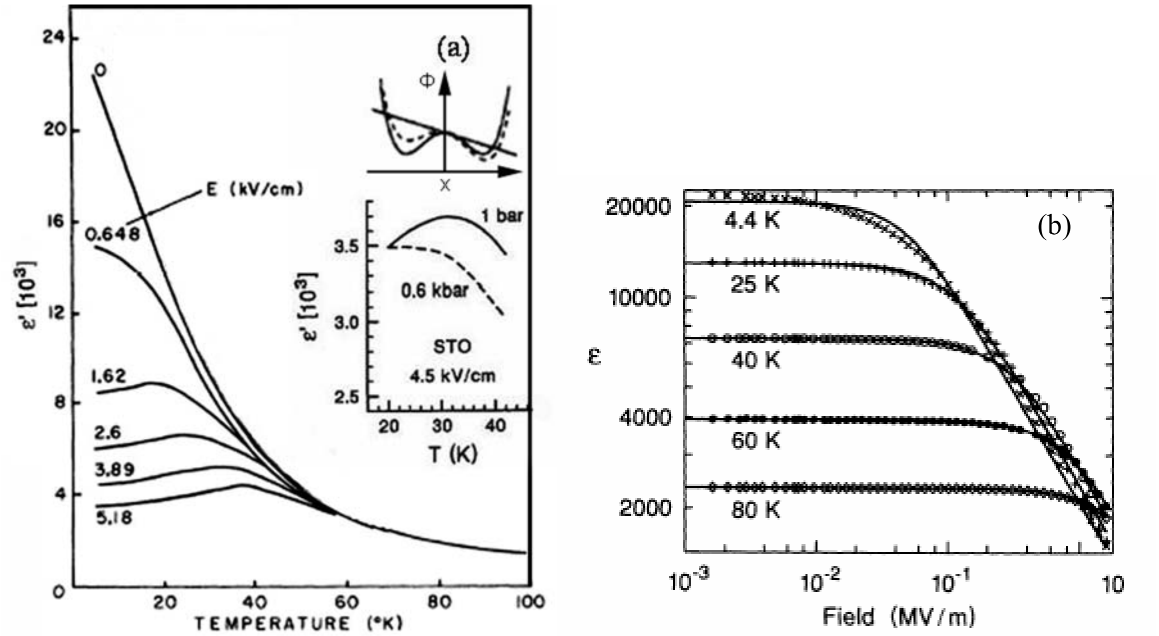

FIGURE 1.9. Dielectric constant of $SrTiO_3$ single crystals at 1 kHz as a function of temperature under different dc fields (**a**) (Saifi and Cross, 1970) and as a function of dc field at different temperatures (**b**) (Christen et al., 1994). The insets depict the effect of the bias on the potential for the hopping of dipolar entities and the suppression of the field induced ferroelectric instability in $SrTiO_3$ by hydrostatic pressure (Venturini et al., 2003).

The maxima occurred in ε'(T) of ST were reported to be accompanied with a double loop hysteresis (Saifi and Cross, 1970; Eriksson et al., 2003), and to look as normal ferroelectric hysteresis with non-zero remnant polarisation (Hemberger et al., 1995; Itoh et al., 1999). The former was attributed to the dc field-induced processes associated with impurities (Gevorgian et al., 2002), while the latter indicates the onset of induced displacive-type ferroelectric state (Hemberger et al., 1995; Itoh et al., 1999). In addition, the field induced ferroelectric instability in $SrTiO_3$ was shown to be easily suppressed by applying moderate hydrostatic pressure (Venturini et al., 2003), as shown in bottom inset of Figure 1.9a.

Figure 1.9b presents the wide range bias-field dependence of the dielectric constant of $SrTiO_3$ single crystal (Christen et al., 1994), exhibiting strong enough decreasing of dielectric constant with field at rather low temperatures. This effect is well explained from

Landau free energy theory: at temperatures close to a ferroelectric phase transition, where the dielectric susceptibility becomes very large, the polarisation which can be induced by even moderate external fields can be very substantial. Under these conditions, dielectric non-linearity becomes very important (Lines and Glass, 1977). Considering the thermodynamic potential term P^4 (here P includes spontaneous and induced polarisation) as a lowest-order non-linear dielectric term in the free energy expansion one obtains:

$$E = \partial\Phi/\partial P = a_0(T-T_0)\,P + b\,P^3 \quad \text{and} \quad \varepsilon^{-1} = \partial^2\Phi/\partial P^2 = a_0(T-T_0) + 3\,b'\,P^2 \qquad (1.8)$$

Then, above T_C, where the spontaneous polarisation $P_s = 0$: ε is proportional to E^{-2} for small field and to $E^{-2/3}$ for higher field, when non-linear term in the first equation (1.8) is dominant (Lines and Glass, 1977). It also can be shown that the phase transition temperature T_C is proportional to $E^{2/3}$ for a ferroelectric with a second-order phase transition (Lines and Glass, 1977).

As presented in Figure 1.10 (a, b), temperature T_m of the peak in $\varepsilon'(T)$ induced by a dc bias field was found to be proportional to $E^{2/3}$ in $SrTiO_3$ crystal implying the ferroelectric origin of the peak (Ang et al., 2000a). An additional evidence of the onset of ferroelectricity by a dc bias field is a field-dependent peak in $tan\delta(T)$, accompanying the peak in temperature dependence of the dielectric constant. The dielectric-loss-peak temperature and magnitude of the peak at 10 kHz as a function of a field are shown in Figure 1.10 (c and d, respectively), where marked as “peak A” (Ang et al., 2000b).

Figure 1.10c also shows that, in contrast to “induced peak A”, a “defect mode I”, mentioned above and attributed to the structural domain wall dynamics (Viana et al., 1994; Mizaras and Loidl, 1997; Ang et al., 2000a), is field independent (Ang et al., 2000b). However, for both loss peaks measured at 10 kHz, their magnitudes increase with the bias field until certain field value, decreasing for higher dc bias, as shown in Figure 1.10d. At the same time, a significant increase of the loss factor of ST with increasing dc field was observed at 1 GHz near liquid nitrogen temperature (Vendik et al., 1995; Gevorgian et al., 1996), and further at 52 and 40 K (Gevorgian et al., 2002; Eriksson et al., 2003).

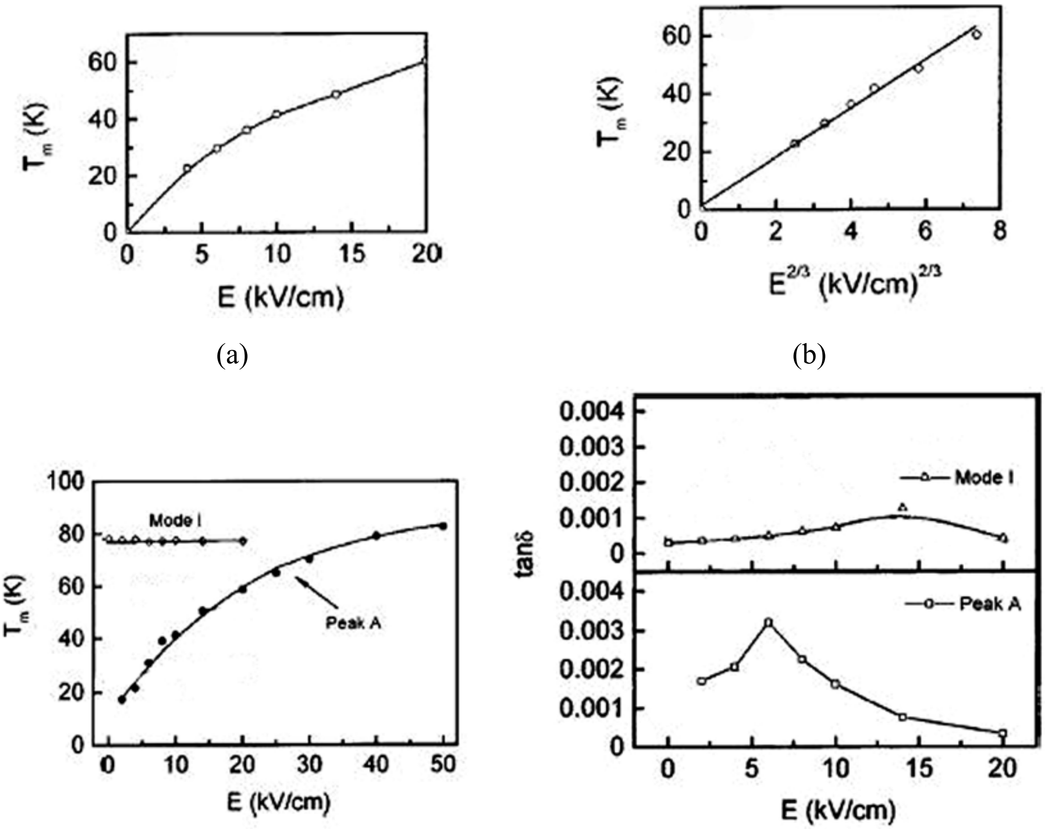

(a) (b)

(c) (d)

FIGURE 1.10. Field dependence of dielectric-constant (**a**, **b**) and dielectric-loss (**c**) peak temperatures and of dielectric-loss peak magnitudes (**d**) for $SrTiO_3$ single crystals at 10 kHz [adapted from (Ang et al., 2000b)].

There are two parameters used for the characterisation of the dependence of the dielectric permittivity on the applied dc bias electric field: 1) tunability n, defined as the ratio of the dielectric constant of the material at zero electric field to the dielectric constant at some non-zero electric field and 2) relative tunability n_r, defined as

$$n_r(E) = [\varepsilon'(0) - \varepsilon'(E)]/\varepsilon'(0) = (n - 1)/n, \qquad (1.9)$$

where $\varepsilon'(0)$ is the dielectric constant at zero field and $\varepsilon'(E)$ is the dielectric constant under applied field E.

Ang et al. (2000a) reported that a relative tunability up to 88% can be reached under 20 kV/cm near 12 K, as shown in Figure 1.11. Besides aforementioned publications, dc electric field dependence of the dielectric properties of $SrTiO_3$ single crystals has been studied in several other works (Vendik and Zubko, 1997; Wooldridge et al., 1999; Dec et al., 1999).

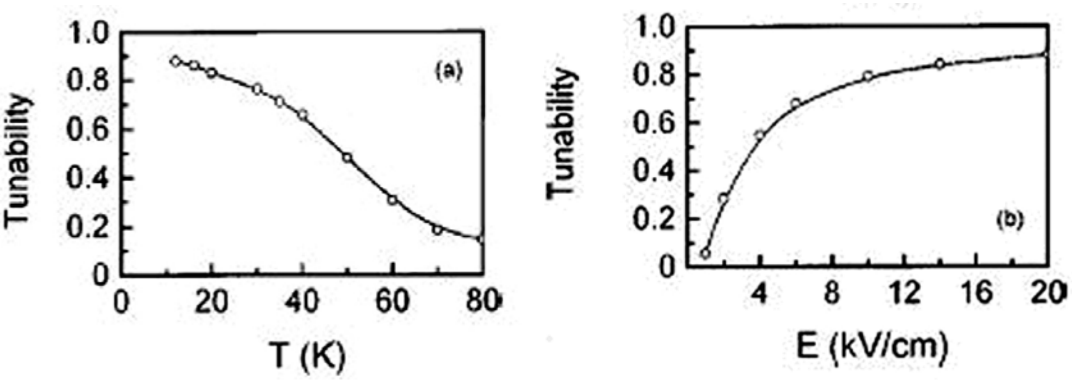

FIGURE 1.11. Relative tunability of $SrTiO_3$ single crystal at 10 kHz as a function of temperature under 20 kV/cm (**a**) and as a function of dc field at 12 K (**b**) (Ang et al., 2000a).

1.2.6. Stress-induced permittivity peak

As mentioned above, ferroelectric phase transitions can generally be analysed by phenomenological theory employing a thermodynamical free energy, though the situation is rather complicated in the case of $SrTiO_3$ at low temperatures due to the coexistence of the two types of soft phonon modes. That is, two kinds of order parameter, one represented by the polarisation and another one by the rotation of the oxygen octahedra, should be involved in the free energy. Interaction between them and also with the lattice strain or stress must be taken into account.

The dielectric constant and the frequencies of the ferroelectric and structural soft modes were derived theoretically as a function of the stress by Uwe and Sakudo (1976). Stress-induced ferroelectricity was experimentally observed in $SrTiO_3$ at liquid helium temperature by using both dielectric measurements and Raman scattering experiments under uniaxial (010) or (110) stress (Uwe and Sakudo, 1976, and references therein). The inverse dielectric susceptibilities γ_i were found to change linearly with stress σ up to critical values where γ_i for polar directions show minima and those for lateral directions exhibit upward kinks, as presented in Figure 1.12a. For the (010) and (110) stresses, the critical values are $\sigma_{c1} = (1.6 \pm 0.2) \times 10^8$ N/m^2 and $\sigma_{c2} = (5.8 \pm 0.2) \times 10^8$ N/m^2, respectively. By means of Raman scattering measurements, the ferroelectric soft modes were observed above the critical stresses (Uwe and Sakudo, 1976). Their frequencies have been found to change concurrently with the behaviour of the dielectric constants, following LST relation. As shown in Figure 1.12b, the frequency of the total symmetric ferroelectric mode has been found to become vanishingly small as the stress approaches the critical values σ_{c1} and σ_{c2}.

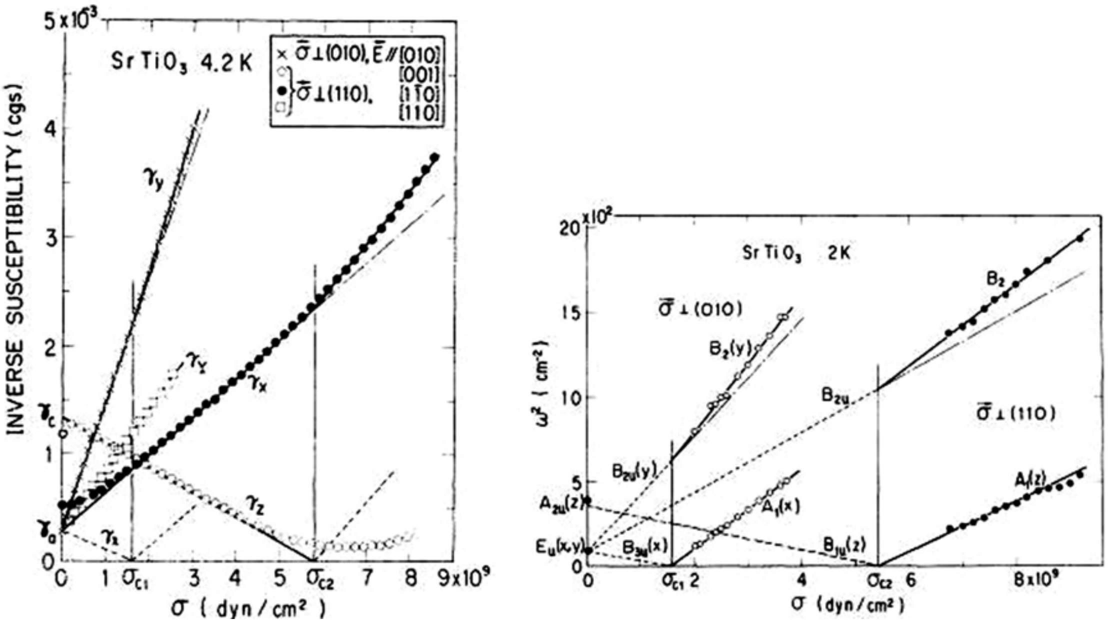

(a) (b)

FIGURE 1.12. Inverse dielectric susceptibilities γ_i (**a**) and squared frequencies of vibrational modes ω^2 (**b**) as a function of stress load σ for $SrTiO_3$ at 4.2 K. γ_x and γ_y are inverse dielectric susceptibilities for (010) stress, and γ_X, γ_Y and γ_Z for (110) stress (Uwe and Sakudo, 1976).

1.2.7. Permittivity peak induced by oxygen isotope exchange

Recently, ferroelectricity below 23 K was induced in $SrTiO_3$ by the isotope exchange of ^{18}O for ^{16}O and was confirmed by the observation of the hysteresis loop supported by the measurement of pyroelectricity (Itoh et al., 1999; Itoh and Wang, 2000). However, in spite of several indications of corresponding lowered symmetry, shown below, no structural change was detected by powder X-ray diffraction and no anomaly was found in heat capacity near T_C (Itoh et al., 1999), thus indicating that the system rather transforms into a disordered or very short-ranged polar state (Dec et al., 2005).

Figure 1.13 presents the temperature dependence of the dielectric constant of single-domain $SrTi(^{16}O_{1-x}{}^{18}O_x)_3$ crystals, measured at frequency 10 kHz and with a test signal amplitude E_0 = 0.4 V/cm. No peak but an increase of low-temperature dielectric constant was observed in the $\varepsilon'(T)$ for samples with x increasing from 0 to 0.26. However, at further increase of x, a strong peak in the $\varepsilon'(T)$ appear with the peak temperature shifting towards higher values with increasing x, as shown in Figure 1.14a.

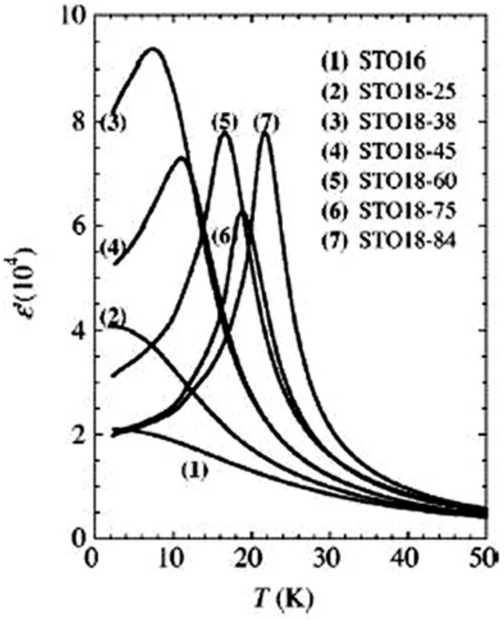

FIGURE 1.13. Temperature dependence of dielectric constant of $SrTi(^{16}O_{1-x}{}^{18}O_x)_3$ single crystals with x = 0 (1), 0.25 (2), 0.38 (3), 0.45 (4), 0.60 (5), 0.75 (6) and 0.84 (7) at 10 kHz (Wang and Itoh, 2001).

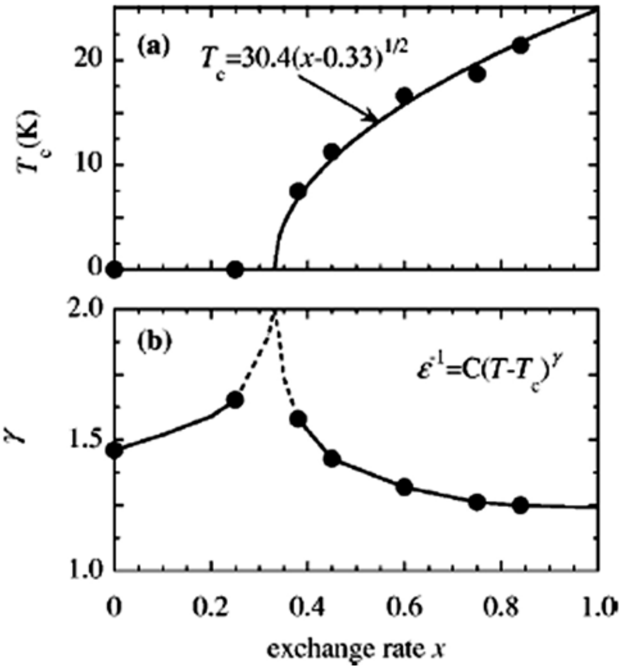

FIGURE 1.14. Compositional dependence of peak temperature (**a**) and effective exponent γ (**b**) of $SrTi(^{16}O_{1-x}{}^{18}O_x)_3$ single-domain crystals (Wang and Itoh, 2001).

Value of 172000 observed for $SrTi(^{16}O_{1-x}{}^{18}O_x)_3$ with $x = 0.37$at 3.1 K and E_0 = 14 V/cm is the largest value ever reported for both classical and quantum ferroelectrics (Itoh and Wang, 2000). However, further studies showed that ε' is considerably enhanced by E_0 for all the compositions at $T \leq 40$ K (Wang and Itoh, 2000). The E_0-enhanced ε' was speculated to come from the motion of sizable domain walls. Thus, the low-temperature state of $SrTi(^{16}O_{1-x}{}^{18}O_x)_3$ is a domain state induced by random fields, probably originated from the twin boundaries, the extrinsic oxygen vacancies and the random Ti-O interaction induced by the ^{18}O-isotope exchange (Wang and Itoh, 2001). The observation of frequency dispersion (Wang et al., 2000b), the long-term non-exponential relaxation of the remnant polarisation and other data (Wang and Itoh, 2001) have been supported this idea.

Though maximum ε' value of single-domain $SrTi(^{16}O_{1-x}{}^{18}O_x)_3$ is just 94000 but not 172000 at E_0 = 0.4 V/cm, the T_C versus x behaviour, shown in Figure 1.14a, expresses the same trends for both single- and multi-domain samples (Wang and Itoh, 2001). In particular, T_C obeys the relation typical for doped incipient ferroelectrics (Vugmeister and Glinchuk, 1990): $T_C = A(x - x_c)^{1/2}$, where factor A = 30.4 K and critical concentration x_c = 0.33. A departure from the Curie-Weiss law was observed in the vicinity of the temperature of the maximum dielectric constant T_m. Thus, $\varepsilon'(T)$ data on the high temperature side of T_m (T_m+25 K < T < T_m+50 K) were fitted well to the formula, as characteristic for relaxor materials (Smolenskii, 1970): $1/\varepsilon' - 1/\varepsilon'_m = (T - T_m)^\gamma / C$, where the exponent γ deviates from a value of 1 and increases considerably in vicinity of x_c = 0.33, as shown in Figure 1.14b.

Brillouin scattering measurements performed on $SrTi^{18}O_3$ have revealed new acoustic anomalies near the ferroelectric phase transition at T_C; the antiferrodistortive transition point was found to be higher for $SrTi^{18}O_3$ (108 K) than for $SrTi^{16}O_3$ (105 K), but no other obvious differences were observed (Yamaguchi et al., 2001). However, afterwards light scattering measurements showed that $SrTi^{18}O_3$ undergoes a phase transition of displacive type to low-temperature phase of *Pmm2* point group, which is caused by the condensation of the ferroelectric soft mode about 20 K, although this mode does not soften completely (Hasebe et al., 2003).

Ferroelectric domain structure of $SrTi^{18}O_3$ was determined by tensor analyse of the second-harmonic response below T_C (Zhang et al., 2002a). Low-temperature properties of $SrTi^{18}O_3$ single crystal were found to be intimately related to the change of the local multidomain state, formed by eight types of triclinic polar domains, which transform into an orthorhombic single domain under an electric field. This complex mixture of domains and interplay between different symmetries could explain the difficulties in the observation of a distinct soft mode in ferroelectric phase with Raman scattering (Yagi et al., 2002).

A systematic research of the effects of pressure on the ferroelectricity of multidomain (100)-oriented $SrTi^{18}O_3$ and the quantum paraelectricity of $SrTi^{16}O_3$ revealed: 1) depressing ε' for both $SrTi^{18}O_3$ and $SrTi^{16}O_3$; 2) extending quantum paraelectric range to higher temperatures; and 3) suppressing T_C for $SrTi^{18}O_3$ (Wang et al., 2000b). The initial pressure derivative of $T_C(p)$ dependence and critical pressure value, at which phase transition is suppressed, was estimated to be -13.5 K/kbar and 0.5-0.7 kbar, respectively.

Further more complete studies showed qualitatively similar behaviour for single-domain 110-oriented SrTi^{18}O$_3$, presented in Figure 1.15, though initial slope dT_C/dp = -20 K/kbar was obtained. $T_C(p)$ data were found to follow the equation $T_C = A(1 - p/p_C)^{1/2}$, with A = 23.9 K and p_C = 0.69 kbar, as shown in the inset to Figure 1.15 (Venturini et al., 2004). In addition, T_C for SrTi^{18}O$_3$ was found to shift with bias electric field with a rate of 7 K·cm/kV, what is almost 4 times bigger than the shift rate of the temperature of the bias-field induced-peak for SrTi^{16}O$_3$.

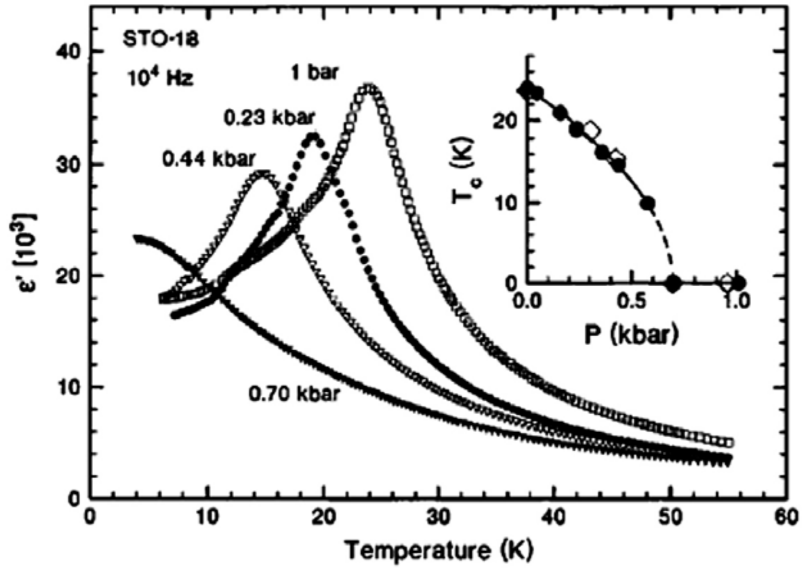

FIGURE 1.15. Temperature dependence of dielectric constant of SrTi^{18}O$_3$ single crystal at 10 kHz under different pressure (Venturini et al., 2004). Inset shows the shift of T_C with pressure for (110)-oriented single-domain crystal (solid circles) and (100)-oriented multidomain crystal [open diamonds from (Wang et al., 2000b)].

The substitution of heavy isotope ^{18}O for ^{16}O in SrTiO$_3$ simultaneously results in a significant enhancement of relative tunability and in a large reduction of driving electric field at cryogenic temperatures, as shown in Figure 1.16. For 36% oxygen isotope exchanged SrTiO$_3$ at 2-10 K, the driving electric field for the relative tunability of 0.82 is about 1 kV/cm, what is half an order lower than that for an unexchanged one (Wang and Itoh, 2002).

Further more detailed analysis of the non-linear dielectric response of SrTi^{18}O$_3$ as a function of temperature and dc bias field strength showed that the classic field scaling applies to strong fields and high temperatures $T > 1.1T_C$ (Kleemann et al., 2003). In weak electric fields and within $T_C < T < 1.1T_C$, the existence of a fluctuation-controlled quantum ferroelectric phase transition was proved by the sudden drop of non-linearity coefficient $b'/(a')^4$ (see Eqs. 1.2 and 1.8). In addition, it was concluded that random-field-induced domain state evolving at $T < T_C$ does not represent a new glassy phase (Kleemann et al., 2003).

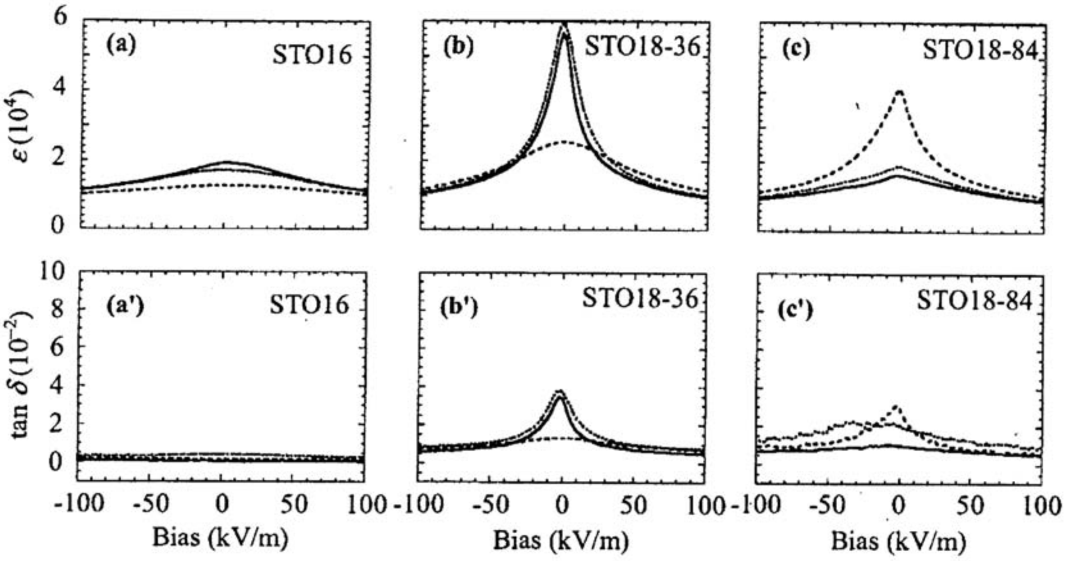

FIGURE 1.16. The dielectric constant ε and loss $\tan\delta$ as a function of bias field for $SrTi^{16}O_3$ (**a** and **a'**), $SrTi(^{16}O_{0.64}{}^{18}O_{0.36})_3$ (**b** and **b'**) and $SrTi(^{16}O_{0.16}{}^{18}O_{0.84})_3$ (**c** and **c'**) at temperatures 2 K (solid), 10 K (dotted) and 20 K (dashed), respectively (Wang and Itoh, 2002).

The evolution of ferroelectricity in $SrTi^{18}O_3$ was ascribed mainly to the suppression of the quantum fluctuations in $SrTi^{16}O_3$ by the heavy oxygen isotope substitution (Wang and Itoh, 2001; Kvyatkovskii, 2001) and the additional softening of soft mode (Venturini et al., 2004). However, this ferroelectric differs from the prototype in two aspects: the exhibition of domain state at $T < T_C$ (Wang and Itoh, 2000) and the existence of ferroelectric microregions at $T > T_C$ (Yagi et al., 2002).

Very recently Ti and Sr nuclear magnetic resonance (NMR) spectra of ^{18}O enriched $SrTiO_3$ provided direct evidence that the ferroelectric phase transition occurs in two steps (Blinc et al., 2005). Below 70 K, rhombohedral polar clusters are formed in a non-polar tetragonal matrix. Subsequently, these clusters grow in concentration, freeze out, and percolate, leading to an inhomogeneous ferroelectric state below T_C. This shows that the ferroelectric transition in $SrTi^{18}O_3$ is indeed connected with the local symmetry lowering and implies the existence of an order-disorder component in addition to the displacive soft mode one. Rhombohedral clusters, Ti disorder, and a two-component state are found for $SrTi^{16}O_3$ as well, though the concentration of the rhombohedral polar clusters is not enough to allow for percolation (Blinc et al., 2005).

Thus, recent studies on isotopically exchanged $SrTi^{18}O_3$ confirm that “normal” $SrTi^{16}O_3$ is actually very close to the ferroelectric transition, which does not occur at measurable temperatures (Itoh et al., 1999).

1.3. Dielectric behaviour of doped $SrTiO_3$

As demonstrated in the previous section, the dielectric constant of undoped $SrTiO_3$ is strongly dependent on dc bias field in the low temperature range. However, in order to shift the high-tunability temperature range to room or at least liquid nitrogen temperature, much work has been carried out through doping $SrTiO_3$ with different impurities (Lemanov, 1999).

In strontium titanate perovskite structure with a general formula ABO_3, there are two kinds of possible substitution sites: 1) Sr^{2+} site (or A-site) and 2) Ti^{4+} site (or B-site).

From the reported results, it appears that isovalent B-site dopants, such as Zr^{4+}, Sn^{4+}, Ge^{4+}, have much smaller effect on dielectric properties of $SrTiO_3$, comparing with isovalent A-site dopants (Ca^{2+}, Ba^{2+}, Pb^{2+}, Cd^{2+}) (Lemanov et al., 2002). On the other hand, dielectric transition-like anomalies with remarkable frequency dispersion were observed in $SrTiO_3$ doped with A-site aliovalent dopants, such as rare-earth ions (Johnson et al., 1970; Iguchi and Lee, 1993) and Bi^{3+} (Ang et al., 1998). Thus, the influence of A-site isovalent and aliovalent dopants on dielectric behaviour of ST-based solid solutions is reviewed in the following subsections.

1.3.1. $Sr_{1-x}Ba_xTiO_3$ solid solutions

Based on extrapolation of the Curie temperature of the $BaTiO_3$ - $SrTiO_3$ (BST) solid solution, Rushman and Strivens were the first who came in 1946 to the conclusion that strontium titanate is a ferroelectric, whose Curie temperature is near 0 K (Smolenskii, 1984). Since that time, BST solid solutions have been a subject of extensive study, mostly for high $BaTiO_3$ concentration range and at temperatures above 100 K (Jaffe et al., 1971; Lin and Wu, 1990). Barium strontium titanate $Sr_{1-x}Ba_xTiO_3$, as its end members $SrTiO_3$ and $BaTiO_3$, has a perovskite-type structure and a solid solution can be obtained in the whole composition range, as can be seen from the phase diagram shown in Figure 1.17a. In contrast to quantum paraelectric $SrTiO_3$, $BaTiO_3$ transforms from cubic paraelectric phase (point group *Pm3m*) to three ferroelectric phases below 393 K: first to *P4mm* tetragonal, then to *Pmm2* orthorhombic at about 273-278 K and finally to *R3m* trigonal phase below 183 K. The polar axis for three ferroelectric phases is [001], [011] and [111] respectively and all three phase transitions are displacive type ones of first order (Lines and Glass, 1977).

Decreasing $BaTiO_3$ content leads to a linear decrease of all the phase transition temperatures, but with different rates. Thus, a multicritical point around $x = 0.15$ appear in the phase diagram, where the three phase transition lines converge, and four phases are in equilibrium. Near this point the structural phase transition characteristic of ST is also likely to converge with the ferroelectric transition (Lemanov et al., 1996). At further decrease of x, T_C obeys the relation, typical for doped incipient ferroelectrics (Vugmeister and Glinchuk, 1990):

$$T_C = A(x - x_c)^{1/2}, \tag{1.10}$$

where factor A = 300 K and critical concentration $x_c = 0.035$. And finally a very small addition of $BaTiO_3$ to $SrTiO_3$ ($x < x_c = 0.035$) induces a glasslike state, rather than ferroelectric one. This was supported by: 1) the absence of ferroelectric hysteresis loops; 2) a frequency dispersion of the dielectric constant and 3) a time dependence of the dielectric constant after field cooling (Lemanov et al., 1996).

Later, two relaxation processes were observed in BST ceramics with Ba content x = 0.005-0.1 in temperature ranges 15-50 and 55-100 K. The frequency dispersions of the dielectric response were characterised by Arrhenius law parameters U_1 = 0.04-0.045 eV, $\tau_{01} = (0.5\text{-}50) \times 10^{-11}$ s and U_2 = 0.10-0.12 eV, $\tau_{02} = (1\text{-}10) \times 10^{-11}$ s, respectively, although their mechanisms are not quite clear at present (Sotnikov et al., 1999).

The temperature dependence of the dielectric constant of BST bulk ceramics is illustrated in Figure 1.17b. It is evident that the temperature of the paraelectric-ferroelectric phase transition in $Sr_{1-x}Ba_xTiO_3$ increases linearly with x with the slope $dT_C/dx \approx 360$ K (Lemanov, 1999). T_C versus x dependence was found to be close for BST ceramics and single crystals (Tagantsev et al., 2003; Lemanov et al., 1996). In addition, a diffused phase transition is observed for $x < 0.5$ (Benguigui and Bethe, 1976).

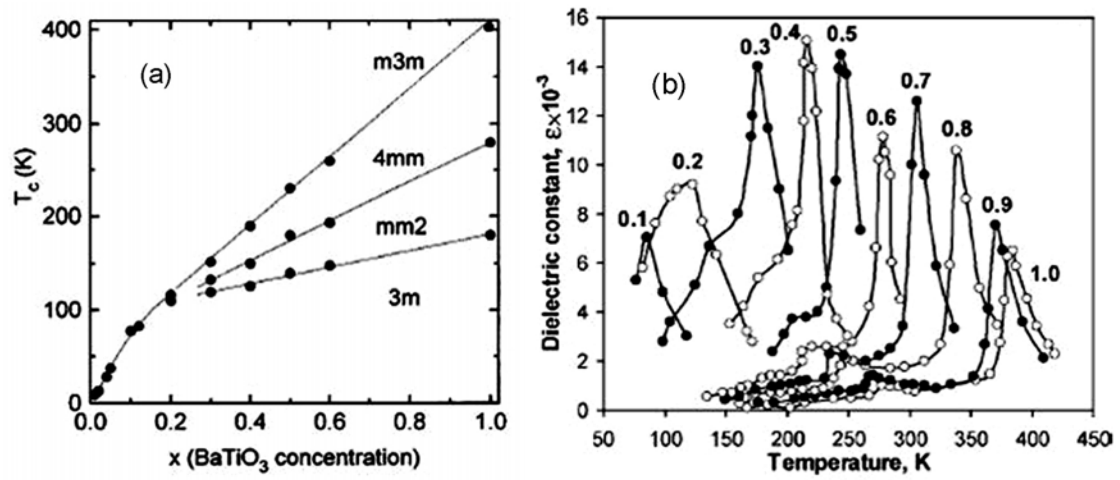

FIGURE 1.17. The phase diagram (**a**) (Lemanov et al., 1996) and temperature dependences of the dielectric constant (**b**) (Tagantsev et al., 2003) of $Sr_{1-x}Ba_xTiO_3$ system.

It is known that $BaTiO_3$ has loosely packed oxygen octahedra due to the presence of large Ba^{2+} ions in the perovskite lattice and the spontaneous polarisation results from cooperative displacements of Ti ions in oxygen octahedra (Lin and Wu, 1990). When Ba^{2+} ions with 12-coordination ionic radius 1.61 Å are substituted with smaller Sr^{2+} ones with 12-coordination ionic radius 1.44 Å (Shannon, 1976), the adjacent oxygens displace towards the substituents forming a more closely packed structure. This causes a decrease of the unit cell volume, thereby lowering T_C in the same manner as the hydrostatic pressure (Merz, 1950), i.e., closing-up of open space for the movement of Ti ions. Such explanation conforms to the lattice parameter a increasing with x practically by a linear Vegard law: $\Delta a = 0.1x$ (Å) (Lemanov et al., 1996).

The BST solid solution is a suitable material for tunable applications (Varadan et al., 1992; Babbit et al., 1992; de Flaviis et al., 1997). As is clearly seen from Figure 1.17b, for a given temperature a high enough value of the dielectric constant can be obtained by choosing a proper $BaTiO_3$ concentration.

The dielectric constant of $Sr_{0.9}Ba_{0.1}TiO_3$ ceramics as a function of temperature and applied electric dc bias field at 100 kHz is displayed in Figure 1.18a, showing a relative dielectric tunability of about 83% under a dc bias field of 25 kV/cm at the transition temperature of 86 K (Wu et al., 1994). However, the operational temperature range does not correspond to a close vicinity to T_C where the dielectric constant and relative tunability are maximal. The reason for this is the low temperature stability of ε' at T close to T_C. The upper limit of the operational temperature range is roughly determined by the condition $\varepsilon' \approx 1000$. In addition, the coefficient of the dielectric non-linearity of BST is expected to be smaller than that of ST (Tagantsev et al., 2003), whereas microwave loss increasing with $BaTiO_3$ concentration in operational temperature range was observed, as one can see in Figure 1.18b (Vendik et al., 1999). The latter is related to a very big difference between the damping of soft-mode phonons in the end members of BST solid solution. This damping essentially controls the level of the intrinsic dielectric loss at microwave frequencies (Tagantsev et al., 2003). Thus, higher insertion loss of BST has restricted its application in phased array antennas.

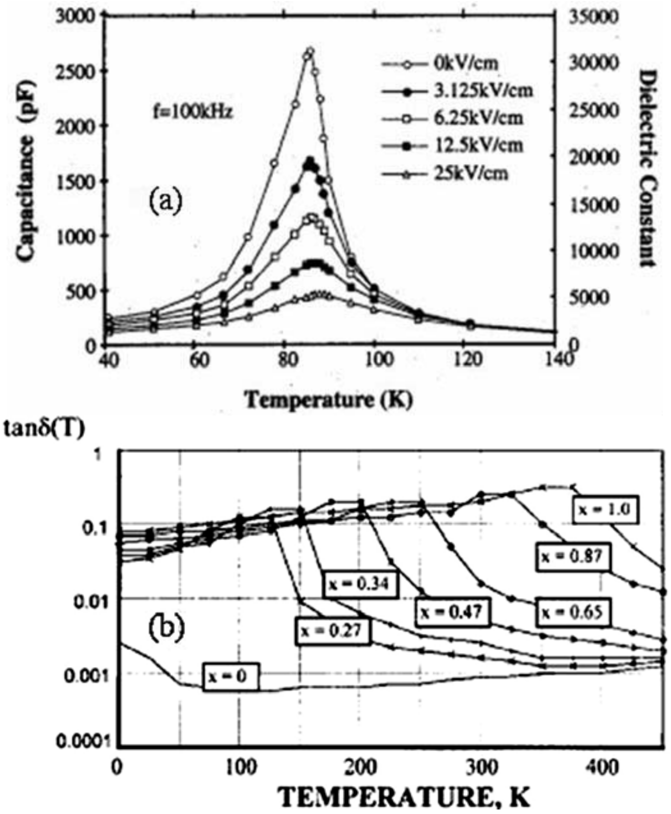

FIGURE 1.18. Temperature dependences of the capacitance (left) and dielectric constant (right) of $Sr_{0.9}Ba_{0.1}TiO_3$ ceramics under 0, 3.125, 6.25, 12.5 and 25 kV/cm at 100 kHz (**a**) (Wu et al., 1994) and of the loss factor of $Sr_{1-x}Ba_xTiO_3$ system scaled to 10 GHz (**b**) (Vendik et al., 1999).

Recently, in order to reduce the dielectric loss, modification of BST by admixing of non-ferroelectric materials, such as MgO (Sengupta and Sengupta, 1999; Chang and Sengupta, 2002) and Al_2O_3 (Wu et al., 1999; Wu et al., 2000) up to a very high concentrations has been attempted.

A rather complete set of experimental data was reported for BST-MgO system, showing that MgO doping has produced the best effect on the lowering of dielectric loss tangent at microwave frequencies and room temperature (Sengupta and Sengupta, 1999). However, the dielectric constant and relative tunability was also distinctly reduced, as shown in Figure 1.19 for MgO-mixed $Ba_{0.6}Sr_{0.4}TiO_3$ ceramics at room temperature and rather high bias field 80 kV/cm (Chang and Sengupta, 2002). In addition, MgO doping changes the dielectric behaviour of BST versus temperature (Figure 1.20a). At the MgO content of 1.0 wt%, the cubic-tetragonal phase transition peak shifts to a lower temperature and the peak width become broader. At higher MgO contents, the peak becomes depressed and further broadened, but the phase transition peak stay at the same temperature as in 1.0 wt% MgO-mixed BST bulk ceramics.

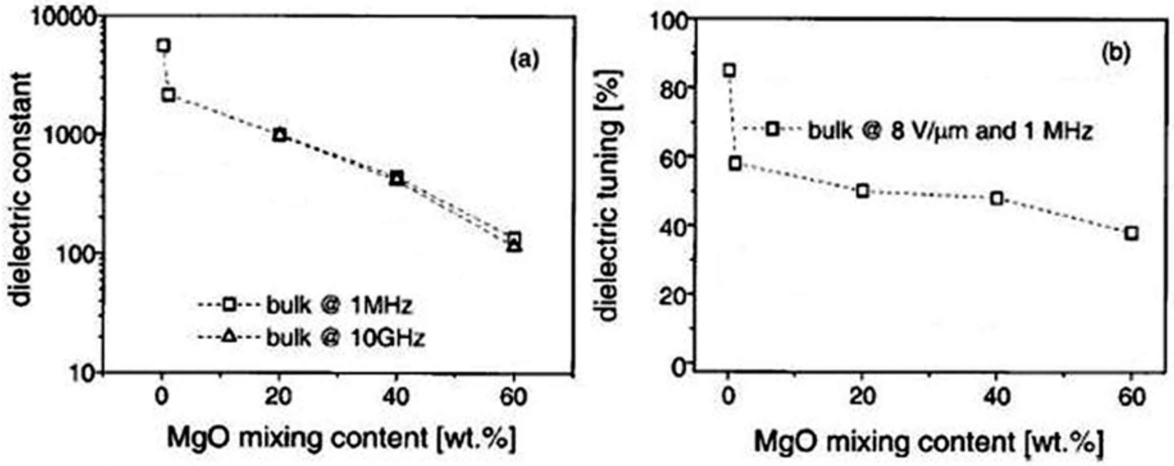

FIGURE 1.19. Dielectric constant (**a**) and relative tunability (**b**) of $Ba_{0.6}Sr_{0.4}TiO_3$ ceramics with 0, 1, 20, 40 and 60 wt% of MgO (Chang and Sengupta, 2002).

The tetragonal-orthorhombic phase transition for all the bulk ceramics appears at the same temperature regardless the MgO content. The shift of T_C to lower temperature has been explained by the partial Mg insertion into BST, what has also contributed to decrease of dielectric constant and tuning at room temperature. However, scanning electron microscopy (SEM) analysis with energy dispersion spectroscopy (EDS) data showed small sized (<0.5 μm) MgO, distributed in the matrix of BST. Further slow decrease in ε' and n_r with the higher MgO content has been thought as a mixing effect between Mg-doped BST and MgO (Chang and Sengupta, 2002). Figure 1.20b presents the similar effect for $Ba_{0.8}Sr_{0.2}TiO_3$ ceramics with critical MgO content of 2 mol% (0.4 wt%).

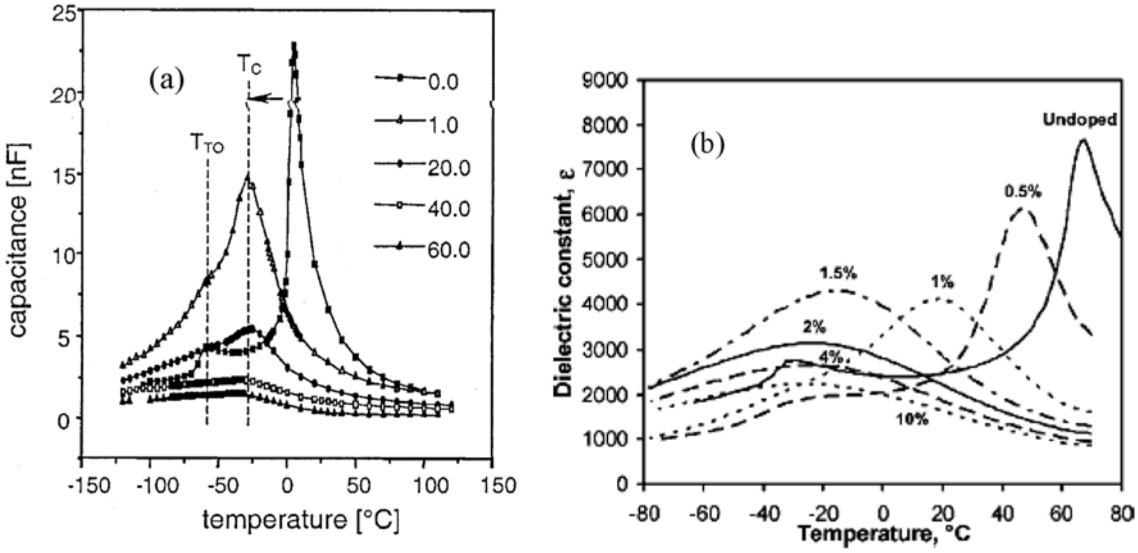

FIGURE 1.20. Temperature dependences of the dielectric constant of $Ba_{0.6}Sr_{0.4}TiO_3$ with 0.0, 1.0, 20.0, 40.0 and 60.0 wt% of MgO (**a**) (Chang and Sengupta, 2002) and of $Ba_{0.8}Sr_{0.2}TiO_3$ ceramics with 0.0, 0.5, 1.0, 1.5, 2.0, 4.0 and 10.0 mol% of MgO (**b**) (Tagantsev et al., 2003).

Kim et al. (1998) reported the $0.8BaTiO_3$-$0.1SrTiO_3$-$0.1MgTiO_3$ ceramics as a suitable composition for capacitors with the temperature coefficient of capacitance below 3% in T range 263-343 K, the dielectric constant higher than 1300 and the dissipation factor smaller than 0.03.

1.3.2. $Sr_{1-x}Pb_xTiO_3$ solid solutions

$Sr_{1-x}Pb_xTiO_3$ (SPT) system may serve as a classical illustration of ferroelectric solid solutions with the perovskite structure. Studying this solid solution in 1947, Jonker and van Santen have assumed that $PbTiO_3$ is a ferroelectric, what was experimentally proved by Smolenskii and by Shirane et al. (Smolenskii, 1984). In fact $PbTiO_3$ is a classic example of a displacive ferroelectric transition. It undergoes a first order transition at around 770 K from cubic perovskite *Pm3m* to a tetragonal ferroelectric *P4mm* phase. PT is isomorphic with tetragonal BT at room temperature, however in contrast to $BaTiO_3$ no additional transitions were established for $PbTiO_3$ (Lines and Glass, 1977). $Sr_{1-x}Pb_xTiO_3$ forms a continuous solid solution over the entire range of concentration x. The structural phase transition temperature in SPT at small x behaves similarly to BST, strongly decreasing with x and finally converging with the ferroelectric transition at $x \approx 0.04$ (Smirnova et al., 2005). Because of the high ferroelectric transition temperature of $PbTiO_3$, SPT solid solution reveals a peak of the dielectric constant near the room temperature already at $x = 0.3$, as one can see from the phase diagram shown in Figure 1.21a.

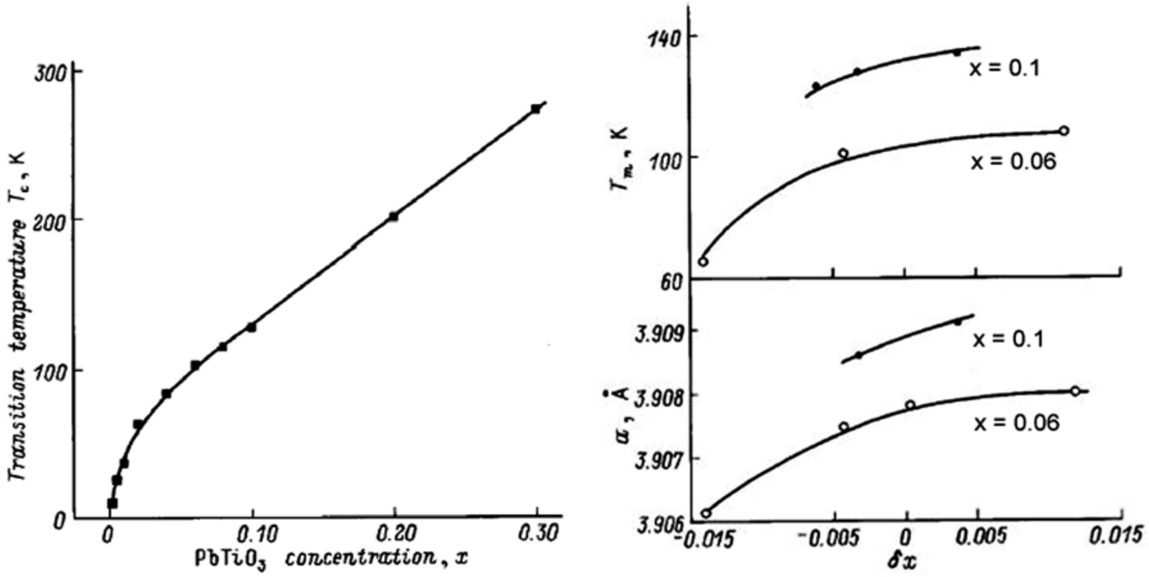

(a) (b)

FIGURE 1.21. **a** - Phase diagram of $Sr_{1-x}Pb_xTiO_3$ solid solutions; **b** - temperature of the maximum dielectric constant T_m and lattice parameter a as a function of deviation of PbO concentration δx from the stoichiometric values $x = 0.1$ and 0.06 (Lemanov et al., 1997a).

As follows from Figure 1.21a, the transition temperature T_C depends linearly on x down to 0.04 as $T_C = 40 + 770x$. On the other hand, for $x \leq 0.04$ the experimental points fit to the $T_C = A(x - x_c)^{1/2}$ line, where A = 440 and $x_c = 0.002$. Note that this relation is based on the assumption that there is no ferroelectric phase transition ($T_C = 0$) at $x = 0.002$, since no ferroelectric hysteresis loops at this concentration were observed (Lemanov et al., 1997a). The usual explanation for higher transition temperature of $PbTiO_3$ comparing with $BaTiO_3$ and, consequently, for the faster T_C increasing with the concentration of the second member in $Sr_{1-x}Pb_xTiO_3$ than in $Sr_{1-x}Ba_xTiO_3$ system is as follows. Although Pb^{2+} has a smaller ionic radius (1.49 Å for coordination number $N_c = 12$) than Ba^{2+} (1.61 Å)

(Shannon, 1976), it has a higher electronic polarisability than Ba^{2+} and Sr^{2+}. This polarisability intensifies the interactions between the Ti ions and thus raises the T_C (Mitsui and Westphal, 1961). However, the fact that the ionic size of Pb^{2+} is bigger than that of Sr^{2+} (1.44 Å) (Shannon, 1976) also assists to the displacement of Ti ions and consequently to the increase of T_C of $Sr_{1-x}Pb_xTiO_3$ solid solutions with x. Room temperature measurements of the lattice parameter a made on samples having different compositions showed it to vary practically linearly with the slope $da/dx = 3.7 \times 10^{-2}$ Å (Lemanov et al., 1997a).

SPT solid solutions did not any commercial application because of the well-known difficulty in obtaining the precise stoichiometry in lead-containing compounds, connected with a high volatility of Pb at high temperatures. At the same time, the temperature of the maximum dielectric constant T_m (as well as lattice parameter) was shown to be strongly dependent on composition non-stoichiometry, as presented in Figure 1.21b for nominal concentrations $x = 0.1$ and 0.06. As evident from Figure 1.21b, the variation of T_m under variation of PbO concentration δx may be quite large, what is attributed to the presence of vacancies (Lemanov, 1997a). However, the attempt to use $Sr_{0.685}Pb_{0.315}TiO_3$ as a ferroelectric variable capacitance in microwave switch has been done (Amoss et al., 1965). More recent study (Somiya et al., 2001) suggested the potentiality of SPT system for field tunable devices. Suppression of the dielectric constant was observed under dc bias field, as shown in Figure 1.22 for $Sr_{1-x}Pb_xTiO_3$ ceramics ($x = 0.2$, 0.25 and 0.3), and dielectric loss held small values. Loss tangent values, less than 0.1%, and relative dielectric tunability, 3, 15 and 70% under 20 kV/cm bias field were measured on $Sr_{1-x}Pb_xTiO_3$ ceramics with $x = 0.2$, 0.25 and 0.3 at room temperature and at 10 kHz (Somiya et al., 2001). In addition, composites fabricated from SPT and Al_2O_3 were developed that show $\varepsilon' \sim 100$, $tan\delta < 0.005$, $\tau_\varepsilon \sim 700$ ppm and n(20 kV/cm) ~0.05 at 10 kHz over the range ~313-423 K (Somiya et al., 2004).

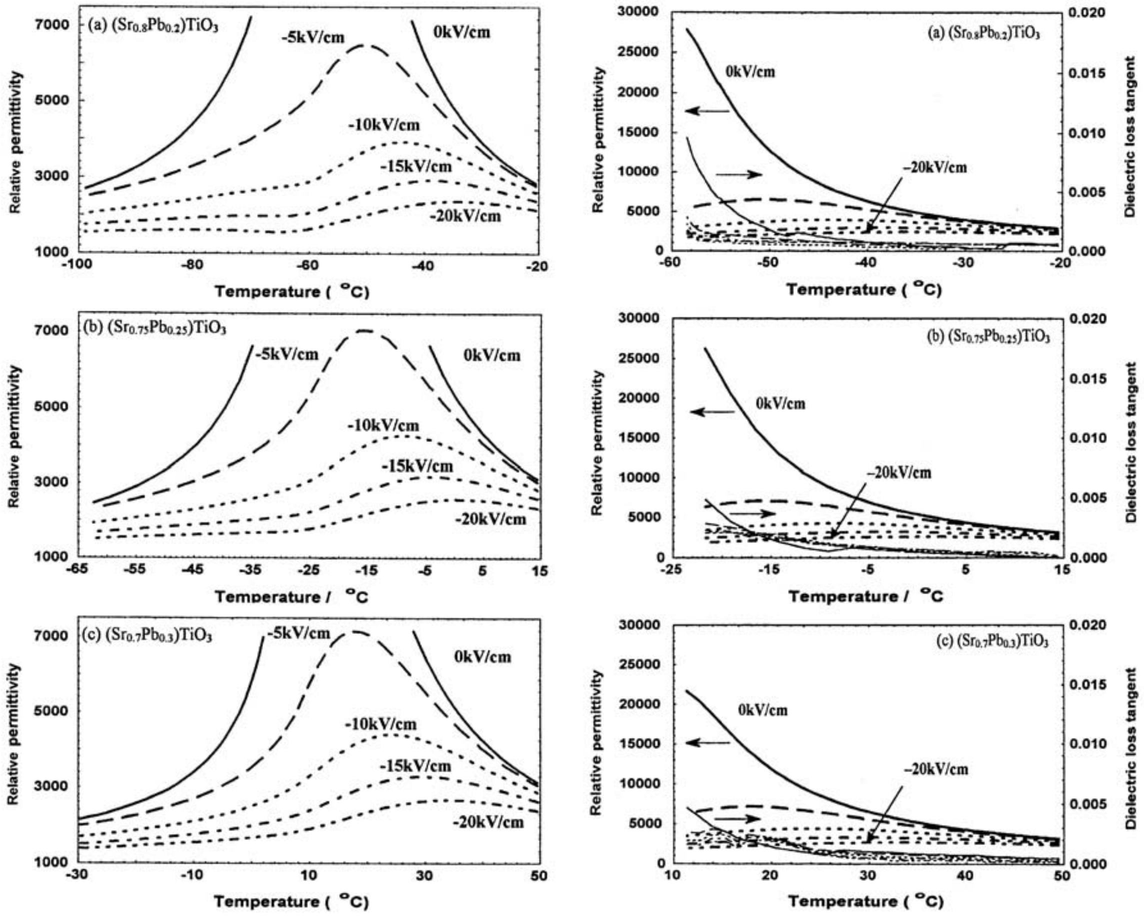

FIGURE 1.22. Dielectric responses of $Sr_{1-x}Pb_xTiO_3$ ceramics with $x = 0.20$ (**a**) 0.25 (**b**) and 0.30 (**c**) at 10 kHz as a function of temperature under -20, -15, -10, -5 and 0 kV/cm (Somiya et al., 2001).

1.3.3. $Sr_{1-x}Cd_xTiO_3$ solid solutions

Ferroelectric phase transition in $CdTiO_3$ was discovered by Smolenskii in 1950 in ceramic samples at 50 K (Smolenskii, 1984). However, recent and more detailed studies exhibit the first-order (but close to second-order) ferroelectric phase transition at 76.5 K (Guzhva et al., 2001). Hence, ferroelectric phase transition can be induced in ST by diluting with perovskite ferroelectric $CdTiO_3$, in line with $SrTiO_3$ - $BaTiO_3$ and $SrTiO_3$ - $PbTiO_3$ solid solutions. The structural and dielectric properties of $Sr_{1-x}Cd_xTiO_3$ solid solution were studied also by Guzhva et al. (2001).

$Sr_{1-x}Cd_xTiO_3$ was found to constitute a solid solution, but with limited solid solubility. For $x \leq 0.1$ room temperature X-ray diffraction (XRD) lines are consistent with the perovskite structure, however, second phase was observed for $x \geq 0.2$.

Figure 1.23a presents the dielectric behaviour of some of the $Sr_{1-x}Cd_xTiO_3$ ceramic samples, in which clear dielectric anomaly is observed. The appearance of the maxima in $\varepsilon'(T)$ dependence, supported by the maxima in $tan\delta(T)$ can be related to polar state, induced by the Cd^{2+} ions. Transition into the polar state with non-zero value of spontaneous polarisation P_s in $Sr_{1-x}Cd_xTiO_3$ solid solution with $0.01 \leq x \leq 0.05$ at low temperatures was confirmed by a slim hysteresis loop, observed below T_C (see inset of Figure 1.23a). Dependence of T_C on Cd content x in $Sr_{1-x}Cd_xTiO_3$ solid solution for $x \leq 0.05$ is presented in Figure 1.23b. Fitting of the experimental results to the Eq. 1.10 gives values A = 139 K and $x_c = 0.002$. The value of the critical concentration is close to those of $Sr_{1-x}Ca_xTiO_3$, $Sr_{1-x}Ba_xTiO_3$ and $Sr_{1-x}Pb_xTiO_3$ solid solutions (Bednorz and Müller, 1984; Lemanov et al., 1997a).

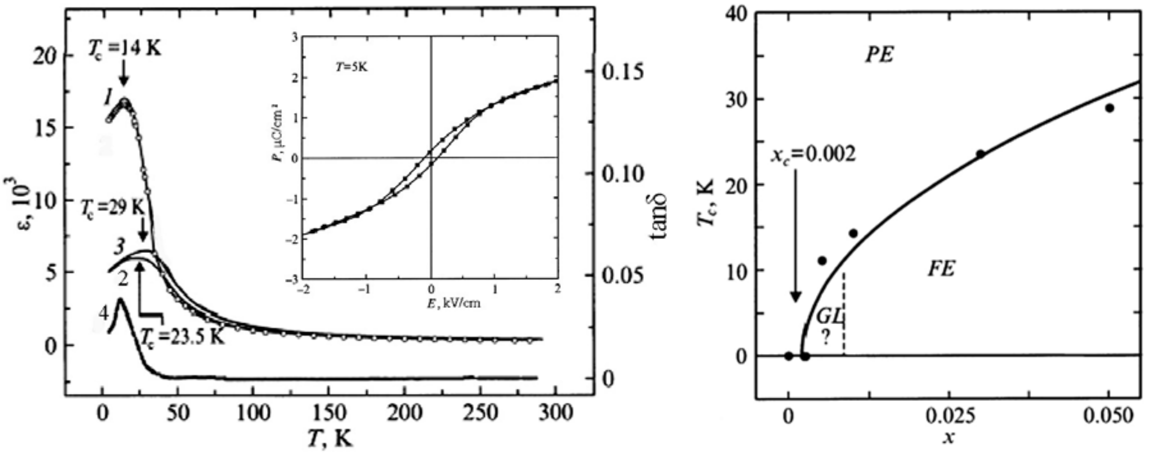

(a) (b)

FIGURE 1.23. **a** - Temperature dependence of dielectric constant ε' of $Sr_{0.99}Cd_{0.01}TiO_3$ (1), $Sr_{0.97}Cd_{0.03}TiO_3$ (2), $Sr_{0.95}Cd_{0.05}TiO_3$ (3) ceramics and of dielectric loss *tanδ* of $Sr_{0.99}Cd_{0.01}TiO_3$ ceramics (4) at 1 kHz. Inset shows P(E) hysteresis loop of $Sr_{0.99}Cd_{0.01}TiO_3$ ceramics.
b - Phase diagram of $Sr_{1-x}Cd_xTiO_3$ solid solutions for $x \leq 0.05$ [adapted from (Guzhva et al., 2001)].

However, hysteresis loop was not detected for x = 0.075 and 0.1. Moreover, T_C, reaching maximum 29 K at x = 0.05 decreases through 25 K for x = 0.075 to 22 K for x = 0.1, implying that long-range ferroelectric order, induced in $Sr_{1-x}Cd_xTiO_3$ at Cd content x = 0.01, is destroyed already at x = 0.075 (Guzhva et al., 2001).

1.3.4. $Sr_{1-x}Ca_xTiO_3$ solid solutions

An extraordinary number of oxides and fluorides of the general form ABX_3 are described as having a structure of perovskite, i.e., of mineral $CaTiO_3$. $CaTiO_3$ has a cubic *Pm3m* structure at $T > 1523$-1580 K and orthorhombic *Pcmn* structure at $T <$ ~1380 K (Redfern, 1996; Kennedy et al., 1999), although the deviation from the cubic perovskite structure is small. The dielectric behaviour of $CaTiO_3$ is typical of incipient ferroelectrics: relatively high dielectric constant ($\varepsilon' \approx 170$ at room temperature), large and negative value of $d\varepsilon'/dT$, and saturation of the dielectric constant at low temperatures ($\varepsilon' \approx 330$ at 4.2 K). However, extrapolation of $1/\varepsilon'(T)$ dependence to $1/\varepsilon'(T_0) = 0$ in $CaTiO_3$ gives a Curie-Weiss temperature $T_0 \approx -130$ K, whereas $T_0 \approx +40$ K in $SrTiO_3$ and $T_0 \approx +13$ K in $KTaO_3$ (Lemanov et al., 1999). Orthorhombic $CaTiO_3$ does not undergo a ferroelectric phase transition down to $T = 0$ and the paraelectric state would be stable even without effect of quantum fluctuations, which suppress the ferroelectric phase transition in $SrTiO_3$. As a result, $CaTiO_3$ should be classified as an incipient ferroelectric but not a quantum paraelectric.

$Sr_{1-x}Ca_xTiO_3$ (SCT) system makes a complete solid solution. As is evident from the phase diagram, shown in Figure 1.24, the structure of SCT is cubic above certain critical temperature, increasing with x. For $0.12 \le x \le 1$, this cubic phase undergoes a succession of structural phase transitions due to softening and freezing of the non-polar zone-boundary R and M phonon modes, becoming orthorhombic, similarly to $CaTiO_3$. A crossover from $CaTiO_3$-like structural phase transition behaviour to $SrTiO_3$-like with only one structural transition temperature is expected with decreasing calcium content below $x = 0.12$ (Ranjan and Pandey, 1999).

The behaviour of SCT phase transitions, connected with dielectric anomalies is also rather complicated. In 1961, Mitsui and Westphal reported the dielectric anomaly in $\varepsilon'(T)$ of SCT ceramic samples with Ca content up to $x = 0.20$. However, slim hysteresis loops were observed at 4.3 K for $Sr_{1-x}Ca_xTiO_3$ ceramics with $x \le 0.10$ only. The field dependent remnant polarisation decreased with increasing temperature, but the loop did not disappear at the temperature where the dielectric constant reached its maximum (see Figure 1.25). The ferroelectric phase produced by the small Ca addition was ascribed to enlarged atomic polarisability of Ca^{2+} in the SCT compound (in spite of its smaller electronic polarisability comparing to Sr^{2+}), due to the smaller ionic radius of Ca^{2+} (0.134 Å) than Sr^{2+} (0.144 Å) (Shennon, 1976) and occupy off-centre positions at Sr^{2+} sites (Mitsui and Westphal, 1961).

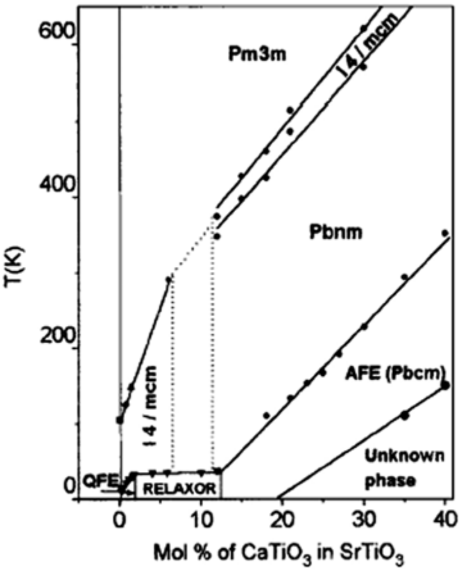

FIGURE 1.24. Phase diagram of $Sr_{1-x}Ca_xTiO_3$ solid solutions for $0 \le x \le 0.4$ (Ranjan et al., 2000).

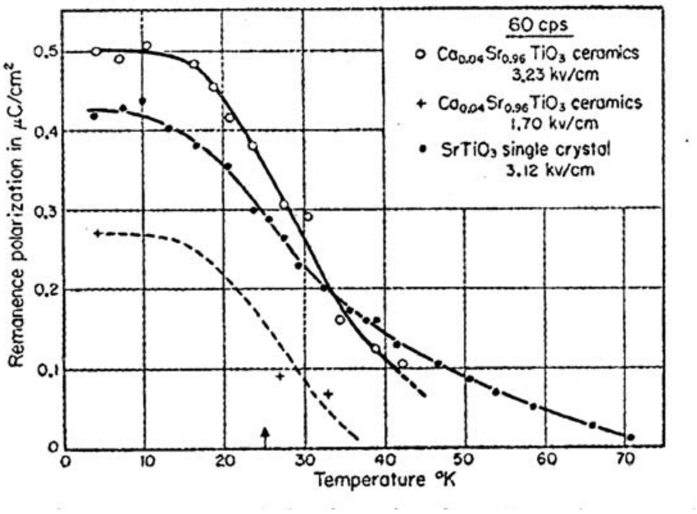

FIGURE 1.25. Variation of remnant polarisation of a $Sr_{0.96}Ca_{0.04}TiO_3$ ceramic and $SrTiO_3$ crystal with temperature. Arrow shows ε' peak temperature of $Sr_{0.96}Ca_{0.04}TiO_3$ (Mitsui and Westphal, 1961).

More detailed studies of the dielectric properties of $Sr_{1-x}Ca_xTiO_3$ system have been done by Bednorz and Müller (1984) on single crystals with $0.0 \le x \le 0.12$ in the temperature range 4.2 - 300 K at ~1.6 kHz (Figure 1.26a) and completed by Ranjan et al. (2000) on ceramics with $0.18 \le x \le 0.40$ in the temperature range 100 - 400 K at 10 kHz (Figure 1.26b).

The dielectric anomaly in $\varepsilon'(T)$ of $Sr_{1-x}Ca_xTiO_3$ system in composition range $0.12 < x \le 0.40$ with $dT_C/dx \approx 1100$ K was ascribed to an antiferroelectric phase transition. Structural and dielectric measurements (see Figure 1.26b) revealed: 1) superlattice reflections in XRD patterns, connected with antiparallel displacement of cations/anions in the low temperature state; 2) that $\varepsilon'(T)$ above the T_C strictly follows the Curie-Weiss law with negative T_0 (see inset to Figure 1.26b); 3) that peak in the $\varepsilon'(T)$ becomes less smeared and its temperature coincides with the dielectric loss peak temperature; 4) no hysteresis loop, characteristic of either ferroelectric or relaxor, below the T_C even after applying fields as high as 60 kV/cm (Ranjan et al., 2000; Ranjan and Pandey, 2001), supporting the assumption of the suggested antiferroelectric phase transition. In addition, a very broad dielectric anomaly of yet unknown nature was observed below antiferroelectric phase transition, as shown in Figure 1.24 also (Ranjan et al., 2000).

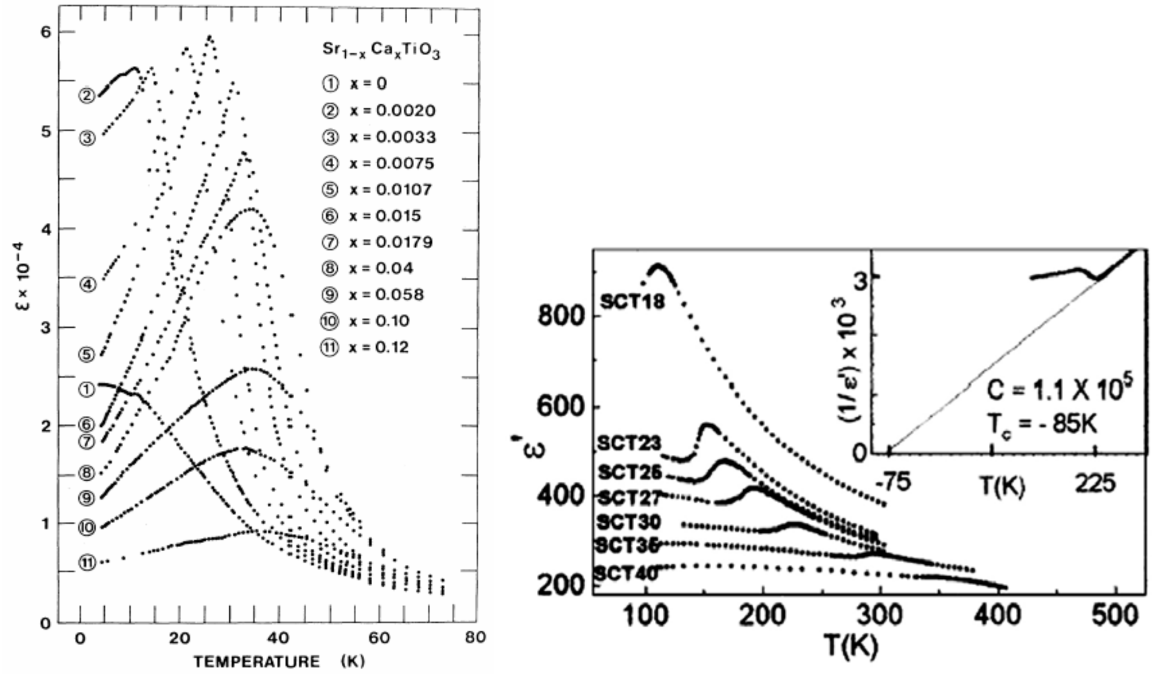

(a) (b)

FIGURE 1.26. Temperature dependence of dielectric constant ε' of $Sr_{1-x}Ca_xTiO_3$ crystals ($x = 0.00$-0.12) at ~1.6 kHz (**a**) (Bednorz and Müller, 1984) and of $Sr_{1-x}Ca_xTiO_3$ ceramics ($x = 0.18$-0.40) at 10 kHz (**b**). Inset shows Curie-Weiss fit for $x = 0.30$ (Ranjan et al., 2000).

Bednorz and Müller have shown the strong increase of the maximum dielectric constant (comparing to undoped ST) for $Sr_{1-x}Ca_xTiO_3$ single crystals with Ca content as small as $x = 0.002$ together with the peak occurring in the $\varepsilon'(T)$. The transition temperature has been found to rise with Ca concentration, following the relation $T_C = 298(x - 0.0018)^{1/2}$ up to $x \approx 0.016$ (Bednorz and Müller, 1984). Also the frequency dispersion, fitted to the Arrhenius law with $U = 0.015$ eV and $\tau_0 = 1.4 \times 10^{-11}$ s, and slim S-shaped hysteresis loops, characteristic for relaxor, have been reported on $Sr_{0.993}Ca_{0.007}TiO_3$ single crystal throughout the ferroelectric regime $T \leq 18$ K by Bianchi et al. (1995). For the compositions with $x = 0.002$, 0.005 and 0.011, a small zero-field polarisation was detected by pyroelectric current measurements (Lacerda-Arôso et al., 2001). In addition, the inclusion of calcium in ST was shown to induce a weak non-ergodic regime at low temperatures (Lacerda-Arôso et al., 2001). The relaxor-ferroelectric / dipole-glass behaviour in the quantum ferroelectric regime ($0.002 < x < 0.016$) has been explained in terms of phonon associated dissipative quantum tunnelling of the Ca^{2+} dipoles between potential minima in the four-well potential (Bianchi et al., 1995).

At further increase of Ca content from 0.016 to 0.12, a crossover from quantum to the classical regime, where T_C is nearly temperature independent, was suggested (Bednorz and Müller, 1984). In ferroelectric composition range, the peak heights decrease, the variation of dielectric constant with temperature become more smeared as x increased, and $\varepsilon'(T)$ does not obey the Curie-Weiss law. Instead it follows the relation:

$$1/\varepsilon' - 1/\varepsilon'_m = (T-T_m)^\gamma/C \tag{1.11}$$

in which the exponent γ approaches 1.75 for $x = 0.06$ (Bednorz and Müller, 1984), close to what is known for relaxor ferroelectrics (Smolenskii, 1970; Viehland et al., 1992a).

The smearing of the peak in the $\varepsilon'(T)$ in the classical regime has been attributed to the coupling of random strains (due to ionic size difference between Ca^{2+} and Sr^{2+} ions) to the polarisation. Alternatively, the random fields, generated by Ca^{2+}-V_O centre dipoles (probably due to a partial Ca incorporation into Ti site) are believed to be responsible for the ferroelectric domain state, induced by random fields in this regime and characterised by the rounded ε' peaks (Bednorz and Müller, 1984). Moreover, the relaxor-ferroelectric or dipole-glass behaviour in the classical regime ($0.016 < x < 0.12$) has been attributed to ferroelectric cluster and domain wall dynamics (Kleemann and Schremmer, 1989). Thus, the relaxor-like phenomena in Ca-doped ST are believed to result from polar nanodomains, which were evidenced to exist in the temperature range between high-temperature para- and low-temperature ferroelectric regime by second harmonic generation of light, Brillouin and Raman scattering (Kleeman et al., 2000).

Later, the dielectric behaviour of $Sr_{1-x}Ca_xTiO_3$ system for $x < 0.12$ was explained, considering that impurity-polarized clusters induce the second order phase transition, while quenched random fields give rise to a smeared peak in the $\varepsilon'(T)$ (Zhang et al., 2002b). Frozen fields result in the appearance of a multidomain state and due to that SCT has no global ferroelectric polarisation. However, the reversal of domains under an ac field can induce a “remnant polarization”. The deviation of T_C from $(x-x_c)^{1/2}$ law for $x > 0.016$

together with the decrease of maximum dielectric constant is attributed to the decrease of cell volume with increasing Ca content in SCT (Zhang et al., 2002b). The local reduction of the unit cell, caused by the substitution of bigger Sr^{2+} ions by smaller Ca^{2+} ones, is obvious and has an effect on the dielectric constant, an analogous effect to that of hydrostatic pressure known to strongly reduce the polarisability.

Lattice dynamics of the most studied SCT composition, $Sr_{0.993}Ca_{0.007}TiO_3$, was studied by Raman scattering (Bianchi et al., 1994). The phase transition at $T_C \approx 18$ K from tetragonal (*I4/mcm*) to orthorhombic (presumably *Pmm2*) symmetry was evidenced by the splitting into three components of the ferroelectric soft mode in Raman spectra below T_C. The structural phase transition occurred in this composition at $T_a = 125$ K was also proved by the appearance of two additional modes, which stiffen with the temperature decrease (Bianchi et al., 1994). Raman scattering measurements were also used to support the idea of antiferroelectric transition in $Sr_{0.7}Ca_{0.3}TiO_3$. The sudden enhancement of intensity of two lines at $T = 236$ K (at which XRD superlattice reflections were observed) suggests that these lines are not due to the zone centre phonons ($\mathbf{q} = 0$) but corresponds to phonons of symmetry points with $\mathbf{q} \neq 0$ in the Brillouin zone. Those phonons have become Raman active due to the folding of the Brillouin zone below the cell-doubling antiferroelectric phase transition temperature (Mishra et al., 2001).

Recently, the influence of high pressure on dielectric properties and phase transition on $Sr_{0.993}Ca_{0.007}TiO_3$ single crystal has been also reported (Venturini et al., 2003). A large shift of the dielectric constant peak temperature T_m to lower temperatures, with the slope $dT_m/dp \approx -35$ K/kbar, was observed at very modest pressures, as shown in Figure 1.27a. The data of Figure 1.27a also show a decrease in the magnitude of the ε' peak with increasing pressure and the complete suppression of the transition for pressures as high as 0.5 kbar. In addition, a frequency dispersion, with dynamics shown in the inset as an Arrhenius plot, vanishes at 0.5 kbar, and the dielectric response of $Sr_{0.993}Ca_{0.007}TiO_3$ becomes akin to the frequency independent response of undoped $SrTiO_3$, shown in Figure 1.27a for comparison. Moreover, the application of a dc bias to $Sr_{0.993}Ca_{0.007}TiO_3$ at 0.5 kbar produces results qualitatively similar to those of undoped ST (see Figs. 1.27b and 1.9a). There is a large suppression in the magnitude of ε' and an induction of ferroelectricity with a very broad and shallow ε' peak. However, an order of magnitude smaller bias field is necessary to induce the ferroelectric state in SCT in this case (Venturini et al., 2003).

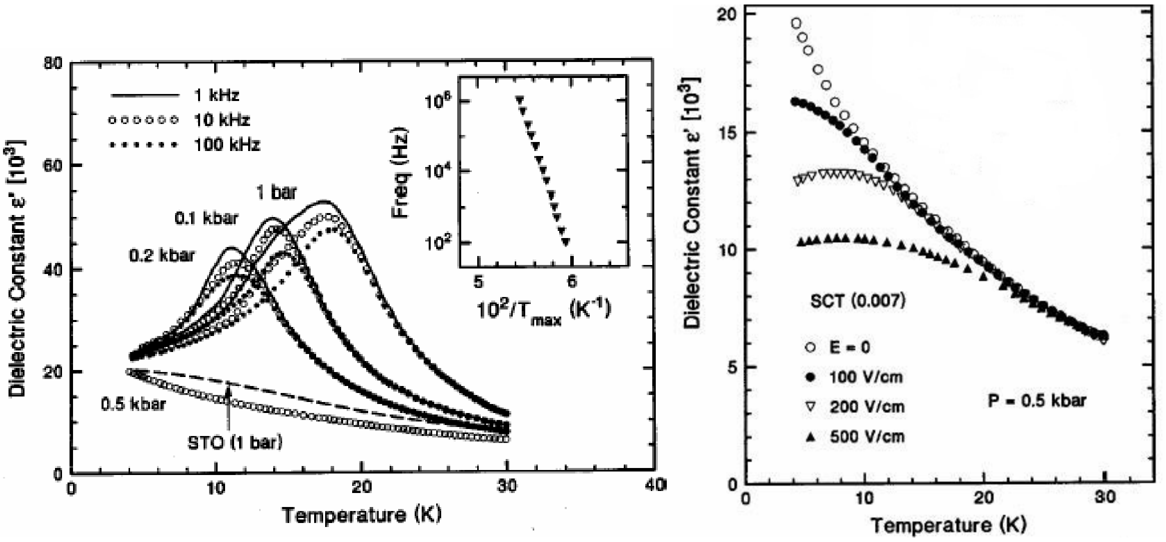

(a) (b)

FIGURE 1.27. Temperature dependence of the dielectric constant ε' of $Sr_{0.993}Ca_{0.007}TiO_3$ single crystal: at pressures of 1-500 bar and frequencies of 1-100 kHz (**a**) (inset shows an Arrhenius plot of the relaxation frequency) and at 500 bar under bias field of 0-0.5 kV/cm (**b**) (Venturini, 2003).

The field influence on both real and imaginary parts of the dielectric response of $Sr_{0.993}Ca_{0.007}TiO_3$ single crystal without applied pressure was studied by Kleemann et al., (1998). As shown in Figure 1.28, the real part peak decreases from ~60000 to ~10000 in value and shifts from 17.5 to 27 K with bias field increasing from 0 to 1 kV/cm. This effect was explained later by the stabilization of the local potential wells of the off-centre Ca^{2+} dipoles under applying external electric fields (Bianchi et al., 1995). It is worth to mention that $\chi'(T)$ curves converge already at a temperature ~32 K, that corresponds to a strong reduction of the relative tunability. The bias field has also a significant influence on the imaginary part χ''. Loss starts to increase in the paraelectric state (below ~20 K) and reach its peak values at 11 K, i.e., below the observed phase transition point. In contrast with the peak of the real part χ', the peak of the loss does not shift with increasing bias field: it only gradually reduces in magnitude. The vanishing loss in ferroelectric but fully aligned single-domain state was related to the elimination of domain wall dynamics (Kleemann et al., 1998).

Very recently, the effect of the bias electric filed on the dielectric response of $Sr_{1-x}Ca_xTiO_3$ ceramic system was studied by the present author. Samples with $x = 0.003$ and 0.01 were shown to reveal a monotonous increase of the low-temperature dielectric constant, corresponding to an enhancement of the tunability and a reduction of the driving electric field at 10-30 K for $x = 0.01$. For $Sr_{1-x}Ca_xTiO_3$ ceramic samples with $x = 0.04$ and 0.10 the ferroelectric phase transition around 20 K was observed together with the enhanced tunability of the dielectric constant at 30-85 K for $x = 0.10$. However, it was found that maximum relative tunability n_{max} does not exceed that of undoped ST starting from about of 85 K. On the other hand, $Sr_{0.70}Ca_{0.30}TiO_3$ sample was found to be almost insensitive to dc electric field in all the temperature range 10-300 K, revealing n_{max} about of 0.07%.

Before closing this subsection, it is interesting to mention that in SCT ceramic sample with A-site excess, i.e., in $(Sr_{0.85}Ca_{0.15})_{1.02}TiO_3$ the dielectric constant is shifted to the lower-temperature region and increase in magnitude, as shown in Figure 1.29 (Fujimoto et al., 1998). An observed shift of the peak dielectric constant of the A-site-excess specimen to low temperature was attributed to the selective occupation of the cation sites of the planar faults by calcium ions.

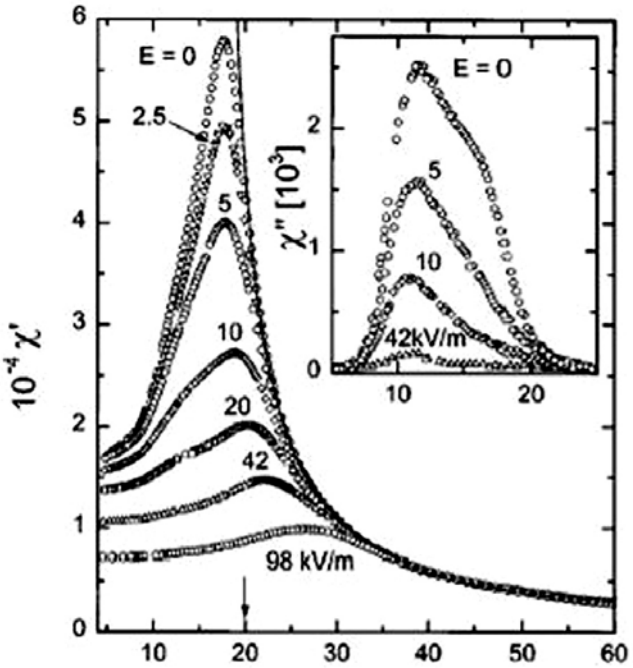

FIGURE 1.28. Variation of real part of dielectric susceptibility χ' (variation of imaginary part χ'' shown in inset) of $Sr_{0.993}Ca_{0.007}TiO_3$ single crystal at 1 kHz with temperature under various bias fields E (Kleemann et al., 1998).

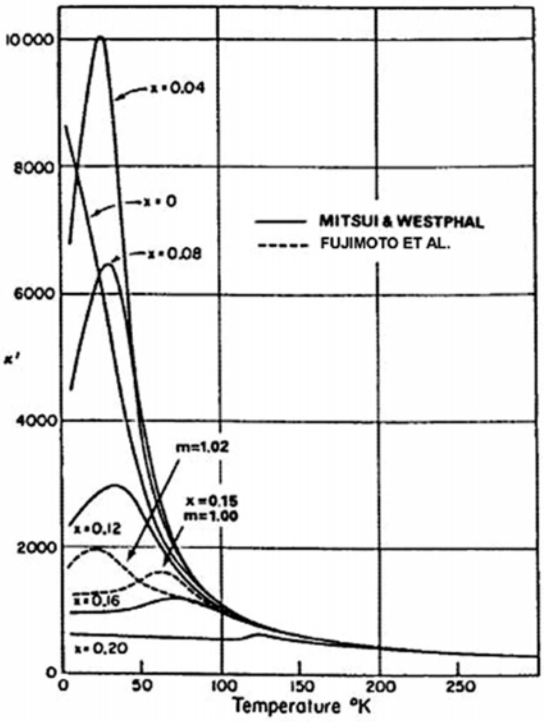

FIGURE 1.29. Dielectric constant ε' of stoichiometric $Sr_{1-x}Ca_xTiO_3$ ($x = 0.00$-0.20) and A-site excess $(Sr_{0.85}Ca_{0.15})_{1.02}TiO_3$ ceramics as a function of temperature (Fujimoto et al., 1998).

1.3.5. $Sr_{1-1.5x}Bi_xTiO_3$ solid solutions

Dielectric properties of $Sr_{1-1.5x}Bi_xTiO_3$ (SBiT) system were first investigated by Skanavi et al. in 1957 (Yu, 1997). In this study, a high permittivity peak with frequency dispersion, induced by moderate Bi doping in ST was reported. The authors suggested a polarisation mechanism by “hopping ions”, rather than the occurrence of ferroelectricity. However, based on the observation of the slim hysteresis loop in Bi-doped ST, Smolenskii and co-workers and Gubkin and co-workers suggested a ferroelectric mechanism with the so called “diffuse phase transition” (Yu, 1997). Later Yu (1997) systematically studied Bi-doped ST system, establishing the relations between the structural and the dielectric response of the ceramics.

In contrast to $Sr_{1-x}Ba_xTiO_3$, $Sr_{1-x}Pb_xTiO_3$ and $Sr_{1-x}Ca_xTiO_3$ systems, $Sr_{1-1.5x}Bi_xTiO_3$ is a solid solution in which the host lattice ions Sr^{2+} are substituted by aliovalent Bi^{3+} ions. Thus to satisfy the charge neutrality, one strontium vacancy V_{Sr} has to be created upon the substitution of three divalent Sr^{2+} by two trivalent Bi^{3+}. Hence the appropriated chemical formula should be written as $[Sr_{1-1.5x}(V_{Sr})_{0.5x}Bi_x]TiO_3$.

Room temperature XRD profiles exhibit a cubic structure for Bi-doped ST and indicated a solubility of Bi in the $SrTiO_3$ lattice restricted to $x = 20$ mol%, very probably because of formation of V_{Sr}. A uniform distribution of Bi throughout the ceramics was confirmed by SEM / EDS analysis (Yu, 1997; Ang et al., 1998). Recently, additional EDS analysis with transmitting electron microscopy (TEM) measurements performed by the present author showed that Bi is incorporated into the ST grains.

Only $Sr_{1-1.5x}Bi_xTiO_3$ ceramics, which are not optically transparent, have been studied up to now. This is probably related to difficulties in growing single crystal, since SBiT is a non-stoichiometric compound with a large number of vacancies. Therefore, no optical measurements of refractive index, birefringence and second harmonic generation are available for SBiT. However, Raman-scattering measurements have been carried out on SBiT ceramics (Ang and Yu, 2000; Almeida et al., 2003; Porokhonskii et al., 2004), and some of the results are shown in Figure 1.30. The most prominent feature observed in these spectra is the presence of the forbidden TO_2 and TO_4 modes, whose intensity is progressively increasing with increasing Bi content and temperature lowering. The appearance of these polar modes proves the loss of the inversion centre at least locally. It is also worth to notice that one of the R-point modes (at ~140 cm^{-1}), which should become active below the antiferrodistortive phase transition in undoped $SrTiO_3$ (Fleury and Worlock, 1968), can be observed up to the room temperature. This fact point to the simultaneous existence of impurity induced local order of both antiferrodistortive and polar types. The splitting of the soft mode below the phase transition temperature (as in $Sr_{1-x}Ca_xTiO_3$), as well as detailed behaviour of the soft mode frequency as function of temperature was difficult to observe because of its high damping of the mode (Almeida et al., 2003).

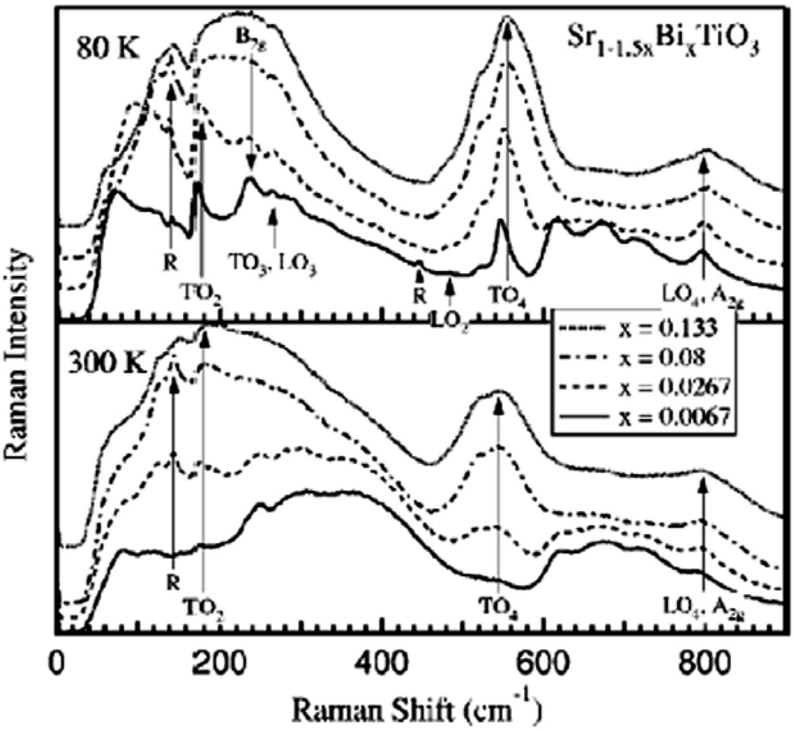

FIGURE 1.30. Micro-Raman spectra of $Sr_{1-1.5x}Bi_xTiO_3$ ceramics ($x = 0.0067$-0.133) at 80 and 300 K. A tentative mode assignment is included (Porokhonskyy et al., 2004).

Recently, more detailed study of the dielectric properties of $Sr_{1-1.5x}Bi_xTiO_3$ system has been done and a complex structure of the dielectric response was revealed. Several relaxation processes were observed as in the temperature dependence (Ang et al., 1999) as in the frequency spectra (Porokhonskyy, 2004) of the complex dielectric permittivity.

Considering the relaxation processes deduced from $\varepsilon(T)$, lets start from those more pronounced at higher temperatures in samples with Bi content $x = 0.0133$-0.133, which were found to be closely related to the presence of oxygen vacancies (Yu, 1997; Ang et al., 2000c). Some of them, as shown in Figure 1.31, can be completely suppressed by annealing in oxidizing atmosphere, whereas annealing in nitrogen enhances their dielectric values. Their complex permittivity can be empirically described by the Cole-Cole equation:

$$\varepsilon^* = \varepsilon_\infty + [\varepsilon_{\mathrm{dc}} - \varepsilon_\infty]/[1 + (i\omega\tau)^{1-\alpha}], \tag{1.12}$$

where $\varepsilon_{\mathrm{dc}}$ is the static permittivity, ε_∞ is the permittivity at the high frequency, ω is the angular frequency, τ is the mean relaxation time and α is the angle of the semicircular arc, an empirical parameter describing diffuseness of the spectrum, with τ, following the Arrhenius law (see Figure 1.32 with insets). By fitting to Arrhenius law rather high activation energy (U_{relaxA} = 0.32-0.48 eV; U_{relaxB} = 0.74-0.89 eV) and pre-exponential factor $\tau_0 = (0.5\text{-}7) \times 10^{-12}$ s were obtained (Ang et al., 2000c).

Relaxation with activation energy of 0.212-0.496 and τ_0 of 7×10^{-14} - 9×10^{-10} s was also observed for ST doped with La^{3+} and other rare-earth ions (Johnson et al., 1970; Iguchi and Lee, 1993), although no hysteresis loops were observed in $Sr_{1-1.5x}La_xTiO_3$ system (Yu, 1997). The relaxation was explained by the Skanavi model, which postulates the appearance of more than one off-centre equilibrium position for Ti ion due to the distortions introduced by rare-earth ions and associated Sr-site vacancies. So, thermally activated motion between these equivalent minima leads to the observed relaxation. However, a modification of Scanavi model was made by Yu (1997), supposing that the motion is not only limited to Ti ions, but involves also Sr-site and oxygen vacancies. The importance of the latter was confirmed by dielectric measurements of the $Sr_{1-1.5x}La_xTiO_3$ samples after long-time annealing in oxidizing and reducing atmospheres. All the dielectric permittivity peaks were greatly decreased or eliminated by annealing in oxygen and/or air.

The ε(T) anomaly with T_m, dependent on Bi content, was found to dominate below room temperature in $Sr_{1-1.5x}Bi_xTiO_3$ samples with x = 0.0033-0.2 (Ang et al., 1999), as presented in Figure 1.33 both for real ε' and imaginary ε'' parts of complex dielectric permittivity (for x = 0.0033-0.0133 marked as C). The quantum ferroelectric relationship $T_m \sim (x\text{-}0.0005)^{1/2}$ holds for $x \leq 0.0267$ (Ang et al., 1998).

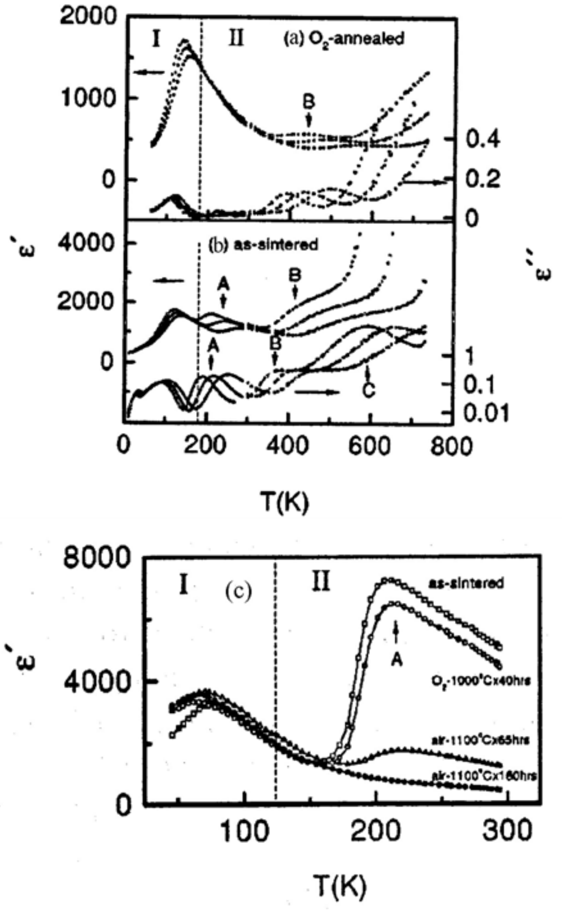

FIGURE 1.31. Temperature dependence of ε' and ε'' of $Sr_{0.92}Bi_{0.0533}TiO_3$ annealed in O_2 at 0.1, 1 and 10 kHz (**a**), as-sintered $Sr_{0.92}Bi_{0.0533}TiO_3$ at 0.1, 1 and 10 kHz (**b**) and of $Sr_{0.96}Bi_{0.0133}TiO_3$ annealed at different conditions at 1 kHz (**c**) (Ang et al., 2000c).

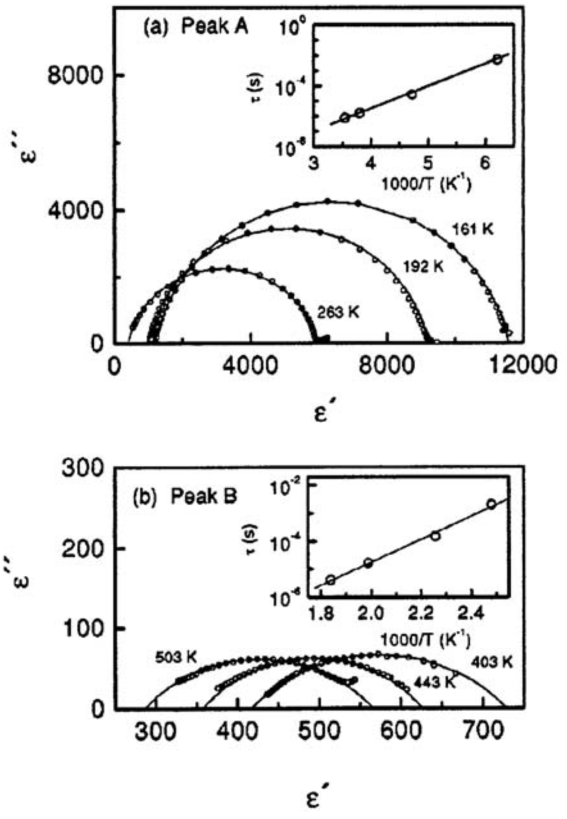

FIGURE 1.32. Cole-Cole plot (ε'' versus ε') of the as-sintered $Sr_{1-1.5x}Bi_xTiO_3$: in the temperature range where peak A occurs for $x = 0.0133$ (**a**) and in the temperature range where peak B occurs for $x = 0.0533$ (**b**). Inset shows Arrhenius plot of relaxation time τ (Ang et al., 2000c).

In addition, the dielectric constant peak value decreases and temperature increases with frequency. It was found that the temperature dependence of the relaxation time for this anomaly can be well fitted to the Vögel-Fulcher law:

$$\tau = \tau_0 \exp[U/k_B(T_m - T_f)], \tag{1.13}$$

where k_B is the Boltzmann's constant, τ_0 is the pre-exponential factor, U is activation energy, T_m is the temperature of the permittivity maximum, T_f is the static freezing temperature at which relaxation time τ tends to infinity (Viehland et al., 1990), as shown in Figure 1.34. The fitting parameters U = 0.024-0.047 eV, τ_0 = (0.10-5.26) × 10^{-9} s and T_f increasing monotonously from 30.7 to 131.9 K were obtained for $Sr_{1-1.5x}Bi_xTiO_3$ system with x = 0.0133-0.2. Slim but obvious hysteresis loops, shown for $Sr_{0.92}Bi_{0.0533}TiO_3$ as an example in Figure 1.35, were observed. When temperature is higher then 40 K, the remnant polarisation P_r, obtained from the hysteresis loops, first increases with temperature increase until a maximum at about 80 K and then decreases with further temperature increase. However it does not go to zero at T_m, but inflects and tails to zero, what indicates a typical relaxor characteristic. So, this relaxation process was assigned as ferroelectric relaxor behaviour, originated from off-centre Bi dipoles, forming dipole clusters due to local inhomogeneous distribution of Bi ions (Ang and Yu, 2002).

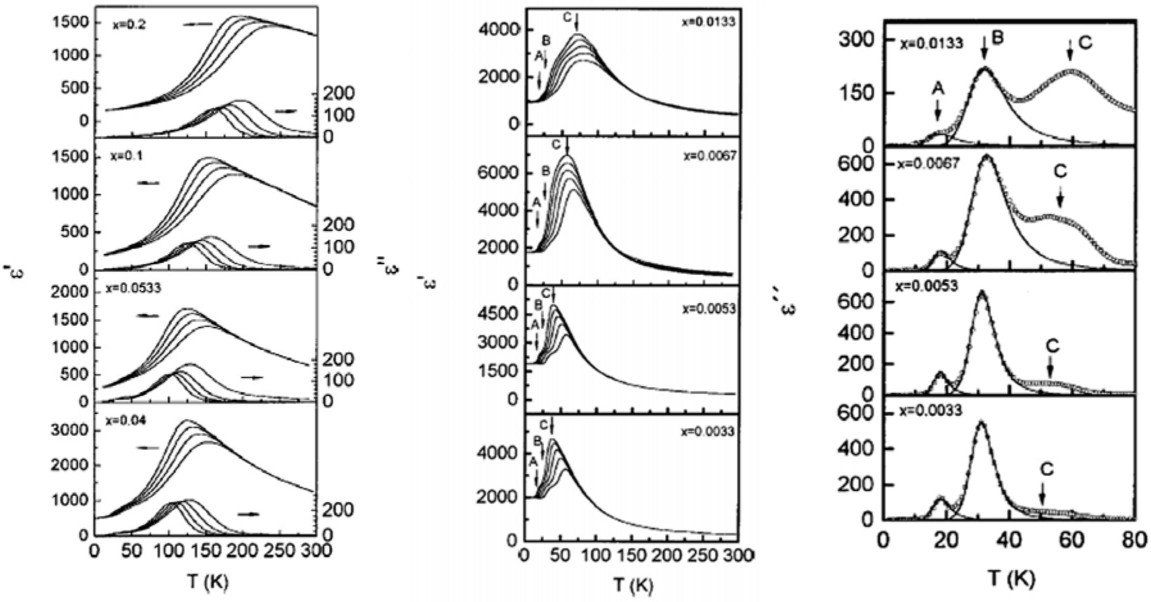

(a) (b) (c)

FIGURE 1.33. Temperature dependences: of ε' and ε'' of $Sr_{1-1.5x}Bi_xTiO_3$ with x = 0.2, 0.1, 0.053 and 0.04 at 0.1, 1, 10 and 100 kHz (**a**); of ε' of $Sr_{1-1.5x}Bi_xTiO_3$ with x = 0.0133, 0.0067, 0.0053 and 0.0033 at 0.1, 1, 10, 100 and 1000 kHz (**b**); and of ε'' of $Sr_{1-1.5x}Bi_xTiO_3$ with x =0.0133, 0.0067, 0.0053 and 0.0033 at 0.1 kHz (**c**). Frequency increases from top to bottom for ε' and from left to right for ε'' (Ang and Yu, 2002).

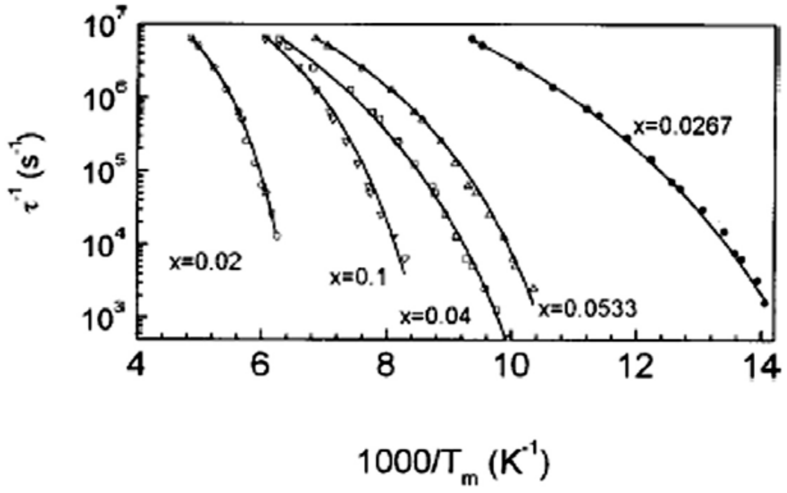

FIGURE 1.34. Arrhenius plots (inverse relaxation time τ^{-1} versus inverse temperature of maximum dielectric permittivity $1000/T_m$) for $Sr_{1-1.5x}Bi_xTiO_3$ with x = 0.2, 0.1, 0.04, 0.0533, 0.0267 (Ang and Yu, 2002).

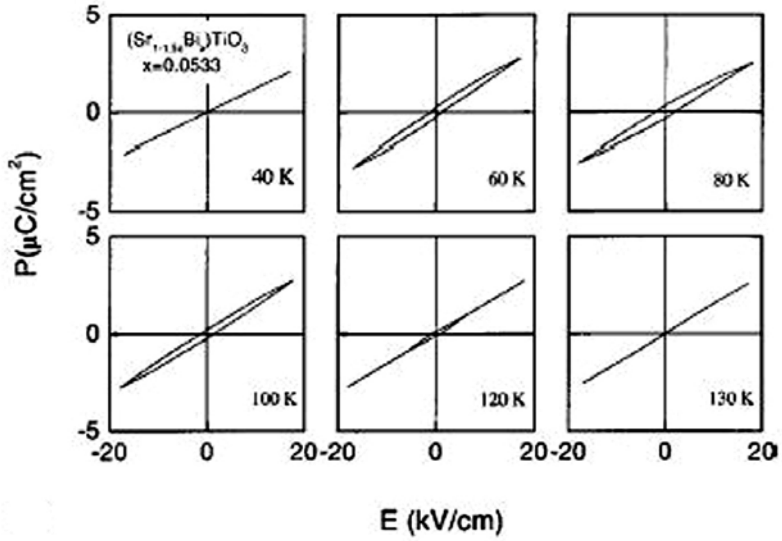

FIGURE 1.35. P(E) hysteresis loops of $Sr_{0.92}Bi_{0.0533}TiO_3$ at different temperatures (Ang et al., 2000d).

With decreasing Bi concentration, the interaction between the dipoles becomes much weaker, and less dipole clusters are formed. Thus, the ferroelectric relaxor mode C almost disappear at $x < 0.0033$. However, in this concentration range, lower-temperature modes A and B are dominant, as one can see from Figure 1.36, especially from ε'' data shown in the insets. T_m's of the modes A and B are independent on doping content, but shift with frequency.

The Cole-Cole plot of the complex permittivity data at temperatures in the vicinity of T_m for $Sr_{1-1.5x}Bi_xTiO_3$ with $x \leq 0.002$, exemplified in Figure 1.37 by $x = 0.0005$, gives $\alpha \leq 0.3$ for both modes A and B. On the other hand, Figure 1.38a exhibits α value increasing strongly with Bi concentration, suggesting a broad distribution of relaxation times. It was also found that the mean relaxation rates for modes A and B follow strictly the Arrhenius relation with the activation energy $U = 0.062 \pm 0.002$ eV and the pre-exponential term $\tau_0 = (0.4\text{-}1) \times 10^{-13}$ s for mode B, and $U = 0.033 \pm 0.001$ eV and $\tau_0 = (0.4\text{-}2) \times 10^{-12}$ s for mode A, for the samples with $x = 0.0005\text{-}0.0267$ (Ang and Yu, 2002). An example of the Arrhenius plot is shown in Figure 1.38b for $Sr_{1-1.5x}Bi_xTiO_3$ with $x = 0.002$.

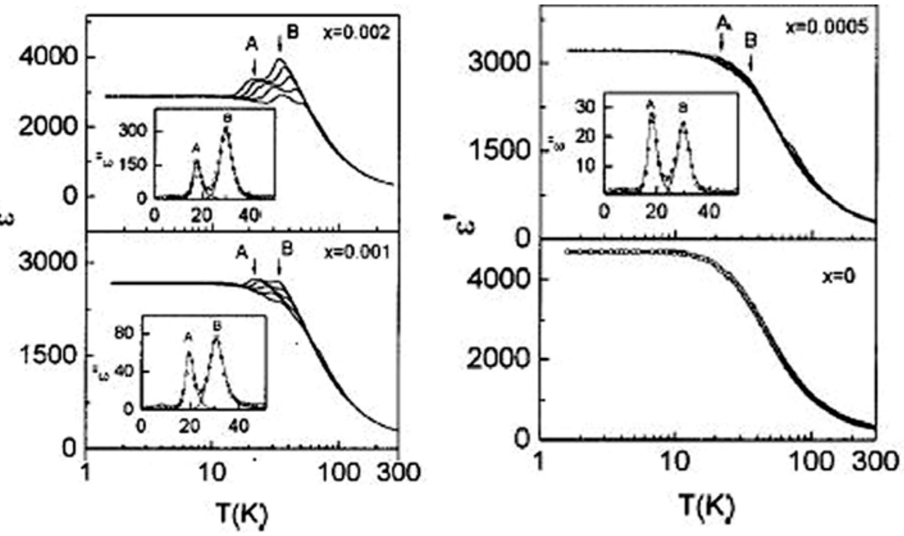

FIGURE 1.36. Temperature dependence of ε' for $Sr_{1-1.5x}Bi_xTiO_3$ with x = 0.002, 0.001, 0.0005 and 0 at 0.1, 1, 10, 100 and 1000 kHz (from top to bottom). Insets show the temperature dependence of ε'' at 0.1 kHz (Ang and Yu, 2002).

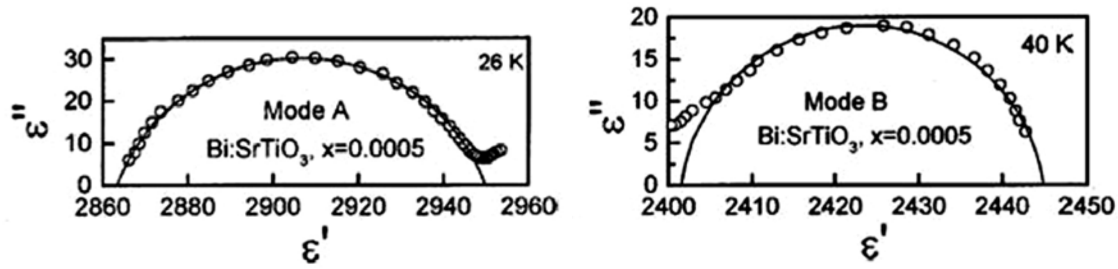

(a) (b)

FIGURE 1.37. Cole-Cole plot (ε'' versus ε') at 26 K for mode A (**a**) and at 40 K for mode B (**b**) of $Sr_{0.9925}Bi_{0.0005}TiO_3$ (Ang and Yu, 2002).

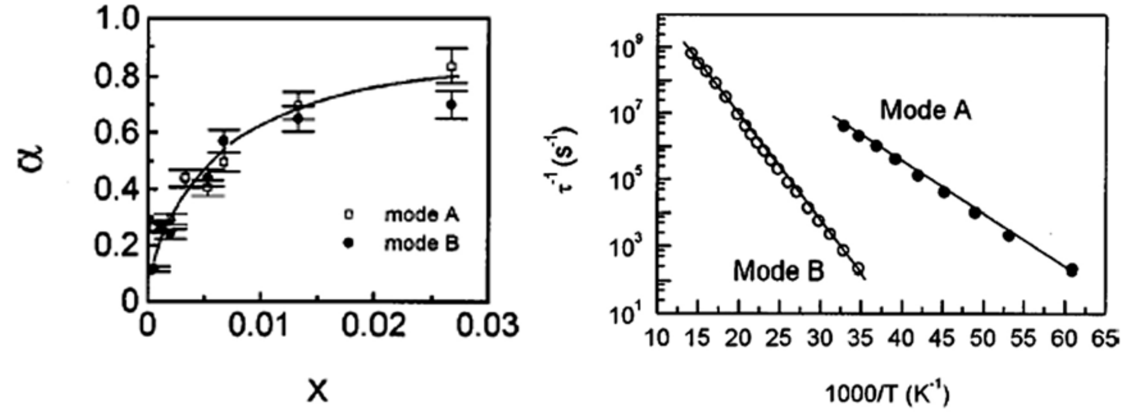

(a) (b)

FIGURE 1.38. **a** - Cole-Cole equation parameter α for modes A (at 22 K) and B (at 37 K) of $Sr_{1-1.5x}Bi_xTiO_3$ as a function of Bi content; **b** - Arrhenius plot (τ^{-1} versus 1000/T) for modes A and B of $Sr_{0.997}Bi_{0.002}TiO_3$ (Ang and Yu, 2002).

The temperature dependence of the dielectric constant under a dc electric field up to 35 kV/cm is shown in Figure 1.39a for $Sr_{1-1.5x}Bi_xTiO_3$ with x = 0.002 as a representative sample. With application of a dc bias, the amplitudes of the A and B modes are gradually decreased, but their T_m's are not shifted, what is more clearly seen from ε'' data, shown in the inset of Figure 1.39a. The latter fact provides evidence that modes A and B are different from the dipole glass mode or ferroelectric relaxor mode, whose T_m's are electric-field dependent (Ang and Yu, 2002). At higher fields a broad ε' peak, similar to that observed in undoped ST under dc bias, is induced, although the temperature range of the field dependent dielectric constant is expanded from about 0-80 K for undoped ST (see Figure 1.9) to about 0-150 K for Bi-doped ST.

It is worthwhile also to mention about the polarisation data, obtained from the measurement of the hysteresis loops for x = 0.002, at 1 Hz after zero field cooling / field heating (ZFC/FH) and field cooling / field heating (FC/FH) at 1 kV/cm, with cooling and heating rates 1 K/min. From the temperature dependence of the polarisation P, shown for $Sr_{1-1.5x}Bi_xTiO_3$ with x = 0.002 as an example in Figure 1.39b, two clear steps of the polarisation processes ΔP_A = 0.08 μC/cm^2 and ΔP_B = 0.11 0.08 μC/cm^2 are seen, which corresponds well to the modes A and B, respectively (Ang and Yu, 2000).

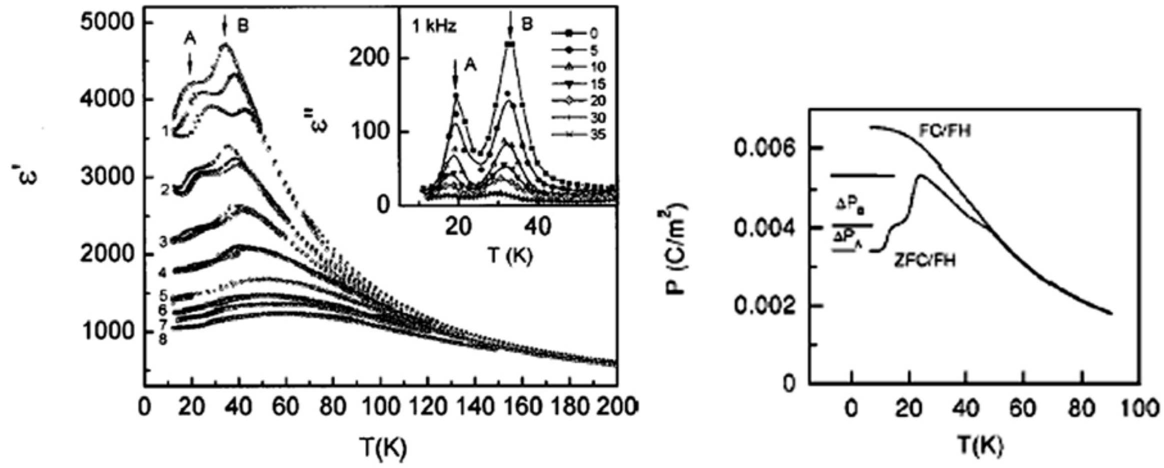

(a) (b)

FIGURE 1.39. Variation of real part of dielectric permittivity *ε*' at 10, 50 and 100 kHz (from top to bottom) (variation of imaginary part *ε*" at 1 kHz shown in inset) under 0 (1), 5 (2), 10 (3), 15 (4), 20 (5), 25 (6), 30 (7) and 35 (8) kV/cm (**a**); and of the polarisation under ZFC/FH and FC/FH at 1 kV/cm (**b**) of $Sr_{0.997}Bi_{0.002}TiO_3$ with temperature *T* (Ang and Yu, 2002; Ang and Yu, 2000).

The dielectric behaviour of $Sr_{1-1.5x}Bi_xTiO_3$, characterised by a broadened permittivity peak near its ferroelectric phase transition temperature, with the temperature of the permittivity maximum shifted to higher temperatures as the frequency increases, has been defined by Smolenskii as a diffused phase transition (DFT) (Ang and Yu, 2002). Now it is generally called relaxor behaviour and is the case for mode C. However, Ang and Yu (2002) have explained modes A and B occurring in the low concentration range of Bi-doped ST alternatively, as follows. As mentioned above, Sr-sites vacancies are induced in Bi-doped ST due to the charge balance, i.e., two Bi^{3+} ions substitute for two Sr^{2+} ions with creation of one Sr vacancy. Thus, Bi ions can be classified into two types, considering their local environment in the real lattice: A – Bi ions without any Sr vacancy nearby and B – Bi ions with a Sr vacancy nearby, as shown in a schematic illustration of Figure 1.40. On the other hand, Bi ions at Sr sites are supposed to be off-centre ions, based on ionic size consideration (Ang et al., 1998), that hence leads to the formation of dipoles. Thus, the occurrence of two dielectric modes A and B arises from existence of the two different types of dipoles: off-centre Bi ions with and without Sr vacancy, with different allowed displacements (Ang and Yu, 2002).

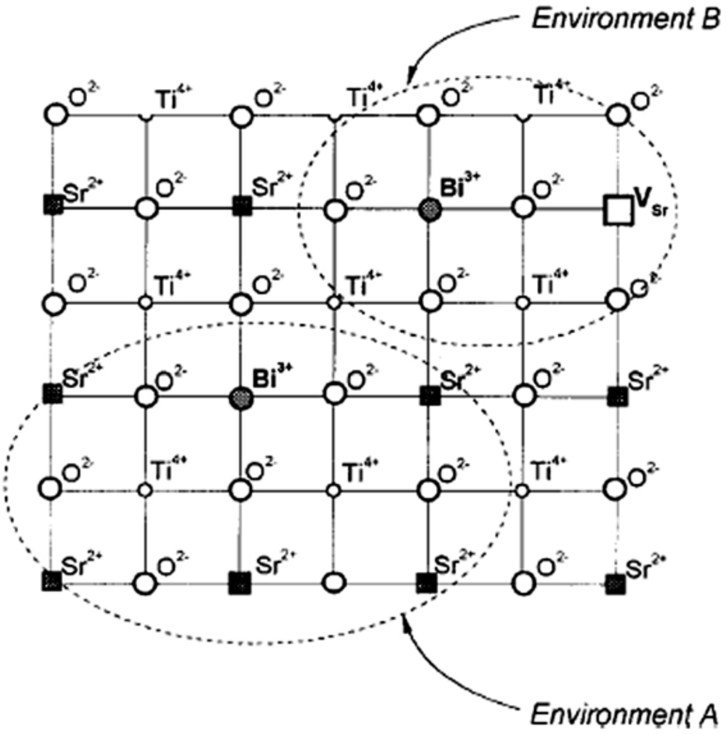

FIGURE 1.40. Schematic projection on the (100) plane for $Sr_{1-1.5x}Bi_xTiO_3$, showing two types of local environment of Bi ions (Ang and Yu, 2002).

$Sr_{1-1.5x}Bi_xTiO_3$ system has been also investigated by broad-band dielectric spectroscopy, including rf, microwave (MW), time-domain terahertz (TDT) and infrared (IR) spectroscopy (Porokhonskyy et al., 2004). The experimentally observed spectra and their fitting are presented in Figs. 1.41 and 1.42 for $Sr_{1-1.5x}Bi_xTiO_3$ with x = 0.0067 and 0.08. This investigation has shown that the polar TO_1 soft mode in IR spectra is strongly stiffened by Bi doping and its softening on cooling is gradually stopped. In addition, several polarisation mechanisms of non-phonon origin were found to contribute also to the dielectric permittivity. These mechanisms cause dispersions, marked as I-V in spectra of Figs. 1.41 and 1.42, in almost entire accessible frequency range (10^2 - 10^{12} Hz), including the immediate vicinity of polar phonon frequencies. The enhanced absorption I in the THz range, which vanishes at low temperatures, does not originate from a thermally activated process and was assigned to anharmonic quasi-Debye loss (phonon-density fluctuations) due to local breaking of the inversion symmetry. The relaxation II obeying Arrhenius law with U = 0.064 eV and τ_0 = (0.8-1.23) × 10^{-13} s was assigned to reorientation of dipoles created by the off-centre Bi ions (individual hopping of the Bi ions). The relaxation III was attributed to dynamics of the polar nanoclusters surrounding the Bi ions, which interact with each other via the highly polarisable host crystal lattice (cooperative hopping of the off-centre Bi ions). Additionally, oxygen-vacancy related relaxations IV and V also contribute also contribute to the dielectric response and the latter one is attributed to the electron-density local transport process (Porokhonskyy et al., 2004).

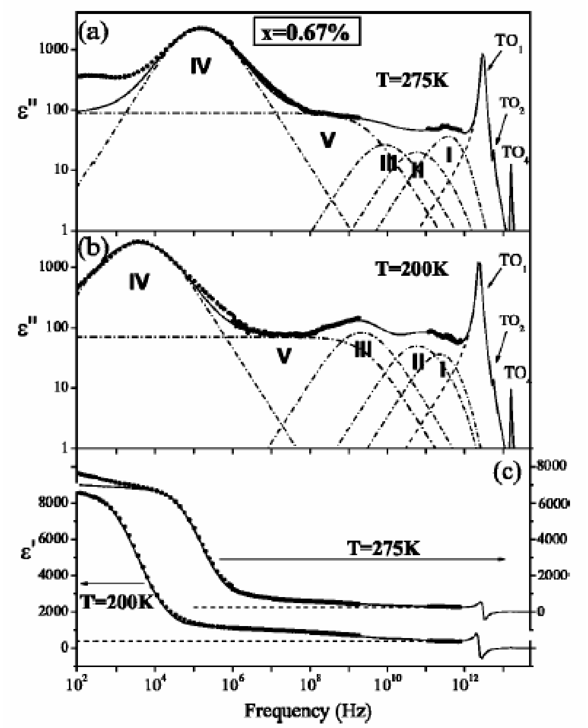

FIGURE 1.41. Dielectric loss ε'' at 275 K (**a**) and at 200 K (**b**) and constant ε' (**c**) at 275 K (right-side scale) and at 200 K (left-side scale) spectra of $Sr_{0.99}Bi_{0.0067}TiO_3$: experimental data in rf, MW and THz range (full circles), fits in IR range (dashed lines), full dielectric function fits (solid lines), loss part corresponding to individual distribution function (dash-dotted lines) (Porokhonskyy et al., 2004).

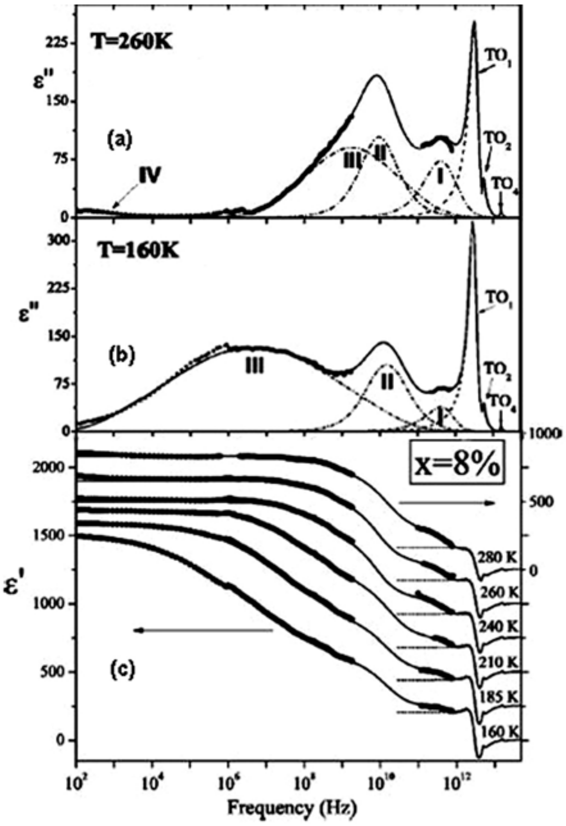

FIGURE 1.42. ε'' at 260 K (**a**) and at 160 K (**b**) and ε' (**c**) from 160 K (left-side scale) to 280 K (right-side scale) spectra of $Sr_{0.88}Bi_{0.08}TiO_3$ (each subsequent ε' spectrum starting from 160 K is shifted up by 250 with respect to the previous one): data in rf, MW and THz range (full circles), fits in IR range (dashed lines), full dielectric function fit (solid lines), loss part corresponding to individual distribution function (dash-dotted lines) (Porokhonskyy et al., 2004).

1.3.6. Summary and comments

Based on the review of the dielectric properties of ST system doped with Ba, Pb, Cd, Ca and Bi in this section, two main mechanisms proposed for an inducing of a polar state might be defined. These mechanisms are: 1) the cooperative displacements of the Ti^{4+} ions in the loosely packed oxygen octahedra, proposed for the ST systems diluted by ferroelectric $BaTiO_3$, $CdTiO_3$ and $PbTiO_3$, and 2) the polar clusters formed by the off-centre dopant ions, such as Ca and Bi, as summarised in Table 1.1.

Thus, the first mechanism is related with the distortion of highly polarisable Ti^{4+} ions out of oxygen octahedra centre. The magnitude of distortion evidently increases with the ionic size of A-site cation. In general, out-of-centre distortions were found to be related with electronic structure of B-site ions of perovskite type materials, being favourable around octahedrally coordinated d^0 transition metals (Kunz and Brown, 1995; Halasyamani and Poeppelmeier, 1998; Halasyamani, 2004). The magnitude of distortion was found to scale as $Mo^{6+} > V^{5+} > W^{6+} > Nb^{5+} > Ta^{5+} > Ti^{4+} > Hf^{4+} > Zr^{4+}$ (Halasyamani, 2004).

The occurrence of out-of-centre distortions d^0 transition metal cations can be understood on the basis of the second-order Jahn-Teller effect (SOJT) (Kunz and Brown, 1995).

Table 1.1. General mechanisms proposed for the formation of a polar state in doped $SrTiO_3$.

STUDIED SYSTEM	PROPOSED POLAR MECHANISM
Ba:$SrTiO_3$, Cd:$SrTiO_3$	Cooperative displacements of Ti^{4+} ions in loosely packed oxygen octahedra
Pb:$SrTiO_3$	Cooperative displacements of Ti^{4+} ions in loosely packed oxygen octahedra intensified by high electronic polarisability of Pb^{2+}
Ca:$SrTiO_3$	Polar clusters formed by off-centre dopant ions
Bi:$SrTiO_3$	Polar clusters formed by off-centre dopant ions with high electronic polarisability

The first-order Jahn-Teller effect (FOJT) deals with molecular distortions attributable to degenerate electronic ground states, whereas the SOJT is concerned with structural changes owing to a non-degenerate ground-state interacting with a low-lying excited state. An SOJT distortion occurs when the energy gap between the highest occupied (HOMO) and lowest unoccupied (LUMO) molecular orbital is small and there is a symmetry allowed distortion permitting the mixing of the HOMO and LUMO states (Halasyamani and Poeppelmeier, 1998). For the octahedrally coordinated d^0 transition metals, SOJT effects occur when the empty d-orbitals of the metal mix with the filled p-orbitals of the ligands (Kunz and Brown, 1995).

Since the lattice stresses and the electronic distortion do not have directional preferences, the direction of the distortion is determined by the bond network asymmetry and (if present) cation-cation repulsions (Halasyamani and Poeppelmeier, 1998).

On the other hand, the SOJT effect, the HOMO-LUMO interaction, can also be used to explain the distorted environments of metals with non-bonded electron pairs, Tl^+, Pb^{2+}, Sn^{2+}, Sb^{3+}, Bi^{3+}, Se^{4+}, and Te^{4+}. The situation with the lone-pair cations is somewhat more complex. The interaction of the s- and p-orbitals of the metal cation with the oxide anion p-states is critical for lone-pair formation. Regardless of how the lone pair is created, its structural consequences are profound, as the lone-pair “pushes” the oxide ligands towards one side of the cation, resulting in a highly asymmetric coordination environment (Halasyamani, 2004).

Thus, two families of cations are susceptible to an SOJT distortion, d^0 transition metals and cations with non-bonded electron pairs. In such a way, the additional effect of Pb^{2+} lone-pair ion on the increase of the temperature of phase transition induced in ST, comparing with even bigger Ba^{2+} ion is understandable.

As seen from Table 1.1., the second mechanism proposed for a formation of polar state is related with the off-centre displacements of small dopant ions in the large Sr site. Hence, as smaller dopant ion as higher its ionic polarisability and consequently more pronounced dielectric anomaly should be expected. However, on the other side the smaller the dopant ion the higher stress is induced in perovskite lattice, what can be reflected in the low solid solubility limit. Moreover, this stress promotes the diffuseness of the dielectric anomaly. In addition, the high electronic polarisability also promotes stronger effect on the increase of the temperature of dielectric anomaly induced in ST, as one can see comparing ST system doped with Ca and ST system doped with lone-pair Bi.

1.4. Characterization of relaxor and doped incipient ferroelectrics

In the previous section the relaxor type behaviour has been shown to be possible for $SrTiO_3$-based solid solutions, along with classic ferroelectric type behaviour. The relaxor behaviour has been widely observed in a great number of complex perovskites and their solid solutions. The broadening of the peak in the $\varepsilon'(T)$ in relaxors satisfied quite well the need to produce capacitors with a high value and a weak temperature dependence of the dielectric constant.

The ferroelectric relaxors display the following main features:

1) a rounded peaks in the temperature dependence of dielectric permittivity, in contrast to the sharp peak at the phase transition temperature observed for the classic ferroelectrics;

2) temperature of the dielectric constant peak always higher than the temperature of the dielectric loss peak;

3) temperature dependence of the dielectric constant obeying to relation: $1/\varepsilon'-1/\varepsilon'_m = (T-T_m)^\gamma/C$, with exponent γ close to 2 (Smolenskii, 1970; Viehland et al., 1992a), but not to 1 as for the classic ferroelectrics with the $\varepsilon'(T)$ following the Curie-Weiss law;

4) a frequency dispersion of permittivity around the permittivity peaks in the rf range and a long relaxation time, while the properties of classic ferroelectrics do not vary intensely with the frequency in the radio frequency range:

a) maximum of the real part of the dielectric permittivity decreases in value and its temperature shifts to higher temperatures with increasing measurement frequency;

b) maximum of the dielectric loss tangent increases in value and its temperature shifts to higher temperatures with increasing measurement frequency;

5) a square-to-slim transition of the hysteresis loops with the remnant polarisation decreasing with increasing temperature and tailing to zero in the diffuse range, in contrast to a sharp decrease to zero in classic ferroelectrics;

6) a non-ergodicity of permittivity (Viehland et al., 1992b):

a) for zero-field-cooling (ZFC) state, the polarisation displays a peak, whereas for field-cooling (FC) state, the polarisation decreases monotonically with increasing temperature;

b) ZFC and FC polarisation is the same above a characteristic temperature (dependent on the applied electric field) but below it, the irreversibility occurs and the FC polarisation is larger than ZFC one;

7) a compliance with a Vögel-Fulcher law: $\tau = \tau_0 \exp[U/k_B(T_m - T_f)]$, where k_B is the Boltzmann's constant, τ_0 is the pre-exponential factor, U is activation energy, T_m is the temperature of the permittivity maximum, T_f is the static freezing temperature at which relaxation time τ tends to infinity (Viehland et al., 1990);

8) existence of nanometer scale polar clusters (Randall et al., 1990; Bhalla et al., 2000) along with the absence of a macro-volume structural changing to a polar phase below the temperature of the permittivity maximum, usually observed in classic ferroelectrics:

a) at temperatures well below the permittivity peak, no evidence of optical anisotropy or of X-ray line splitting is found.

b) no macroscopic domain state can be observed except when strong electric fields are applied (during hysteresis or under bias).

c) in the absence of a field, relaxors contain very small nanodomains (polarisation clusters) whose size can be evaluated by scattering experiments.

The ferroelectric relaxor behaviour has been the subject of research for many years and several models have been proposed to explain it.

The relaxor behaviour was first explained by a compositional fluctuation model, supposing that, due to a statistical distribution of two or more type of ions in the same site of the lattice, the solid solution might possess a range of Curie points. Then, the ferroelectric phase transitions take place at different T_C, corresponding to the transition temperature of each local region, of the bulk solid solution, and thus a smeared and diffused phase transition (DPT) occurs (Smolenskii, 1970). The compositional fluctuation model, based on the Curie range concept from Smolenskii (1970) has been widely cited. However, although the DTP model of Smolenskii was adopted to explain the diffuse permittivity peak, the frequency dispersion observed in the radio frequency (rf) range could not be well explained. Smolenskii also proposed that the small compositional homogeneous regions exist with dimensions of 10-100 nm (Kanzig regions).

Later, Burns and Dacol (1983) deduced from the observation of the refractive index, that polar micro-regions could be sustained well above temperature of the dielectric constant peak T_m until a characteristic Burns temperature T_B.

A considerable amount of work involving transmission electron microscopy (TEM), Raman spectroscopy, dielectric constant and polarisation measurements evidenced that in relaxors the micro-regions of about 2-100 nm, in which homogeneous polarisation persist, exist, and the polar micro-regions play an important role in the relaxor behaviour (Cross, 1987). Considering the regions of short-range chemical order as nanoscale polar clusters, Cross proposed that the dipole moment of the clusters thermally switches between equivalent directions so macroscopic polar domains never form after the structural transition, as in classical ferroelectrics (superparaelectric model). By analogy with superparamagnetic behaviour it was proposed that there is no interaction between clusters. In this model the frequency dependence of the temperature of the dielectric maximum should obey a simple Debye relationship. However, physically unrealistic values for both activation energy and characteristic frequency were obtained.

The dipolar glass-like behaviour, suggested by Viehland et al. (1990, 1991), is an extension of the Cross superparaelectric model, in which the interactions between polar clusters are considered. Accordingly, the interactions between the polar microregions control the kinetics of the polarization fluctuations and the development of a frustration state near the freezing temperature (T_f) leading to a broadening of the relaxation-time distribution and strong deviations from the Curie Weiss behaviour near T_f. Above T_f the ferroelectric clusters are superparaelectric with dipole moments fluctuating between identical orientations and, as the temperature decreases, the superparaelectric moments freeze into a glassy state due to correlations between dipole moments.

Another theory invokes the contributions from a quenched random field which is again due to the compositional heterogeneity (Kleemann and Klossner, 1993). In this model the relaxor state is a ferroelectric state broken up into nanodomains under the constraint of quenched random fields. Charged compositional fluctuations are considered as the sources of random fields.

In a more recent theory, spherical random-bond - random-field model (Blinc et al., 2000), the relaxor is considered as a new type of dipolar glasses, namely, the spherical vector glass, in which the polar clusters are formed when two or more cations, moving in a multisite potential, create a single reorientable polar unit. Accordingly the regions of compositional fluctuations – "chemical clusters" are essentially static.

The above mentioned models generally agree that the physical origin of the dielectric peak in relaxors is then different from the one in classical ferroelectrics. In relaxors it is related to the thermal slowing of dynamic polar nanoregions rather than a paraelectric-ferroelectric phase change as in classical ferroelectrics. However, the relationships between the local chemical heterogeneities, the local polar clusters and their dynamics are not yet clearly established. Some of the models consider the regions of short-range chemical order as nanoscale polar clusters (Cross, 1987; Cross, 1994; Viehland et al., 1990; Viehland et al., 1991) and others, the charged compositional fluctuations as sources of random fields. An universal model for ferroelectric relaxor behaviour is still missing.

A general structure of the dielectric spectrum of relaxor ferroelectrics, as shown in Figure 1.43b, has been proposed by Bovtun et al. (2001). This spectrum is based on the analysis of dielectric spectra of $PbMg_{1/3}Nb_{2/3}O_3$ (PMN), $(Pb_{1-x}La_x)(Zr_{0.65}Ti_{0.35})O_3$ (PLZT) and $PbSc_{1/2}Ta_{1/2}O_3$ (PST).

The polar phonon contribution to the permittivity was supposed to be dominant above Burns temperature T_B. Below T_B the phonon contribution slightly decreases on cooling and the contributions caused by polar clusters dynamics prevail. Both dipole reversal of polar clusters and fluctuations of polar cluster boundaries contribute to the dielectric response at $T_f < T < T_B$. The reversal process is frozen out below T_f, but the contribution of cluster boundary fluctuations remains down to low temperatures. Thus, dynamics of the polar nanoclusters, which appear below T_B, evidently due to the structural disorder, is considered to be responsible for the relaxor behaviour. Two kinds of disorder can be considered in lead containing relaxor ferroelectrics of the perovskite structure: compositional (chemical) disorder of B-site (PMN, PST) or both B- and A-site (PLZT), and A-site dynamical disorder, caused by anharmonic motion of Pb. MW dielectric spectroscopy experiments on PST clearly prove that the correlated dynamic clusters, related to the Pb disorder, dominate (Bovtun et al., 2001).

However, along with numerous features similar to those of relaxor ferroelectrics, the doped incipient ferroelectrics have also some differences.

While short-range order extends over as small as nanometre scale in relaxors, the existence of large macroscopic polar regions with a length scale at least 0.1-1 μm, where the polarisation is approximately uniform, was recognised in $KTaO_3$:Li, Na and Nb crystals (Vugmeister and Glinchuk, 1990). A scheme of the dielectric behaviour of moderately doped incipient ferroelectrics, constructed from the analysis of dielectric spectra of $Ka_{1-x}Li_xTaO_3$ and $Sr_{1-1.5x}Bi_xTiO_3$ (Bovtun et al., 2004), exhibits divergence from relaxor behaviour also, as shown in Figure 1.43a and 1.43b. The main difference consists of the presence of individual off-centre ions hopping mechanism and in the absence of a specific temperature, below which the polar clusters appear (Burns temperature). The hopping of individual off-centre ions provides dielectric contribution, marked as (2) in Figure 1.43a, with a maximum at low temperatures. On the other hand, the dynamics of polar clusters, including dipole reversal of polar clusters and fluctuations of polar cluster boundaries, provide two dielectric contributions with a single unresolved maximum similarly to relaxor ferroelectrics (Bovtun et al., 2001). These processes are formed at a higher temperature than that of maximum of the individual ions contribution.

Thus, the contributions of individual ions (2), polar clusters (4) and their boundaries (3) are dominant in the dielectric spectra (Figure 1.43a). The contribution (2) dominates at lower concentrations of the off-centre ions, while the contributions (3) and (4) prevail at the higher concentrations. Below T_C, where flipping of polar clusters (i.e., correlated hopping of the off-centre ions) is frozen-out, the individual ion hopping (2) and cluster boundaries breathing (3) are the leading mechanisms. Only near helium temperatures, where all relaxation processes are effectively frozen, the phonon contribution (1) becomes dominant. The soft mode phonon contribution to the dielectric permittivity, characteristic for $KTaO_3$ and $SrTiO_3$, becomes lower and less temperature dependent with increasing concentration of the off-centre ions, being suppressed by the interaction with off-centre ions and polar clusters.

The contributions to static permittivity will switch off with increasing frequency in the sequence: polar clusters reversal, breathing of cluster boundaries, individual ion hopping and phonon contribution. Temperature evolution of characteristic frequencies of the main dielectric contributions is schematically presented in Figure 1.44a. Soft phonon mode frequency f_{SM} weakly decreases with lowering temperature. Mean relaxation frequency of individual off-centre ions f_{IH} and mean relaxation frequency of polar cluster boundaries $f_B(T)$ obey the Arrhenius law, while mean relaxation frequency of polar clusters reversal $f_{CL}(T)$ obeys the Vögel-Fulcher law with a freezing temperature equal to T_C.

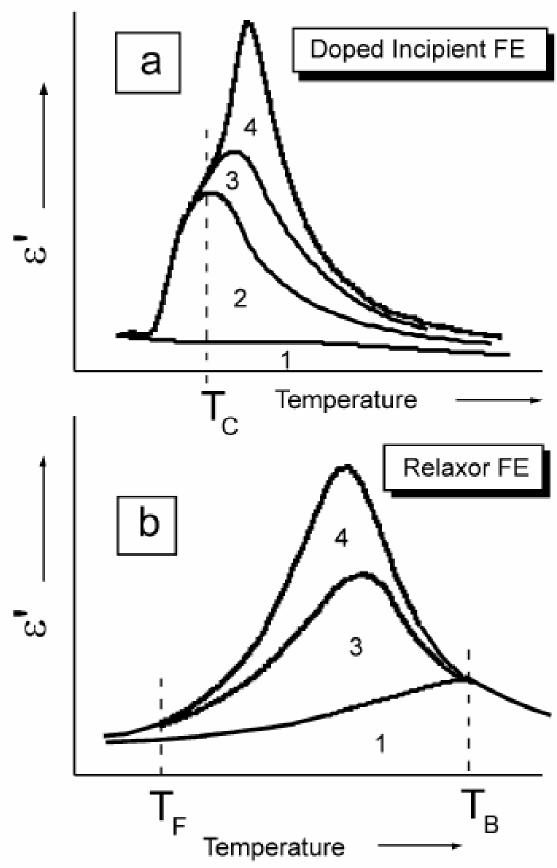

FIGURE 1.43. Structure of dielectric spectra of moderately doped incipient ferroelectrics (**a**) and relaxor ferroelectrics (**b**), consisting of dielectric contributions caused by: phonon polarisation mechanism (1), hopping of individual off-centre ions (2), fluctuations (breathing) of polar cluster boundaries (3) and polar cluster reversal (4).

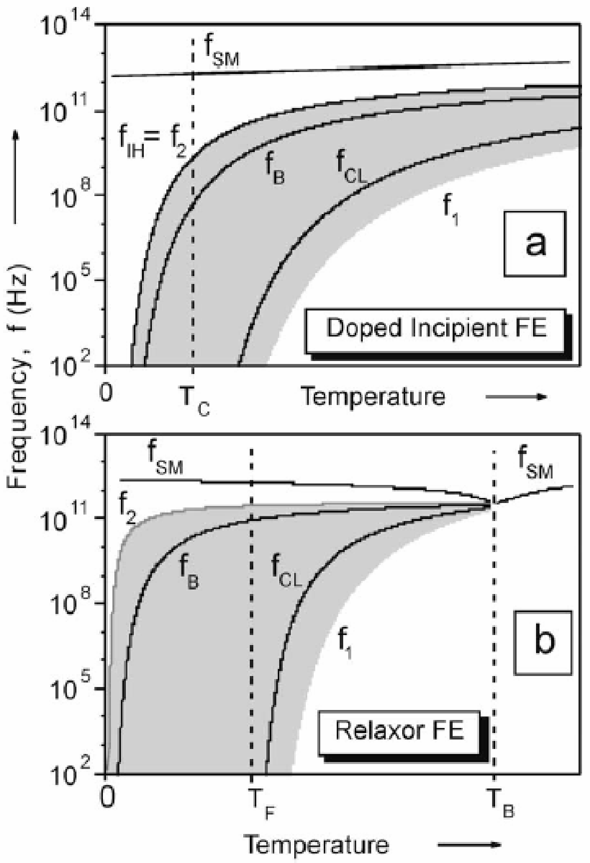

FIGURE 1.44. Temperature evolution of soft phonon mode frequency f_{SM}, mean relaxation frequency of individual off-centre ions f_{IH}, mean relaxation frequency of polar cluster boundaries f_B and mean relaxation frequency of polar clusters reversal f_{CL} of moderately doped incipient ferroelectrics (**a**) and relaxor ferroelectrics (**b**). The grey region between f_1 and f_2 curves denotes the frequency-temperature range of the relaxation processes caused by the off-centre ions (**a**) or of relaxor behaviour (**b**).

Both polarisation mechanisms, related to the cluster dynamics, are characterised by broad distributions of the relaxation times/frequencies. That is why the contributions of polar clusters reversal and breathing of cluster boundaries are not well resolved in the frequency domain and form a single range of relaxational dispersion, limited by the upper f_2 and lower f_1 relaxation frequencies. $f_2(T)$ obeys the Arrhenius law and is close or equal to the f_{IH}, while $f_1(T)$ obeys the Vögel-Fulcher law with the same freezing temperature as $f_{CL}(T)$ equal to T_C. Consequently, the grey region in Figure 1.44a between $f_2(T)$ and $f_1(T)$ denotes the frequency-temperature range of the relaxation processes caused by the off-centre ions. The range of relaxation time distribution seems to be wider in the case of relaxor ferroelectrics, probably because of the dominant role of the polar clusters. It should be noted that very slow relaxation processes and dielectric response below 100 Hz were outside of the consideration (Bovtun et al., 2004).

1.5. Mg- and Mn-doped $SrTiO_3$ ceramics: crystallochemistry and dielectric properties

1.5.1. Mg-doped strontium titanate

As has been shown above the ferroelectric anomaly can be easily induced in ST by the application of high enough electric field (Fleury et al., 1968), uniaxial stress (Uwe and Sakudo, 1976), oxygen isotope exchange (Itoh et al., 1999) or chemical substitutions in the lattice (Lemanov, 1999). Isovalent A-site substitution with Ca^{2+} (Bednorz and Müller, 1984), Ba^{2+} (Lemanov et al., 1996), Pb^{2+} (Lemanov et al., 1997a) and Cd^{2+} (Guzhva et al., 2001) have been reported to induce the low-temperature polar state. However, as shown in Figure 1.45, no ferroelectric-type anomaly was reported for A-site substitution with 1% of Mg^{2+} (Wang el al., 2000a).

The formation of solid solutions between $SrTiO_3$, $BaTiO_3$, $CaTiO_3$, etc. is easily expected due to the almost equivalent crystallographic structure of perovskite type and the close values of ionic radii of A-site cations.

Figure 1.46 illustrates the ionic radii of several ions according to Shannon (1976). Since there is no data for the ionic radii of Mg^{2+} and Mn^{2+} with coordination number $N_c = 12$, these values were obtained by the linear extrapolation of the data for smaller coordination number, reported also by Shannon (1976).

As one can see from Figure 1.46, the ionic radii of Mg^{2+} are substantially smaller than that of Sr^{2+}: $Mg^{2+}/Sr^{2+} = 0.835$ for coordination number $N_c = 12$. More than 15 % difference between the ionic size of Mg^{2+} and Sr^{2+} cations, as well as the crystallization of $MgTiO_3$ with the ilmenite-type structure instead of the perovskite, have been indicated as the restricting factors for the solid solubility of Mg^{2+} in Sr site of ST lattice (Kawada and

Fujimoto, 1990; Hirata et al., 1996). However, the data on solid solubility limit for Mg in Sr site of ST lattice are contradictory: Kawada and Fujimoto (1990) reported a solubility limit under 0.01, but Hirata et al. (1996) has found that formation of $Sr_{1-x}Mg_xTiO_3$ solid solutions are restricted to $x \leq 0.2$.

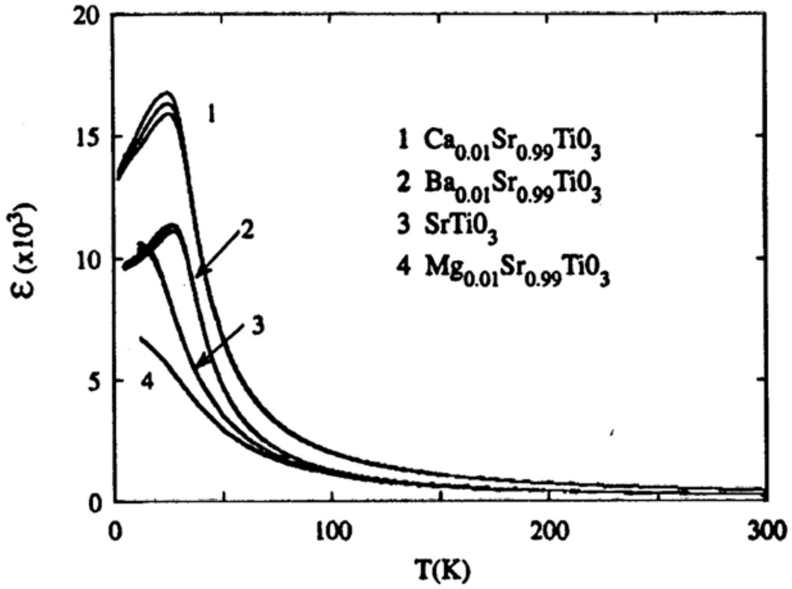

FIGURE 1.45. Dielectric constant of $Ca_{0.01}Sr_{0.99}TiO_3$ (1), $Ba_{0.01}Sr_{0.99}TiO_3$ (2), $SrTiO_3$ (3) and $Mg_{0.01}Sr_{0.99}TiO_3$ (4) ceramics at 10, 100 and 500 kHz versus temperature (Wang et al., 2000a).

In addition, relatively small Mg^{2+} ions are favourable to occupy the off-centre positions at the Sr sites, forming in such a way polar dipoles. Therefore, a ferroelectric anomaly may be induced in ST by Mg doping in spite of the fact that the electronic polarisability of Mg^{2+} is rather low (Shannon, 1993), especially compared with that of Sr^{2+} (see legend of Figure 1.46).

On the other hand, Mg ions may occupy Ti site of ST perovskite lattice accompanied by compensating oxygen vacancies. However, Mg solubility should be restricted since Mg^{2+} ion seems to be much bigger than Ti^{4+} ion (as can be deduced from Figure 1.46 the ratio $Mg^{2+}/Ti^{4+} = 1.19$ for $N_c = 6$). Thus, a second phase should appear as it was already recognized for $SrTi_{0.90}Mg_{0.10}O_{3-\delta}$ composition (Inoue et al., 1991). Moreover, the lattice parameter of $SrTi_{1-y}Mg_yO_{3-\delta}$ system was reported to increase linearly with Mg^{2+} content up to $y = 0.08$ and to keep invariable above this value, which is thought to be a solid solubility limit of Mg in Ti site of ST (Inoue et al., 1991). In addition, the concentration of oxygen vacancy increases and a p-type semiconductivity is promoted, when Ti ions are substituted for acceptor Mg^{2+}. Thus, $SrTi_{1-y}Mg_yO_{3-\delta}$ system, is a promising material for oxygen sensors, also sensitive to CO_2 and water vapour (Zheng and Sorensen, 1999).

No dielectric characterization was reported for this system so far.

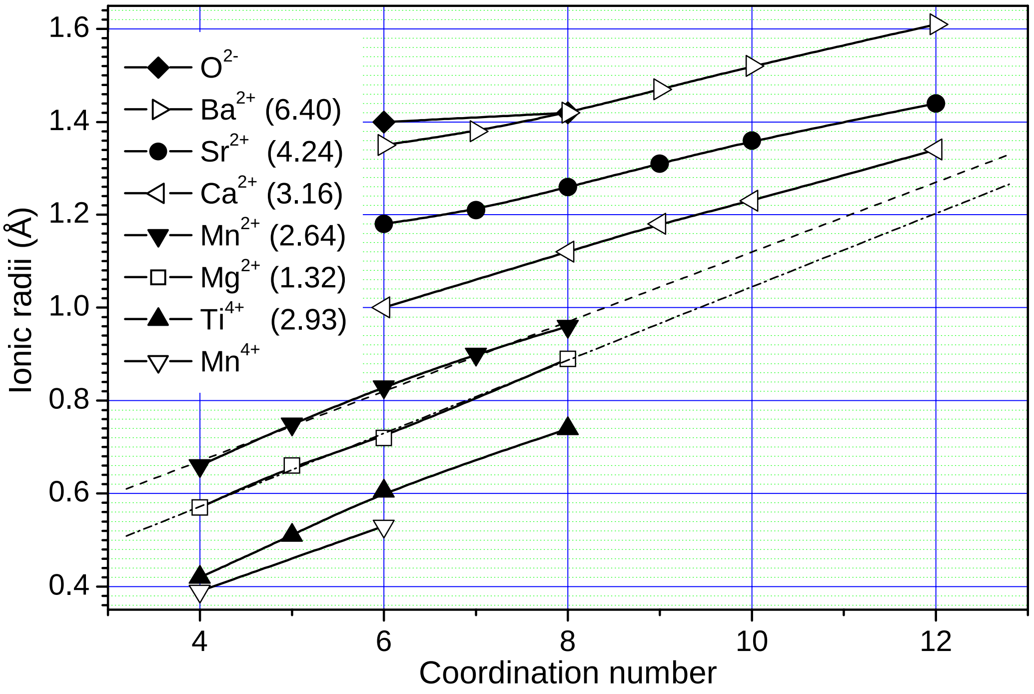

FIGURE 1.46. Ionic radii of several ions versus coordination number following Shannon (1976). Electronic polarisabilities of the ions in $Å^3$ are presented in brackets following Shannon (1993).

Recently Kvyatkovskii (2002) has calculated the local potential for impurity ions in A-site of ST using the non-empirical Hartree-Fock-Roothaan formalism. According to these calculations, Ca, Ba, Pb and Cd, substituting Sr, move in a single-well potential and the corresponding solid solutions are displacive-type ferroelectrics. On the other hand, Mg in Sr site occupying off-centre positions is suggested to move in a multi-well local potential, shown in Figure 1.47 for the [001] direction. The displacement from the central position and corresponding energy was estimated to be 0.32 Å and 0.007 eV respectively. Thus, a relaxation mechanism, which could lead to the relaxor-like behaviour similar to that observed in $K_{1-x}Li_xTaO_3$, was predicted for $Sr_{1-x}Mg_xTiO_3$ (Kvyatkovskii, 2002).

According to the above description there are several crystallochemical reasons that could lead to the appearance of a ferroelectric type anomaly in ST by doping with Mg.

However, no systematic study on the crystallographic structure, microstructure and dielectric behaviour of both $Sr_{1-x}Mg_xTiO_3$ and $SrTi_{1-y}Mg_yO_{3-\delta}$ systems has been reported so far. Moreover, the solid solubility limit for Mg in Sr site of ST lattice should be refined, because of the contradiction reported in previous works (Kawada and Fujimoto, 1990; Hirata et al., 1996). Hence further studies on strontium titanate doped with magnesium systems are required.

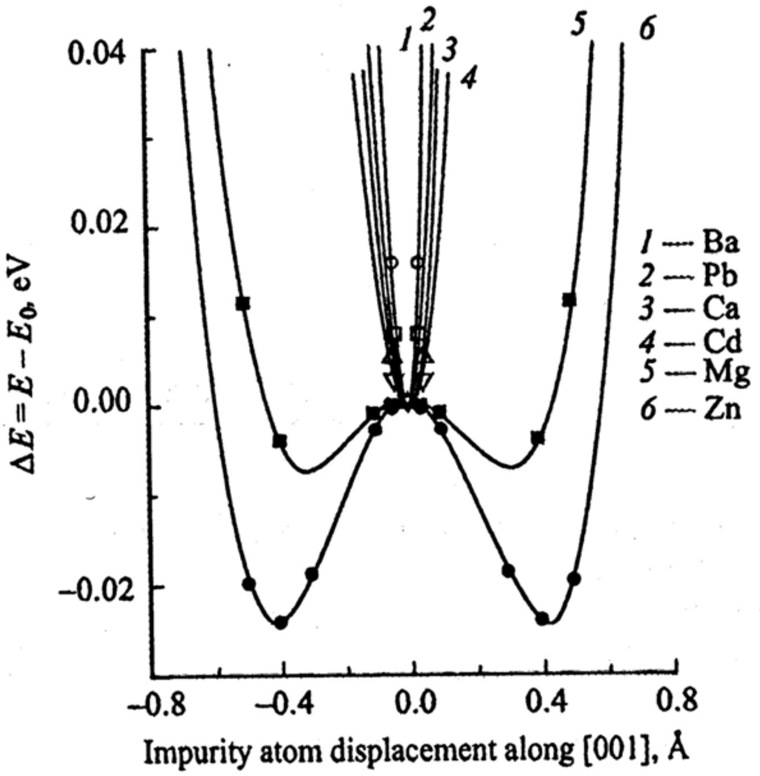

FIGURE 1.47. Local adiabatic potential for Ca (1), Ba (2), Pb (3), Cd (4), Mg (5) and Zn (6) doping atoms at Sr site of strontium titanate (Kvyatkovskii 2002).

1.5.2. Mn-doped strontium titanate

In 1959, Müller has published the earliest report on Mn-doped ST, in which the electron paramagnetic resonance (EPR) of as-grown single crystal was investigated. The obtained EPR spectrum of ST doped with 0.01 wt% of MnO_2 was attributed to Mn^{4+} ($3d^3$, $S = 3/2$) substitution of Ti^{4+} (Müller, 1959). The suggestion that Mn ions may occupy the Ti sites of ST perovskite lattice can be supported by the proximity of ionic sizes between Mn^{4+} and Ti^{4+}. As seen from Figure 1.46, the ratio between Mn^{4+} and Ti^{4+} is 0.876 for coordination number $N_c = 6$ (Shannon, 1976). Later, EPR investigation of ST single crystal doped with 0.48 mol% of Mn has provided the evidence that the thermal annealing of such a crystal in a reducing atmosphere for several hours converts Mn^{4+} ions into the lower valence state ions such as Mn^{3+} ($3d^4$, S = 2) and Mn^{2+} ($3d^5$, S = 5/2) (Serway et al., 1977). Oxygen vacancies were proposed as a charge compensation species for trivalent and divalent impurity ions in Ti^{4+}-site. More recently, EPR response of polycrystalline samples of ST with 1, 2.5, and 3 mol% of Ti substituted by Mn were measured between 120 and 300 K (Azzoni et al., 2000a). Lines attributed to Mn^{2+} ions at Ti-site were observed in the EPR spectra, in addition to those of Mn^{4+} ions at Ti-site.

EPR and Raman scattering measurements were performed for related system $Sr_{1-x}La_xTi_{1-y}Mn_yO_3$ with $x = y \leq 10$ mol% (Azzoni et al., 2000b). Such system with La and Mn contents x, $y \leq 5$ mol% reveals weak and narrow EPR signals of Mn^{2+} and Mn^{4+}, indicating the nearly complete stabilisation of the Mn^{3+} state. However, more heavily doped samples showed very broad EPR signal with intensity and resonance field strongly dependent on temperature. For this system, the Raman spectra at room temperature are very different from that of undoped ST, in which the second-order scattering completely dominate due to the cubic structure of ST (Petzelt et al., 2001). In spectrum of Mn-doped ST sample, the first-order scattering feature at about 500 cm^{-1} was observed in Raman spectra at room temperature, implying that the cubic structure is strongly distorted (Azzoni et al., 2000b).

Raman scattering measurements performed in the temperature range of 10-300 K on undoped and annealed in manganese vapour at 1350 ºC during 120 s ST single crystals revealed no considerable difference (Marjanovic and Popovic, 1998). Two zone-centre phonon modes appeared in both spectra at cooling below the structural phase transition temperature $T_a \approx 106$ K, however, the frequency of the modes shifts to somewhat lower energies for Mn-doped ST crystals under further cooling (Marjanovic and Popovic, 1998). No systematic research of Mn effect on structure, microstructure and dielectric behaviour of ST ceramics has been undertaken so far.

As seen from Figure 1.46, Mn^{2+} ionic radius value, extrapolated to the $N_c = 12$ from the values obtained by Shannon (1976) for smaller coordination numbers, gives the ratio $Mn^{2+}/Sr^{2+} = 0.882$. Thus, Mn^{2+} might occupy the off-centre position in Sr site similarly to Mg^{2+}. In addition, due to the smaller ionic radius of Mn^{4+} as compared to that of Ti^{4+}, displacement of Mn^{4+} ions from the centre position of the oxygen octahedra may also occur. Hence either in Sr or Ti site of ST lattice, polar dipoles due to the off-centre positions of Mn ion may be formed. Thus, in spite of the lack of the reports and absence of theoretical works on dielectric properties of $Sr_{1-x}Mn_xTiO_3$ and $SrTi_{1-y}Mn_yO_3$ systems, a ferroelectric anomaly might be induced in ST by Mn doping from the ionic size consideration.

Just few studies have been devoted to the dielectric properties of Mn-doped ST. Popovic et al. (1998) and Kulagin et al. (2001) reported a continuous lowering of the dielectric constant in ST single crystals with addition of 0.05-0.10 wt% of Mn, in the temperature range of 10-300 K.

Regarding investigations on ceramic samples, $(Sr_{1-3x/2}La_x)(Ti_{1-y}Mn_y)O_3$ system with x = 1.4 mol% and y = 0.1 mol% was studied by Iguchi and Lee (1993). The dielectric relaxation observed around 170 K was shown to consist of two relaxation peaks: one due to thermal motions of Ti^{4+} between potential minima produced by lattice distortions and another due to Mn^{4+} with activation energy somewhat smaller than that of Ti^{4+}. The activation energies and the relative intensities of these relaxation processes were attributed to the difference in ionic radii of Mn^{4+} and Ti^{4+} and to the difference in energies of formation of a strontium vacancy adjacent to Mn^{4+} and to Ti^{4+} (Iguchi and Lee, 1993).

During the preparation of this thesis, Lemanov and co-workers (2004) reported a dielectric relaxation in the $SrTiO_3$:Mn ceramic system with Mn concentration up to 0.05. Although the dopant site occupancy was not clearly stated in the text, the authors assume a Ti-site preferential substitution for the Mn ion and that the observed relaxation is related to defects of the $\{Mn^{2+}_{Ti}\text{-}O^-\}$ type. The oxygen post-sintering annealing treatment of the samples, conducted in the above mentioned work, should favour the oxidation of Mn ion to Mn^{4+} in the case of Ti-site occupation, or at least to Mn^{3+}, reducing the number of polar defects and, consequently, reducing the relaxation strength. However, the relaxation parameters were reported to be insensitive to the post-sintering annealing in an oxygen flow and to the dopant concentration. In addition, the Mn solid solubility in ST ceramics was determined from the lattice parameter variation to be restricted to 5% (Lemanov et al., 2004).

Thus, to the authors' best knowledge, no systematic research of Mn lattice site occupancy effect on structure, microstructure and dielectric behaviour of ST ceramics as well as on the solid solubility limit of Mn in ST, either at Sr- or at Ti-site, has been undertaken.

1.5.3. Objectives of the present work

As shown above, no systematic study on the crystallographic structure, microstructure and dielectric behaviour of both magnesium and manganese doped strontium titanate systems has been reported so far. Nevertheless, the off-centre displacements of small dopant ions at the large Sr site have been shown to induce the dielectric anomaly in ST (see Table 1.1). The effect of such doping is expected to be higher for the dopants with higher electronic and ionic polarisability. The latter increases with the ionic size decrease.

Hence, Mg and Mn are suitable elements to induce the ferroelectric instability in strontium titanate. On the other hand, Mg^{2+} and Mn^{4+} ions may occupy Ti site of ST perovskite lattice. The lack of the reports and the absence of theoretical works on the dielectric properties of such systems are evident. Based on this, the following questions are raised:

(1) What is the solid solubility limit for magnesium and manganese at Sr and Ti sites of ST?

(2) Does the dielectric anomaly and polarisation really appear at low temperatures in Mg- and Mn-doped strontium titanate?

(3) What is the effect of dopant content, doping site occupation and processing conditions on the properties of Mg:$SrTiO_3$ and Mn:$SrTiO_3$?

(4) May magnesium and manganese doped ST be used as tunable components for electronic devices?

In relation to the first question, ***the first objective of the present work*** is to fabricate dense $Sr_{1-x}Mg_xTiO_3$, $Sr_{1-x}Mn_xTiO_3$, $SrTi_{1-y}Mg_yO_{3-\delta}$ and $SrTi_{1-y}Mn_yO_3$ ceramics and to determine their solid solution limits, structure and microstructure. The main steps to achieve this objective are:

1) Preparation of the ceramic samples with the compositions $Sr_{1-x}Mg_xTiO_3$, $Sr_{1-x}Mn_xTiO_3$, $SrTi_{1-y}Mg_yO_{3-\delta}$ and $SrTi_{1-y}Mn_yO_3$;
2) Phase, microstructure and local chemical analysis;
3) Crystallogarphic structure and lattice parameter characterisation.

Attemting to answer the second and third questions, ***the second objective of the present work*** is to perform a complete dielectric characterisation of the obtained ceramic samples. The main steps are:

1) Measurements of dielectric properties in wide temperature (10-300 K), frequency (10^2-10^{12} Hz) range;
2) Analysis of the experimental results, including a validation of the Curie-Weiss law and Barrett relation, as well as of the Arrhenius law and Vögel-Fulcher relation;
3) Measurements of the hysteresis loops to confirm the polar nature of the anomaly;
4) Comparison of the results in terms of dopant content, doping site occupation and processing conditions.

Concerning the third and forth questions, ***the third objective of the present work*** is to develop $SrTiO_3$-based ceramics with high tunability of the dielectric constant and low loss to be used as tunable components for electronic devices. The main steps are:

1) Measurements of dielectric properties including the dielectric constant and loss under bias electric field;
2) Analysis of the experimental results, including calculation of tunability and quality factor for tunable components (QFTC);
3) Comparison of the results in terms of dopant content, doping site occupation and processing conditions.

2. Experimental Procedure

Four ceramic systems: $Sr_{1-x}Mg_xTiO_3$, $SrTi_{1-y}Mg_yO_{3-\delta}$, $Sr_{1-x}Mn_xTiO_3$ and $SrTi_{1-y}Mn_yO_3$ are prepared by solid state reaction in the present work. This chapter is mainly concerned with the experimental procedure, including sample preparation, crystal structure examination, microstructure observation and measurements of dielectric properties.

2.1. Sample preparation

2.1.1. Nominal compositions

Magnesium-doped $SrTiO_3$ samples

Magnesium can be doped at either Sr (Kawada and Fujimoto, 1990; Hirata et al., 1996) or Ti (Inoue et al., 1991; Zheng and Sorensen, 1999) sites of $SrTiO_3$, depending on the starting compositions.

Two series of samples, i.e., $Sr_{1-x}Mg_xTiO_3$ and $SrTi_{1-y}Mg_yO_{3-\delta}$, were prepared in this work. In the former formula, magnesium (Mg^{2+}) was assumed to isovalently substitute strontium (Sr^{2+}). In the latter, magnesium ions (Mg^{2+}) were supposed to be incorporated at Ti sites, with the extra charges, being compensated by oxygen vacancies. The nominal compositions are listed in Table 2.1.

Table 2.1. Mg-doped $SrTiO_3$-based compositions.

COMPOSITION	
$Sr_{0.99}Mg_{0.01}TiO_3$	$SrTi_{0.99}Mg_{0.01}O_{3-\delta}$
$Sr_{0.98}Mg_{0.02}TiO_3$	$SrTi_{0.98}Mg_{0.02}O_{3-\delta}$
$Sr_{0.97}Mg_{0.03}TiO_3$	$SrTi_{0.95}Mg_{0.05}O_{3-\delta}$
$Sr_{0.92}Mg_{0.08}TiO_3$	$SrTi_{0.90}Mg_{0.10}O_{3-\delta}$
$Sr_{0.85}Mg_{0.15}TiO_3$	$SrTi_{0.85}Mg_{0.15}O_{3-\delta}$

Manganese-doped $SrTiO_3$ samples

The doping behaviour of manganese (Mn) ions in $SrTiO_3$ is studied in this work with manganese concentration up to 15%, i.e., higher than the concentrations used in earlier works (Müller, 1959; Serway et al., 1977; Popovic et al. 1998; Marjanovic and Popovic, 1998; Azzoni et al., 2000a; Kulagin et al., 2001). $Sr_{1-x}Mn_xTiO_3$ and $SrTi_{1-y}Mn_yO_3$ series of samples were prepared. Manganese is a multivalent element with the possible charge states 2+, 3+, 4+, 6+ and 7+. So Mn^{2+} was supposed to occupy a Sr site in the former formula and Mn^{4+} was assumed to substitute for Ti^{4+} in the latter formula without any extra charges to compensate. The nominal compositions of the samples prepared are tabulated in Table 2.2. In addition, $Sr_{0.975}Mn_{0.025}TiO_3$ ceramics was prepared for cold-stage TEM analysis.

Table 2.2. Mn-doped $SrTiO_3$-based compositions.

COMPOSITION	
$Sr_{0.9975}Mn_{0.0025}TiO_3$	$SrTi_{0.99}Mn_{0.01}O_3$
$Sr_{0.995}Mn_{0.005}TiO_3$	$SrTi_{0.95}Mn_{0.05}O_3$
$Sr_{0.99}Mn_{0.01}TiO_3$	$SrTi_{0.90}Mn_{0.10}O_3$
$Sr_{0.98}Mn_{0.02}TiO_3$	$SrTi_{0.90}Mn_{0.15}O_3$
$Sr_{0.97}Mn_{0.03}TiO_3$	
$Sr_{0.95}Mn_{0.05}TiO_3$	
$Sr_{0.90}Mn_{0.10}TiO_3$	
$Sr_{0.85}Mn_{0.15}TiO_3$	

2.1.2. Preparation of ceramic samples

The sample powders were prepared by mixed oxide method. The following procedures were undertaken according to the conventional processing method for ceramic samples.

Preparation of the raw powders of the nominal compositions

The row powders of $SrCO_3$, TiO_2, $MgCO_3$, $Mn(NO_3)_2$ and MnO_2 were firstly weighed according to the nominal compositions shown in Table 2.1 and 2.2. The powders were then mixed with ball milling in alcohol with a planetary mill and zirconia balls for 5-8 hours. Further the mixtures were dried in an oven at 80 ºC for about 12 hours.

Calcination

The above mentioned powders were closely packed in alumina crucibles and were calcined at 1150 ºC for 2 hours in order to fully release carbon dioxide (CO_2) from the

$SrCO_3$ and $MgCO_3$ nitrogen oxide from $Mn(NO_3)_2$ raw powders and to achieve a reaction of the final product between the raw powders.

Second ball milling

In order to get fine particles and also improve the solid state reaction reactivity (or sinterability) of the powders, a second ball milling was performed. The calcined powders were milled in alcohol on a planetary mill with zirconia balls for 5-8 hours. The particle size distributions together with the average particle size after the ball milling were determined using Particle Size Analyzer (Coulter LS 230). After being dried in an oven at 80 ºC for about 12 hours, the powders were screened with a 180 μm mesh sieve.

Pressing of pellets

The powders from the previous step were pressed with a steel die into green pellets of 1 cm in diameter and about 2 mm in thickness under a pressure of 20 MPa (Carver Laboratory Press, Fred S. Carver Inc., USA). The pellets were then isostatically pressed in fluid of oil under 200-300 MPa (Stansted Fluid Power Ltd., England / Autoclave Engineer, Inc., USA).

Sintering

The pressed samples were sintered in air at different temperatures and for different dwelling times to investigate the sinterability of the ceramic samples. Then appropriate sintering temperatures were chosen, evaluated by shrinkage and sintering density. The procedure adopted for sintering was as follows: room temperature, heating at 5 ºC/min, → sintering temperature (T_s) and dwelling time (t_s) → cooling in furnace at 5 ºC/min.

Selected Mn-doped ST samples ($Sr_{0.98}Mn_{0.02}TiO_3$ and $SrTi_{0.95}Mn_{0.05}O_3$) were sintered in different atmospheres such, as oxygen, nitrogen and air.

After sintering, the two faces of the samples were carefully polished with 800# grinding paper in order to remove the as-sintered surface layers. The samples were than thoroughly cleaned and dried.

2.2. Density measurements

The densities of the sintered samples were measured by the Archimedes' method using diethylphthalat ($C_{12}H_{14}O_4$) as the immersion liquid. The value of the measured density was calculated by the following equation (Pratten, 1981):

$$D = (d_{liq}W_1 - d_{air}W_2)/(W_1 - W_2)\ (g/cm^3), \tag{2.1}$$

where W_1 and W_2 are, respectively, the weights of the sample in air and in liquid; d_{air} and d_{liq} are the densities of the air and liquid at 1 atm and room temperature, here with d_{air} = 0.001185 g/cm^3 and d_{liq} = 1.119 g/cm^3, respectively for the air and for diethylphthalat ($C_{12}H_{14}O_4$). The relative density, therefore, was calculated as:

$$D_r = D/(M/N_A a^3), \tag{2.2}$$

where D is the measured density, M is the one-molecule unit molar mass, $N_A = 6.022 \times 10^{-23}$ mol^{-1} is the Avogadro number, and a is the cubic one-molecule unit cell parameter, obtained from X-ray diffraction profiles.

Only when the sample density was estimated to be lower than 90%, geometric method has been used.

2.3. Crystallographic and microstructure characterisation

2.3.1. Phase assemblage and crystallography

The phase assemblage in calcined powders and in sintered samples was examined by the powder X-ray diffraction (XRD) technique. Because the wavelength of X-rays (from few angstroms to 0.1 angstrom) is comparable to the size of atoms, they are ideally suited for probing the structural arrangement of atoms and molecules in a wide range of materials. Bragg's law of X-ray diffraction is given by the following formula:

$$2\ d \sin\theta = k\ \lambda \tag{2.3}$$

A monochromatic X-ray beam with a wavelength λ incident onto a crystalline material at an angle θ leads to diffraction when the distance travelled by the rays reflected from successive planes differs by a complete number *k* of wavelengths. By varying the angle *theta*, the Bragg's law conditions are satisfied for different *d*-spacings in polycrystalline materials (Jenkins and Snyder, 1996).

In this work, the XRD measurements at room temperature were performed on a powder X-ray diffractometer (Rigaku, CuKa radiation, Geigerflex C/max- C series). The samples were first ground with an agate mortar and a pestle. For qualitative analysis of the calcined powders, the diffraction angle (2θ) was in range 4-80° with a scanning rate of 3 °/min and a sampling step of 0.05°. For the quantitative analysis of the sintered samples (e.g. lattice parameters and crystallography), the diffraction angle (2θ) was in range of 20-108° with a scanning rate of 1 °/min and a sampling step of 0.02°. The lattice parameter was calculated by a least square approach fitting of the XRD data using Rietveld refinement WinPLOTR software.

2.3.2. Microstructure

The microstructures of the fractures and / or the polished and thermally etched sections of the samples were studied with scanning electron microscopy / energy dispersive spectroscopy (SEM / EDS).

In SEM, an electron beam source emits electrons which are then collected and focused by lenses to form few nanometres sized probes. Deflection coils are used to operate electron beam and scan sample surface. Simultaneously, another electron beam runs over a TV monitor screen in a synchronized mode. The image magnification is the ratio of the scanned monitor range to the scanned sample range, and it is easily controllable by beam deviation elements. Primary electron beam interacts with the specimen surface in a complicated manner resulting in different emitted signals (secondary and back scattered electrons, X-ray radiation, etc.), which could be registered with the appropriate detector (Goldstein, 1992).

In this work, for SEM, sections of the samples were polished with diamond pastes stepwise from 15 to 1/4 μm. Then the sections were thermally etched in a furnace at temperatures 50-100 ºC lower than the sintering temperatures. The etching depth was controlled by the dwelling time (from 3 to 10 min) and observed with optical microscope

(Nikon, HFX-IIA). Finally, the microstructures, micro-chemical analysis and X-ray map profiles were performed with the scanning electron microscope (Hitachi, S-4000 SEM / EDS).

The local microstructure and chemical analysis of ceramics was carried out on sintered samples by means of transmission electron microscopy / energy dispersive spectroscopy (TEM / EDS). Transmission electron microscope Hitachi 9000 was used.

In a TEM setup, a thin specimen is illuminated with electrons (the primary electrons). Whatever part is transmitted is projected onto a phosphor screen for the user to see. The darker areas of the image represent those areas of the sample, where fewer electrons were transmitted through (they are thicker or denser). The lighter areas of the image represent those areas of the sample that more electrons were transmitted through (they are thinner or less dense). An image in TEM can be formed by using the central spot of unscattered electrons, or by some or all of the scattered electrons. The kind of the electrons is chosen by an insertion of aperture into the back focal plane of the objective lens, thus blocking out most of the diffraction pattern except that which is visible through the aperture. If the direct beam is selected, the resultant image is called a bright-field image, and if we select scattered electrons of any form, we call it a dark-field image. If no aperture is inserted, we observe electron diffraction pattern (Williams and Carter, 1996).

In this work, the two faces of the samples were carefully polished with 800# grinding paper in order to reduce their thickness to approximately 30 μm. The samples were then glued to copper ring and ion beam milled using a BAL-TEC Ion Mill (RES 100). The angle between ion beam and the sample plane of 20º, the voltage of 6 kV and the current of 2.3 mA were used until the appearance of the hole in the centre of the sample. Then the milling was conducted during 10 min with the angle decreased to 8º in order to improve the area near the hole, later used for TEM / EDS analysis. For selected samples, TEM analysis was carried out from at several fixed temperatures 16 to 300 K.

2.3.3. Average grain size measurements

The average grain size of the sintered pellets was measured on at least 3 SEM micrographs, by a Leica Quantimet Q500+ and AnalySIS (Soft Imaging System GmbH) software.

2.4. Raman spectroscopy measurements

Raman scattering is inelastic scattering of light by elementary excitations in a material. In this thesis, Raman spectroscopy was used for more detailed structural characterisation on the samples of the selected compositions. Raman scattering is a two-phonon process, simultaneously annihilating the incident phonon ($\hbar\omega_{in}$) and creating the scattering phonon ($\hbar\omega_{sc}$). Scattering from time-dependent vibration of atoms is accompanied with conservation of energy:

$$\hbar\omega_{in} = \hbar\omega_{sc} \pm \hbar\Omega \tag{2.4}$$

where $\hbar\Omega$ is the energy associated with the phonon created (Stokes) or annihilated (anti-Stokes) in the scattering process. The positive frequency difference $\Delta\omega = \omega_{in} - \omega_{sc}$ is most commonly measured in Raman experiments and is called the Raman shift. Only those vibrations, which modulate polarisability, appear in the Raman spectra. Usually a Raman spectrum consists of the set of frequencies or bands. Each band corresponds to a specific elementary excitation of lattice (Ibach and Lüth, 1993).

In this work, Raman spectra were acquired in the back scattering geometry using a Renishaw Raman microscope after the ceramics were excited by the argon laser beam with the wavelength of 514.5 nm and the spot size of 1-2 μm in diameter (micro-Raman spectroscopy measurements). The measurements were performed at room temperature and at several fixed temperatures down to 80 K. These measurements were carried out at the Department of Dielectrics, Institute of Physics, Academy of Sciences of the Czech Republic, in the group of Dr. Jan Petzelt.

2.5. Dielectric measurements

2.5.1. Electrodes

Au was used as the electrode material, being sputtered onto the two faces of the sintered ant polished samples using the SEM coating unit (E5000, Polaron Equipment Limit).

2.5.2. Weak-field dielectric permittivity measurements in radio frequency range

The complex permittivity was measured as a function of temperature and frequency in the capacitive cell illustrated in Figure 2.1a.

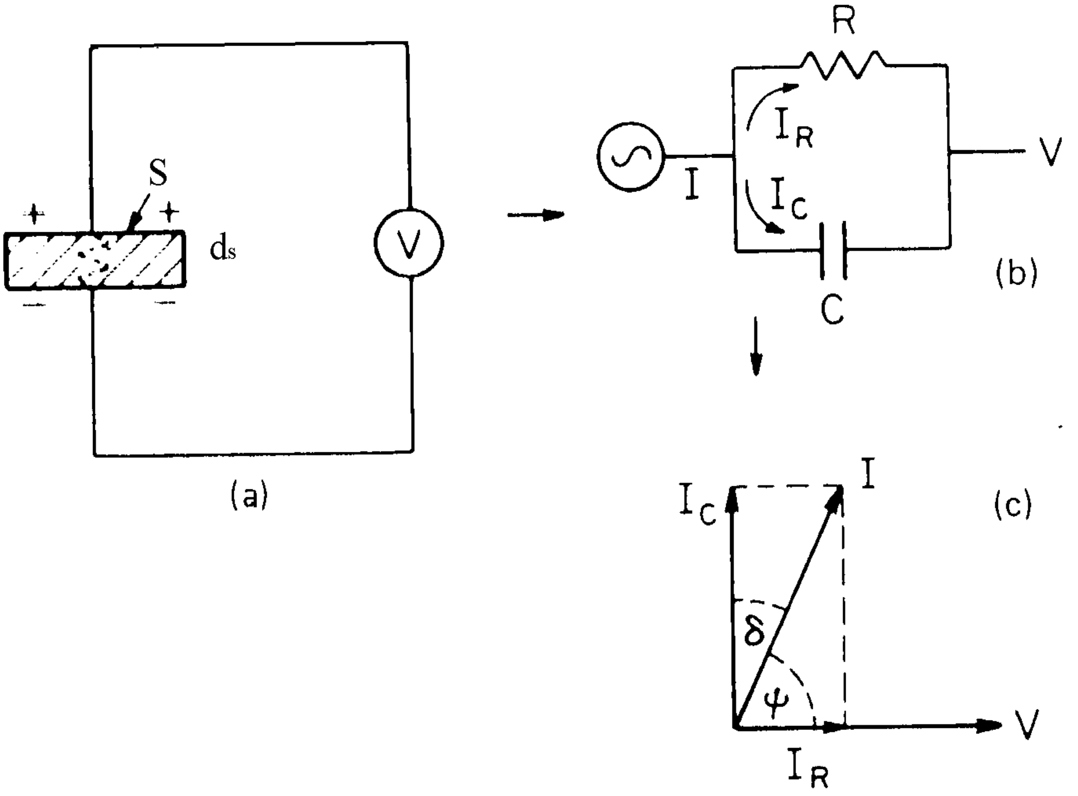

FIGURE 2.1. Equivalent circuit diagrams of capacitive cell (**a**) of charging and loss current (**b**) and of loss tangent for a typical dielectric (**c**) (Buchanan, 1991).

For the case of sinusoidal applied voltage *V*, the current discharge flow *I* of the capacitive cell may be written as:

$$I = i\omega\varepsilon^* V\varepsilon_0 S/d_s = i\omega(\varepsilon'\text{-}i\varepsilon'')V\varepsilon_0 S/d_s = I_C + I_R \qquad (2.5)$$

where i is the imaginary operator, $\omega = 2\pi f$ is the angular frequency, ε_0 is the dielectric constant of the vacuum with the value 8.85×10^{-12} F/m, S is the area of the electrodes for a sample capacitor, d_s is the distance between electrodes or sample thickness, ε^* is the complex permittivity, ε' is the real part of the permittivity, and ε'' is the imaginary part of the permittivity, related to dielectric loss. Therefore, because the dielectric loss exists in dielectric materials, it can be represented by the circuit analogue of a resistance in parallel with a capacitor, and the current I has vector components I_C and I_R, as illustrated in Figure 2.1 (b, c). The current I_C represents a capacitive current proportional to charge stored in the capacitor. It is frequency dependent and lead voltage by 90°. The current I_R is an ac conduction current in phase with the voltage V, which represents the energy loss or power dissipated in the dielectric. From the ratio of the magnitude of I_R to magnitude of I_C, therefore, one can define a dissipation factor $tan\delta = \varepsilon''/\varepsilon'$ (Buchanan, 1991).

In this work, dual impedance parameter Z-ψ were measured by Precision LCR Meter (HP 4284A) under an applied alternative electric field $E_0 = V/d_s$ of about 0.1 V/cm at 21 frequencies in the frequency range of 100 Hz - 1 MHz with further recalculation to

$$\varepsilon' = d_s \sin\psi/\omega Z \varepsilon_0 S \quad \text{and} \quad tan\delta = tan(90°-\psi) \tag{2.6}$$

Measurements in the temperature range of 10-300 K were performed during samples were cooled at a rate of 0.75 K/min in a He closed cycle cryogenic system (Displex ADP-Cryostat HC-2) till the lowest attainable temperature (~10 K), stabilized for 1 hour and further heated at the same rate. The temperature of the sample was controlled by a Scientific Instrument Model 9650 Digital temperature controller with silicon diode thermometers.

2.5.3. Strong-field dielectric measurements in radio frequency range

Permittivity under bias field

For the measurements of dc field dependence of the dielectric permittivity (tunability), sintered samples were polished to a thickness of ~0.45 mm and gold electrodes were sputtered on the both sides. Dielectric constant and loss were measured at constant temperature and a frequency of 10 kHz, as a function of dc electric field in range from 0 to ~20 kV/cm, using a blocking circuit, a Precision LCR Meter (HP 4284A) and a high voltage dc power source (Glassman PS/EH10P10.0-22), as shown in figure 2.2. Resistances R1, R2 protect the source against short circuits (resistance is much smaller than the resistance of the sample but high enough to limit the current). Capacitances C1, C2 are high-voltage capacitances that are at least one order of magnitude greater than the maximum capacitance of sample.

For the dielectric tunability measurements at low temperatures in the range of 10-300 K, samples were cooled/heated in a He closed cycle cryogenic system (Displex ADP-Cryostat HC-2) controlled by a digital temperature controller (Scientific Instrument Model 9650) with silicon diode thermometers till the required temperature and stabilised (30 min at least).

Polarisation versus electric field

The commonly accepted criterion of ferroelectricity is a P-E hysteresis loop. Usually, it is observed with the oscilloscope and Sawyer-Tower circuit, shown in Figure 2.3. The method consists of applying an alternating voltage and relating the stored charge to the instantaneous voltage. A large integrating capacitor is placed in series with the sample. The voltage across it measures the charge stored on the test sample and is conventionally displayed as the vertical deflection (in Figure 2.3 marked V) of an oscilloscope. The applied voltage is displayed as the horizontal deflection (in Figure 2.3 marked H). For convenience, it is usually sampled through a capacitive voltage divider, as shown (Jaffe et al., 1971). The hysteresis arises from the energy needed to reverse the metastable dipoles during each excursion of the field, therefore the experiment is usually run at low frequencies.

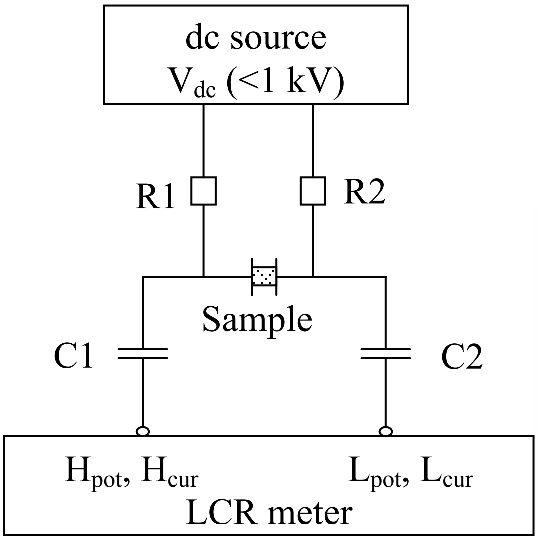

FIGURE 2.2. Blocking circuit configuration (see text).

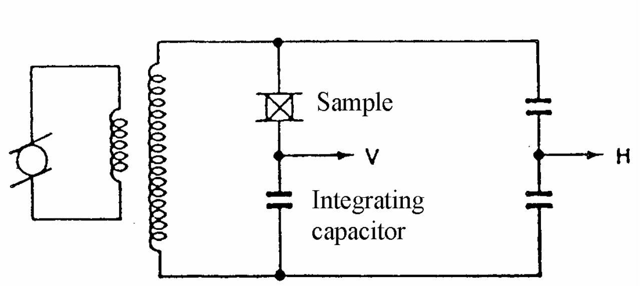

FIGURE 2.3. Sawyer-Tower circuit configuration (Jaffe et al., 1971).

In this work, the hysteresis loops were measured on the samples polished to thickness ~0.45 mm with the standard Sawyer-Tower circuit and a digital oscilloscope (LeCroy LT322) at 50 Hz. For the measurements in the temperature range of 10-300 K, samples were cooled under zero field in a He closed cycle cryogenic system (Displex ADP-Cryostat HC-2) controlled by a digital temperature controller (Scientific Instrument Model 9650) with silicon diode thermometers till the lowest temperature and stabilised. Then the samples were successively heated till the required temperature and stabilized at each temperature for at least 30 min before measuring. The remnant polarisation was, thus, obtained as a function of temperature.

2.5.4. Dielectric characterisation in microwave range

Cylinder-shaped samples with a diameter about 1 mm and height of 5-14 mm were used for the dielectric measurements in the microwave (MW) range. The dimensions of studied samples were chosen to match the impedance of radial transmission line containing the sample with the impedance range, where detection accuracy of the analyzer is the highest, using rf dielectric data for estimation. The measurements were carried out both as a function of frequency (in the range of 1 MHz - 1.8 GHz) and as a function of temperature (in the range of 100-300 K). MW-frequency–temperature dependences of complex dielectric permittivity were obtained using a computer controlled high-frequency dielectric spectrometer equipped with HP 4291B Impedance Analyzer, a NOVOCONTROL BDS 2100 coaxial sample cell, and a SIGMA SYSTEM M18 temperature chamber. Measured impedance spectra were recalculated into those of the complex permittivity taking into account the sample dimensions and the electromagnetic field distribution inside the samples. The measurements were carried out at the Department of Dielectrics, Institute of Physics, Academy of Sciences of the Czech Republic, in the group of Dr. Jan Petzelt.

2.5.5. Terahertz spectroscopy measurements

Time-domain terahertz (TDT) transmission spectroscopy has become a standard method for measurements of complex dielectric constant of dielectrics in the millimeter and submillimeter spectral range. The technique is based on the measurement of the temporal profile of the electric field of a picosecond terahertz (THz) pulse transmitted through an investigated sample. The complex spectrum of this pulse is normalized by a reference spectrum, obtained without the sample. Finally, the complex transmittance and, consequently, the complex dielectric function of the sample in the whole frequency range studied is obtained through numerical solution of a system of two real non-linear equations for the transmittance. (Pashkin, 2004)

In this work, samples for TDT transmission spectroscopy measurements were polished to a thickness 0.117 mm. A custom-made time-domain terahertz transmission spectrometer was used to obtain the complex dielectric response of samples, in the range from 3 to 50 cm^{-1} (90 - 1500 GHz). This spectrometer uses a femtosecond Ti:Sapphire laser and (011)-oriented ZnTe crystal as a THz emitter, generating pulses owing to optical rectification effect. The detection of THz waveforms is performed by an electro-optic sampling technique using another ZnTe crystal. An Optistat CF cryostat with mylar windows was used for measurements down to 10 K. The measurements were carried out at the Department of Dielectrics, Institute of Physics, Academy of Sciences of the Czech Republic, in the group of Dr. Jan Petzelt.

2.5.6. Infrared spectroscopy measurements

Infrared (IR) spectroscopy involves the absorption of infrared light causing vibrational excitation of covalently bonded atoms and groups. The motion of positive ions relative to the negative ones gives rise to an instantaneous dipole moment, which couples with the electromagnetic field of IR radiation and, therefore, forms polar variation modes. In other words, infrared radiation is not only selectively absorbed, but also reflected. Both effects are complementary, allowing to reflection spectroscopy to give information on vibrational modes in IR region (Ibach and Lüth, 1993).

In this work, cylinder-shaped samples with a diameter of 8 mm and thickness of 1 mm were polished for infrared spectroscopy measurements. Room temperature IR reflectivity spectra were obtained using a Fourier transform spectrometer (Bruker IFS 113v) with pyroelectric deuterated triglycine sulfate detectors in the frequency range of 20-3300 cm^{-1} (0.6-100 THz) with the resolution of 0.5 cm^{-1}. Terahertz data were used to normalize IR data and a joint generalised multi-oscillator fit was used to calculate the real and imaginary parts of the dielectric permittivity. The measurements were carried out at the Department of Dielectrics, Institute of Physics, Academy of Sciences of the Czech Republic, in the group of Dr. Jan Petzelt.

2.6. Electron spin resonance measurements

Electron spin resonance provides a powerful tool for studying the unpaired electrons in condensed matter systems. When the molecules of a solid exhibit paramagnetism as a result of unpaired electron spins, transitions can be induced between spin states by applying a magnetic field and then supplying electromagnetic energy, usually in the microwave range of frequencies, i.e.,

$$E_2\text{-}E_1 = \hbar\omega = g\mu_B B \tag{2.7}$$

where E_2-E_1 is the difference between spin states, ω is angular frequency in microwave range, ħ is the reduced Plank constant, B is the magnetic field, $\mu_B = e\hbar/2m_e = 9.27 \times 10^{-24}$ J/T is the Bohr magneton, e and m_e are the elementary charge and mass, respectively, and g factor is a characteristic property of the paramagnetic species. Thus, when an incident microwave has a frequency equal to the difference frequency of two states, resonance absorption of the microwave occurs. The resulting absorption spectra are described as electron spin resonance (ESR) or electron paramagnetic resonance (EPR) (Weil et al., 1993).

In this work, room-temperature ESR spectra were recorded on the ground samples of Mn-doped ST in the *X*-band microwave region. RADIOPAN spectrometer, operating at 9.4 GHz has been used. The measurements were carried out at the Institute for Problem of Material Sciences, Ukrainian Academy of Sciences, in the group of Prof. Maia Glinchuk.

Several ESR measurements were carried out also in the University of Aveiro on a Bruker ESP 300E spectrometer mounted with *X*-band microwave bridge and corresponding cylindrical TE_{011} microwave resonator.

3. Magnesium-doped Strontium Titanate Ceramics: Microstructure, Crystal Structure and Low Temperature Dielectric Properties

3.1. Introduction

In 1990, Kawada and Fujimoto (1990) reported Mg solid solubility limit at Sr site of ST lattice to be below 1%, using TEM technique. However, no second phase was observed in $Sr_{1-x}Mg_xTiO_3$ system for $x \leq 0.20$ by Hirata et al. (1996), using XRD technique, although no dependence of the lattice parameter on Mg content was observed. In addition, the only report on the dielectric properties of $Sr_{1-x}Mg_xTiO_3$ system is for the composition with $x = 0.01$ (Wang el al., 2000a), showing ST-like behaviour with slightly reduced values of the dielectric constant at low temperatures (see Figure 1.43).

For $SrTi_{1-y}Mg_yO_{3-\delta}$, system no dielectric properties were reported at all, although conductivity measurements were carried out (Inoue et al., 1991; Zheng and Sorensen, 1999). Inoue et al. (1991) reported also a linear increase of the lattice parameter, deduced from XRD data for $SrTi_{1-y}Mg_yO_{3-\delta}$ system with Mg^{2+} content up to $y = 0.08$. At further increase of Mg content the lattice parameter kept unchanged, implying that the Mg solid solubility limit in Ti site of ST lattice was reached. Thus, the study of structural, microstructural and dielectric properties of Mg-doped ST is rather incomplete and some contradictory results were reported.

Considering the charge and ionic radius, Mg^{2+} ions can occupy both the A- and B-site of ST perovskite lattice with general formula ABO_3. Taking this into account, strontium titanate ceramics doped with Mg, $Sr_{1-x}Mg_xTiO_3$ (hereafter designated SMT) and $SrTi_{1-y}Mg_yO_{3-\delta}$ (hereafter designated STM), were synthesised in this work with intentional stoichiometric variations.

For SMT system, it was supposed that the Mg^{2+} ions will preferably occupy A-site positions, substituting Sr^{2+} ions. In this case, no charge imbalance is created.

In STM system, it was assumed that Mg^{2+} ions will preferably occupy B-site positions as substituting Ti^{4+} ions. In this case, Mg^{2+} acts as an acceptor dopant and a local charge compensation is needed. The charge compensation mechanism can occur through the formation of either oxygen vacancies ($V^{\bullet\bullet}_O$) in the ST lattice or electronic holes. Due to the well-documented high stability of anionic deficient perovskite lattices (Galasso, 1969) the formation of the [$Mg''_{Ti} - V^{\bullet\bullet}_O$] pair is very possible. Moreover, the origin of the dielectric relaxation in the $SrTiO_3 - Sr(Mg_{1/3}Nb_{2/3})O_3$ system was recently attributed to the formation of the impurity pair [$Mg''_{Ti} - V^{\bullet\bullet}_O$] (Lemanov, 1999).

The stability of the perovskite lattice is related to the high degree of ionic bonding and to the proper value of the tolerance factor *t* that defines the relation between the ionic radii in the perovskite lattice (Galasso, 1969). Using the relation,

$$t = \frac{r_A + r_O}{\sqrt{2}(r_B + r_O)}, \tag{3.1}$$

where r_A and r_B stand for the average ionic radius at A and B-site respectively, and r_O stand for the ionic radius of the oxygen, the effect of Mg doping on the stability of the ST perovskite lattice was analysed. The tolerance factors for SMT and STM compositions were calculated and are presented in Figure 3.1.

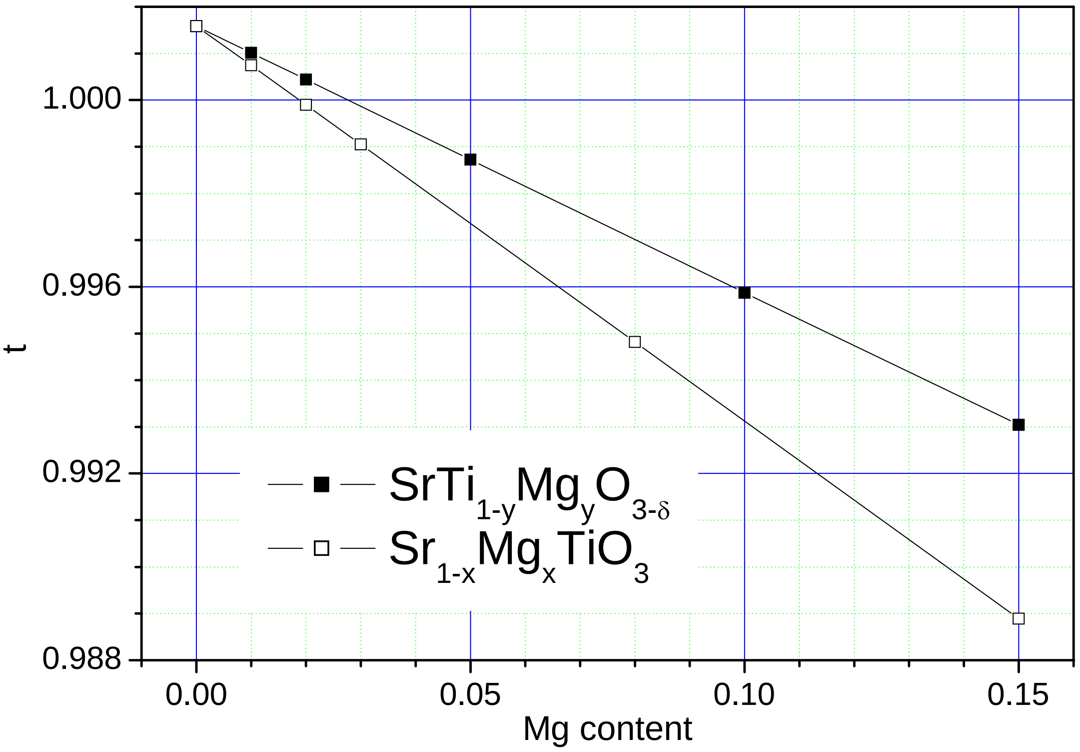

FIGURE 3.1. Tolerance factor *t* versus Mg content, calculated for SMT and STM compositions.

For these calculations, the radius considered for A and B cations with 12- and 6-coordination, respectively, were $r_{Sr}^{2+}(N_c=12) = 1.44$ Å, $r_{Mg}^{2+}(N_c=6) = 0.72$ Å, $r_{Ti}^{4+}(N_c=6) = 0.605$ Å along with the $r_O^{2-}(N_c=6) = 1.40$ Å (Shannon, 1976). For the case of SMT compositions, since there is no available data for the ionic radius of Mg^{2+} with 12-coordination, the value of $r_{Mg}^{2+} = 1.20$ Å was extrapolated considering a linear relation between the ionic radius and the coordination number, resting on data from (Shannon, 1976).

The tolerance factor for ST was calculated to be 1.0016, what is very close to unity, displaying that the A and B ions are closely packed in the ST lattice. As the Mg content increases, either in A- or B-site of the ST lattice, the tolerance factor decreases, indicating that the ions in the A site become less packed. In addition, the tolerance factor decreases faster for SMT system, implying the favourable off-centre positions for Mg at the A-sites. Therefore, the impurity polar dipoles, interacting with the host lattice may be created, markedly affecting the polar behaviour or the system. Thus, a ferroelectric anomaly or a relaxor-type behaviour may be induced.

However, dielectric measurements indicated that Sr-site substitution with 1% of Mg^{2+} caused no ferroelectric-type anomaly (Wang et al., 2000). In spite of that, a relaxation mechanism which could lead to the glass-like behaviour in $Sr_{1-x}Mg_xTiO_3$ system, similar to that observed in $K_{1-x}Li_xTaO_3$, was predicted based on theoretical calculations (Kvyatkovskii, 2002).

According to the above description there are several crystallochemical reasons that could lead to the ferroelectric anomaly in $Sr_{1-x}Mg_xTiO_3$ system. In addition, to the author's best knowledge, no dielectric measurements have been reported on $SrTi_{1-y}Mg_yO_{3-\delta}$ system. Consequently, in order to clarify the influence of Mg doping at both Sr- and Ti-sites of ST on the dielectric behaviour, the temperature dependence of the complex permittivity of the two series of Mg-doped ST, i.e., $Sr_{1-x}Mg_xTiO_3$ (SMT) and $SrTi_{1-y}Mg_yO_{3-\delta}$ (STM), is systematically studied in a wide frequency range (10^2-10^{14} Hz). The dielectric response of the SMT and STM at low or radio frequency (rf), microwave (MW), time-domain terahertz (TDT), infrared (IR) spectroscopy data are presented in this chapter. The effect of electric field on the dielectric permittivity in a dc bias range of 0-20 kV/cm is examined also. The dynamics of the relaxation observed in the dielectric loss is analysed, fitted to Arrhenius law and its origin is discussed.

3.2. Synthesis and characterisation

3.2.1. Solid state reaction

As described in Chapter 2, Mg-doped ST ceramics were prepared by the mixed oxide method. The compositions $Sr_{1-x}Mg_xTiO_3$ (SMT) with $x = 0$, 0.01, 0.02, 0.03, 0.08, 0.15 and $SrTi_{1-y}Mg_yO_{3-\delta}$ (STM) with $y = 0.01$, 0.02, 0.05, 0.10, 0.15, as tabulated in Table 2.1, were prepared.

After reagent grade $SrCO_3$, TiO_2 and $MgCO_3$ were weighed, calcined and subsequently sintered, as described in Chapter 2, $Sr_{1-x}Mg_xTiO_3$ system was assumed to be formed according to the following equations:

$$SrCO_3 + TiO_2 \rightarrow SrTiO_3 + CO_2\uparrow \tag{3.2}$$

$$MgCO_3 + TiO_2 \rightarrow Mg_{Sr} + Ti_{Ti} + 3O_O + CO_2\uparrow \tag{3.3}$$

For $SrTi_{1-y}Mg_yO_{3-\delta}$ system, the solid state reaction Eq. (3.2) holds and Ti is substituted with Mg according to the equation:

$$SrCO_3 + MgCO_3 \rightarrow Sr_{Sr} + Mg''_{Ti} + V^{\bullet\bullet}_O + 2O_O + 2CO_2\uparrow \tag{3.4}$$

Eq. (3.4) indicates that with the introduction of Mg into Ti site, the divalent Mg ions replace quadrivalent Ti ions, forming oxygen vacancies $V^{\bullet\bullet}_O$, as a charge compensation mechanism, in the solid state range.

3.2.2. Sintering

After the second ball milling, a particle size analysis of the selected calcined powders revealed an average values ≤ 1 μm and maximum values < 5 μm. The powders were then pressed into the disks and sintered, as described in Chapter 2.

The effect of the sintering temperature on the density of both Sr-site and Ti-site Mg-doped ST ceramics has been studied in the temperature range 1400-1550 °C. $Sr_{1-x}Mg_xTiO_3$ system was represented by composition with $x = 0.01$, while composition with $y = 0.02$ has been used as an example of $SrTi_{1-y}Mg_yO_{3-\delta}$ system. Dependence of the density of undoped $SrTiO_3$ ceramics on the sintering temperature at a constant time was also investigated.

Figure 3.2 presents the effect of the sintering temperature at a constant time, t_s = 5 hours, on the density of $SrTiO_3$, $Sr_{0.99}Mg_{0.01}TiO_3$ and $SrTi_{0.98}Mg_{0.02}O_{3-\delta}$ ceramics. At $T_s \leq$ 1450 °C, $SrTiO_3$ and $SrTi_{0.98}Mg_{0.02}O_{3-\delta}$ ceramics exhibit similar density, increasing markedly with temperature increase. For T_s > 1450 °C, the density reaches a saturation at about 97±1% of the theoretical density, as the sintering temperature increases. On the contrary, the density of $Sr_{0.99}Mg_{0.01}TiO_3$ keeps almost invariable (> 95% of the theoretical density) in all the experimental temperature range.

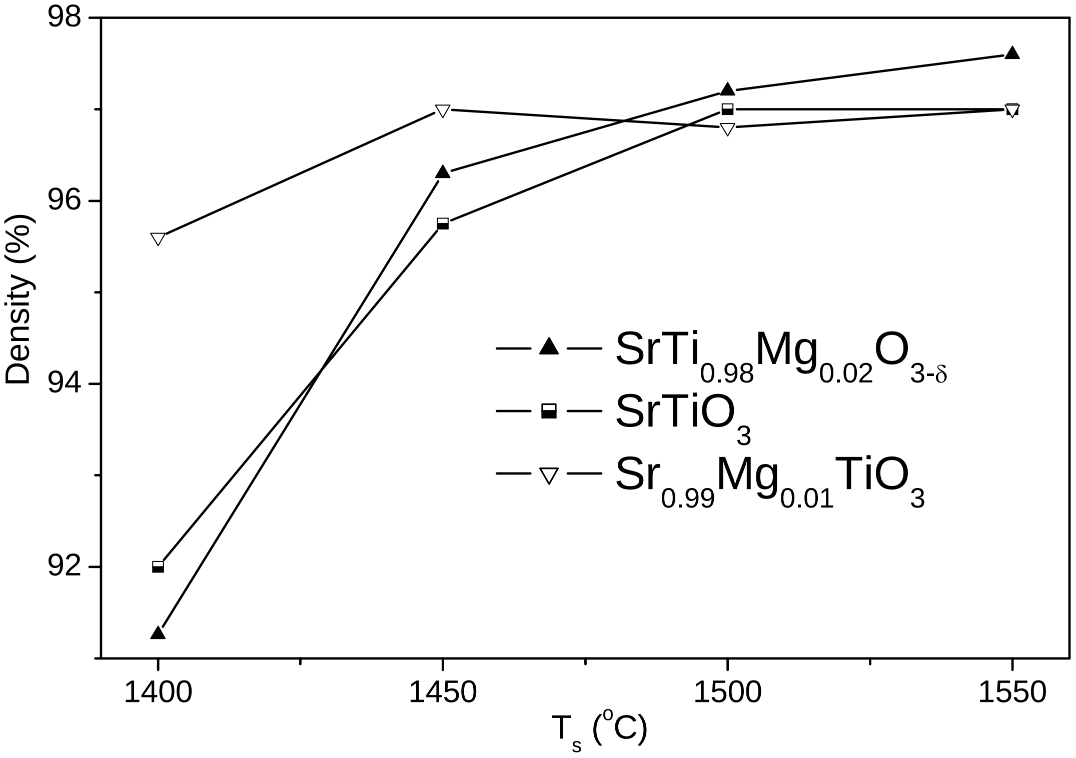

FIGURE 3.2. Relative density as a function of sintering temperature for $SrTiO_3$, $Sr_{0.99}Mg_{0.01}TiO_3$ and $SrTi_{0.98}Mg_{0.02}O_{3-\delta}$ ceramics sintered for 5 hours.

Thus, the sintering temperature for all the compositions of Mg-doped ST ceramics has been chosen to be 1500 °C. Table 3.1 shows the measured density (D), theoretical density (D_t) and relative density (D_r) of $Sr_{1-x}Mg_xTiO_3$ and $SrTi_{1-y}Mg_yO_{3-\delta}$ ceramics sintered at 1500 °C, 5 hours. D was measured by the Archimede's method and D_t was calculated as follows:

$$D_t = [(1 - x)\times M(Sr) + x\times M(Mg) + M(Ti) + 3\times M(O)]/(N_A\times a^3) \qquad \text{for SMT} \qquad (3.5a)$$

$$D_t = [M(\mathrm{Sr}) + (1 - y)\times M(\mathrm{Ti}) + y\times M(\mathrm{Mg}) + (3-y)\times M(\mathrm{O})]/(N_A\times a^3) \quad \text{for STM} \qquad (3.5b)$$

where M(Sr) = 87.62 g/mol, M(Mg) = 24.312 g/mol, M(Ti) = 47.9 g/mol and M(O) = 15.9994 g/mol are molar masses of Sr, Mg, Ti and O respectively, $N_A = 6.022\times10^{-23}$ mol^{-1} is Avogadro number and a is lattice parameter in cm, obtained from XRD spectra (see the following subsection). As seen from the Table 3.1 the relative densities of the samples are greater than 95.6%.

Table 3.1. Measured (D), theoretical (D_t) and relative densities (D_r) of $Sr_{1-x}Mg_xTiO_3$ and $SrTi_{1-y}Mg_yO_{3-\delta}$ ceramics sintered at 1500 °C for 5 hours.

x	D (g/cm^3)	D_t (g/cm^3)	D_r	y	D (g/cm^3)	D_t (g/cm^3)	D_r
0	4.96	5.11	97.0%	0	4.96	5.11	97.0%
0.01	4.93	5.10	96.8%	0.01	4.88	5.10	95.6%
0.02	4.90	5.08	96.6%	0.02	4.95	5.09	97.2%
0.03	4.90	5.06	96.8%	0.05	4.88	5.07	96.4%
0.08	4.76	4.97	95.8%	0.10	4.93	5.06	97.4%
0.15	4.65	-*	-*	0.15	4.87	-*	-*

* multiphases

3.3. Crystal structure and lattice parameter

3.3.1. XRD results

XRD profiles of the sintered samples are shown in Figure 3.3. For all the compositions the observed X-ray lines are consistent with the cubic crystallographic structure of undoped ST, also shown in Figure 3.3 for comparison. For SMT system, additional diffraction lines, corresponding to the $MgTiO_3$ phase are clearly visible for $x = 0.15$ composition. For STM, a distinct MgO second phase was detected for $y = 0.15$ composition.

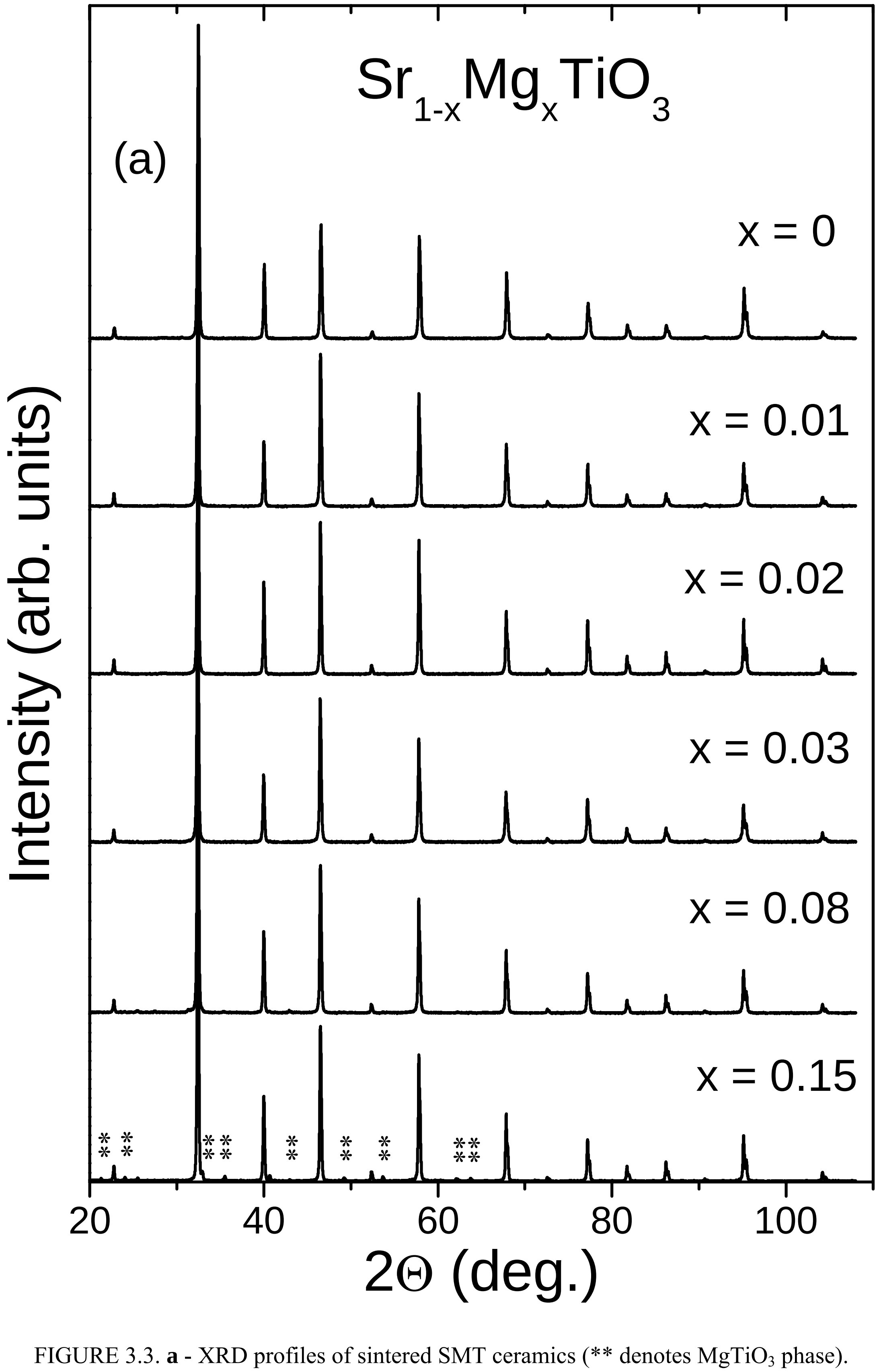

FIGURE 3.3. **a** - XRD profiles of sintered SMT ceramics (** denotes $MgTiO_3$ phase).

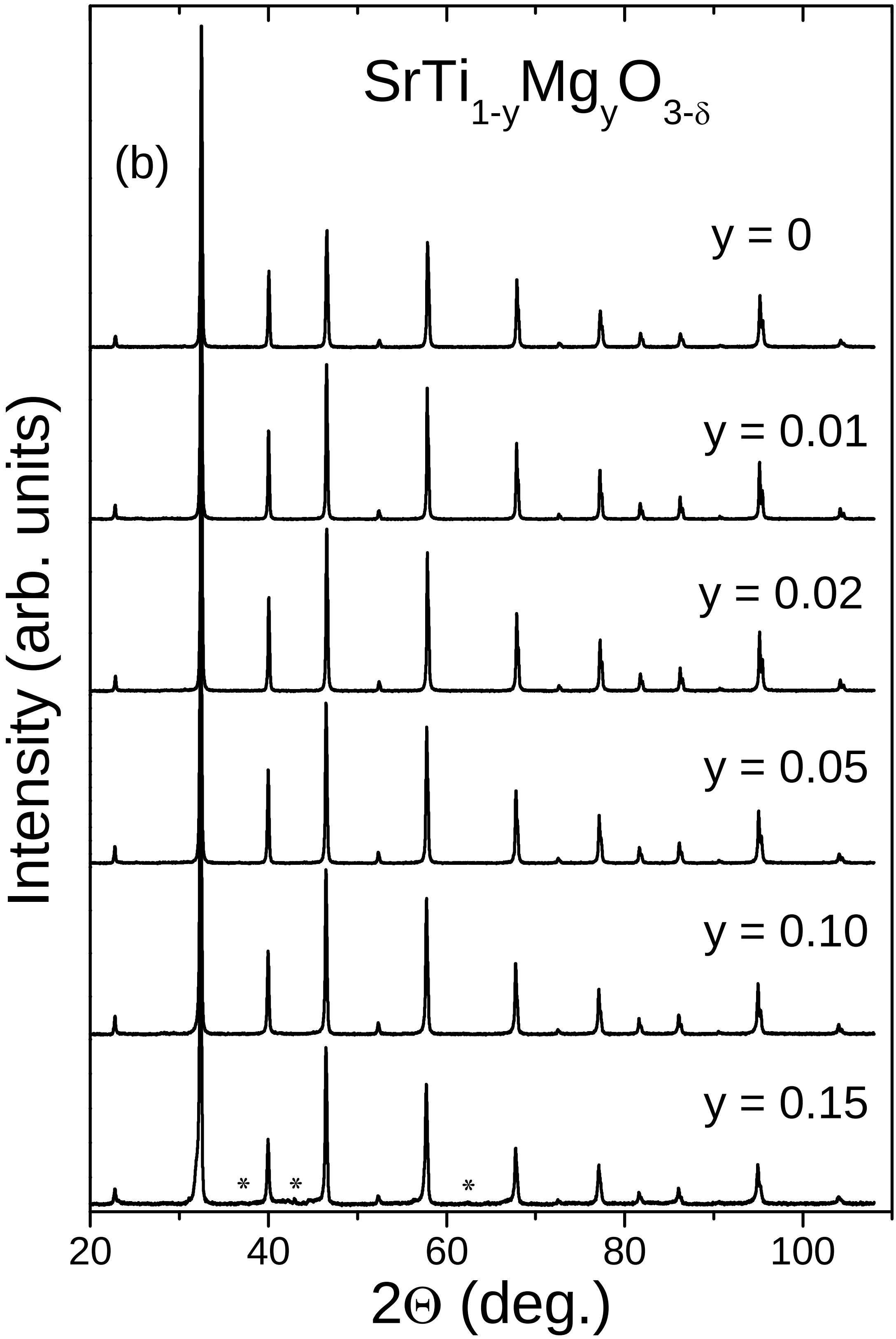

FIGURE 3.3. **b** - XRD profiles of sintered STM ceramics (* denotes MgO phase).

The lattice parameter of undoped ST was found to be 3.90674(8) Å, what is in close agreement with literature data for pure ST (Mitsui and Westphal, 1961). An increase of the lattice parameter *a* with Mg content was found for STM system (see Figure 3.4), compared with almost no variation of the lattice parameter for SMT. Based on size considerations the substitution of Ti^{4+} by bigger Mg^{2+} ions can lead to expansion of the cubic lattice, as observed in this work, confirming the introduction of Mg in the octahedral BO_6 sub-lattice of ST. The lattice parameter dependence on Mg content *y* for STM can be fitted by a linear relationship with a slope $da/dy = 0.05$ Å, as shown in Figure 3.4. Using the same ionic radius considerations, a lattice contraction should occur for the substitution of Sr^{2+} by smaller Mg^{2+} ions in SMT system, similarly to the reported lattice variation for $Sr_{1-x}Ca_xTiO_3$ with increasing *x* (Mitsui and Westphal, 1961).

The lattice parameter variation observed in this work for the SMT system indicates a very weak Mg solubility in the Sr-site of ST grains. An invariance of the lattice parameter with Mg doping content for SMT was also reported by Hirata et al. (1996).

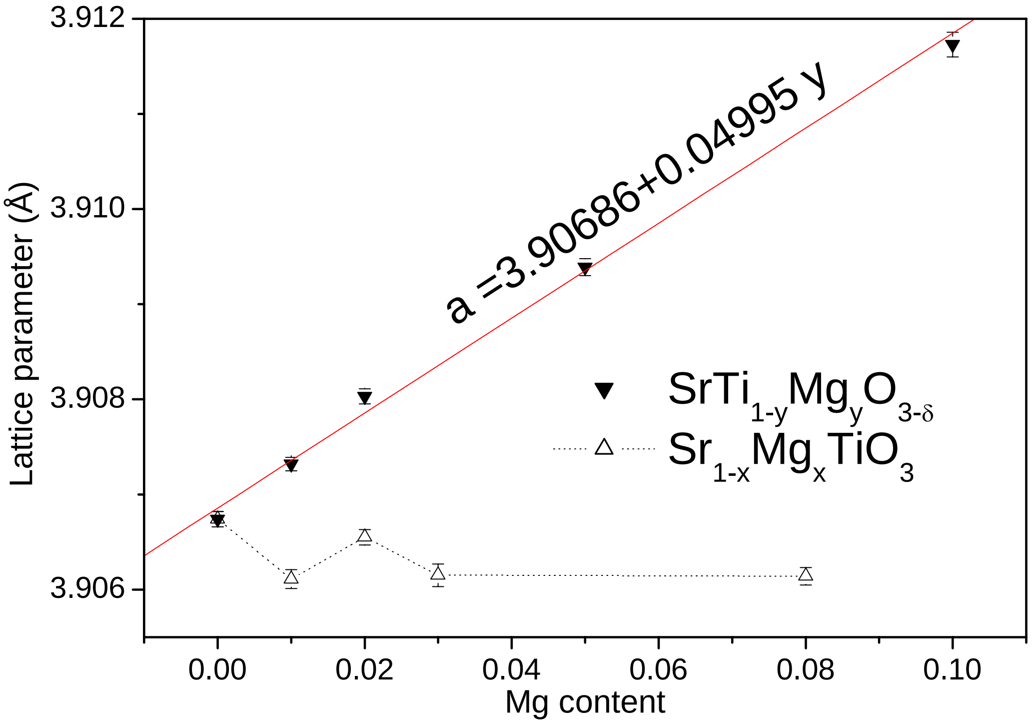

FIGURE 3.4. Lattice parameter of sintered SMT and STM ceramics as a function of Mg content.

3.3.2. Raman spectroscopy results

Micro-Raman spectra of SMT (*x* = 0.01) and STM (*y* = 0.01, 0.05) ceramic samples together with the spectrum of undoped ST for comparison are shown in Figure 3.5 for temperatures of 300, 150 and 80 K.

As well described in the literature the spectra of undoped ST are characterised by dominant second-order features at room temperature, while first order modes TO_2, TO_4 and LO_4 (at 172, 546 and 792 cm^{-1}, respectively) as well as two R-modes (at 144 and 447 cm^{-1}) are clearly seen at 80 K, below the temperature of the structural cubic-to-tetragonal phase transition T_a in ST (Petzelt et al., 2001). However, TO_1 and TO_2 modes (at 81 and 174 cm^{-1}, respectively) appear also above T_a, as were observed in other ST ceramics and were attributed to a local loss of inversion centre due to frozen polarisation (independent on temperature), existing at grain boundaries (Petzelt et al., 2001).

Comparing Figures 3.5a and 3.5b, it is evident that the Raman spectra of SMT look very similar to those of undoped ST ceramics.The spectra of undoped ST, in turn, are in a good agreement with those reported earlier by Petzelt et al. (2001).

As the temperature decreases to 150 K, the additional IR-active TO_4 and LO_4 modes (at 545 and 795 cm^{-1}, respectively) become visible along with TO_1 and TO_2. All the first-order modes strengthen on further cooling. In the spectra measured at 80 K, modes activated from the R point of the Brillouin zone due to Brillouin-zone folding below the antiferrodistortive transition temperature $T_a \approx 105$ K (Petzelt et al., 2001) appear at 144 and 446 cm^{-1}.

Room temperature micro-Raman spectra for STM (see Figure 3.5c and 3.5d), besides the IR-active TO_1, TO_2, TO_4 and LO_4 modes, exhibit additional modes at 118 and 762 cm^{-1}, whose intensities increase not only on cooling but also with increasing Mg content. The latter mode is likely to be a “breathing” mode related to simultaneous shrinkage and expansion of the neighbouring oxygen octahedra with different ions in the centre (Kolev et al., 2002).

No significant differences are seen in the spectra of STM at lower temperatures, except for the intensity decrease of R-point modes for the $SrTi_{0.99}Mg_{0.01}O_{3-\delta}$ composition, which seem to disappear for $SrTi_{0.95}Mg_{0.05}O_{3-\delta}$. This may imply vanishing of the structural phase transition or its shift to lower temperatures.

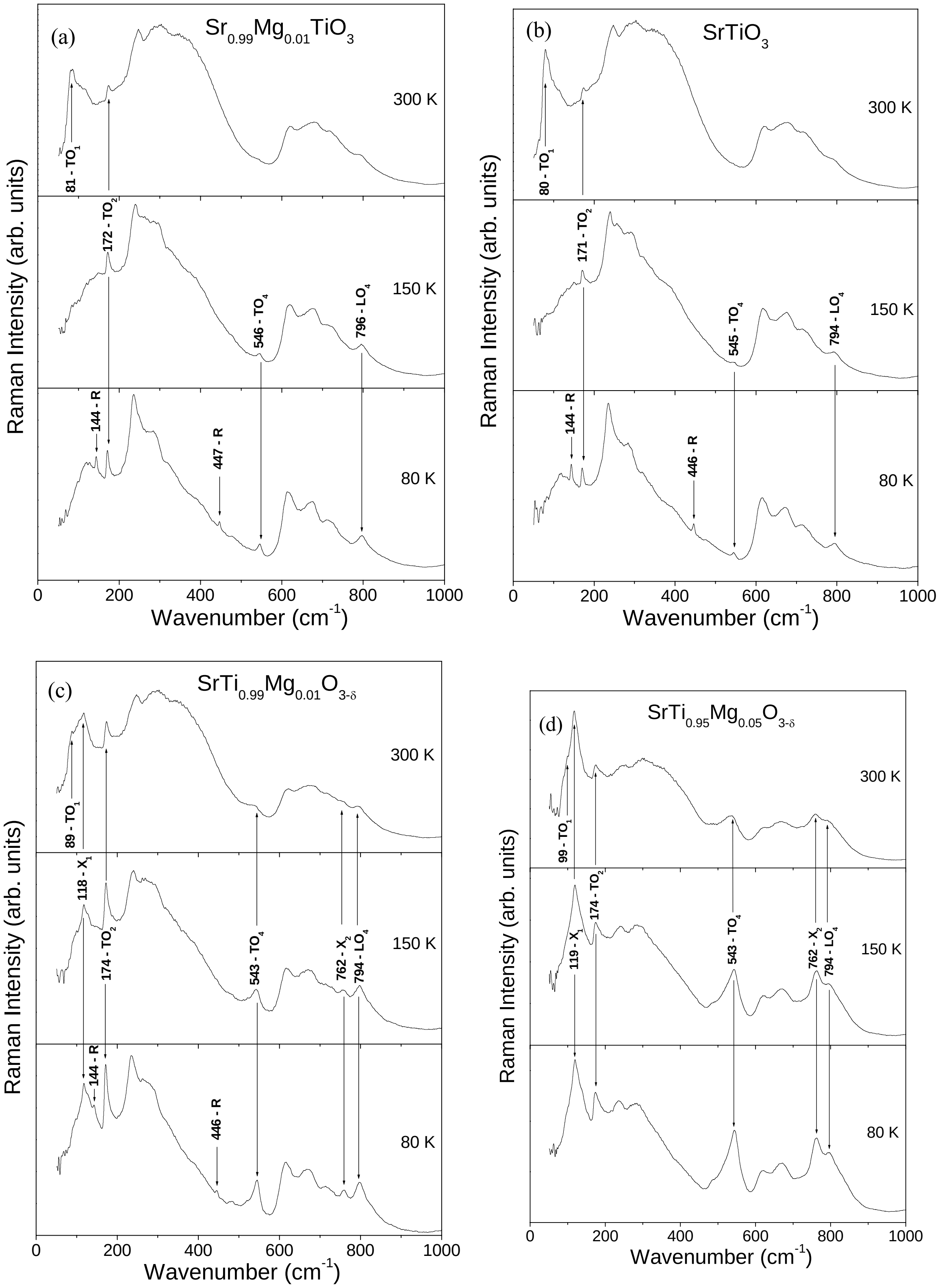

FIGURE 3.5. Raman spectra of $Sr_{0.99}Mg_{0.01}TiO_3$ (**a**), $SrTiO_3$ (**b**), $SrTi_{0.99}Mg_{0.01}O_{3-\delta}$ (**c**) and $SrTi_{0.95}Mg_{0.05}O_{3-\delta}$ (**d**) ceramics at 300, 150 and 80 K with indication of the approximate mode position in cm^{-1}.

Thus, the substitution of Ti^{4+} ion by Mg^{2+} can be also confirmed from the Raman spectroscopy point of view. Moreover, this substitution leads to the local loss of the inversion centre and to the breaking of the ST cubic symmetry, as evidenced by the observation of the first-order features in the room-temperature spectra.

3.4. Microstructure

3.4.1. Microscopic morphology and grain size

The microstructure and local chemical ordering of $Sr_{1-x}Mg_xTiO_3$ and $SrTi_{1-y}Mg_yO_{3-\delta}$ ceramics were analysed by SEM / EDS and TEM / EDS. The SEM micrographs of polished and thermally etched sections of SMT and STM ceramics sintered at 1500 °C are shown in Figure 3.6. All the samples reveal quite dense microstructures, however, bigger grains and some intragranular porosity are distinctively observed for SMT compositions.

The average grain size of A-site Mg-doped ceramics was found, from the SEM micrographs, to be in the range of tens of microns, whereas B-site doping yields ceramics with the grain size in the micron or even submicron range (see Table 3.2). The appearance of the intragranular porosity seems to be related to the marked increase in the grain size of SMT samples, not observed in STM ones.

The difference in the grain growth of SMT and STM ceramics is clearly visible from Figure 3.7, which represents the grain size distribution of $Sr_{0.97}Mg_{0.03}TiO_3$, $SrTi_{0.99}Mg_{0.01}O_{3-\delta}$ and $SrTi_{0.95}Mg_{0.05}O_{3-\delta}$ samples, as well as $SrTiO_3$ for comparison. A narrow grain size distribution of the Gaussian type characterises the STM sample with a maximum at 2-3 μm. On the other hand, a multimodal distribution of grain size for SMT sample is observed, with maxima at ca. 0 - 5, 35 - 40 and 60 - 65 μm, respectively. The multipeak distribution attests to the accelerated grain growth (GG) in SMT.

The sintering behaviour presents also an evidence for the different site occupancy for Mg in ST, since the densification and GG behaviour is markedly different between SMT and STM samples. SEM (Figure 3.6) analysis revealed a grain size of one order of magnitude smaller for STM samples in comparison to SMT compositions.

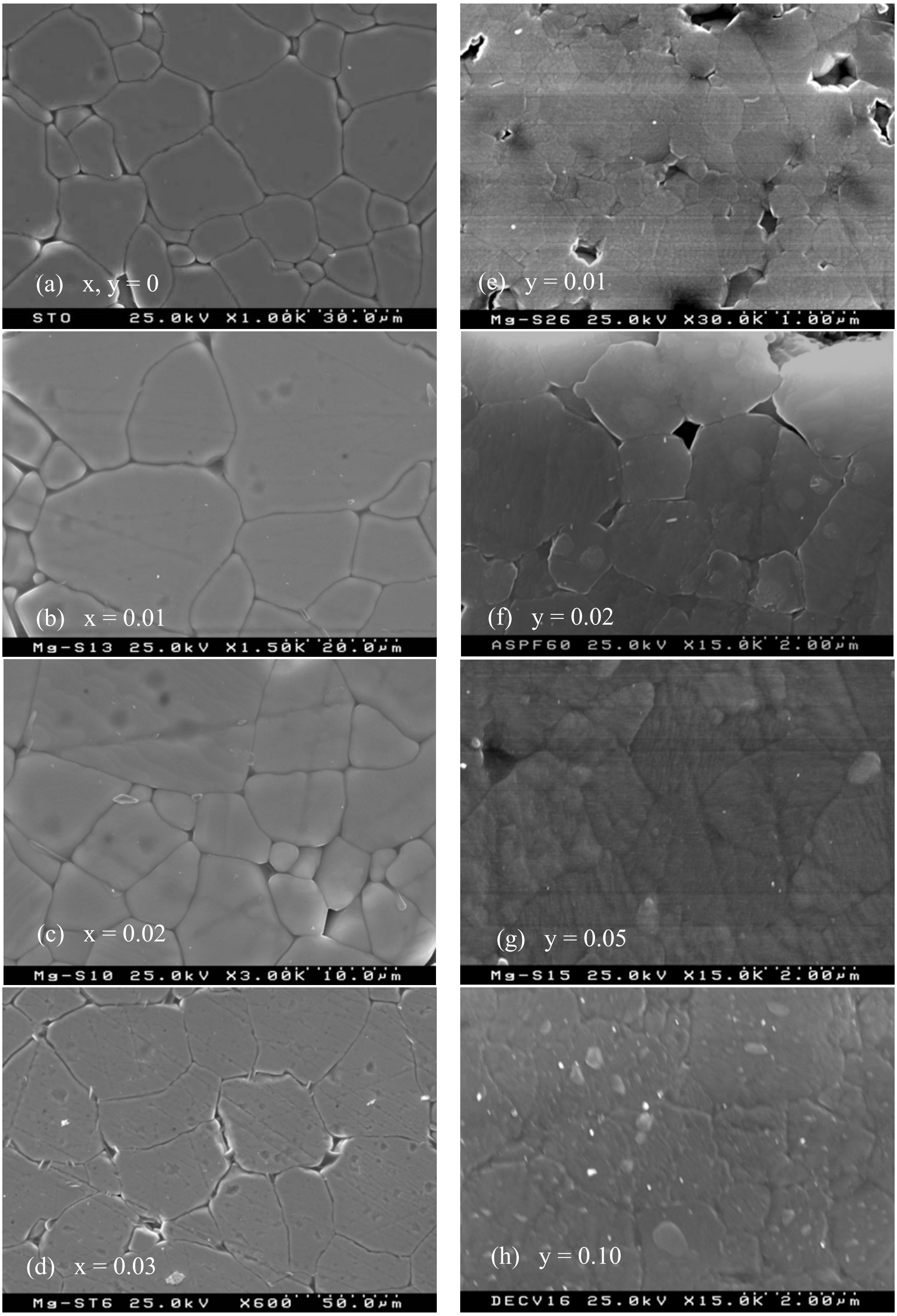

FIGURE 3.6. SEM micrographs of $SrTiO_3$ (**a**), $Sr_{1-x}Mg_xTiO_3$ with $x = 0.01$ (**b**), $x = 0.02$ (**c**), $x = 0.03$ (**d**) and $SrTi_{1-y}Mg_yO_{3-\delta}$ with $y = 0.01$ (**e**), $y = 0.02$ (**f**), $y = 0.05$ (**g**), $y = 0.10$ (**h**) ceramics.

Table 3.2. Average grain size G of $Sr_{1-x}Mg_xTiO_3$ and $SrTi_{1-y}Mg_yO_{3-\delta}$ ceramics sintered at 1500 °C for 5 hours.

x	G (μm)	y	G (μm)
0	30.0	0.01	0.5
0.01	25.4	0.02	1.1
0.02	9.1	0.05	2.2
0.03	31.0	0.10	1.5

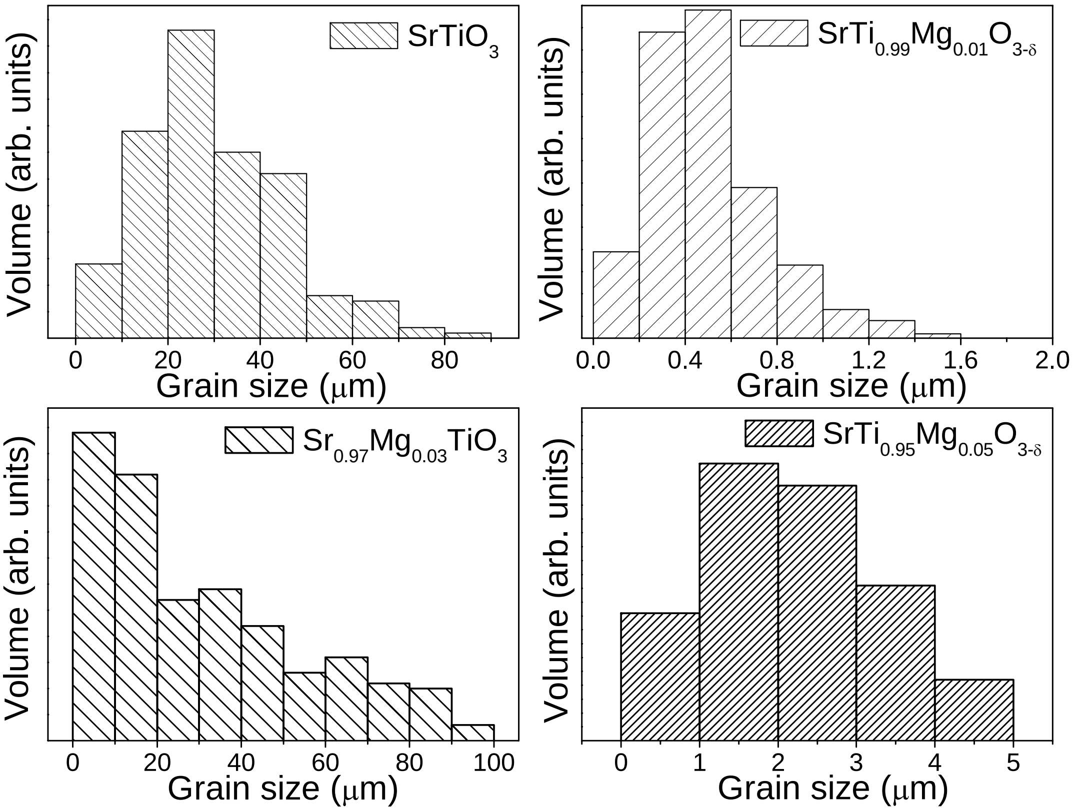

FIGURE 3.7. Grain size distribution of $SrTiO_3$, $Sr_{0.97}Mg_{0.03}TiO_3$, $SrTi_{0.99}Mg_{0.01}O_{3-\delta}$ and $SrTi_{0.95}Mg_{0.05}O_{3-\delta}$ ceramics.

The role of MgO, as dopant retarding the grain growth, is well known for alumina ceramics (Sung et al., 1992). However, the grain growth mechanism in Mg-doped ST seems to depend on the Mg dopant location, on the A/B site ratio, as well as on the oxygen vacancies content. It is well-known that dopants located at the grain boundaries usually act as GG inhibitors, while dopants incorporated into the solid solution (Fernandez et al.,

1992) can produce exaggerated GG. On the other hand, in the ABO_3 type perovskites, A-site rich lattices tend to exhibit normal GG, but enhanced GG has been observed for B-site rich lattices (Yang and Lo, 1997). Exaggerated grain growth was reported for $BaTiO_3$ ceramics with TiO_2 excess (Yoo et al., 1997). Considering that in the case of SMT system the Mg^{2+} ions are not incorporated into the ST lattice, remaining at the grain boundary, a non-stoichiometric Ti-rich ST is formed and the GG mechanism is changed, promoting the growth of the grains. In this system, even though Mg is located at the grain boundaries, the B-site rich lattice seems to be the major contribution for the observed GG.

3.4.2. Distribution of the chemical elements

The X-ray mapping over several grains and grain boundaries has been performed by SEM / EDS for selected compositions.

Figure 3.8 shows the X-ray maps of the elements Sr, Mg and Ti for $Sr_{1-x}Mg_xTiO_3$ composition with $x = 0.01$.

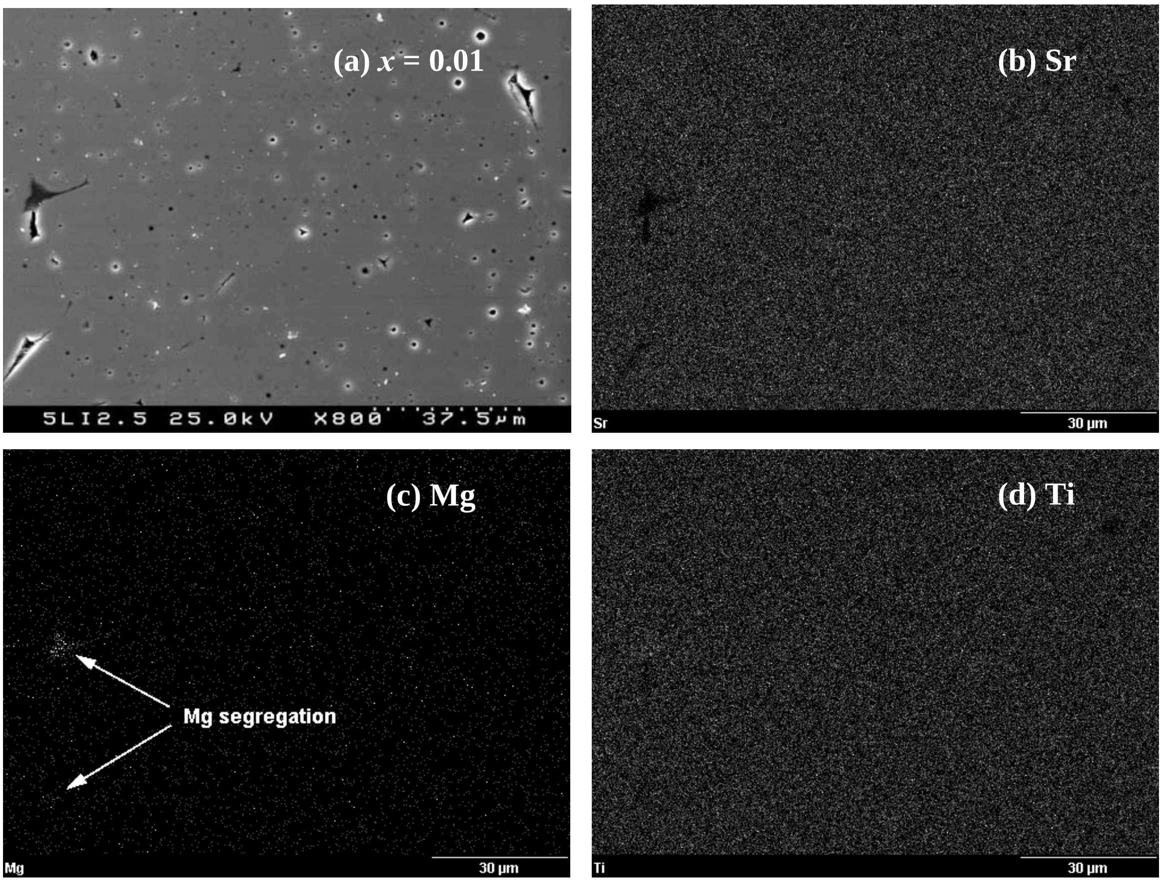

FIGURE 3.8. SEM micrograph (**a**) and corresponding elemental X-ray maps of Sr (**b**), Mg (**c**) and Ti (**d**) for $Sr_{0.99}Mg_{0.01}TiO_3$ ceramics.

It can be seen that the distribution of Ti is uniform. At the same time, Sr is distributed homogeneously just over the grains and escapes the wide grain boundaries, where Mg segregation was detected.

The elemental X-ray maps for the $SrTi_{1-y}Mg_yO_{3-\delta}$ composition with $y = 0.05$ are presented in Figure 3.9. Homogeneous distribution of Sr, Mg and Ti and no segregation of any element, either in grains or in grain boundaries, was detected.

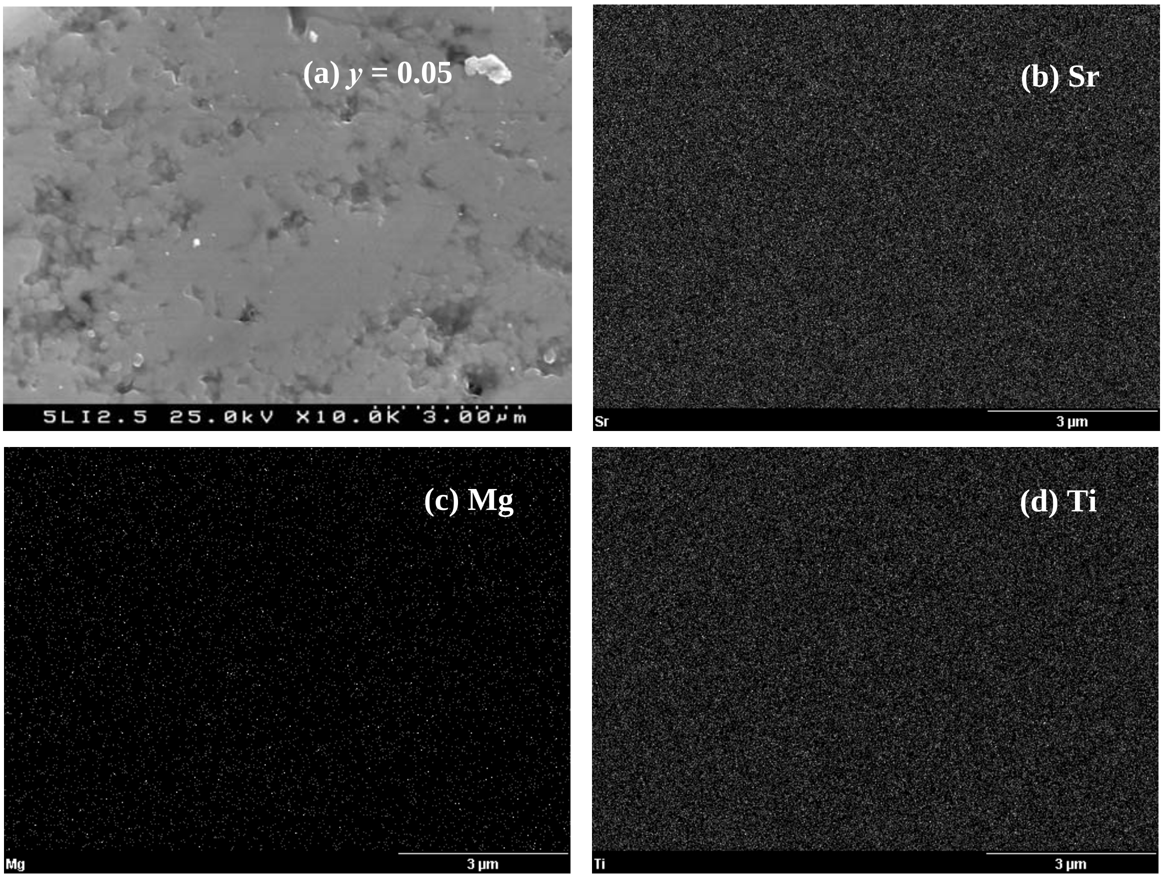

FIGURE 3.9. SEM micrograph (**a**) and corresponding elemental X-ray maps of Sr (**b**), Mg (**c**) and Ti (**d**) for $SrTi_{0.95}Mg_{0.05}O_{3-\delta}$ ceramics.

3.4.3. Local microstructural and chemical analysis

In order to determine the structure of the phase forming at the Mg segregation in the grain boundaries of $Sr_{1-x}Mg_xTiO_3$ ceramics, as well as to confirm the incorporation of Mg into grains of $SrTi_{1-y}Mg_yO_{3-\delta}$ ceramics, the local microstructural and chemical analysis of ceramics was carried out on sintered samples by TEM / EDS.

TEM micrographs of ST (Figure 3.10a), $Sr_{1-x}Mg_xTiO_3$ with $x = 0.01$ and 0.02 (Figures 3.10b - 3.10d) and $SrTi_{1-y}Mn_yO_3$ with $y = 0.05$ and 0.10 (Figure 3.11) samples show dense and homogeneous microstructure, confirming the SEM results. The perovskite crystalline structure of the grains was verified by electron diffraction (ED), as shown in the bottom insets of Figures 3.10 and 3.11.

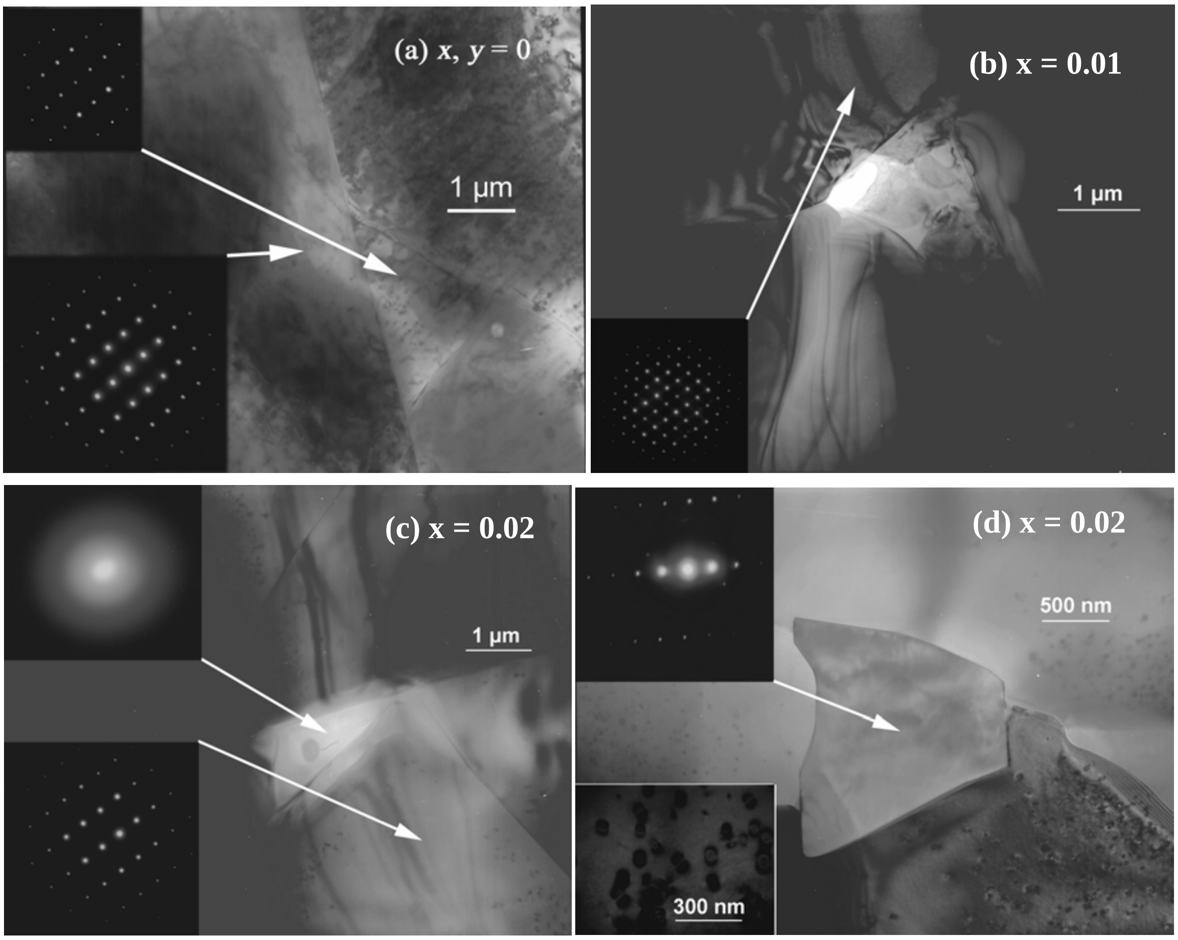

FIGURE 3.10. TEM micrographs of: $SrTiO_3$ ceramics **(a)** with insets of ED patterns for small (in top corner) and for big (in bottom corner) crystalline perovskite grains; $Sr_{0.99}Mg_{0.01}TiO_3$ ceramics (**b**) with inset of ED pattern for crystalline perovskite grains; $Sr_{0.98}Mg_{0.02}TiO_3$ ceramics (**c**) with insets of ED patterns for crystalline perovskite grains (in bottom corner) and for amorphous grain junctions (in top corner); $Sr_{0.98}Mg_{0.02}TiO_3$ ceramics (**d**) with insets of ED pattern for crystalline non-perovskite grain and enlarged dislocation loops (in bottom corner).

Figures 3.10a display clear grain boundaries without any second phase for $SrTiO_3$ samples. Both big and small grains were observed for ST, although their electron diffraction patterns were similar (see insets of Figure 3.10a). As shown in Figures 3.10b - 3.10d, SMT reveals a more complicated structure, including mostly big perovskite grains as well as a small amount of grain boundary phases. The nature of the phase formed at grain boundaries of $Sr_{0.99}Mg_{0.01}TiO_3$ was difficult to determine due to small size of phase component and proximity of the grains components and hence superimposing of features of one on another. On the other hand, $Sr_{0.98}Mg_{0.02}TiO_3$ clearly reveals a small amount of an amorphous grain boundary phase (see Figure 3.10c and top inset) and some small crystalline non-perovskite grains (see Figure 3.10d and top inset) located at the grain boundaries. At the same time, some dislocation loops were found at grains of $Sr_{0.98}Mg_{0.02}TiO_3$, as shown in bottom inset of Figure 3.10d. Such loops can be attributed to the strains induced in the lattice by introduction of the part of Mg ions with non-homogeneous distribution (Aseev and Fedina; L. Laanab et al.; I. Lhermitte-Sebire et al.; Fourlaris and Baker; Guilemany et al., 1992).

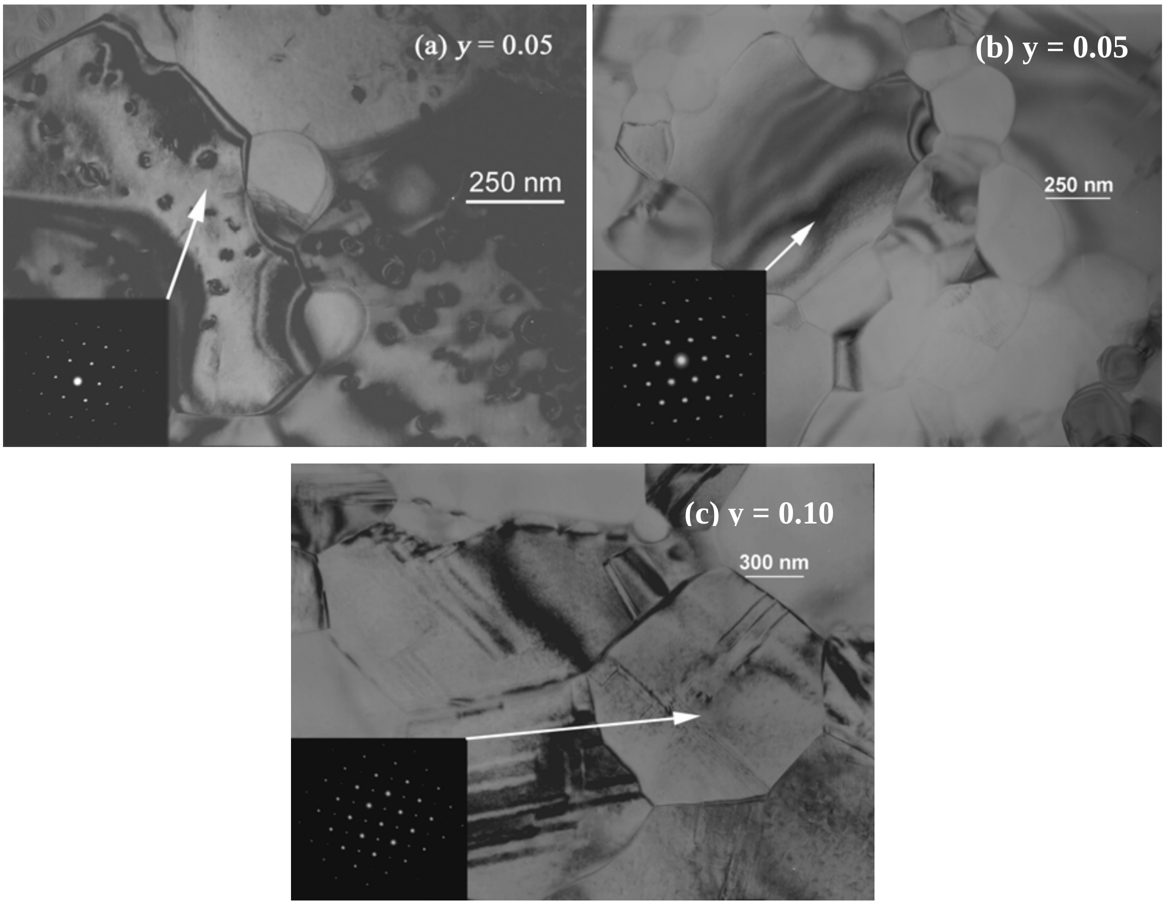

FIGURE 3.11. TEM micrographs of as-prepared $SrTi_{0.95}Mg_{0.05}O_{3-\delta}$ (**a**), of $SrTi_{0.95}Mg_{0.05}O_{3-\delta}$ annealed in oxygen (**b**) and of $SrTi_{0.90}Mg_{0.10}O_{3-\delta}$ ceramics (**c**) with insets of ED pattern for crystalline perovskite grains (in bottom corners).

STM samples display rather small grains and clear grain boundaries without any second amorphous or crystalline phase, as shown in Figures 3.11a - 3.11c. Just dislocation loops, attributed to the strains induced in ST lattice by introduction of Mg ions and their local "precipitation" (Aseev and Fedina; L. Laanab et al.; I. Lhermitte-Sebire et al.; Fourlaris and Baker; Guilemany et al., 1992) were found at grains of $SrTi_{0.95}Mg_{0.05}O_{3-\delta}$ ceramics. This assumption is confirmed by the disappearance of the loops after a long time annealing (see Figure 3.11b).

Spectra obtained by TEM-EDS for representative SMT and STM samples are depicted in Figure 3.12. The spectra of STM grains, exemplified in Figure 3.12a by $SrTi_{0.90}Mg_{0.10}O_{3-\delta}$, are characterised by Sr, Ti, O and, small but clear, Mg peak, confirming the Mg incorporation into the ST grains in STM. Similar spectra were observed on several grains and are representative for all the STM compositions.

On the other hand, the chemical composition of SMT perovskite grains, exemplified by $Sr_{0.98}Mg_{0.02}TiO_3$, is similar to that of ST grains: Sr, Ti and O were the detected elements (Figure 3.12b). Similar spectra were observed on several grains and are representative for all the SMT compositions. For the SMT sample with $x = 0.02$, the spectra obtained by EDS for the glassy phase located at the grain boundary clearly exhibit Mg peaks, along with Zr and Sr ones (Figure 3.12c) and the spectra of non-perovskite grains depicts Mg peaks along with the Ti one of the same magnitude (Figure 3.12d), pointing to the formation of $MgTiO_3$. Thus, the Mg ions were not incorporated into the A-site of the ST lattice remaining located at the grain boundaries.

Thus, it was observed that the solid solubility limit of Mg in the ST lattice depends on the site of the perovskite lattice, in which the substitution occurs. Although the XRD analysis did only detect the second phase for the $x = 0.15$ composition, the solid solubility limit of Mg in A-site was found by TEM / EDS analysis to be < 0.02. No detectable amount of Mg has been found by TEM / EDS in the grains of SMT samples, contrary to the observations for STM, in which Mg was clearly observed in the grain (Figures 3.10-3.12). According to the TEM / EDS information Mg does not enter into the A-sites of ST grains in SMT compositions, remaining located at the grain boundaries and forming either a glassy phase together with Sr and Zr (resulting from contamination from the milling media) or crystalline magnesium titanate. On the other hand, Mg does easily enter into the B-sites of ST. In spite of the charge difference between Ti^{4+} and Mg^{2+} ions, supposedly compensated by oxygen vacancies, the proximity of the ionic radius between these two ions and the high stability of anionic deficient perovskite lattice determine the stability of the STM lattice. Strongly limited solubility of Mg in the A-site of ST lattice is attributed to a substantial difference between the ionic radius size of Sr^{2+} and Mg^{2+} that leads to a less stable perovskite lattice. The present data support the solid solubility limit below 1 % of Mg for SMT reported by Kawada and Fujimoto (1990), but not the 20 % value reported by Hirata et al. (1996).

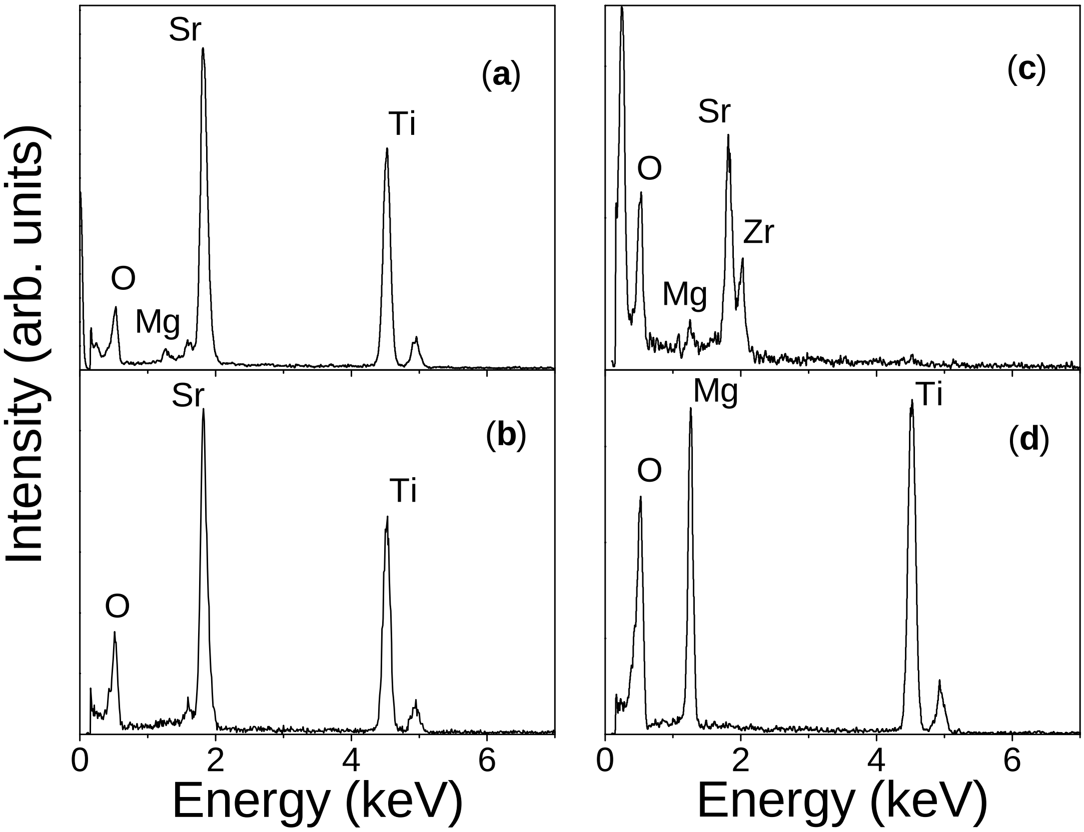

FIGURE 3.12. Spectra obtained by TEM-EDS on grains of $SrTi_{0.90}Mg_{0.10}O_{3-\delta}$ ceramics (**a**), as well as on grains (**b**), grain-boundary glass phase (**c**), grain boundary-crystalline phase (**d**) of $Sr_{0.98}Mg_{0.02}TiO_3$ ceramics.

3.5. Low temperature dielectric properties

3.5.1. Dielectric properties in low frequency range (100 Hz - 1 MHz)

Temperature dependence of the real part of the dielectric permittivity ε' for $SrTiO_3$, $Sr_{1-x}Mg_xTiO_3$ ($x = 0.01$-0.03) and $SrTi_{1-y}Mg_yO_{3-\delta}$ ($y = 0.01$-0.10) in the frequency range of 10^2-10^6 Hz is shown in Figure 3.13a. The steep increase of the ε' and levelling-off at high values, as the temperature approaches 0 K with no dielectric anomaly was observed for undoped ST, as expected for a typical quantum paraelectric (Müller and Burkhard, 1979).

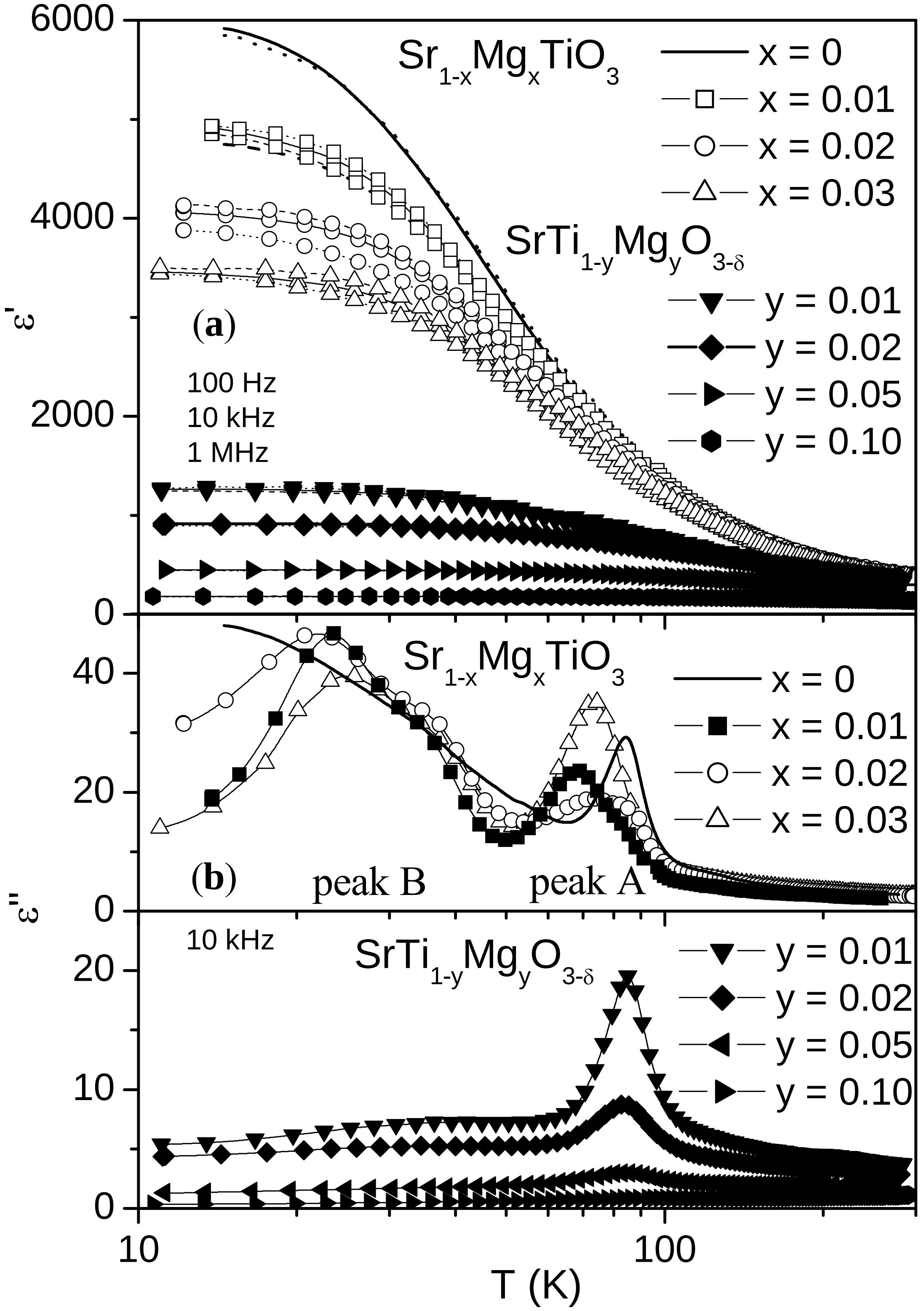

FIGURE 3.13. Temperature dependence of real part of dielectric permittivity *ε*' at 0.1, 10 and 1000 kHz (dot, solid and dash lines respectively) (**a**) and of imaginary part of dielectric permittivity *ε*'' at 10 kHz (**b**) of $SrTiO_3$, $Sr_{1-x}Mg_xTiO_3$ ($x = 0.01$-0.03) and $SrTi_{1-y}Mg_yO_{3-\delta}$ ($y = 0.01$-0.10) ceramics.

Behaviour of the same type is seen for SMT and STM. However, Mg doping lowers the dielectric constant values at low temperatures, slightly in the case of Sr site doping and dramatically in the case of Ti site doping. All the compositions reveal monotonous curves, differing only in maximum and minimum ε' values. Small frequency dispersion was detected.

The temperature dependence of the dielectric loss (imaginary part of the dielectric permittivity ε'' and dissipation factor $tan\delta$) at 10 kHz for $SrTiO_3$, $Sr_{1-x}Mg_xTiO_3$ (x = 0.01-0.03) and $SrTi_{1-y}Mg_yO_{3-\delta}$ (y = 0.01-0.10) is presented in Figures 5.1b and 5.2.

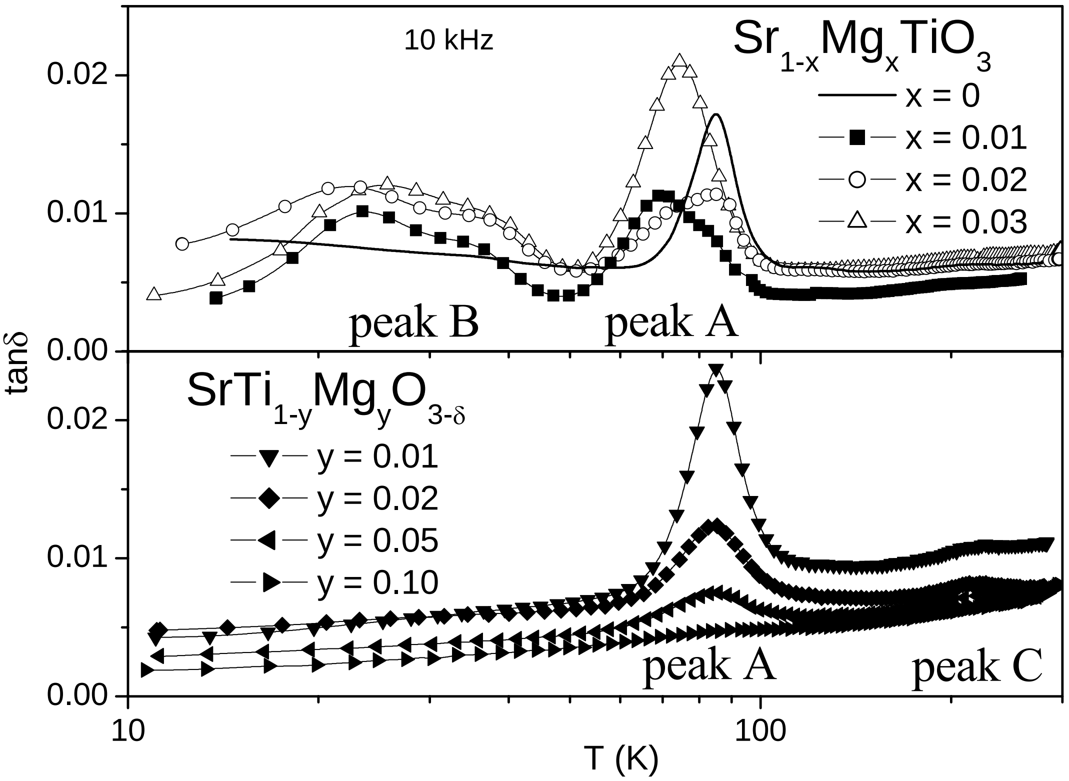

FIGURE 3.14. Temperature dependence of dissipation factor $tan\delta$ of $SrTiO_3$, $Sr_{1-x}Mg_xTiO_3$ (x = 0.01-0.03) and $SrTi_{1-y}Mg_yO_{3-\delta}$ (y = 0.01-0.10) ceramics at 10 kHz.

The dielectric loss of pure ST is characterised by a peak (peak A) at 85 K, that was attributed to the dynamics of the elastic domain walls that occur at the cubic-to-tetragonal phase transition around 105 K (Mizaras and Loidl, 1997).

For the Sr-site Mg-doped ST, the loss peak A becomes broadened towards lower temperature, ~70 K, probably due to interaction of impurities or defects with the soft mode (And e al., 2000a). At the same time, an additional broad peak (peak B) with a maximum around 23.5 K at 10 kHz appears.

In the case of Ti-site Mg doping, the background value decreases monotonically as well as the intensity of the loss peak A. The peak becomes undetectable for Mg content high as $y = 0.10$. However, a smooth peak (peak C) in the range of 200-230 K for $y = 0.01$-0.10 at 10 kHz can be detected in $tan\delta$ vs T curve, as shown in Figure 5.2.

Thus, according to the results obtained in this work (Figure 3.13a), Mg doping itself does not induce ferroelectricity or a relaxor-like behaviour in strontium titanate, either introduced in the Sr- or Ti-site of the ST lattice, in spite of theoretical prediction (Kvyatkovskii, 2002). All the compositions, SMT and STM, exhibit a gradual increase of the dielectric constant on cooling and low-temperature levelling-off similarly to ST (Figure 3.13). No dielectric anomaly was found. The absence of any dielectric anomaly and decreasing the dielectric constant were also reported in the literature by Wang et al. (2000) for $Sr_{0.99}Mg_{0.01}TiO_3$, in agreement with the results reported here. Both SMT and STM systems exhibit a decrease of the maximum ε' value, but, it is much more pronounced in the case of STM than in SMT. Lower polarisability of the Mg ions might accounts for this decrease together with the suppression of the ferroelectric instability.

Regarding the dielectric loss, the loss peak A is characteristic of undoped $SrTiO_3$. Several reports related it to an elastic multi-domain state of ST below the antiferrodistortive phase transition (Viana et al., 1994; Mizaras and Loidl, 1997). No peak in this temperature range was observed for crystals in single-domain state, obtained by cooling under field (Dec et al., 1999). Ti-site Mg doping of ST decreases both the loss in general and the magnitude of the loss peak A. Finally, the peak A vanishes for Mg content $y = 0.10$. This is in a good agreement with the low-temperature Raman data, shown in section 3.2.2, that implied a vanishing of the structural phase transition in STM system with increasing Mg content.

Additional dielectric loss peaks were revealed for SMT and STM. For the case of Ti-site doping, an additional peak C located in the high temperature range can be related to the formation of oxygen vacancies, when Mg^{2+} substitute Ti^{4+} ions. Similar peaks were observed for $Sr_{1-1.5x}Bi_xTiO_3$ ceramics for $x \leq 0.08$ (Yu et al., 1997) and attributed to the relaxation of Ti^{3+}-$V_O^{\bullet}$ dipoles. Thermally activated oxygen vacancies jumping around the impurity ions in perovskites are suggested as the origin of such peaks with dynamics described by Arrhenius law (Lemanov et al., 2002 and references therein). For the case of Sr site doping, an additional broaden peak referred to as peak B can be ascribed to the polaronic relaxation, which is typical for doped perovskites (Bidault et al., 1995; Ang et al., 1999). The electronic origin of peak B was justified by the small activation energy *U* ~0.01 eV, which is typical for the hopping of the polarons between lattice sites (Ang et al., 1999; Lemanov et al., 2002). The obtained results highlight the different interactions of Mg with the ST lattice depending on the lattice site occupancy.

3.5.2. Fitting to Curie-Weiss law and Barrett relation

The temperature dependence of the dielectric constant of $Sr_{1-x}Mg_xTiO_3$ and $SrTi_{1-y}Mg_yO_{3-\delta}$ ceramic samples was characterised by the Curie-Weiss law and Barrett relation. The Curie-Weiss law:

$$1/\varepsilon' = (T-T_0)/C \tag{3.6}$$

where T_0 is the Curie-Weiss temperature and C is the Curie constant, is a typical feature of classical ferroelectrics at temperatures above the ferroelectric phase transition temperature T_C. In order to check its validity for the behaviour of the $Sr_{1-x}Mg_xTiO_3$ and $SrTi_{1-y}Mg_yO_{3-\delta}$ systems, the inverse dielectric constant, measured on heating at 10 kHz, was calculated and plotted versus temperature, as shown in Figure 3.15.

As seen from Figure 3.15, the experimental data rigorously follows the Curie-Weiss law in the temperature range of $100 < T < 200$ K. Below this temperature range, the quantum fluctuations starts to influence the dielectric response. Curie-Weiss temperature and Curie constant, obtained from the straight line parameters, are shown in Table 3.3. The most of the fitting parameters in this thesis were obtained with the maximum error below 3%.

As one can see, T_0, obtained for undoped ST is in close agreement with the value of 35.5 K reported for $SrTiO_3$ single crystals (Müller and Burkhard, 1979) and is almost the same for $Sr_{1-x}Mg_xTiO_3$ samples. The ferroelectric phase transition is supposed to appear at this temperature in the absence of quantum fluctuations. On the contrary, a strong decrease of the Curie-Weiss temperature is observed for $SrTi_{1-y}Mg_yO_{3-\delta}$ ceramics.

In order to characterise both SMT and STM system in a wider temperature range, the fitting of the original experimental data to the Barrett relation was used. It is well known that the paraelectric state of pure $SrTiO_3$ can be described by Barrett relation (Barrett, 1952), which is based on the mean-field theory taking quantum fluctuations into account:

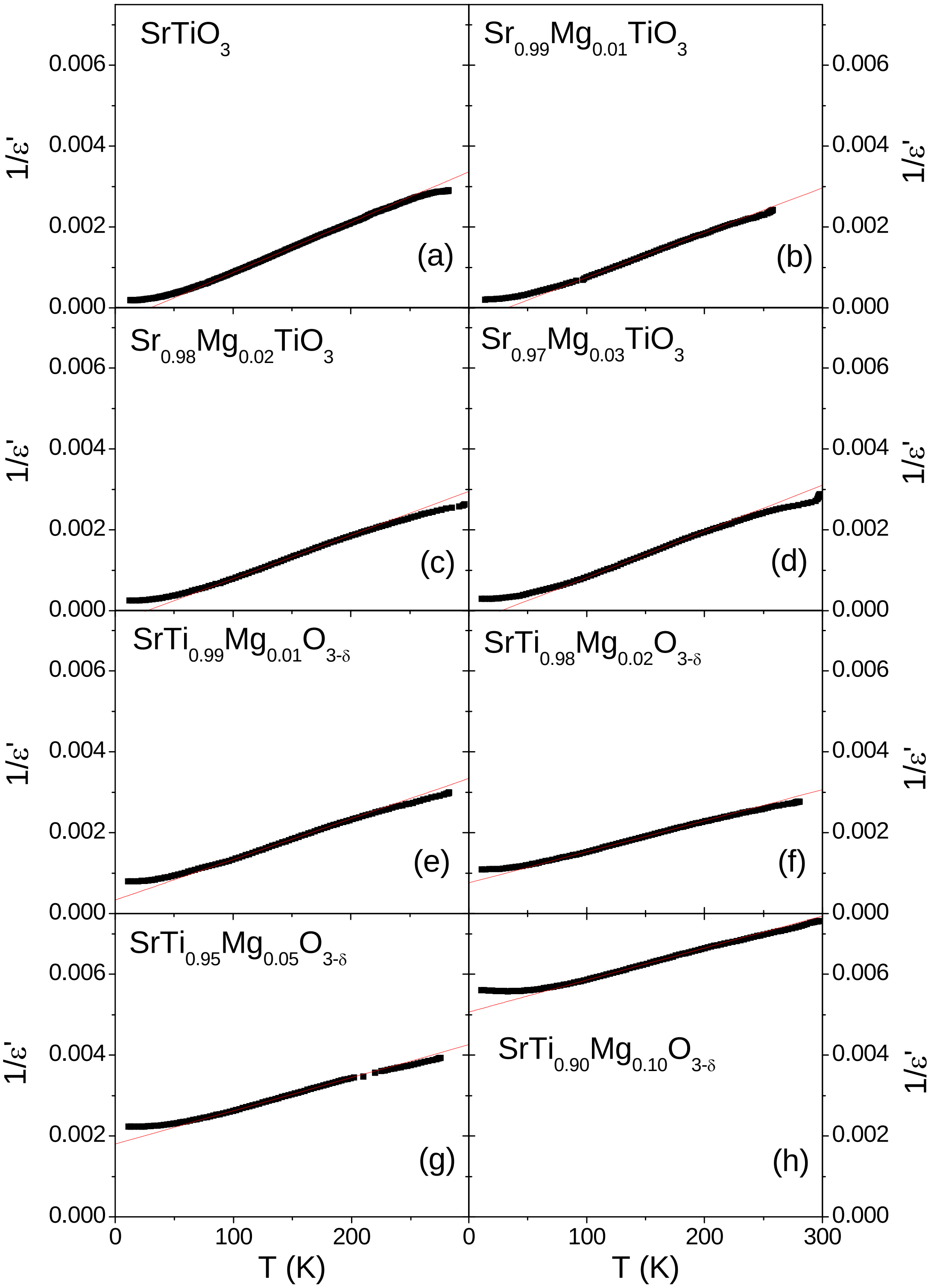

FIGURE 3.15. Temperature dependence of inverse dielectric constant 1/ε' at 10 kHz (solid squares) and fits to the Curie-Weiss law (solid lines) of $SrTiO_3$ (**a**), $Sr_{1-x}Mg_xTiO_3$ with $x = 0.01$ (**b**), 0.02 (**c**), 0.03 (**d**) and $SrTi_{1-y}Mg_yO_{3-\delta}$ with $y = 0.01$ (**e**), 0.02 (**f**), 0.05 (**g**), 0.10 (**h**) ceramics.

$$\varepsilon' = C/[(T_1/2)\coth(T_1/2T)-T_0], \tag{3.7}$$

where C is the Curie-Weiss constant, T_1 is the temperature of the crossover between classical and quantum behaviour, and T_0 is the transition temperature at which the lattice instability would occur in the absence of quantum fluctuations.

Table 3.3. Curie-Weiss law and Barrett relation parameters of SMT and STM ceramics.

	CURIE-WEISS LAW		BARRETT RELATION			
Composition	C, 10^3 K	T_0, K	C, 10^3 K	T_1, K	T_0, K	T_1-$2T_0$, K
$Sr_{0.97}Mg_{0.03}TiO_3$	87	28	90	128	37	54
$Sr_{0.98}Mg_{0.02}TiO_3$	93	27	93	122	38	46
$Sr_{0.99}Mg_{0.01}TiO_3$	90	32.5	94	116	39	38
$SrTiO_3$	80	30	102	105	35	35
$SrTi_{0.99}Mg_{0.01}O_{3-\delta}$	100	-33	104	99	-32	163
$SrTi_{0.98}Mg_{0.02}O_{3-\delta}$	130	-96	136	94	-100	294
$SrTi_{0.95}Mg_{0.05}O_{3-\delta}$	122	-220	123	124	-211	546
$SrTi_{0.90}Mg_{0.10}O_{3-\delta}$	127	-641	126	160	-618	1396

The fitted parameters of the experimental data to the Barrett relation for all the compositions are indicated in Table 3.3. The series of parameters C and T_1 agree well with those reported for a pure $SrTiO_3$ single crystal (Müller and Burkhard, 1979). Sr-site Mg doping does not tend to change the transition temperature T_0 (Table 3.3). However, T_0 is strongly reduced for the B-site doped samples as shown in Table 3.3.

Thus, by fitting the dielectric behaviour to the Barrett law it was shown that Ti-site Mg doping drives the system away from the ferroelectric instability. The positive value of (T_1-$2T_0$) is a signature of the quantum paraelectric behaviour; the higher the value of (T_1-$2T_0$), the more stable is the paraelectric state (Müller and Burkhard, 1979; Barrett, 1952). In this work, the values of (T_1-$2T_0$) increase with increasing Ti-site doping Mg concentration (Table 3.3) implying that Ti-site Mg doping drives the system away from the ferroelectric instability. It seems that the [$Mg^{2+}{}_{Ti}$ – V_O] dipoles strengthen the local field and the quantum fluctuations and, consequently, contribute to suppressing the quantum paraelectric to the ferroelectric transition. This explanation is somehow supported by the calculated tolerance factor *t*. With Mg doping the ions in Ti sites become more packed, decreasing the probability of being in off-centre positions. The possibility of inducing ferroelectric anomaly by the shift of the B ions is thus reduced.

3.5.3. Analysis of low-frequency loss peak dynamics

The frequency effect on the dielectric loss behaviour can be seen from Figure 3.16, which depicts the temperature dependence of imaginary part of the dielectric permittivity ε'' at frequencies of 1, 10 and 100 kHz for $Sr_{0.99}Mg_{0.01}TiO_3$ (Figure 3.16a) and $Sr_{0.99}Mg_{0.01}TiO_{3-\delta}$ (Figure 3.16b) ceramics, exemplifying SMT and STM systems, respectively. Obvious shifts of the ε'' peak positions towards higher temperatures with the frequency increase are observed.

Evident relaxation-type dispersions at constant temperatures can be also seen from Figure 3.17. STM compositions, as exemplified by $SrTi_{0.99}Mg_{0.01}O_{3-\delta}$, reveal a low-frequency dispersion around ~82 K, as shown in Figure 3.17b. This dispersion corresponds to the peak A in the temperature dependence of dielectric loss (see Figures 3.14 and 3.16). As mentioned above, this dispersion is similar to that of undoped ST observed both in ceramics and in single crystals (Ang et al., 1999; Viana et al., 1994). It is supposed to be related to the elastic domains, those occur at antiferrodistortive phase transition, and to the dynamics of the domain walls (Mizaras and Loidl, 1997), since no peak in this temperature range was observed for ST crystals in single-domain state (Dec et al., 1999). The low-frequency dispersion, corresponding to the loss peak A, is presented in Figure 3.17a for SMT ceramics, exemplified by $Sr_{0.99}Mg_{0.01}TiO_3$. Comparing with ST and STM, the dispersion is broadened and shifted towards ~69 K.

Additional broad low-frequency dispersion was observed in the spectra of SMT ceramics around ~21 K, as shown in Figure 3.18a for $Sr_{0.99}Mg_{0.01}TiO_3$. This dispersion corresponds to the peak B in the temperature dependence of dielectric loss (see Figures 3.14 and 3.16), ascribed to the polaronic relaxation (Ang et al., 1999). Weak additional dispersion can bee seen also in Figure 3.18b for $SrTi_{0.99}Mg_{0.01}O_{3-\delta}$ sample. Thermally activated oxygen vacancies jumping around Mg^{2+} ions substituting Ti^{4+} ions are suggested as the origin of such dynamics (Lemanov et al., 2002 and references therein).

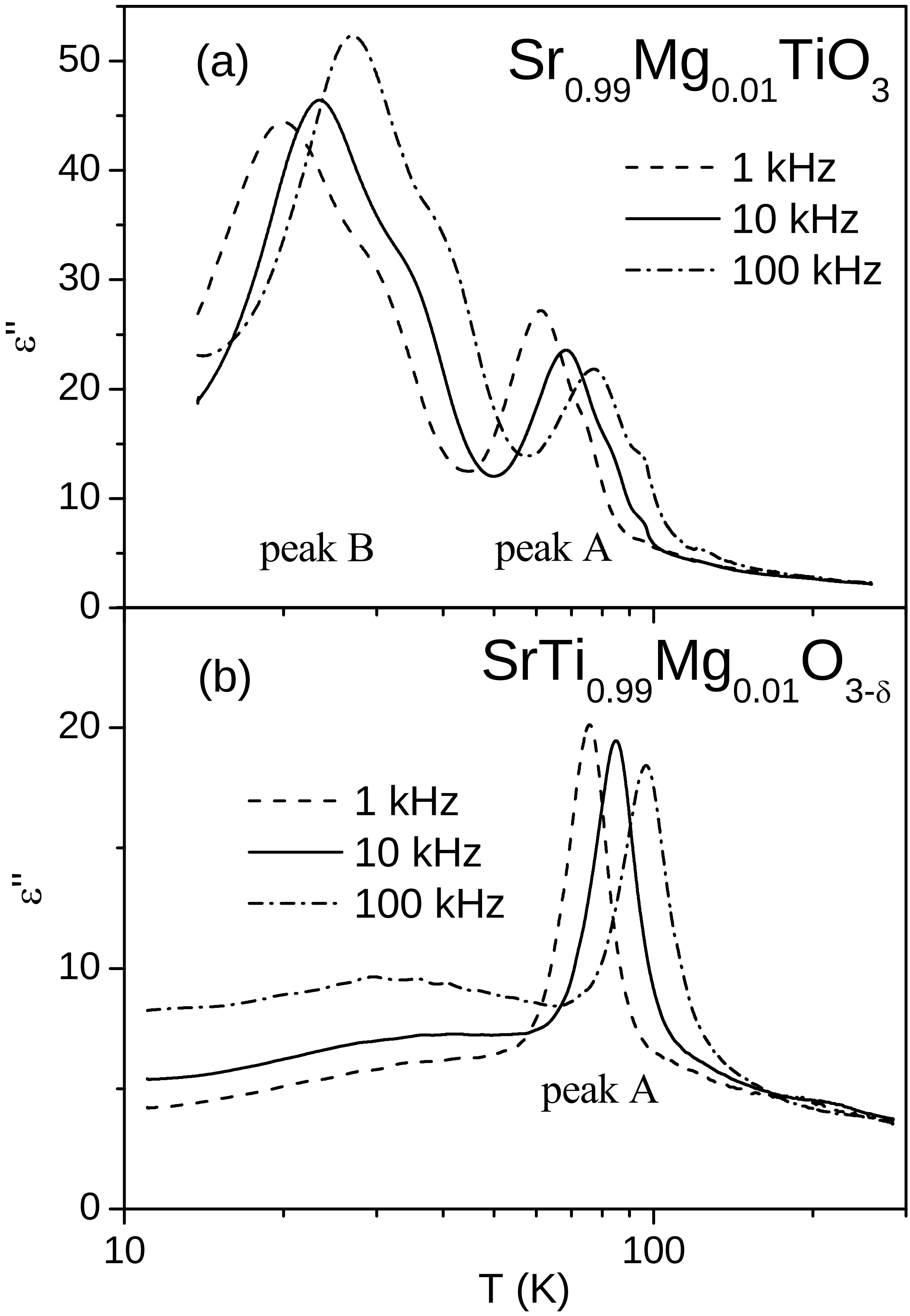

FIGURE 3.16. Temperature dependence of dielectric loss ε" of $Sr_{0.99}Mg_{0.01}TiO_3$ (**a**) and $SrTi_{0.99}Mg_{0.01}O_{3-\delta}$ ceramics (**b**) at 1, 10 and 100 kHz.

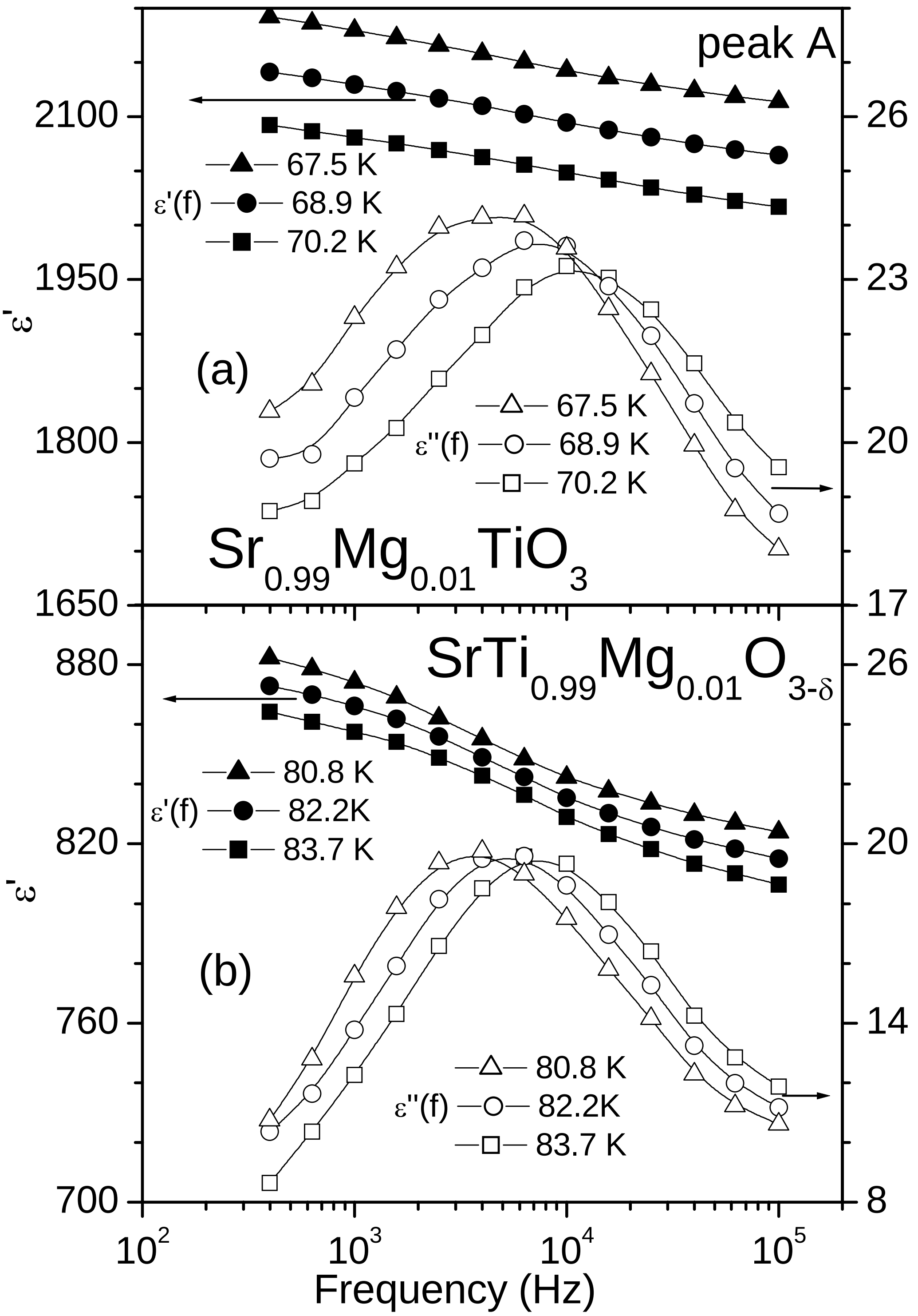

FIGURE 3.17. Frequency dependence of real ε' (left side scale) and imaginary ε'' (right side scale) parts of the dielectric permittivity measured at different temperatures in vicinity of the loss peak A for $Sr_{0.99}Mg_{0.01}TiO_3$ (**a**) and $SrTi_{0.99}Mg_{0.01}O_{3-\delta}$ (**b**) ceramics.

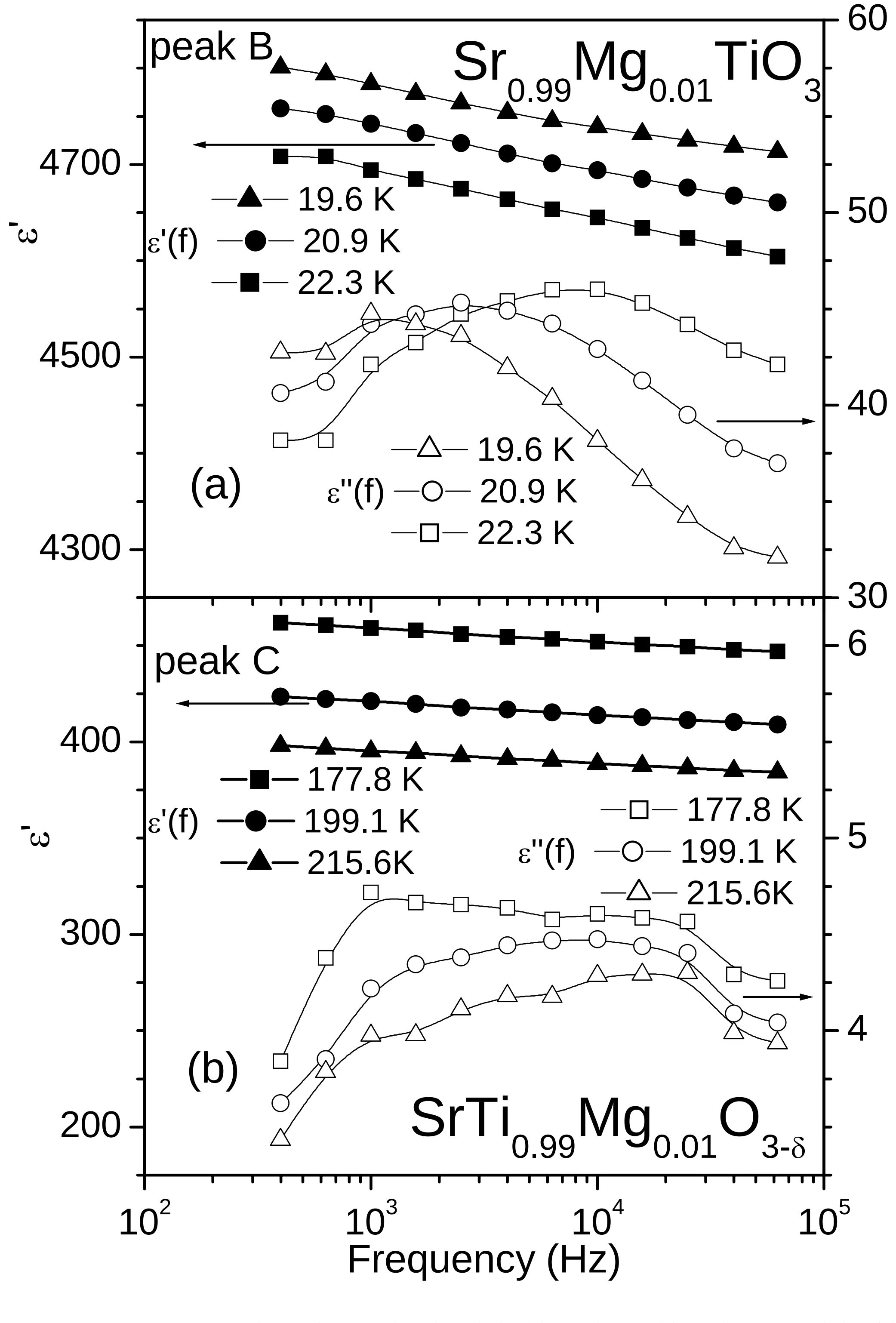

FIGURE 3.18. Frequency dependence of real ε' (left side scale) and imaginary ε'' (right side scale) parts of the dielectric permittivity measured at different temperatures in vicinity of the loss peak B for $Sr_{0.99}Mg_{0.01}TiO_3$ (**a**) and of the loss peak C for $SrTi_{0.99}Mg_{0.01}O_{3-\delta}$ (**b**) ceramics.

The relaxation dynamics parameters of the loss peak A for ST, SMT and STM, as well as of the peak B for SMT and of the peak C for some STM samples were deduced from the temperature and frequency values of ε'' peaks. Figure 3.19 represents the Arrhenius plots $\ln(\tau) = \ln(\omega^{-1})$ versus $1000/T_{\varepsilon''\mathrm{m}}$. As one can see for all the compositions, the logarithm of the relaxation time τ of the peak A linearly depends on the inverse temperature, i.e., the relaxation of the loss peak A exhibits a thermally activated behaviour, which can be described by an Arrhenius law:

$$\tau = \tau_0 \exp(U/\mathrm{k_B}T) \tag{3.8}$$

with the pre-exponential term τ_0 and activation energy U.

The τ_0 and U values were obtained for all the samples except $\mathrm{SrTi_{0.90}Mg_{0.10}O_{3-\delta}}$, for which the peak is not detectable, and are shown in Table 3.4. The deduced parameters are close to the values $\tau_0 = 8.0 \times 10^{-13}$ s and $U = 120$ meV obtained by Viana et al. (1994) for ST single crystals.

The relaxation of the additional peak B for SMT ceramics can also be described by an Arrhenius law, as shown in Figure 3.20, although this peak is diffused. τ_0 and U values, varying in the range $(1.8\text{-}5.0) \times 10^{-12}$ s and 28-34 meV respectively, are presented in Table 3.5. Viana et al. (1994) reported low-temperature relaxation in ST single crystals with $\tau_0 = 2.5 \times 10^{-12}$ s and $U = 13.6$ meV, which origin is supposed to arise from the hopping of the polarons between lattice sites (Ang et al., 1999; Lemanov et al., 2002). On the other hand, dielectric relaxation with dynamics described by Arrhenius law with $\tau_0 = (1.6\text{-}2.3) \times 10^{-11}$ s and $U = 11\text{-}15$ meV was observed for $\mathrm{Sr_{1-\mathit{x}}Ca_{\mathit{x}}TiO_3}$ system and related to the formation of nanoregions around dilute off-centre dopant dipoles (Bianchi et al., 1995; Kleemann et al., 1997). Thus, the loss peak B observed in SMT may be of either polaron or off-centre dopant nature, or of the superposition of this two origins. Though for SCT in contrast to SMT, a peak in $\varepsilon'(\mathrm{T})$ was reported (Mitsui and Westphal; 1961), the limitation of solid solubility of Mg in ST might allow a peak to appear just in the temperature dependence of the dielectric loss, which is know to be more sensitive than the dielectric constant.

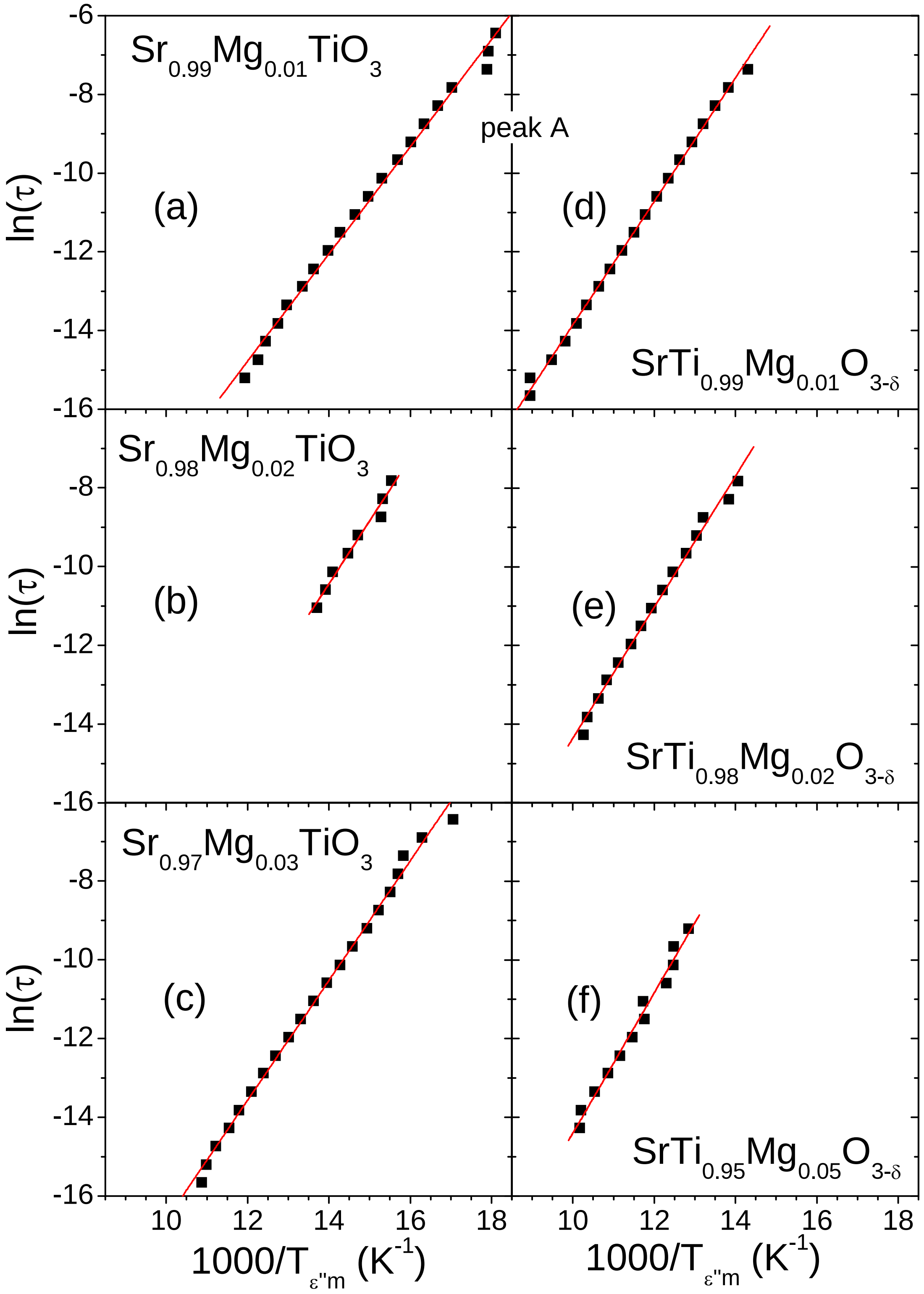

FIGURE 3.19. Arrhenius plots ln(τ) versus 1000/$T_{\varepsilon''\text{m}}$ ($T_{\varepsilon''\text{m}}$ is the temperature at which maximum of ε'' occurs at the angular frequency $w = 2\pi f$; $\tau = w^{-1}$) for the loss peak A of $Sr_{1-x}Mg_xTiO_3$ with x = 0.01 (**a**), 0.02 (**b**), 0.03 (**c**) and of $SrTi_{1-y}Mg_yO_{3-\delta}$ with y = 0.01 (**d**), 0.02 (**e**), 0.05 (**f**).

Table 3.4. Parameters of Arrhenius law describing relaxational dynamics of the loss peak A in $Sr_{1-x}Mg_xTiO_3$ and $SrTi_{1-y}Mg_yO_{3-\delta}$ ceramics.

	ARRHENIUS LAW	
Composition	**U, meV**	**τ_0, 10^{-14} s**
$Sr_{0.97}Mg_{0.03}TiO_3$	131	1.5
$Sr_{0.98}Mg_{0.02}TiO_3$	129	2.9
$Sr_{0.99}Mg_{0.01}TiO_3$	118	3.0
$SrTiO_3$	140	6.4
$SrTi_{0.99}Mg_{0.01}O_{3-\delta}$	135	14.6
$SrTi_{0.98}Mg_{0.02}O_{3-\delta}$	144	3.4
$SrTi_{0.95}Mg_{0.05}O_{3-\delta}$	151	1.4

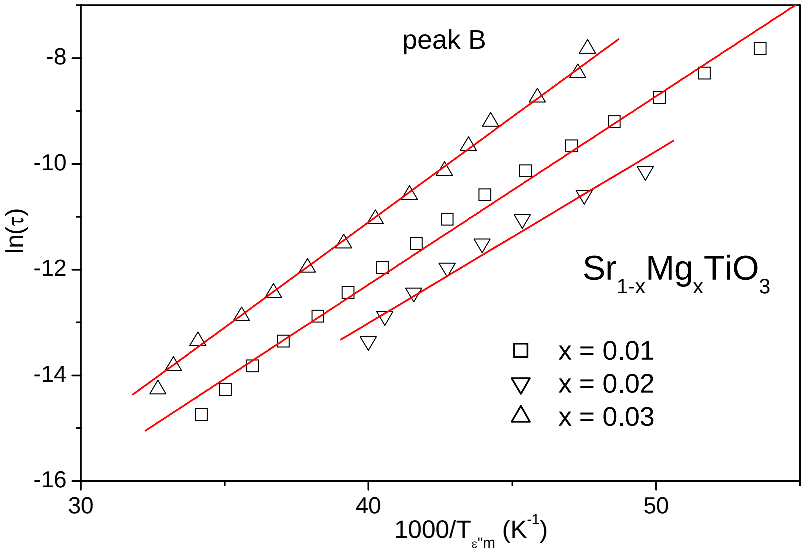

FIGURE 3.20. Arrhenius plots $\ln(\tau)$ versus $1000/T_{\varepsilon''m}$ ($T_{\varepsilon''m}$ is the temperature at which maximum of ε'' occurs at the angular frequency $w = 2\pi f$; $\tau = w^{-1}$) for the loss peak B of $Sr_{1-x}Mg_xTiO_3$ samples with $x = 0.01$, 0.02 and 0.03.

Arrhenius law parameters of the loss peak C, related to the thermally activated jumps of the oxygen vacancies around the impurity ions (Lemanov et al., 2002 and references therein) and observed for STM ceramics, are also tabulated in Table 3.5. However, since the peak C is very weak, the approximate pre-exponential term $\tau_0 = (2.7\text{-}5.1) \times 10^{-12}$ s and activation energy U = 258-294 meV could be only obtained for $SrTi_{0.99}Mg_{0.01}O_{3-\delta}$ and $SrTi_{0.98}Mg_{0.02}O_{3-\delta}$ samples (see Figure 3.21). These values agree well with $U \sim 0.21\text{-}0.3$ eV and $\tau_0 \sim 10^{-11}$ - 10^{-12} s, obtained by Lemanov et al. (2000; 2002) for the frequency dispersion in $SrTiO_3$-$SrMg_{1/3}Nb_{2/3}O_3$ solid solutions, attributed to oxygen-vacancy-related relaxation.

Table 3.5. Parameters of the Arrhenius law describing relaxational dynamics of the loss peaks B in $Sr_{1-x}Mg_xTiO_3$ and C in $SrTi_{1-y}Mg_yO_{3-\delta}$ ceramics.

		ARRHENIUS LAW	
Peak	**Composition**	***U*, meV**	**τ_0, 10^{-12} s**
B	$Sr_{0.97}Mg_{0.03}TiO_3$	34	1.8
B	$Sr_{0.98}Mg_{0.02}TiO_3$	28	5.0
B	$Sr_{0.99}Mg_{0.01}TiO_3$	31	3.0
C	$SrTi_{0.99}Mg_{0.01}O_{3-\delta}$	258	5.1
C	$SrTi_{0.98}Mg_{0.02}O_{3-\delta}$	294	2.7

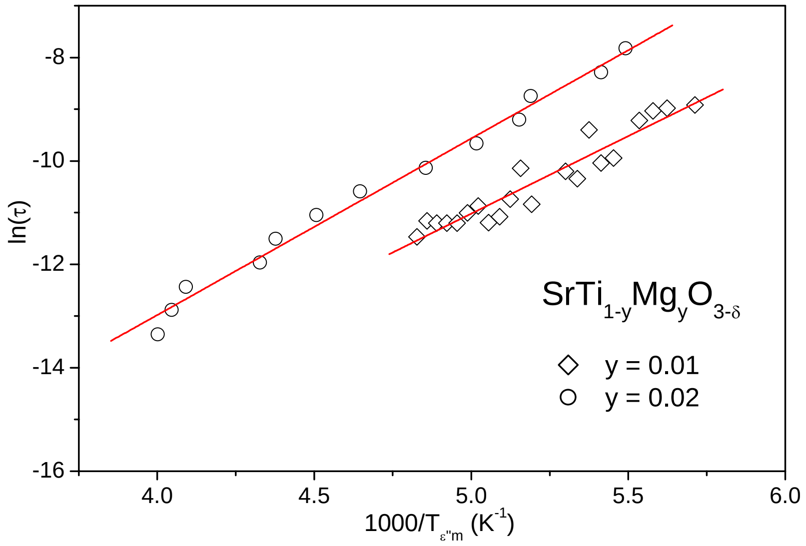

FIGURE 3.21. Arrhenius plots ln(τ) versus 1000/$T_{\varepsilon''m}$ ($T_{\varepsilon''m}$ is the temperature at which maximum of ε'' occurs at the angular frequency $w = 2\pi f$; $\tau = w^{-1}$) for the loss peak C of $SrTi_{1-y}Mg_yO_{3-\delta}$ samples with $y = 0.01$ and 0.02.

3.5.4. Dielectric response in microwave range (1 MHz - 1.8 GHz)

The dielectric spectra of some SMT and STM samples were determined experimentally in the microwave region and are shown in Figures 3.22, 3.23.

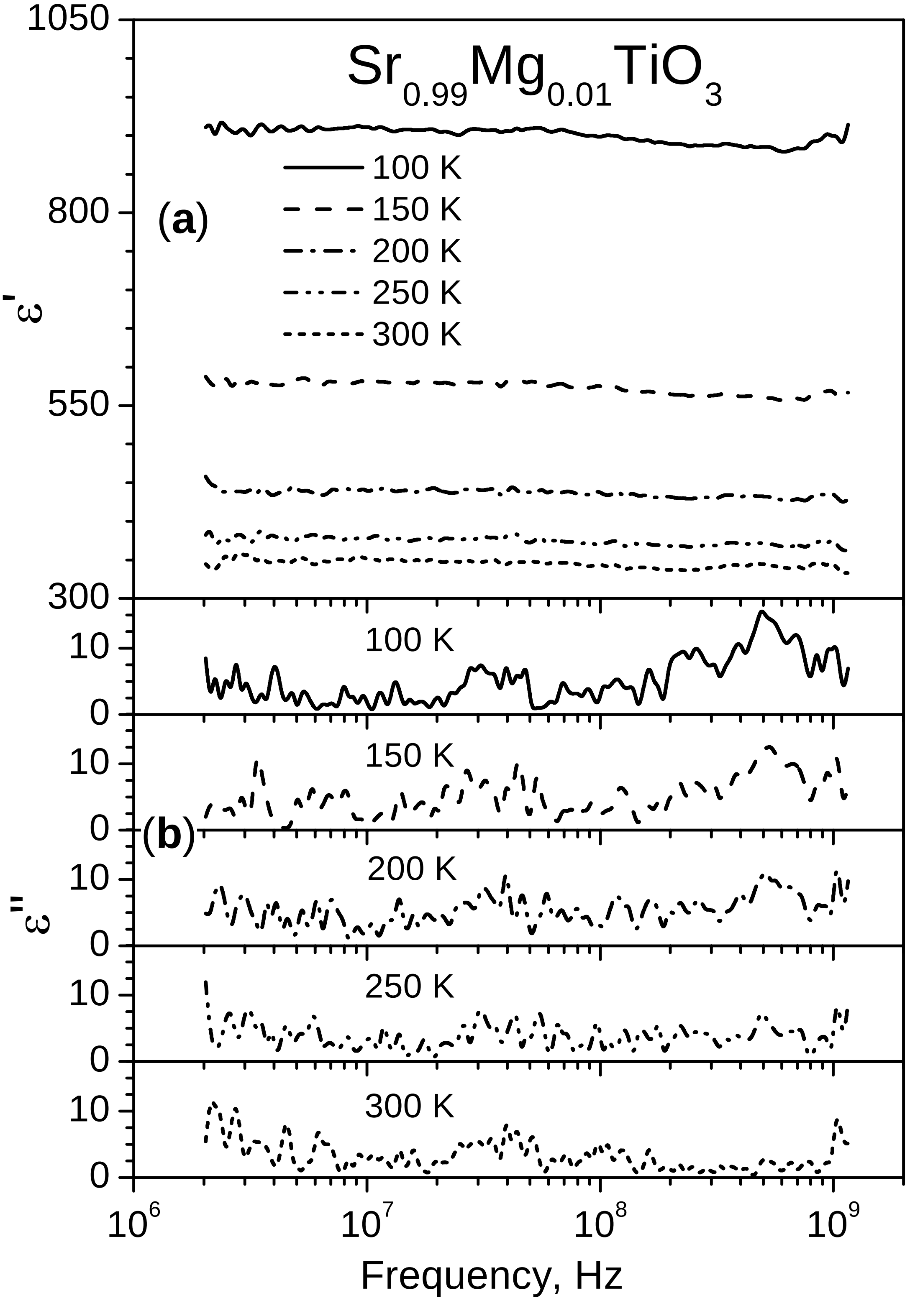

FIGURE 3.22. Frequency dependence of real ε' (**a**) and imaginary ε'' (**b**) parts of dielectric permittivity of $Sr_{0.99}Mg_{0.01}TiO_3$ ceramics in microwave range at 100, 150, 200, 250 and 300 K.

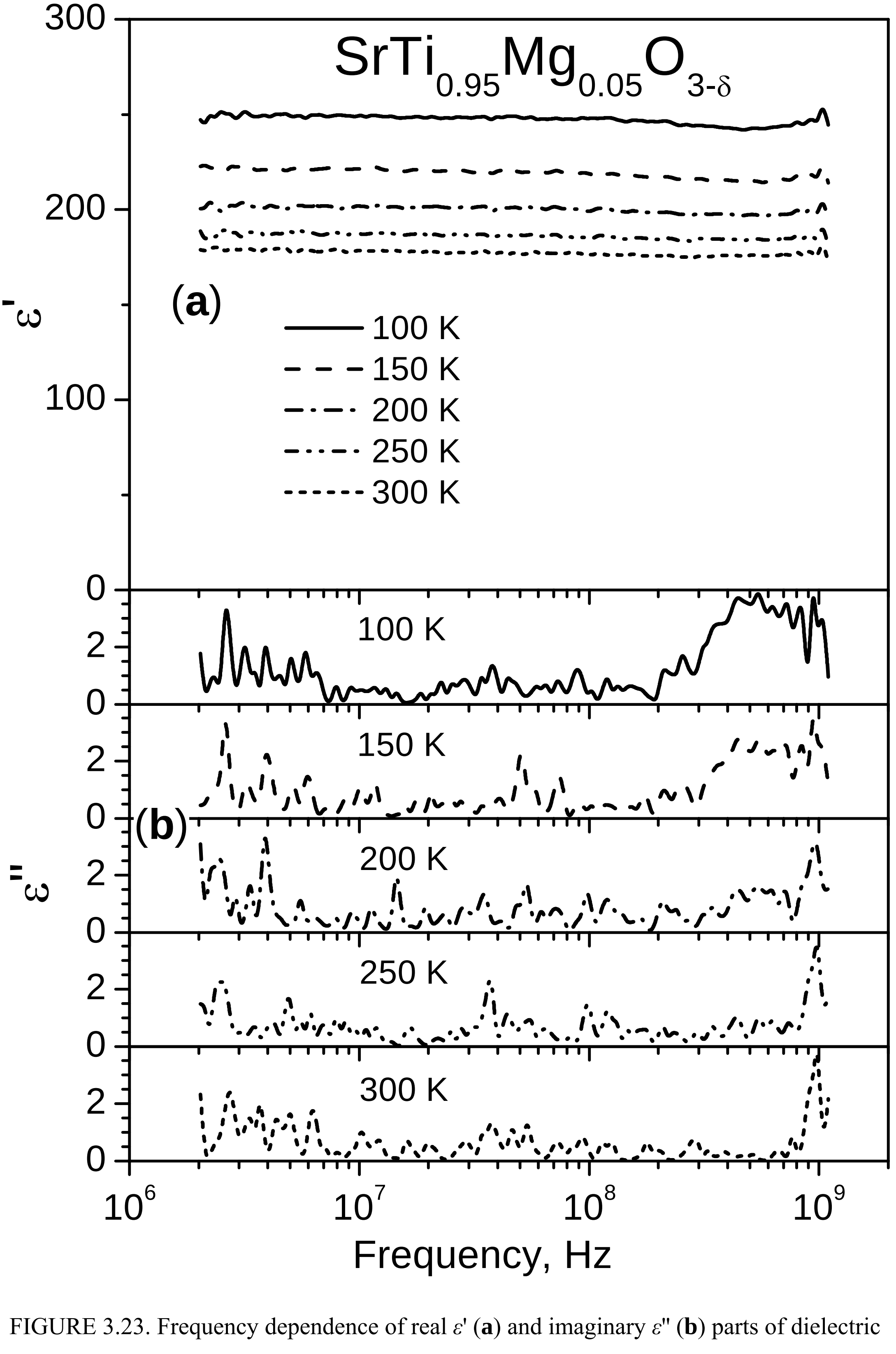

FIGURE 3.23. Frequency dependence of real ε' (**a**) and imaginary ε'' (**b**) parts of dielectric permittivity of $SrTi_{0.95}Mg_{0.05}O_{3-\delta}$ ceramics in microwave range at 100, 150, 200, 250 and 300 K.

Figure 3.22 reveals the spectra for $Sr_{0.99}Mg_{0.01}TiO_3$ ceramics. The continuous increase of the real part of the dielectric permittivity *ε*' with the temperature decrease from 300 to 100 K, similarly to undoped ST, is observed. The imaginary part of dielectric permittivity *ε*'' keeps almost constant at all the temperatures in the range of 100-300 K. Both ε' and ε'' do not also vary with frequency in the microwave range at constant temperature.

From Figure 3.23 that presents the microwave spectra of $SrTi_{0.95}Mg_{0.05}O_{3-\delta}$ ceramics, it is evident that at fixed temperature, ε' keeps constant in almost entire accessible frequency range. As the temperature decrease, ε' increases, but not so much as that of SMT and ST. ε'' almost does not vary neither with frequency nor with temperature, but its value is 4-5 times smaller than that for SMT ceramics. Average value of the $tan\delta = \varepsilon''/\varepsilon'$ in the temperature range of 100-300 K at 1 GHz was found to be only 0.0080±0.0037 for $SrTi_{0.95}Mg_{0.05}O_{3-\delta}$ ceramics, whereas for $Sr_{0.99}Mg_{0.01}TiO_3$ ceramics, average $tan\delta = 0.0293 \pm 0.0063$.

3.5.5. Time domain terahertz and infrared spectroscopy results

The TDT transmittance measurements were performed at low temperatures for some selected SMT ($Sr_{0.99}Mg_{0.01}TiO_3$) and STM ($SrTi_{0.99}Mg_{0.01}O_{3-\delta}$ and $SrTi_{0.95}Mg_{0.05}O_{3-\delta}$) compositions. $Sr_{0.99}Mg_{0.01}TiO_3$ and $SrTi_{0.95}Mg_{0.05}O_{3-\delta}$ were examined down to liquid nitrogen temperature (see Figures 3.24 and 3.25, respectively), while $SrTi_{0.99}Mg_{0.01}O_{3-\delta}$ was studied down to liquid helium temperature (see Figure 3.26).

The results shown in Figures 3.24-3.26 display much higher variation in dielectric constant and loss values for SMT composition than those for STM. This observation implies the softening of the soft mode with decreasing temperature for SMT similarly to undoped ST. At the same time, terahertz values of the dielectric constant and loss for STM vary in a much more limited range with decreasing temperature. The soft mode contribution to the dielectric constant and loss is thus reduced for STM compositions and the soft mode frequency is not approached to the MW range. So, STM system is in a stable paraelectric state, characterised by quite high dielectric constant, thermostability and low dielectric losses at high frequencies.

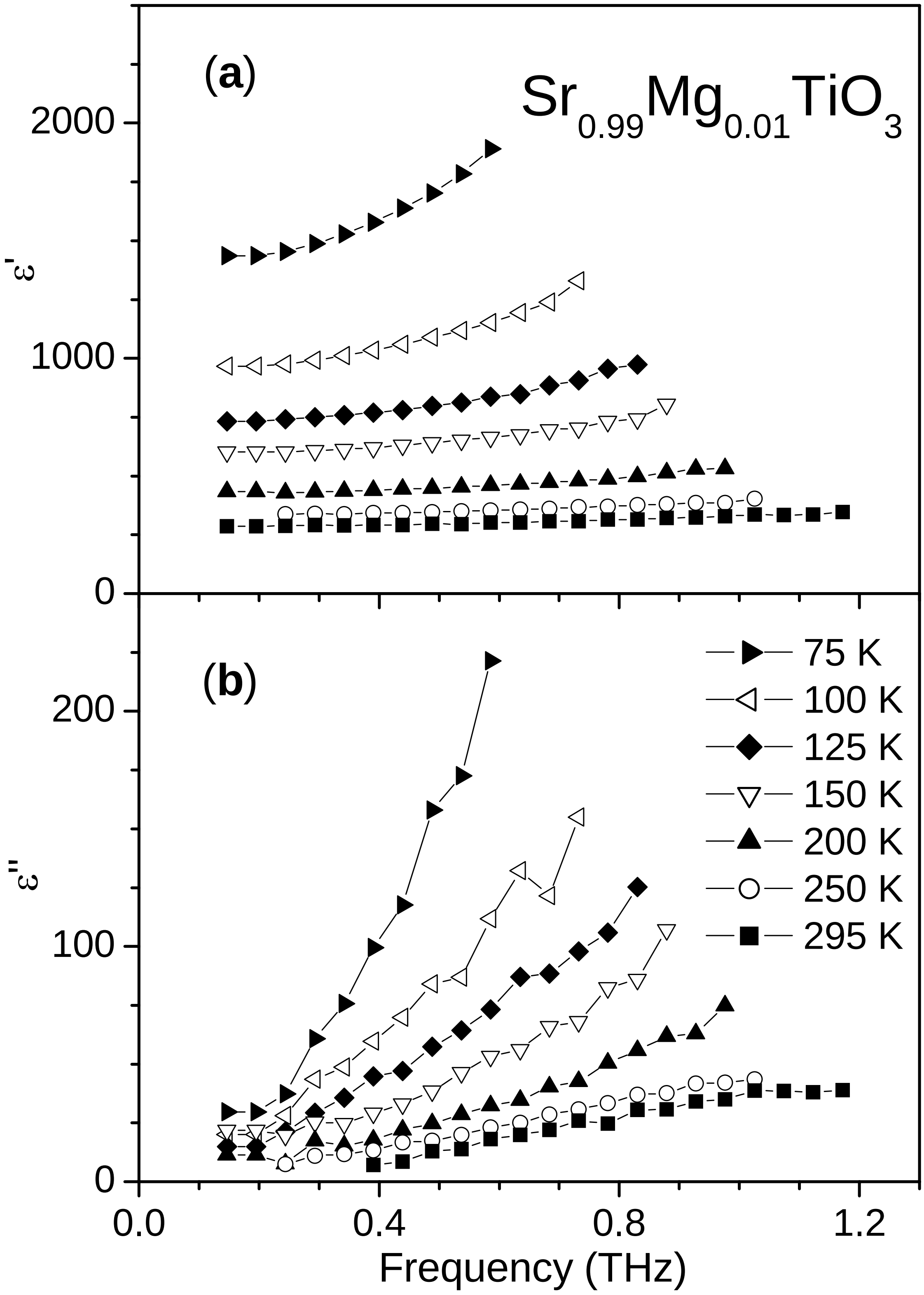

FIGURE 3.24. Frequency dependence of real ε' (**a**) and imaginary ε'' (**b**) parts of dielectric permittivity of $Sr_{0.99}Mg_{0.01}TiO_3$ ceramics in terahertz range at 75, 100, 125, 150, 200, 250 and 295 K.

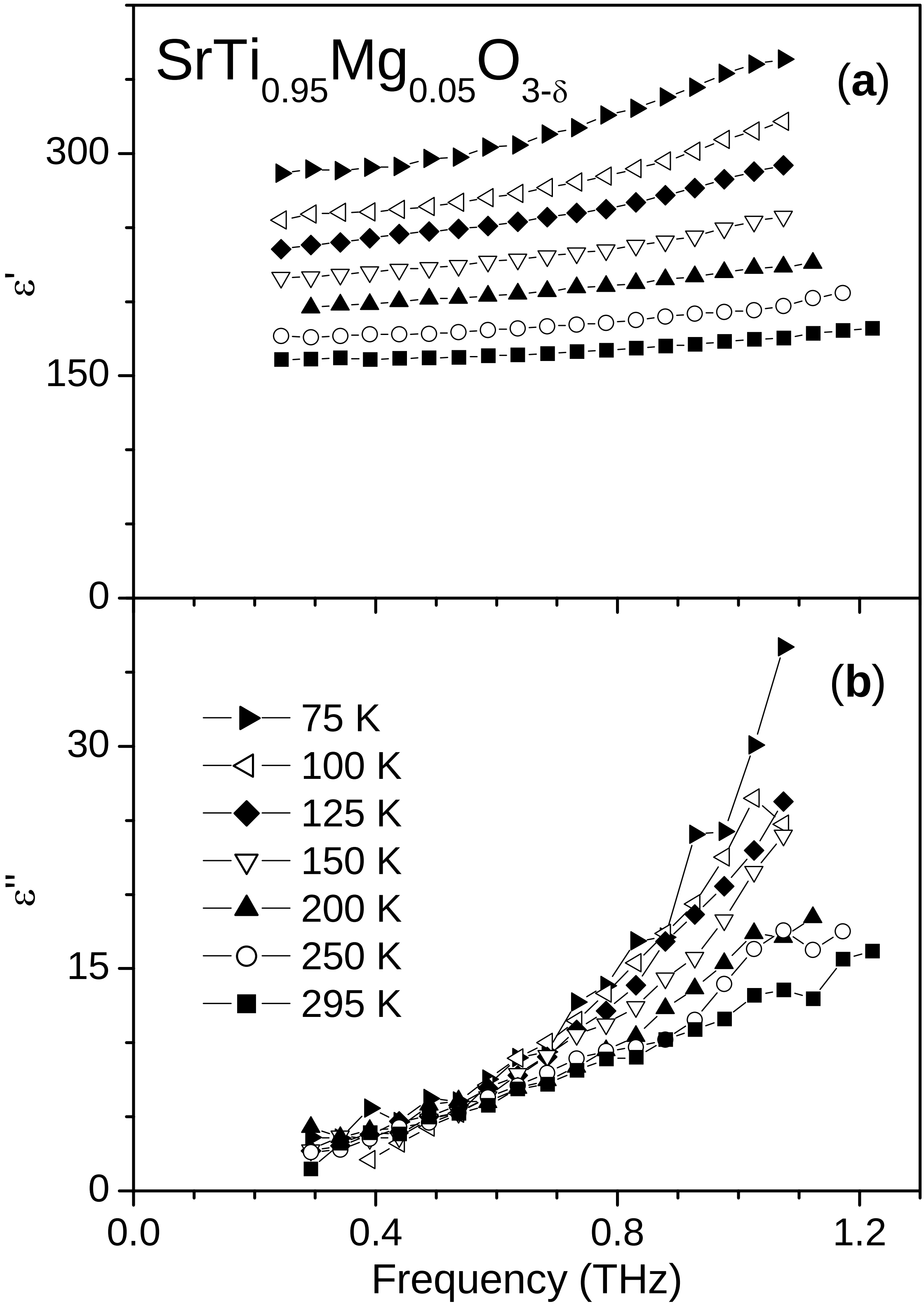

FIGURE 3.25. Frequency dependence of real ε' (**a**) and imaginary ε'' (**b**) parts of dielectric permittivity of $SrTi_{0.95}Mg_{0.05}O_{3-\delta}$ ceramics in terahertz range at 75, 100, 125, 150, 200, 250 and 295 K.

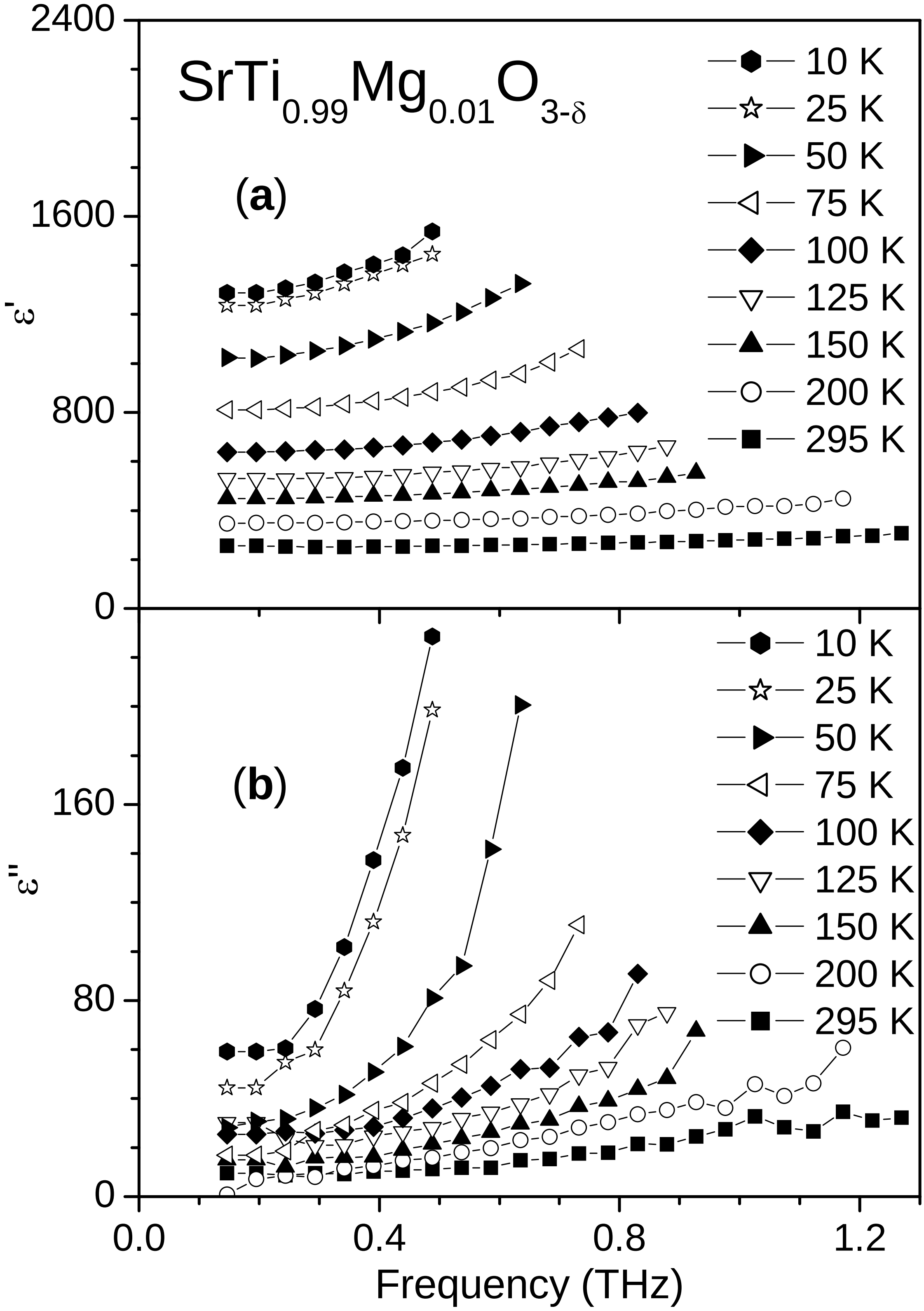

FIGURE 3.26. Frequency dependence of real *ε*' (**a**) and imaginary *ε*'' (**b**) parts of dielectric permittivity of $SrTi_{0.99}Mg_{0.01}O_{3-\delta}$ ceramics in terahertz range at 10, 25, 50, 75, 100, 125, 150, 200 and 295 K.

The low-temperature dielectric properties for $SrTiO_3$, $Sr_{0.99}Mg_{0.01}TiO_3$, $SrTi_{0.99}Mg_{0.01}O_{3-\delta}$ and $SrTi_{0.95}Mg_{0.05}O_{3-\delta}$ compositions from rf to THz frequency are summarised in Figure 3.27 (a, b).

Comparing with the dielectric behaviour of undoped ST, no dielectric anomaly was detected, but just the reduction of the dielectric constant ε' and the change of the dielectric loss behaviour, induced by Mg doping, can be observed. Figure 3.27 demonstrates also the close similarity between the $\varepsilon'(T)$ curves for different frequencies (10 kHz and 0.3 THz), at least above 70 K. It means that no additional dielectric relaxation mechanism appears with Mg doping in this frequency range. The dielectric losses in MW range are also comparable with those in the rf range, being especially low for $SrTi_{0.95}Mg_{0.05}O_{3-\delta}$. Therefore, $SrTi_{0.95}Mg_{0.05}O_{3-\delta}$ composition, that shows rather high thermostability and low loss values from rf to terahertz range, might be used as an active material for low-loss microwave waveguides and/or resonators. For all of the compositions, losses start to increase in the terahertz range because of the proximity to the soft mode frequency, which is especially noticeable in Figure 3.27b for $Sr_{0.99}Mg_{0.01}TiO_3$. Similar behaviour was reported for undoped ST ceramics (Petzelt et al., 2001).

IR reflectivity spectra obtained at room temperature and normalised using THz data are shown in Figure 3.28 for $Sr_{0.99}Mg_{0.01}TiO_3$ ceramics, representing SMT system, and for $SrTi_{0.99}Mg_{0.01}O_{3-\delta}$ and $SrTi_{0.95}Mg_{0.05}O_{3-\delta}$ ceramics, representing STM system. IR spectrum for undoped ST ceramics is also shown for comparison.

Three IR active bands: transverse optic modes TO_1, TO_2 and TO_4, can be observed in spectrum of $SrTiO_3$. Similar spectra were observed in early papers (Barker and Tinkham, 1962; Spitzer et al., 1962), in which the highest frequency mode at about 550 cm^{-1} was assigned to Ti-O stretching vibration, the frequency mode near 178 cm^{-1} (which could be seen directly in the reflectivity curve) was assigned to cation-TiO_6 octahedra vibration, whereas the frequency mode near 88 cm^{-1} (obtained only from the analysis of the reflection data by the oscillator-model fit) was attributed to the vibration of Ti inside oxygen octahedra known as the ferroelectric soft mode. This low-frequency mode exhibits temperature dependence in accordance with the Cochran theory (Barker and Tinkham, 1962). IR spectra of SMT and STM reveal features similar to undoped ST. However, some additional features in the range of 585-675 cm^{-1} can be seen for STM ceramics.

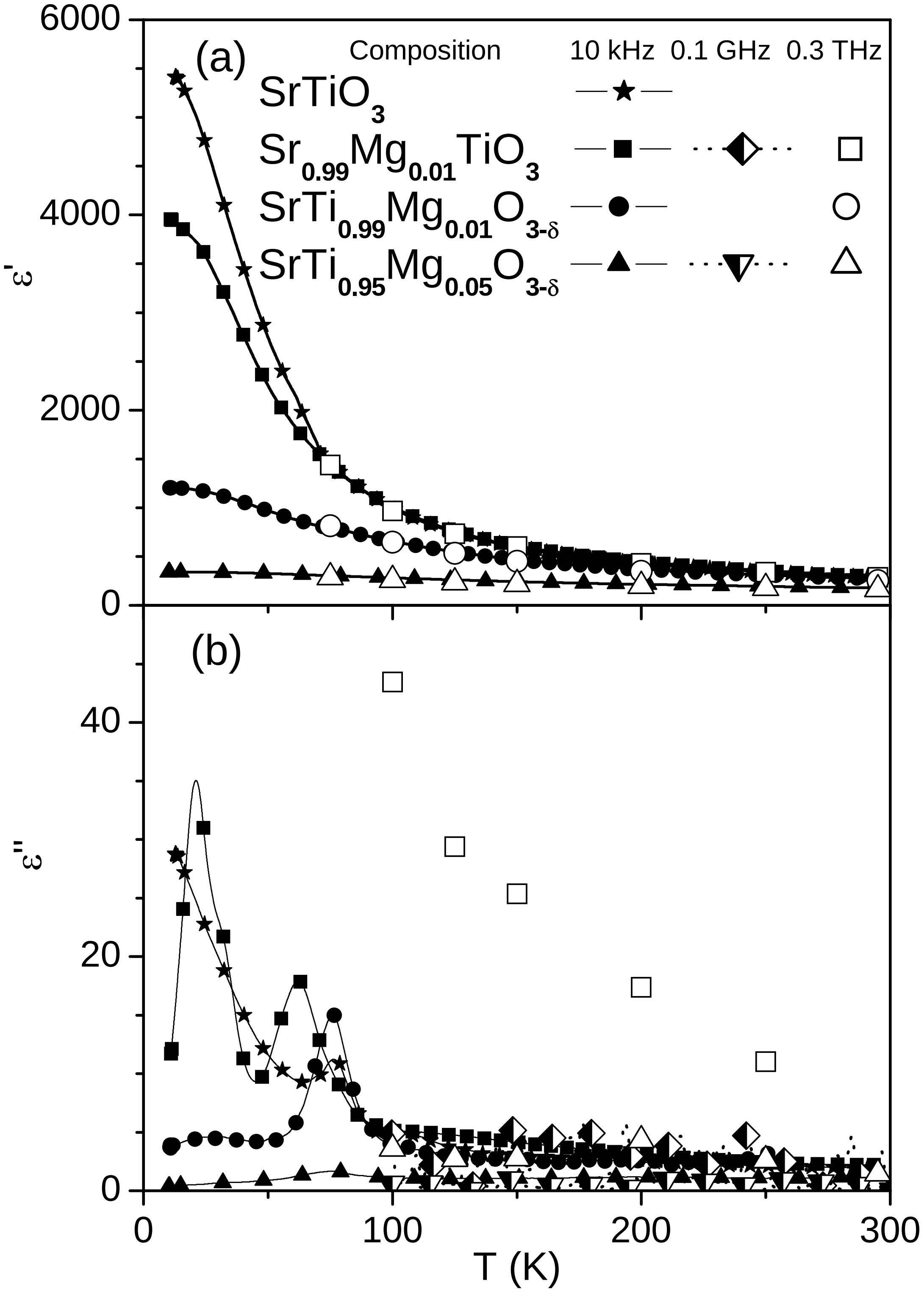

FIGURE 3.27. Temperature dependence of real ε' (**a**) and imaginary ε'' (**b**) parts of dielectric permittivity of $SrTiO_3$, $Sr_{0.99}Mg_{0.01}TiO_3$, $SrTi_{0.99}Mg_{0.01}O_{3-\delta}$ and $SrTi_{0.95}Mg_{0.05}O_{3-\delta}$ ceramics at different frequencies in a wide frequency range.

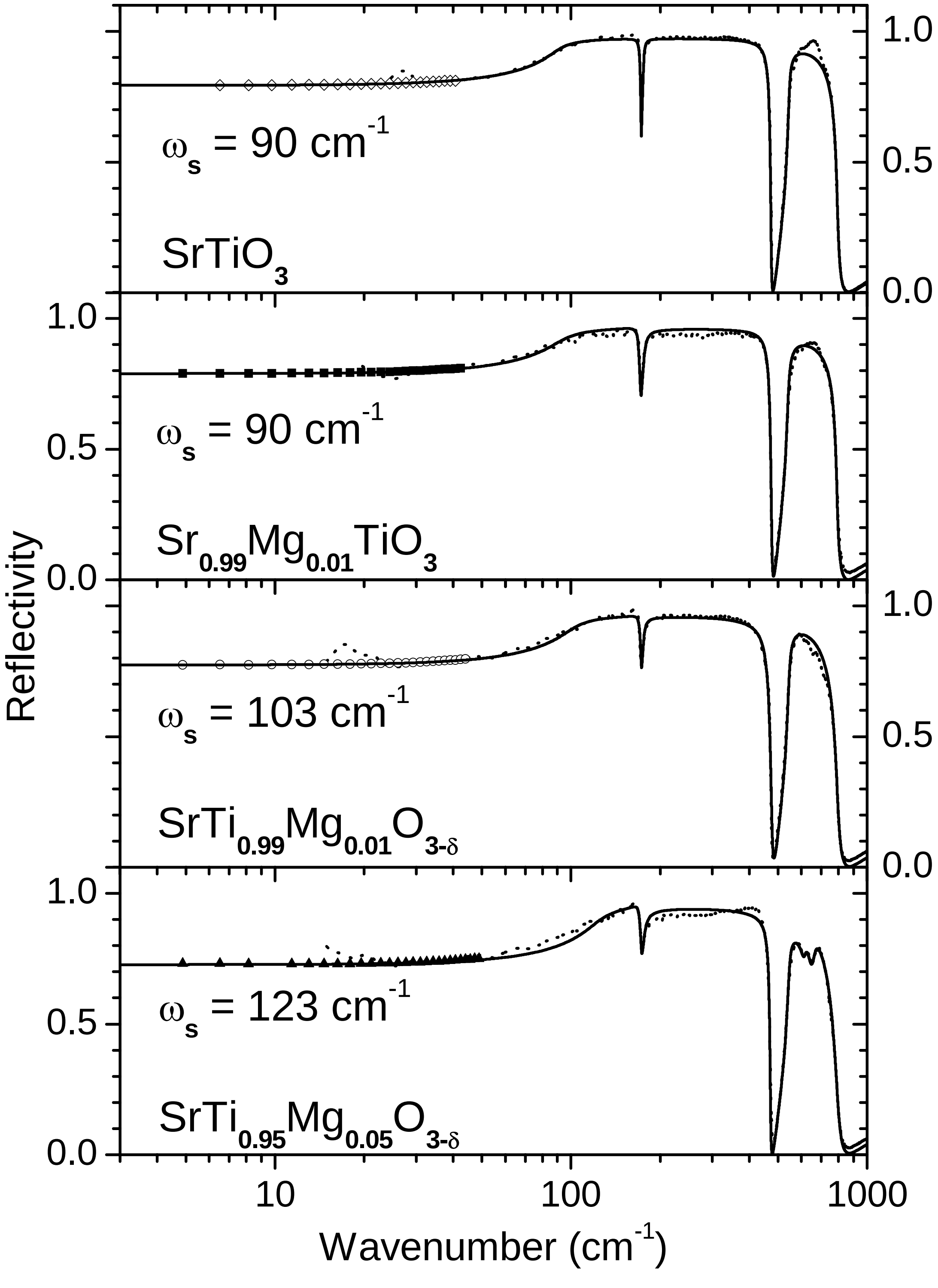

FIGURE 3.28. Room-temperature IR reflectivity spectra (dot lines) of $SrTiO_3$, $Sr_{0.99}Mg_{0.01}TiO_3$, $SrTi_{0.99}Mg_{0.01}O_{3-\delta}$ and $SrTi_{0.95}Mg_{0.05}O_{3-\delta}$ ceramics and their fits (solid lines) together with TDT data (solid and open symbols). Calculated values of soft mode frequency ω_s are pointed for each composition.

The generalized four-parameter damped oscillator model was used to determine the polar phonon parameters from the IR reflectivity spectra and THz data:

$$\varepsilon^*(\omega) = \varepsilon_\infty \prod_j \frac{\omega_{LOj}^2 - \omega^2 + i\omega\gamma_{LOj}}{\omega_{TOj}^2 - \omega^2 + i\omega\gamma_{TOj}} \tag{3.9}$$

where ε_∞ is the optical permittivity, $\omega_{\mathrm{LO}j}$ and $\omega_{\mathrm{TO}j}$ denote the longitudinal and transverse eigen-frequencies of the j-th polar mode, and $\gamma_{\mathrm{LO}j}$ and $\gamma_{\mathrm{TO}j}$ designate the respective damping constants (Porokhonskyy et al., 2004). The fitting curves and corresponding dielectric constant and loss spectra are shown in Figures 3.28 and 3.29, respectively.

A good agreement between the experimental data (dot lines) and fitting curves (solid lines) is seen in Figure 3.28. The soft mode frequency ω_s, obtained from the fitting, was found to be the same for SMT as for undoped ST and equal to 90 cm^{-1}, but the stiffening of the soft mode to 103 and 123 cm^{-1} occurs in $\mathrm{SrTi_{0.99}Mg_{0.01}O_{3-\delta}}$ and $\mathrm{SrTi_{0.95}Mg_{0.05}O_{3-\delta}}$, respectively. As one can see in Figure 3.29, the stiffening of the soft mode in STM samples is accompanied by the lowering of the dielectric constant and loss values in the terahertz range. The frequencies of the transverse optic modes $\mathrm{TO_2}$ and $\mathrm{TO_4}$ are almost independent on the Mg content, as shown in Figure 3.29 also.

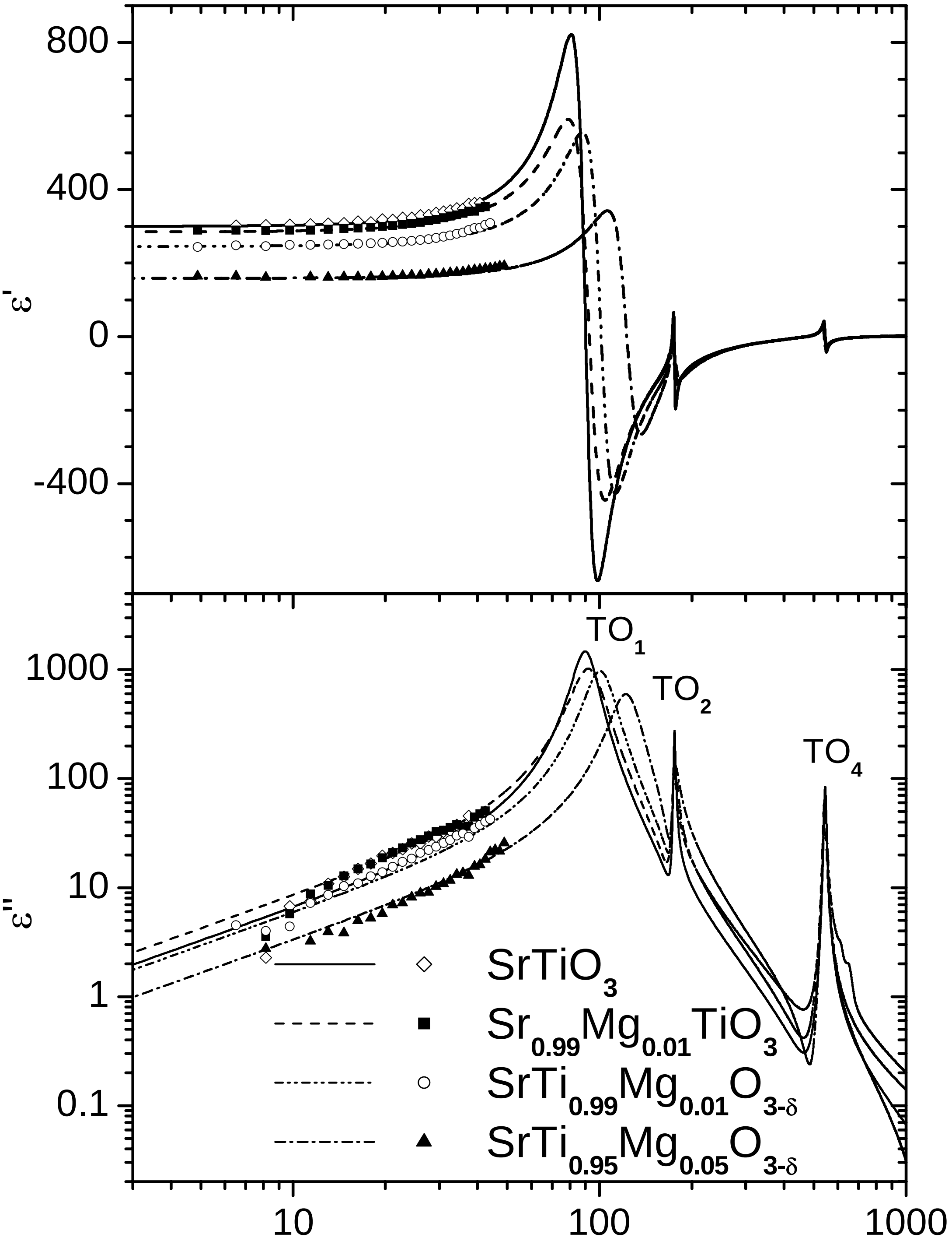

FIGURE 3.29. Room-temperature spectra of real ε' and imaginary ε'' parts of dielectric permittivity in IR range, deduced from the reflectivity fits of $SrTiO_3$, $Sr_{0.99}Mg_{0.01}TiO_3$, $SrTi_{0.99}Mg_{0.01}O_{3-\delta}$ and $SrTi_{0.95}Mg_{0.05}O_{3-\delta}$ ceramics together with data, obtained by TDT transmission spectroscopy.

3.5.6. Dielectric tunability in the temperature range of 10-300 K

Figure 3.30 (a-d) shows the temperature dependence of the real and imaginary parts of dielectric permittivity at 10 kHz under different dc fields for $SrTiO_3$, $Sr_{0.99}Mg_{0.01}TiO_3$, $SrTi_{0.99}Mg_{0.01}O_{3-\delta}$ and $SrTi_{0.95}Mg_{0.05}O_{3-\delta}$. The applied field dependences of the relative tunability at fixed temperatures are represented in Figure 3.31 (a-d) too. The relative tunability is calculated as:

$$n_r(E) = [\varepsilon'(0) - \varepsilon'(E)]/\varepsilon'(0), \qquad (3.10)$$

where $\varepsilon'(0)$ is the dielectric constant at zero field and $\varepsilon'(E)$ is the dielectric constant under applied field E.

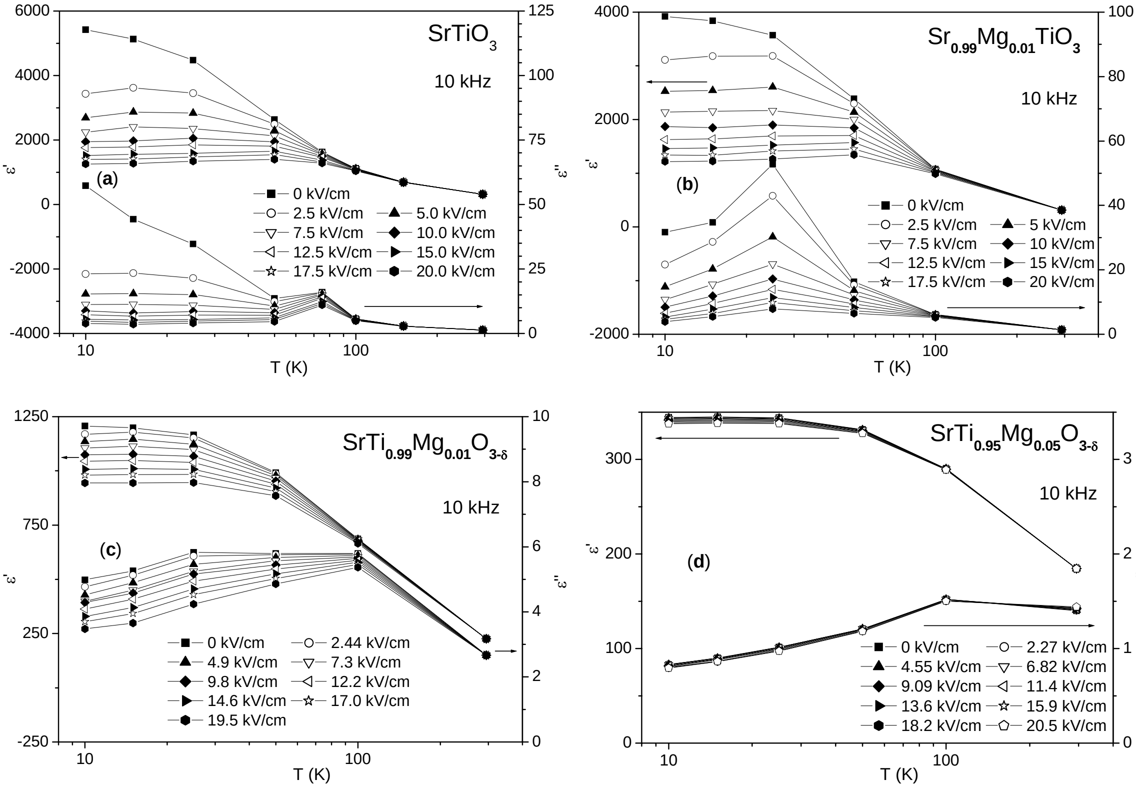

FIGURE 3.30. Variation of real ε' and imaginary ε'' parts of dielectric permittivity at 10 kHz with temperature for $SrTiO_3$ (**a**), $Sr_{0.99}Mg_{0.01}TiO_3$ (**b**), $SrTi_{0.99}Mg_{0.01}O_{3-\delta}$ (**c**) and $SrTi_{0.95}Mg_{0.05}O_{3-\delta}$ (**d**) ceramics under different dc bias fields.

As it can be seen in Figure 3.30a, a peak in the temperature dependence of dielectric constant ε' along with the decrease of ε' values at low temperatures was induced by applying bias fields in the range of 2.5-20.0 kV/cm for both $SrTiO_3$ and $Sr_{0.99}Mg_{0.01}TiO_3$. As the field increases, the peak becomes broadened and shifted to higher temperatures. The bias field-induced ferroelectric order is also known as one of the characteristic properties of undoped strontium titanate single crystals (Saifi and Cross, 1970; Hemberger et al., 1995).

However, for STM compositions the field effect is different (Figure 3.30b). For $SrTi_{0.99}Mg_{0.01}O_{3-\delta}$ the peak induced by the applied field is less pronounced than that for SMT and, for the same field, it occurs at lower temperatures. For $SrTi_{0.95}Mg_{0.05}O_{3-\delta}$ the effect of bias field is progressively suppressed and the peak is almost undetectable. This is an indication that the onset of the induced ferroelectric order in STM samples is shifted to lower temperatures and higher bias fields.

Figure 3.31 shows the relative tunability curves for $SrTiO_3$, $Sr_{0.99}Mg_{0.01}TiO_3$, $SrTi_{0.99}Mg_{0.01}O_{3-\delta}$ and $SrTi_{0.95}Mg_{0.05}O_{3-\delta}$ at different temperatures.

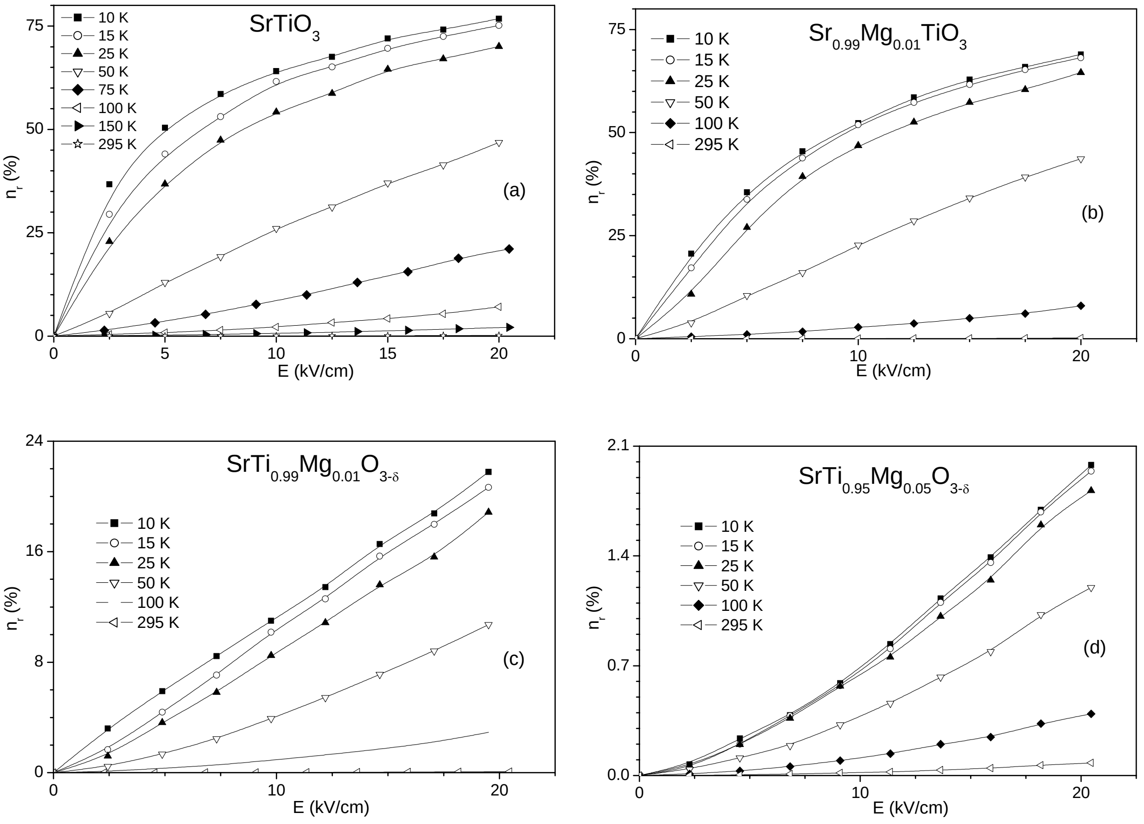

FIGURE 3.31. Variation of relative tunability n_r at 10 kHz, calculated as $n_r(E) = [\varepsilon'(0) - \varepsilon'(E)]/\varepsilon'(0)$, with bias field for $SrTiO_3$ (**a**), $Sr_{0.99}Mg_{0.01}TiO_3$ (**b**), $SrTi_{0.99}Mg_{0.01}O_{3-\delta}$ (**c**) and $SrTi_{0.95}Mg_{0.05}O_{3-\delta}$ (**d**) ceramics at different temperatures.

Undoped ST shows n_r values up to 80%, which agree well with the values already reported in the literature (Ang et al., 2000a). The n_r vs E curves for Sr-site Mg-doped ST with Mg content $x = 0.01$ lie just a bit below that of undoped ST, showing n_r values also up to 80%. However, the Ti-site Mg doping decreases the relative tunability values significantly: down to 25% for $SrTi_{0.99}Mg_{0.01}O_{3-\delta}$ and down to 2% for $SrTi_{0.95}Mg_{0.05}O_{3-\delta}$.

The dc-electric-field on the dielectric constant of Mg-doped ST ceramics in a low temperature range also highlighted the similarity between the dielectric behaviour of ST and SMT, whereas for STM compositions small relative tunability values were observed even at low temperatures, confirming that the temperature region of ferroelectric instability is likely to be shifted below 0 K.

Thus, no improvement of the relative tunability was obtained for STM compositions, i.e., the n_r does not increase in all experimental temperature range and the temperature of the relative tunability maximum does not move towards higher values.

3.6. Summary

The systems, $Sr_{1-x}Mg_xTiO_3$ ($0 \le x \le 0.15$) and $SrTi_{1-y}Mg_yO_{3-\delta}$ ($0 \le y \le 0.15$), were synthesised by solid state reaction. The microstructure and crystal structure of the sintered samples were studied. The main results obtained are:

1. The density of all the samples, sintered at 1500 ºC for 5 hours is 4.65-4.98 g/cm^3. The grain size is found to range from 9 to 31 μm for $Sr_{1-x}Mg_xTiO_3$ system and from 0.2 to 1.5 μm for $SrTi_{1-y}Mg_yO_{3-\delta}$ system, without obvious dependence on Mg content.
2. The solid solubility of Mg in the $SrTiO_3$ lattice is limited and depends on the perovskite lattice site in which the substitution occurs. The solid solubility limit of Mg at Sr-site is about 1%. For higher dopant concentration, $MgTiO_3$ second phase is formed. For Ti-site doping, the Mg solid solubility limit surpasses 10 %, with the appearance of MgO second phase for higher Mg concentrations. Due to the closer ionic radius size and to the high stability of the anionic deficient perovskite lattice, the incorporation of Mg into the Ti-site of the ST lattice is thermodynamically favourable and a higher solid solubility limit was observed. The basis of the Sr-site restriction is the instability of the small Mg^{2+} cations with twelve fold coordination in the cubic perovskite lattice; those cations favour the ilmenite type structure of $MgTiO_3$.

3. The similarity between Raman spectra for SMT ceramics and undoped ST confirms the small incorporation of Mg into the Sr site of the perovskite lattice. At the same time, the appearance of forbidden and additional "breathing" mode in Raman spectra of STM samples confirms the substitution of Ti^{4+} ion by Mg^{2+}. The corresponding local loss of the inversion centre and the breaking of the ST cubic symmetry are evidenced for STM by observation of the first-order features in the room-temperature spectra. Moreover, the intensity decrease and final disappearance of R-point modes in low-temperature spectra of STM with increasing Mg content imply vanishing of the ST structural phase transition or its shift to lower temperatures.

Mg-doped ST ceramic samples prepared by conventional mixed oxide method are examined by rf, MW, TDT and IR spectroscopy. Field-temperature dependences of the dielectric permittivity at 10 kHz are also studied. The low-frequency relaxation dynamics of dielectric loss are analysed. The unambiguous confirmation of the effect of the incorporation of Mg on the ST lattice and its dependence on the lattice site are observed in this chapter.

However, Mg impurity either in Sr- or Ti-site of the perovskite lattice does not induce any ferroelectric-like anomaly. The fitting of rf dielectric response of $Sr_{1-x}Mg_xTiO_3$ ceramics (with x up to 0.03) to Curie-Weiss law and Barrett relation, yields almost invariant fit parameters very similar to those of undoped ST. This is in contradiction with the prediction that ferroelectric- or relaxor-type anomaly can be induced by Mg incorporation into the Sr site likewise the Li atoms at the K site of $KTaO_3$ (Kvyatkovskii, 2002), although may be explained by very low incorporation of Mg into the lattice. However, an additional peak of dielectric loss with dynamics described by Arrhenius law with $\tau_0 = (1.8\text{-}5.0) \times 10^{-12}$ s and U = 28-34 meV is observed. The lattice vibration behaviour and dielectric responses in a wide range of frequency, temperature and dc bias field for ST and SMT samples are found to be similar. The similarity between the data for SMT ceramics and undoped ST confirms the small incorporation of Mg into the Sr site of the perovskite lattice.

On the other hand, the substitution of Ti^{4+} with Mg^{2+} (up to 10%) in ST is found to drive the critical temperature T_0 to negative values, resulting in a strong suppression of ferroelectric instability, clearly visible from the strong reduction of the dielectric constant. This last observation stems from the fact that bigger and less polarisable Mg^{2+} ions substitutes smaller and more polarisable Ti^{4+} ions. Also a breaking of Ti-Ti long-range interaction by the introduction of Mg into oxygen octahedra can be a reason of the stable paraelectric state of STM at low temperature.

The STM behaviour differs markedly from undoped ST as exemplified by:

1. The lower values of the dielectric constant and loss in rf, MW and THz frequency ranges with a very weak temperature dependence;
2. The gradual disappearance of the dielectric loss peak, characteristic for multidomain ST. This together with low-temperature Raman results point to the "cancellation" of the structural phase transition in STM system;
3. The appearance of additional loss peak with dynamics described by Arrhenius law with $\tau_0 = (2.7\text{-}5.1) \times 10^{-12}$ s and $U = 258\text{-}294$ meV and related to oxygen-vacancies;
4. The decrease of the relative tunability in the all temperature range;
5. A soft mode stiffening and additional features in the IR spectra.

All these features become stronger with the increasing Mg content, confirming the substitution of Ti^{4+} ion by Mg^{2+}.

4. Microstructure and Crystal Structure of Manganese-doped Strontium Titanate Ceramics

The microstructure and crystal structure of magnesium-doped $SrTiO_3$ have been reported in Chapter 3. It was found that the solid solubility of Mg in the $SrTiO_3$ perovskite lattice is limited, especially in the case of Sr-site occupancy. Such restriction of Mg solubility was explained by the fact that Mg^{2+} ions are much smaller than Sr^{2+} ones and, together with titanium and oxygen, favour the formation of $MgTiO_3$ with an ilmenite-type structure.

The ilmenite-type structure of $MnTiO_3$ (Sohn et al., 1994) is stable at room pressure and temperature. However, a transformation of $MnTiO_3$ to a $LiNbO_3$ structure at high pressures (6.0-8.0 GPa) and temperatures (1300-1400 ºC) trough a cation reordering process was reported (Ko and Prewitt, 1988; Ross et al., 1989). Moreover, it was found that the quenched phase with the $LiNbO_3$ structure transforms reversibly to a perovskite structure under pressure between 2.0 and 3.0 GPa at room temperature (Ross et al., 1989). Thus, 12-coordinated Mn^{2+}, occupying the A-site of the perovskite lattice, was practically observed under some conditions and not just theoretically supposed, in contrast to Mg^{2+}.

In addition, according to Shannon (1976), ionic radius of Mn^{2+} is higher than that of Mg^{2+} and hence closer to Sr^{2+}. As one can see from Figure 1.44, the ionic radius of Mn^{2+}, estimated for coordination number 12: $r_{Mn}{}^{2+} = 1.27$ Å, while $r_{Sr}{}^{2+} = 1.44$ Å, i.e., $r_{Mn}{}^{2+}/r_{Sr}{}^{2+} = 0.88 > 0.85$ (Shannon, 1976). In view of the facts of closer value of Mn^{2+} ionic size to that of Sr^{2+} and of possibility to obtain the perovskite $MnTiO_3$, the higher solubility of Mn in the Sr-site of $SrTiO_3$ perovskite lattice becomes possible.

Regarding Ti-site substitution, higher solid solubility limit can be also expected. First, besides the charge state 2+, Mn can also have the 4+ charge state, the same as that of Ti. Hence, there is no need for charge compensation and corresponding formation of oxygen vacancies as in the case of Mg^{2+}. Second, $r_{Mn}{}^{4+} = 0.53$ Å, $r_{Ti}{}^{4+} = 0.605$ Å, $r_{Mn}{}^{4+}/r_{Ti}{}^{4+} = 0.88$, i.e., ionic size of Mn^{4+} of the coordination number 6 is smaller and closer to that of Ti^{4+}, while Mg^{2+} ionic size is bigger and differs from that of Ti^{4+}. In addition, Negas and Roth reported that $SrMnO_3$ has the hexagonal 4L structure below 1035 ºC and changes into an anion-deficient perovskite-type structure above 1400 ºC (Hashimoto and Iwahara, 2000).

To the authors' best knowledge, no report on solid solubility limit of Mn in strontium titanate, neither in Sr nor in Ti site, has been reported. Only during the preparation of this thesis, Lemanov et al. (2004) reported that the Mn solid solubility in ST ceramics is limited to 5%, based on lattice parameter variation. However, the lattice site for the dopant occupancy was not clearly stated in their work.

In order to contribute to systematic and comparative investigation of the phase assemblage, lattice parameter behaviour, local chemical ordering, grain size distribution, grain boundary nature and other effects of Mn doping on the structural and microstructural properties, $Sr_{1-x}Mn_xTiO_3$ (hereafter designated SMnT) and $SrTi_{1-y}Mn_yO_3$ (hereafter designated STMn) ceramics were synthesised with intentional stoichiometric variations. For SMnT system, it was supposed that the Mn^{2+} ions will preferably occupy Sr-site. In STMn system, it was assumed that Mn^{4+} ions will preferably occupy Ti-site.

4.1. Synthesis and characterisation

4.1.1. Solid state reaction

Mn-doped ST ceramics were prepared by the mixed oxide method, as described in Chapter 2. Reagent grade $SrCO_3$, TiO_2 and MnO_2 were weighed according to the composition $Sr_{1-x}Mn_xTiO_3$ (SMnT) with x = 0, 0.005, 0.01, 0.02, 0.05, 0.10, 0.15, 1 and $SrTi_{1-y}Mn_yO_{3-\delta}$ (STM) with y = 0.01, 0.05, 0.10, as indicated in Table 2.2.

As follows from the formula, MnO_2 contains Mn^{4+} ions. However, it is known that for an oxide, lower temperature is oxidative and higher temperature is reducing (Jang and Chiang, 2000). Therefore, Mn charge state can be reduced to Mn^{2+} under high temperature treatment and favourable conditions. In SMnT case, the favourable condition is the lack of Sr, whose sites might be occupied with higher probability by Mn^{2+} ions according to charge compensation and ionic size considerations. To confirm that, $Mn(NO_3)_2$ precursor, originally containing Mn^{2+} ions, has been used for the preparation of SMnT compositions with x = 0.0025 and 0.03 and, as will be shown below, the properties of these compositions do not deviate dramatically from the general behaviour trend of the system.

Thus, $Sr_{1-x}Mn_xTiO_3$ system was assumed to be formed according to the following equations:

$$SrCO_3 + TiO_2 \rightarrow SrTiO_3 + CO_2 \uparrow \quad (4.1)$$

$$MnO_2 + TiO_2 \rightarrow Mn_{Sr} + Ti_{Ti} + 3O_O + 1/2O_2 \uparrow \quad (4.2a)$$

in the case of MnO_2 precursor and

$$Mn(NO_3)_2 + TiO_2 \rightarrow Mn_{Sr} + Ti_{Ti} + 3O_O + N_2O_5 \uparrow \quad (4.2b)$$

in the case of $Mn(NO_3)_2$ precursor. For $SrTi_{1-y}Mn_yO_{3-\delta}$ system, the solid state reaction Eq. (4.1) holds and Mn substitutes for Ti according to equation:

$$SrCO_3 + MnO_2 \rightarrow Sr_{Sr} + Mn_{Ti} + 3O_O + CO_2 \uparrow \quad (4.3)$$

Eqs. (4.2, 4.3) indicate that Mn, as a multivalent element, can be introduced into both Sr and Ti site without need for a charge compensation.

4.1.2. Sintering

The procedure adopted for sintering of Mn-doped ST pellets pressed from powders with an average particle size ≤ 1 μm was the same as for Mg-doped ST ceramics: room temperature, heating at 5 ºC/min, → sintering temperature (T_s) and dwelling time (t_s) → cooling in furnace at 5 ºC/min.

The effect of the sintering temperature on the density of both Sr-site and Ti-site Mn-doped ST ceramics has been studied in the temperature range 1400-1500 °C. Dependences of the ceramic density on the sintering temperature at a constant dwelling time of 5 hours are presented in Figure 4.1. For $Sr_{1-x}Mn_xTiO_3$ system, the variation is represented by the composition with $x = 0.02$ and for $SrTi_{1-y}Mn_yO_3$, is represented by the composition with $y = 0.05$. Similar variation is expected for all the compositions of the same series.

It is clearly seen that the sintering behaviour is strongly dependent on the lattice site for Mn substitution. While the density of $SrTi_{0.95}Mn_{0.05}O_{3-\delta}$ increase dramatically from 80 to 97% with T_s increasing from 1400 to 1500 °C, that of $Sr_{0.98}Mn_{0.02}TiO_3$ holds around 96-97% at this sintering temperature range. Thus, the sintering temperature of 1500 °C, at which the density of Mn-doped systems and of undoped ST is close to 97% has been chosen for preparation of all the ceramic samples.

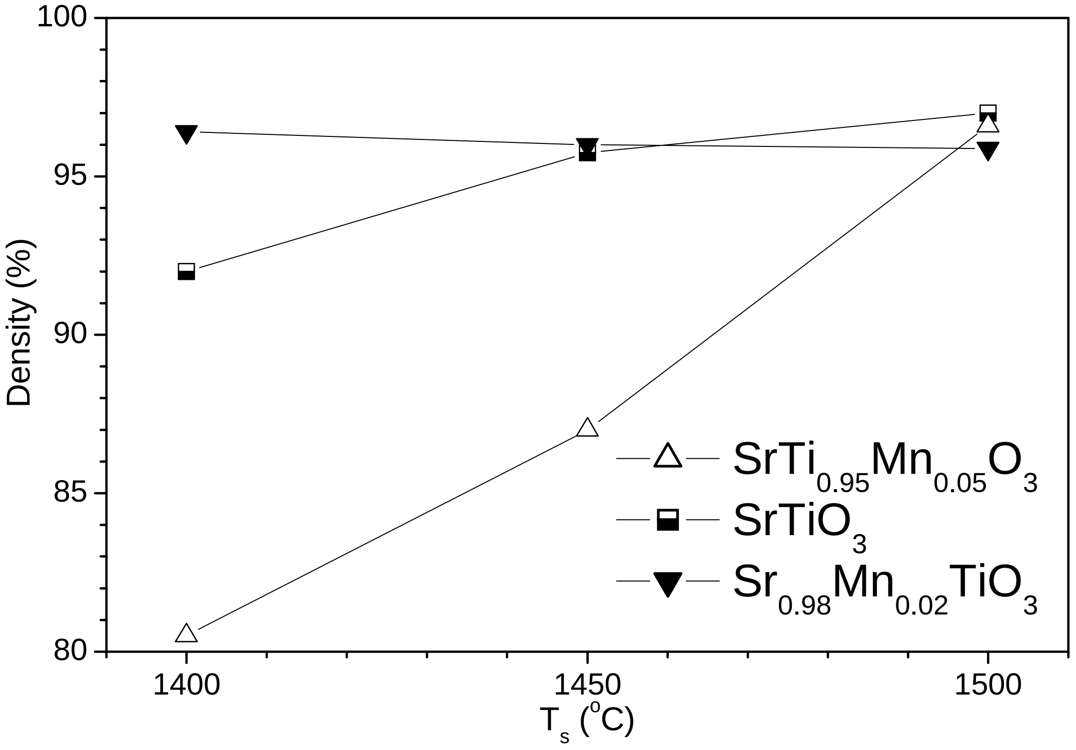

FIGURE 4.1. Relative density as a function of sintering temperature for $SrTiO_3$, $Sr_{0.98}Mn_{0.02}TiO_3$ and $SrTi_{0.95}Mn_{0.05}O_3$ ceramics sintered for 5 hours.

Table 4.1 shows the measured density (D), theoretical density (D_t) and relative density (D_r) of $Sr_{1-x}Mn_xTiO_3$ and $SrTi_{1-y}Mn_yO_3$ ceramics sintered in air at 1500 °C for 5 hours. D was measured by the Archimede's method and D_t was calculated as follows:

$$D_t = [(1 - x)\times M(Sr) + x\times M(Mn) + M(Ti) + 3\times M(O)]/(N_A\times a^3) \qquad \text{for SMnT} \qquad (4.4a)$$

$$D_t = [M(Sr) + (1 - y)\times M(Ti) + y\times M(Mn) + 3\times M(O)]/(N_A\times a^3) \qquad \text{for STMn} \qquad (4.4b)$$

where M(Sr) = 87.62 g/mol, M(Mn) = 54.938 g/mol, M(Ti) = 47.9 g/mol and M(O) = 15.9994 g/mol are molar masses of Sr, Mn, Ti and O respectively, $N_A = 6.022\times10^{-23}$ mol^{-1} is Avogadro number and a is lattice parameter in cm, obtained from XRD spectra (see the following subsection). As seen from the Table 4.1 the relative densities of the samples are superior to 94.3%. Density of $Sr_{0.98}Mn_{0.02}TiO_3$ ceramic samples sintered in oxygen and in nitrogen is close to that of the corresponding samples sintered in air.

Table 4.1. Measured (D), theoretical (D_t) and relative densities (D_r) of $Sr_{1-x}Mn_xTiO_3$ and $SrTi_{1-y}Mn_yO_{3-\delta}$ ceramics sintered in air at 1500 °C for 5 hours.

x	D (g/cm^3)	D_t (g/cm^3)	D_r	y	D (g/cm^3)	D_t (g/cm^3)	D_r
0	4.96	5.11	97.0%	0	4.96	5.11	97.0%
0.0025	4.95	5.11	96.8%	0.01	4.96	5.12	96.9%
0.005	5.00	5.11	97.8%	0.05	4.97	5.15	96.6%
0.01	4.98	5.11	97.5%	0.10	4.97	5.17	96.1%
0.02	4.89	5.10	95.9%	0.15	4.96	5.18	95.7%
0.03	4.86	5.09	95.4%				
0.05	4.78	5.07	94.3%				
0.10	4.57	-*	-*				

* multiphases

4.2. Crystal structure and lattice parameter

4.2.1. XRD results

X-ray-diffraction data of Mn-doped ST is presented in Figure 4.2: $Sr_{1-x}Mn_xTiO_3$ system in Figure 4.2a and $SrTi_{1-y}Mn_yO_3$ system in Figure 4.2b.

As shown in Figure 4.2a, ceramics of $Sr_{1-x}Mn_xTiO_3$ with x up to 0.05 reveal a single-phase cubic perovskite structure, similar to $SrTiO_3$, shown in Figure 4.2a for comparison. Second phase features start to appear in XRD profiles at $x = 0.10$ and are clearly seen for $x = 0.15$. These features are consistent with the $MnTiO_3$ spectra, also shown in Figure 4.2a for comparison.

The lattice parameter a, extracted by Rietveld refinement of XRD profiles of single-phase samples, is presented in Figure 4.3 as a function of Mn content x. Increasing of x leads to a decrease of a, which can be described by a linear Vegard law with the slope $da/dx \approx 0.027$ Å. Such behaviour can be expected from the ionic size considerations. Mn^{2+} ionic radius value, extrapolated to the coordination number 12 from the values obtained by Shannon (1976) for smaller coordination numbers, is 1.27 Å, that is smaller than 1.44 Å of Sr^{2+}. Values of the lattice parameter for the samples prepared from $Mn(NO_3)_2$ precursor do not change the slope of the line. Lattice parameters of $Sr_{0.98}Mn_{0.02}TiO_3$ ceramics sintered in different atmospheres were found to be very similar.

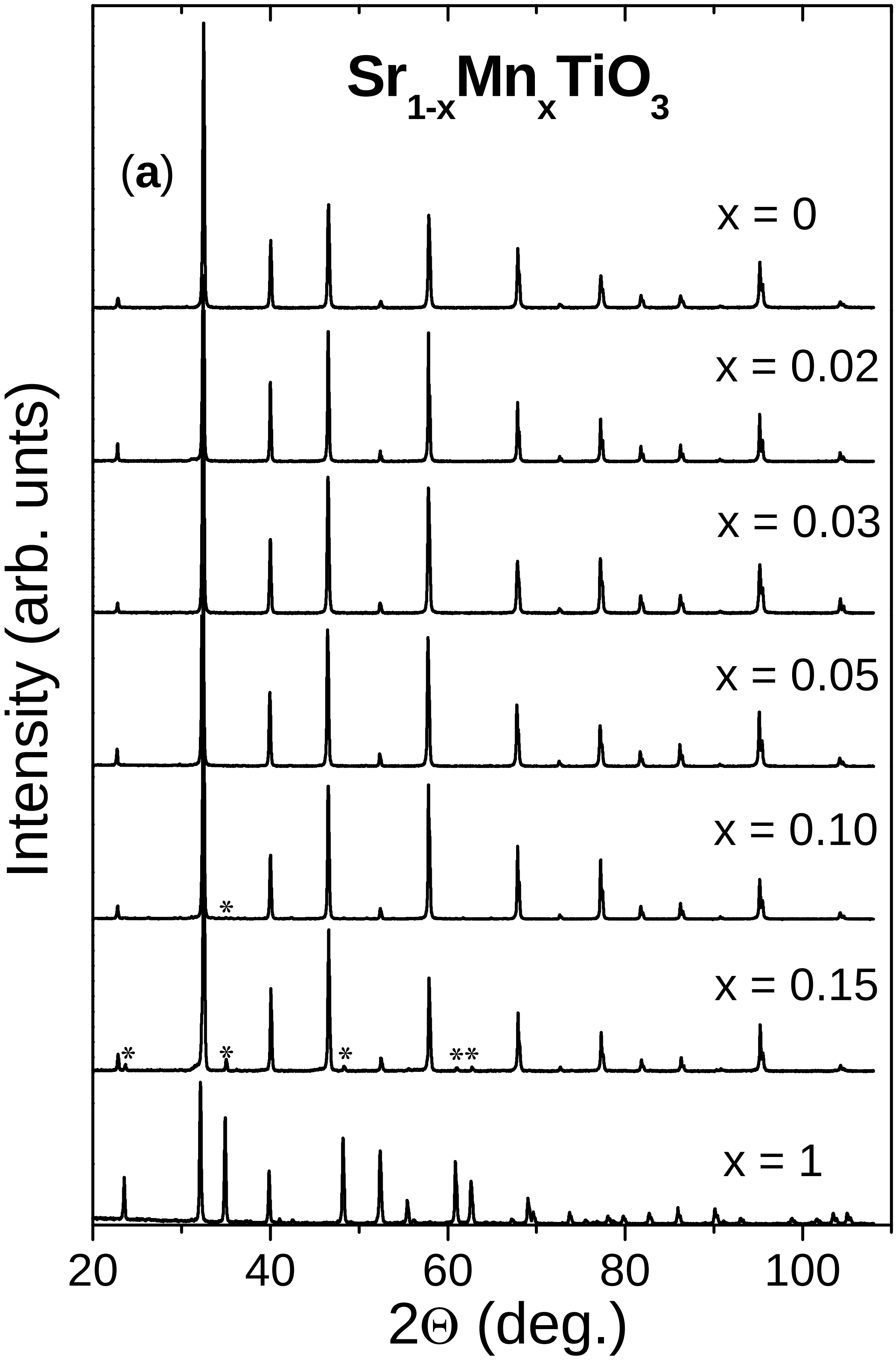

FIGURE 4.2. **a** - XRD profiles of sintered SMnT ceramics (* denotes $MnTiO_3$ phase).

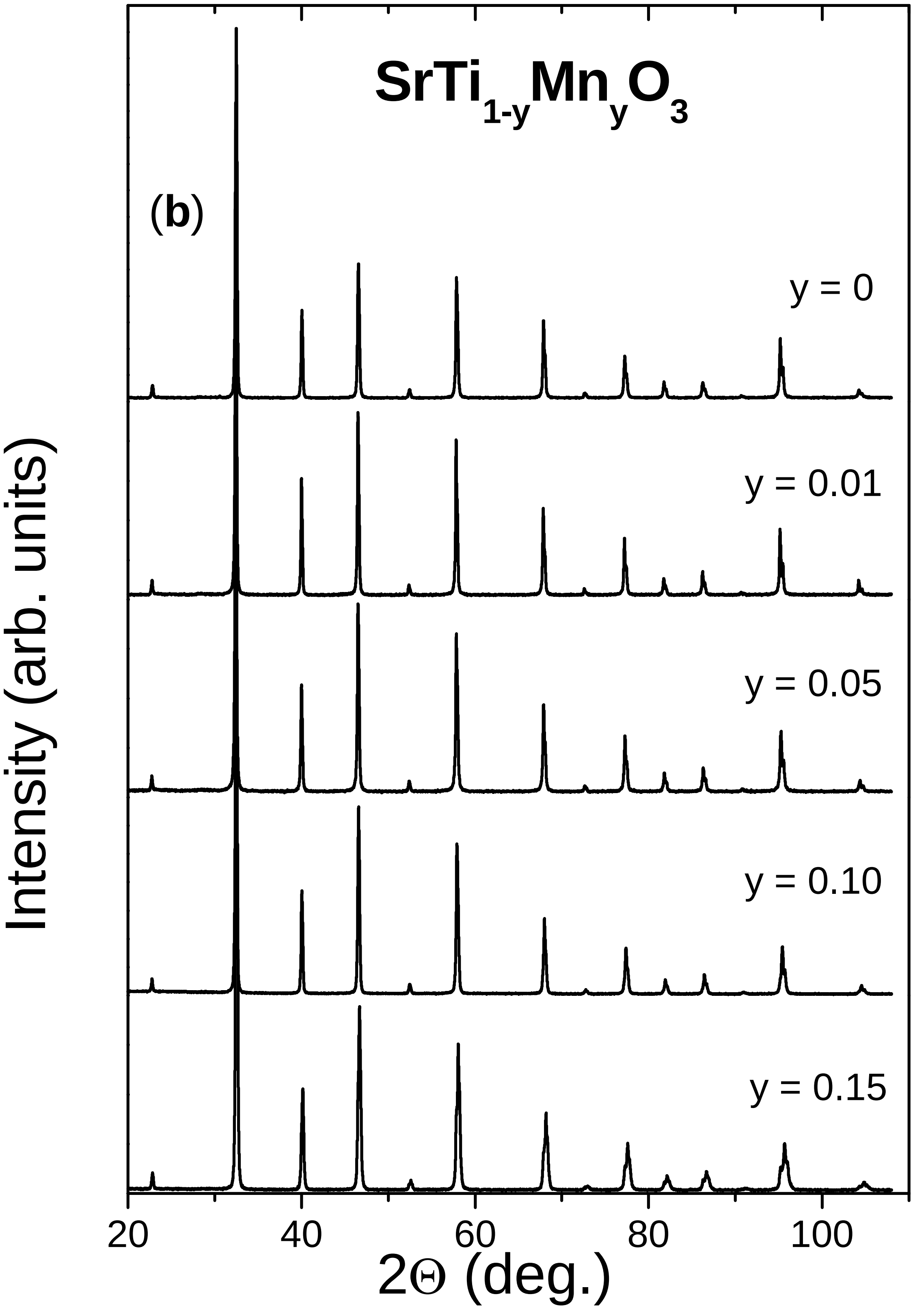

FIGURE 4.2. **b** - XRD profiles of sintered STMn ceramics.

Figure 4.2b presents the XRD profiles for sintered samples of $SrTi_{1-y}Mn_yO_3$ system, exhibiting cubic crystallographic structure similar to undoped ST. No second phase was observed in Mn concentration range under study. The lattice parameter *a* decreases linearly with increasing Mn content with the slope $da/dy \approx 0.1$ Å, as shown in Figure 4.3. Such a behaviour of the lattice parameter is an evidence of that Ti^{4+} with ionic radius of 0.605 Å is preferably substituted by Mn^{4+} with ionic radius of 0.53 Å, and not by reduced Mn^{3+} (0.645 Å) or Mn^{2+} (0.83 Å) (Shannon, 1976).

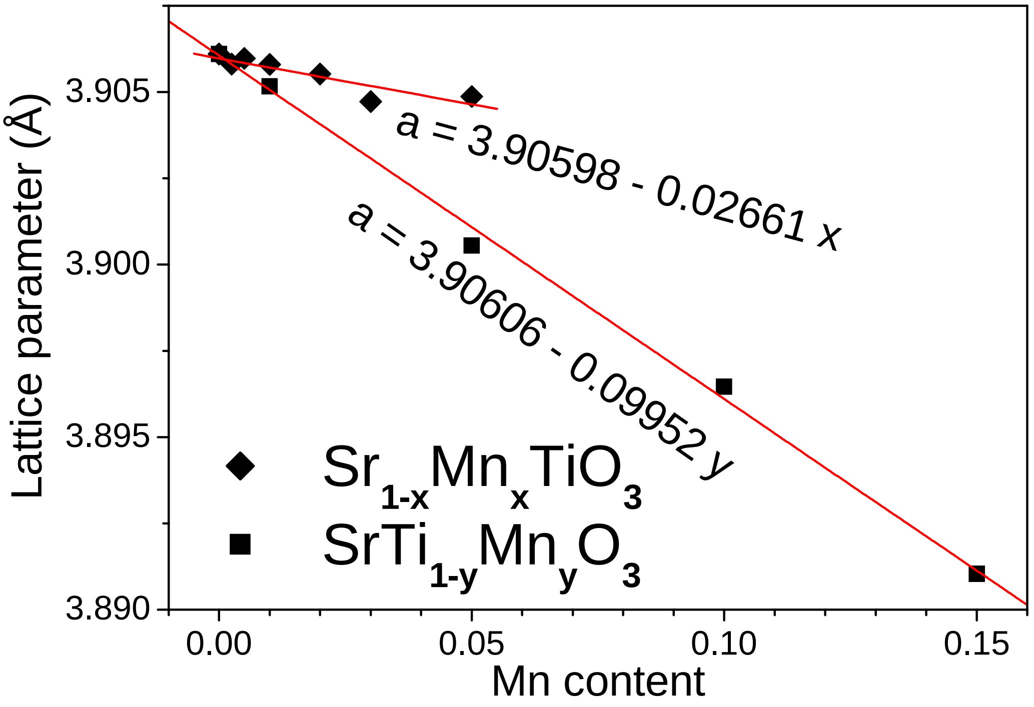

FIGURE 4.3. Lattice parameter of sintered SMnT and STMn ceramics as a function of Mn content.

4.2.2. Raman spectroscopy results

Micro-Raman spectra of SMnT (x = 0.005 and 0.05) and STMn (y = 0.01 and 0.05) ceramic samples are shown in Figure 4.4 for temperatures of 300, 150 and 80 K.

Considering the SMnT spectra, presented in Figures 4.4 (a, b), three modes are observed on background of second-order features at room temperature. Two of them (at 172 and 80 cm^{-1}, respectively) might be indicative of the transverse optic phonon modes TO_2 and TO_1, similarly to undoped ST, although an increase of the intensity of the latter mode, TO_1, with Mn content might imply a superposition with an additional mode, related to the Mn incorporation into the A site of ST perovskite lattice. The third mode (at ~752 cm^{-1}), which intensity increases also with Mn content, is evidently not related with the lattice dynamics of undoped ST, but rather related to the vibrations of Mn ions in the perovskite lattice. As the temperature is decreased to 150 K, more two IR-active TO_4 and LO_4 modes (at 546 and 792 cm^{-1}, respectively) become visible on the spectra of SMnT and undoped ST (see Chapter 3). All the first-order modes strengthen on further cooling down to 80 K. It is worthwhile to mention that while the soft TO_1 mode of undoped ST moved from 80 cm^{-1} towards 0 cm^{-1} with the temperature decrease, moving out from the experimental frequency range, for SMnT the mode at 80 cm^{-1} does not reveal any appreciable temperature dependence, just an anomalous increase in the intensity. This fact confirms the relation of the vibration modes with the Mn incorporation at Sr-site. In addition, the R-modes (at 144 and 447 cm^{-1}), characteristic of undoped ST below its structural phase transition at T_a = 105-110 K, are clearly observed in the 80-K Raman spectra of SMnT and ST. However, the spectrum of $Sr_{0.95}Mn_{0.05}TiO_3$ ceramics (see Figure 4.4b) reveals R-modes already at 150 K, pointing to the raising of the temperature of the structural phase transition T_a.

Considering now STMn, the Raman spectrum of $SrTi_{1-y}Mn_yO_3$ sample with y = 0.05 was found to be very different from those of undoped $SrTiO_3$ and SMnT at all the studied temperatures. Almost all the lines, typical for ST, became uncertain or overlapped with other adjacent lines, as clearly shown in Figures 4.4 (c, d). Thus, three strong and temperature-independent modes, marked in Figure 4.4d as X_2, X_3 and X_4 (at 754 cm^{-1}, 527 cm^{-1} and 479 cm^{-1}, respectively) are seen in Raman spectra of $SrTi_{0.95}Mn_{0.05}O_3$, overlapping the LO_4 and TO_4 lines of $SrTiO_3$. Such considerable transformation of the spectra indicates a strong effect of Mn substitution at the Ti-site on the lattice dynamics of ST, although the nature of the X-modes is still unclear and requires further investigations. The position of X_2 mode is close to that of the mode induced by Mg substitution at the Ti-site in Mg-doped ST ceramics and attributed to a simultaneous shrinkage and expansion of the neighbouring oxygen octahedra with different ions in the centre, i.e., to a “breathing” mode, observed in Chapter 3. In addition, for $SrTi_{0.95}Mn_{0.05}O_3$ sample, R-modes are not clearly detectable even at 80 K, i.e., Ti-site Mn doping reduces the T_a. The Raman spectra of $SrTi_{0.99}Mn_{0.01}O_3$ ceramics, presented in Figure 4.4.c are intermediate between those of ST and $SrTi_{0.95}Mn_{0.05}O_3$, revealing weakened X-modes.

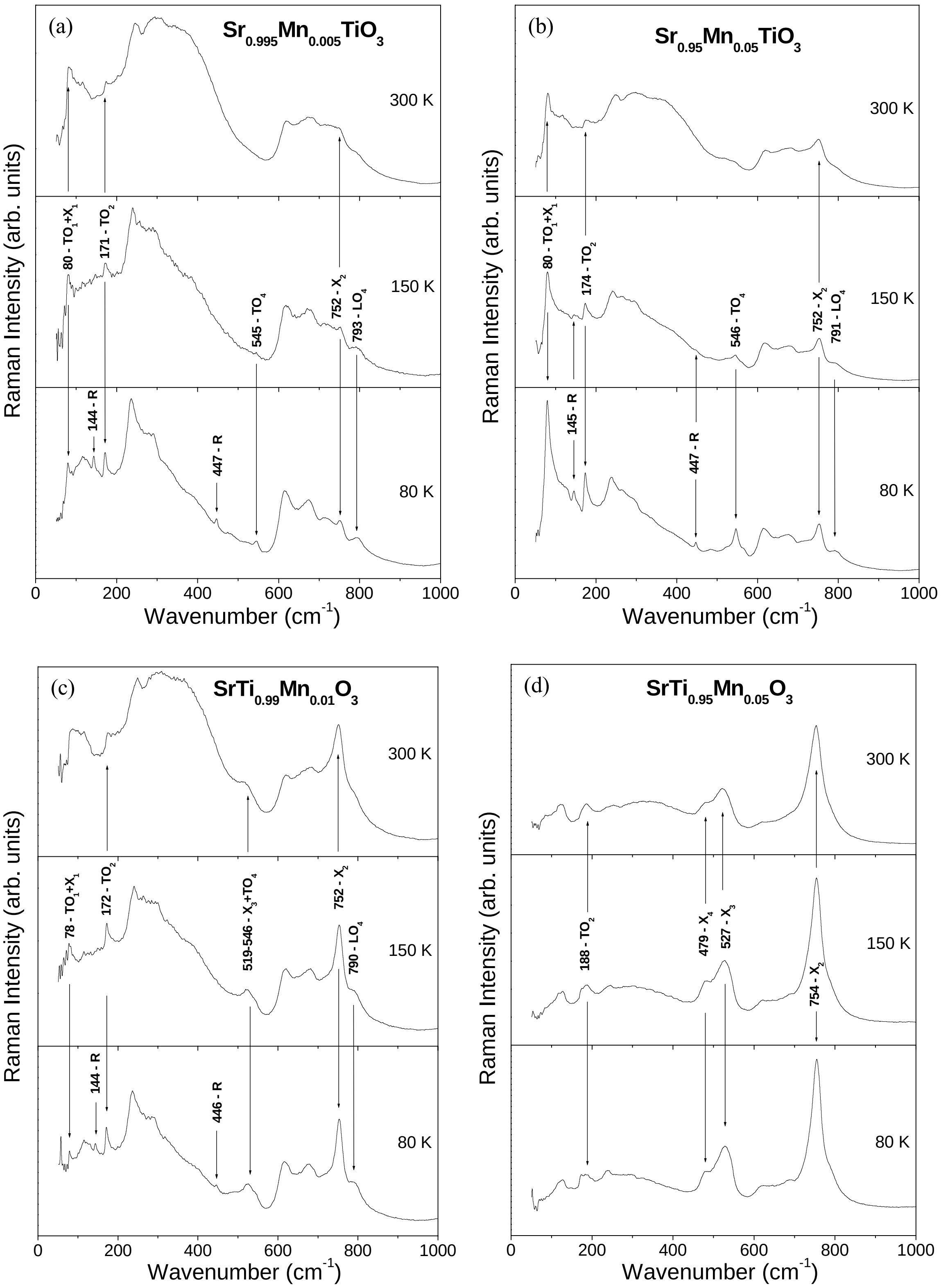

FIGURE 4.4. Raman spectra of $Sr_{0.995}Mn_{0.005}TiO_3$ (**a**), $Sr_{0.95}Mn_{0.05}TiO_3$ (**b**), $SrTi_{0.99}Mn_{0.01}O_3$ (**c**) and $SrTi_{0.95}Mn_{0.05}O_3$ (**d**) ceramics at 300, 150 and 80 K with indication of the approximate mode position in cm^{-1}.

4.3. Microstructure

4.3.1. Microscopic morphology and grain size

SEM micrographs of $Sr_{1-x}Mn_xTiO_3$ ceramic samples (x = 0.0025-0.05) sintered in air at 1500 ºC for 5h are presented in Figure 4.5 (a-f).

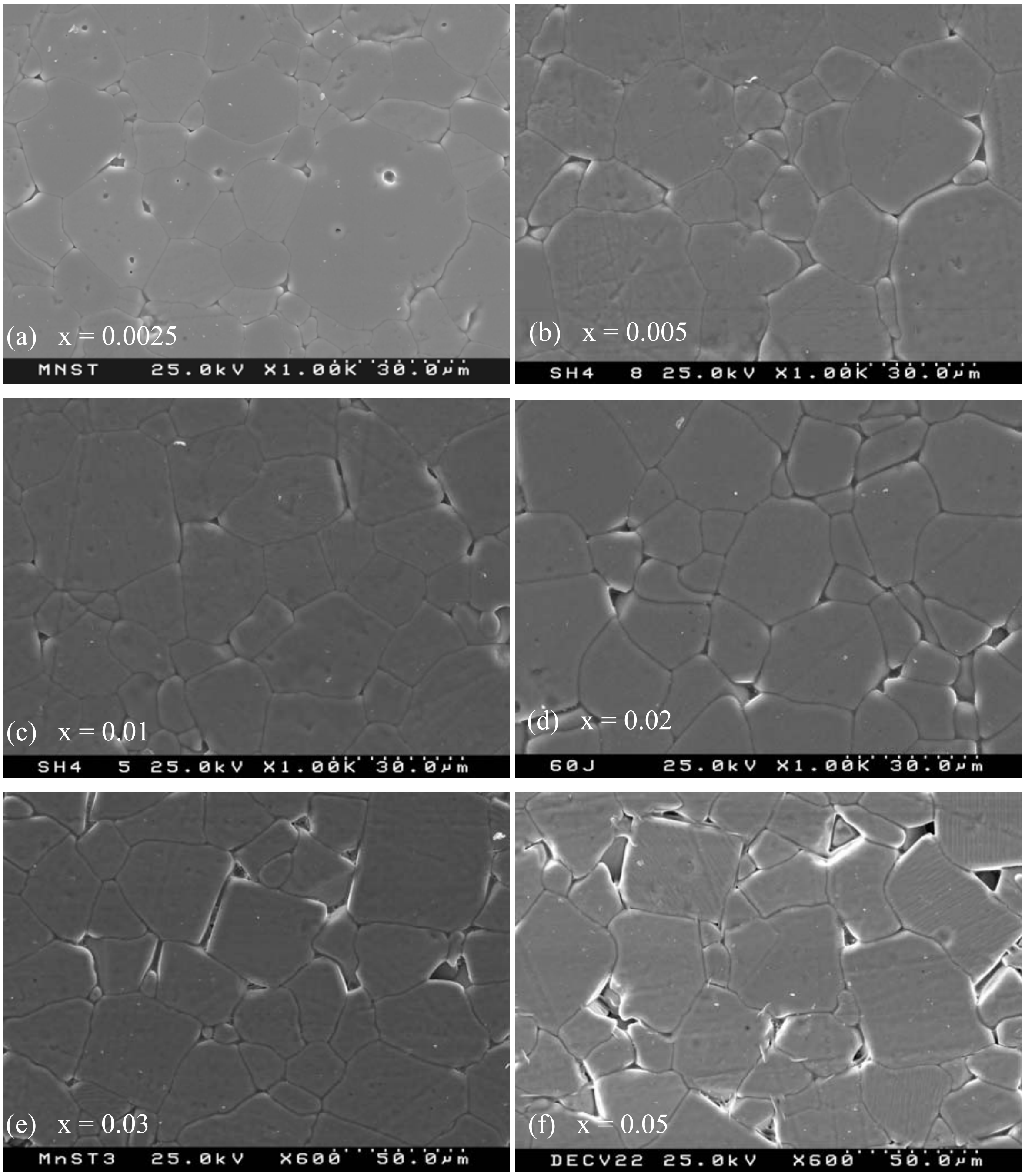

FIGURE 4.5. SEM micrographs of $Sr_{1-x}Mn_xTiO_3$ ceramics with x = 0.0025 (**a**), 0.005 (**b**), 0.01 (**c**), 0.02 (**d**), 0.03 (**e**) and 0.05 (**f**) sintered in air at 1500 ºC for 5 h.

Figure 4.6 shows the images of $Sr_{0.98}Mn_{0.02}TiO_3$ ceramics sintered in nitrogen and in oxygen. All the SEM micrographs reveal dense microstructure with average grain size 27.5±7.5 µm. No appreciable differences in the grain size were observed with the introduction of Mn in ST, as shown in Table 4.2. No marked microstructural variations were detected for $Sr_{0.98}Mn_{0.02}TiO_3$ ceramic samples sintered in different atmospheres.

Dense and homogeneous microstructure was also observed in SEM micrographs of $SrTi_{1-y}Mn_yO_3$ ceramics, exemplified by compositions with $y = 0.01$ and 0.05 in Figure 4.7. However, a marked decrease of the average grain size was observed for Ti-site Mn-doped ST ceramics, similarly to Ti-site Mg-doped ST (see Chapter 3). As also shown in Table 4.2, average grain size of STMn ceramics lies in the range of 0.7±0.1µm. It should be remarked that this difference in the grain growth behaviour is similar to that of Mg-doped ST ceramics and might be related to the variations of the Sr/Ti ratio.

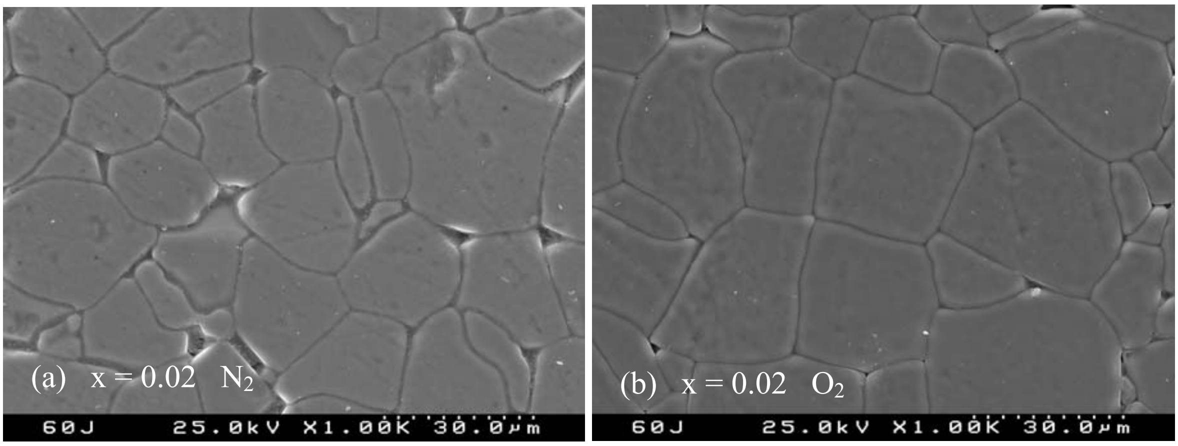

FIGURE 4.6. SEM micrographs of $Sr_{0.98}Mn_{0.02}TiO_3$ ceramics sintered in nitrogen (**a**) and in oxygen (**b**) at 1500 ºC for 5 h.

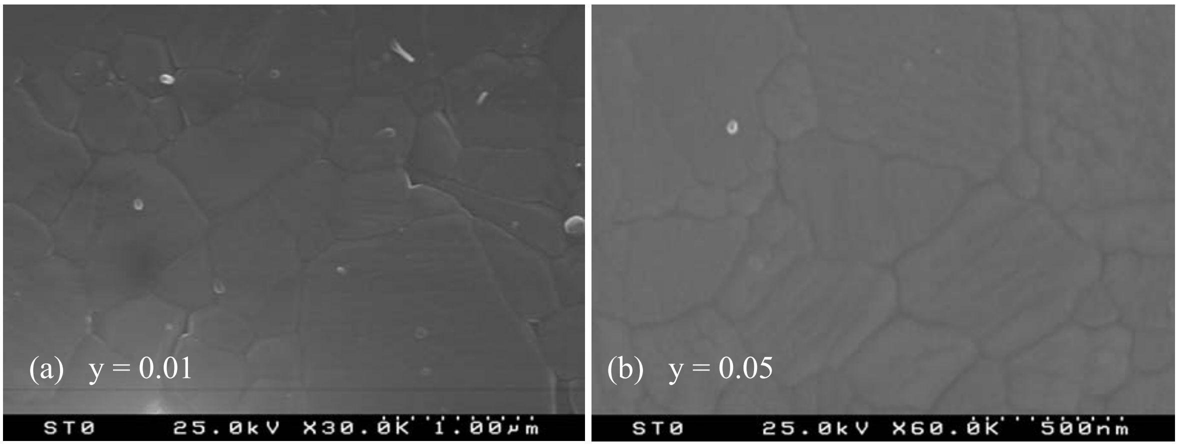

FIGURE 4.7. SEM micrographs of $SrTi_{1-y}Mn_yO_3$ ceramics with $y = 0.01$ (**a**) and 0.05 (**b**).

Table 4.2. Average grain size G of $Sr_{1-x}Mn_xTiO_3$ and $SrTi_{1-y}Mn_yO_3$ ceramics sintered at 1500 °C for 5 hours.

x	G (μm)	*y*	G (μm)
0.0025	20	0.01	0.8
0.005	24	0.05	0.6
0.01	20	0.10	0.7
0.02	32	0.15	0.6
0.03	35		
0.05	34		

4.3.2. Distribution of elements

The X-ray mapping over several grains and grain boundaries, presented in Figures 4.8-4.11, was performed by SEM / EDS on ceramic samples of selected $Sr_{1-x}Mn_xTiO_3$ and $SrTi_{1-y}Mn_yO_3$ compositions.

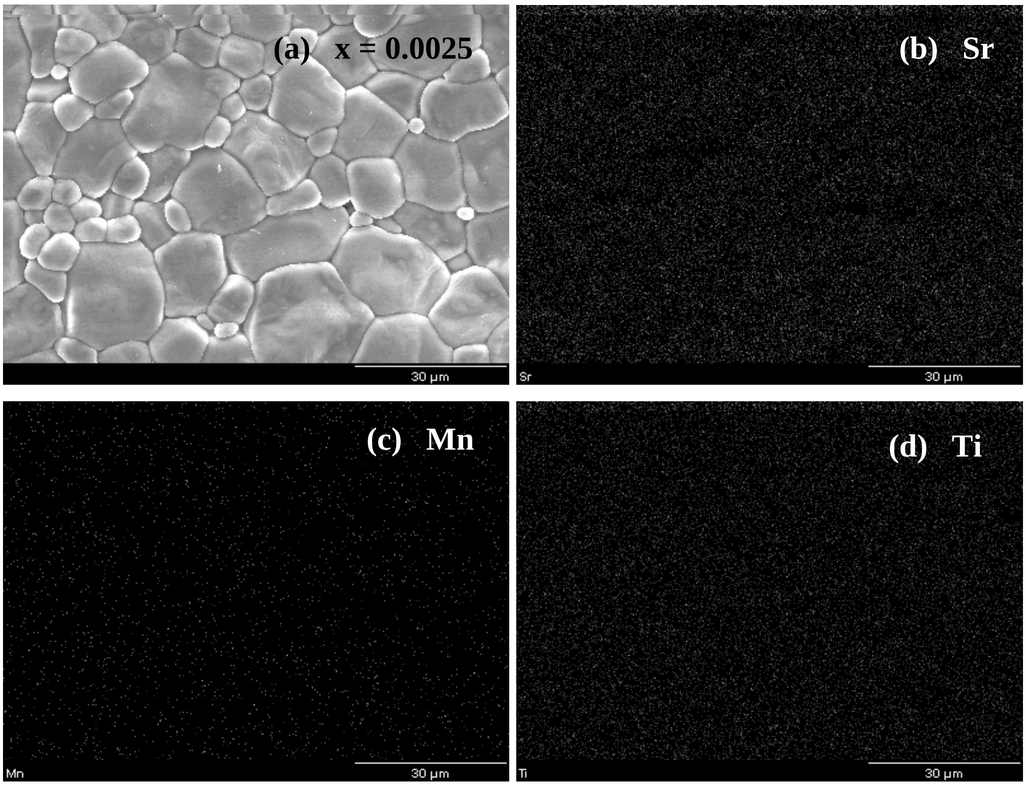

FIGURE 4.8. SEM micrograph (**a**) and corresponding elemental X-ray maps of Sr (**b**), Mn (**c**) and Ti (**d**) for $Sr_{0.9975}Mn_{0.0025}TiO_3$ ceramics.

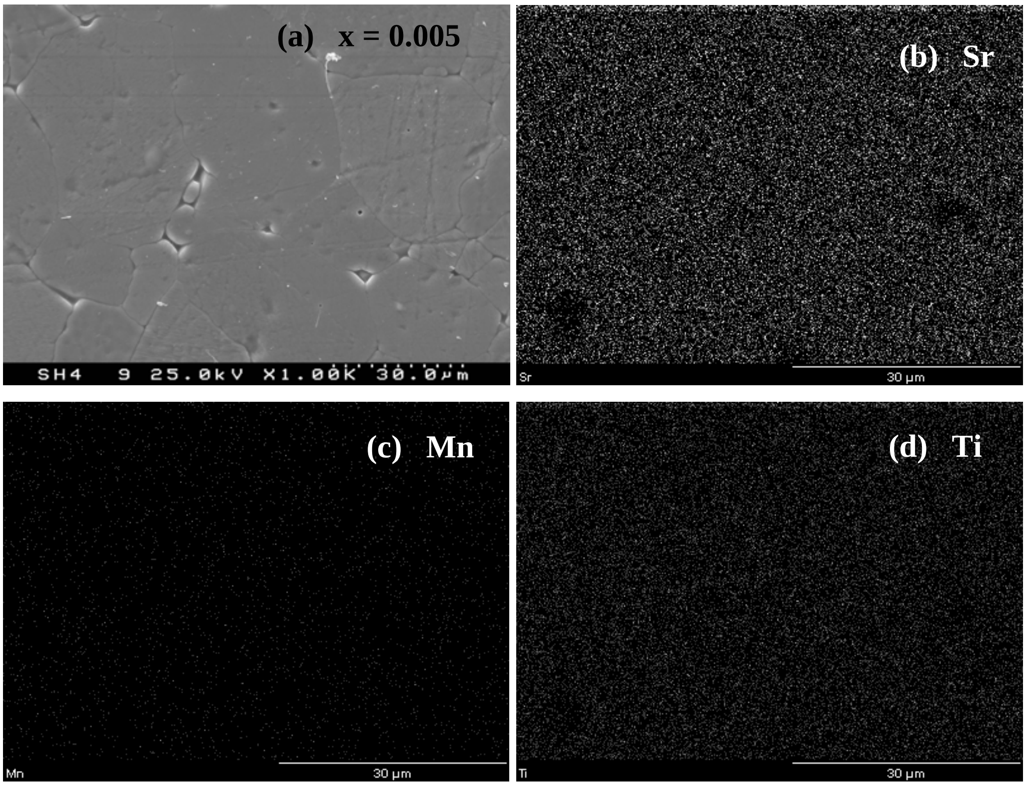

FIGURE 4.9. SEM micrograph (**a**) and corresponding elemental X-ray maps of Sr (**b**), Mn (**c**) and Ti (**d**) for $Sr_{0.995}Mn_{0.005}TiO_3$ ceramics.

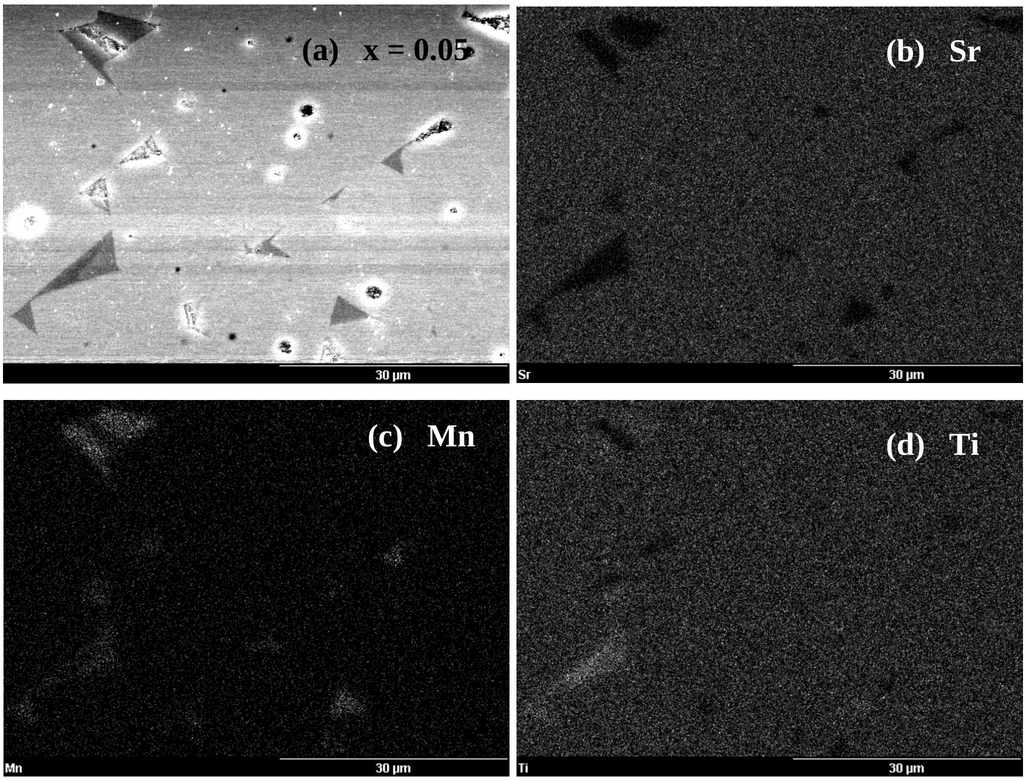

FIGURE 4.10. SEM micrograph (**a**) and corresponding elemental X-ray maps of Sr (**b**), Mn (**c**) and Ti (**d**) for $Sr_{0.95}Mn_{0.05}TiO_3$ ceramics.

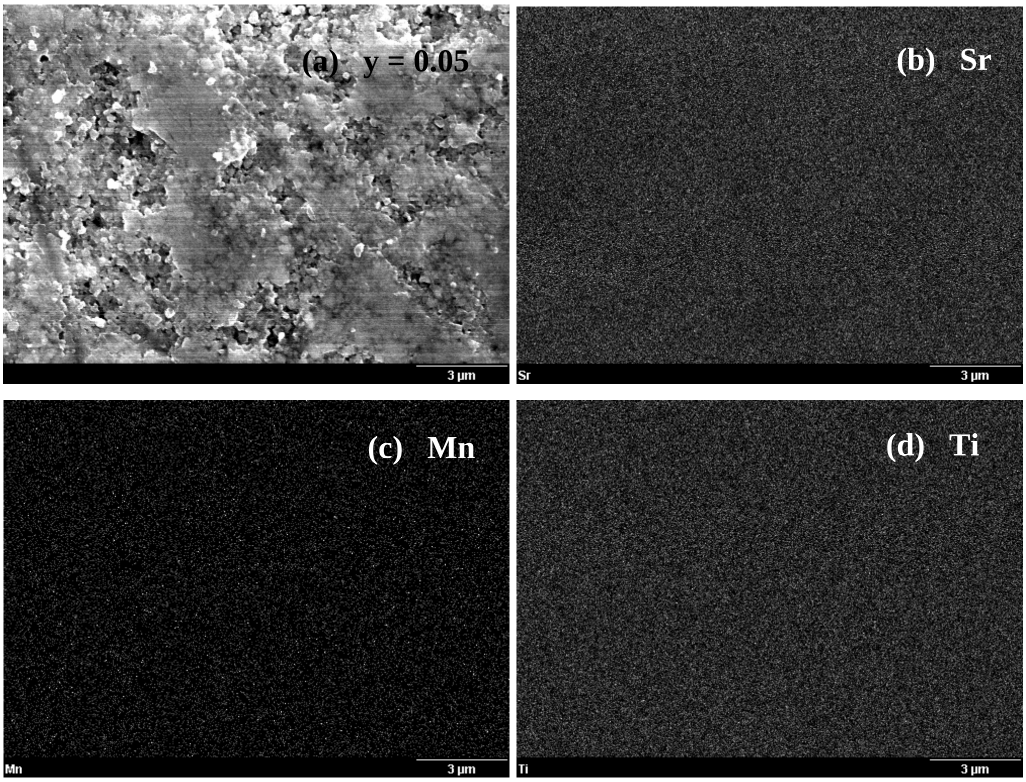

FIGURE 4.11. SEM micrograph (**a**) and corresponding elemental X-ray maps of Sr (**b**), Mn (**c**) and Ti (**d**) for $SrTi_{0.95}Mn_{0.05}O_3$ ceramics.

The X-ray maps of Sr, Mn and Ti elements for $Sr_{1-x}Mg_xTiO_3$ compositions with x = 0.0025, 0.005 and 0.05 are shown in Figures 4.8, 4.9 and 4.10, respectively. No segregation of Mn was detected for $Sr_{0.9975}Mg_{0.0025}TiO_3$ and for $Sr_{0.995}Mg_{0.005}TiO_3$, but intensive spots in the map of Mn corresponding the grain boundaries in SEM micrograph, indicate the segregations of Mn at x as high as 0.05.

The X-ray maps of the elements for $SrTi_{0.95}Mn_{0.05}O_3$ composition are presented in Figure 4.11. Homogeneous distribution of Sr, Mn and Ti and no visible segregation of these elements, either in grains or in grain boundaries, was detected, although submicron grains and grain boundaries will be better investigated with TEM due to its high resolution.

4.3.3. Local microstructure and chemical analysis

The microstructure of Mn-doped ST ceramics was also examined by TEM. TEM bright field images of $Sr_{1-x}Mn_xTiO_3$ with x = 0.005, 0.02 and 0.05 and of $SrTi_{1-y}Mn_yO_3$ with y = 0.05 and 0.15 ceramic samples are shown in Figure 4.12 (a, b, c) and 4.13 (a, b), respectively. Their local structure was analysed by electron diffraction (ED) and chemical compositions by EDS. The energy dispersive spectra of SMnT and STMn ceramics are shown in Figures 4.14 and 4.15, respectively.

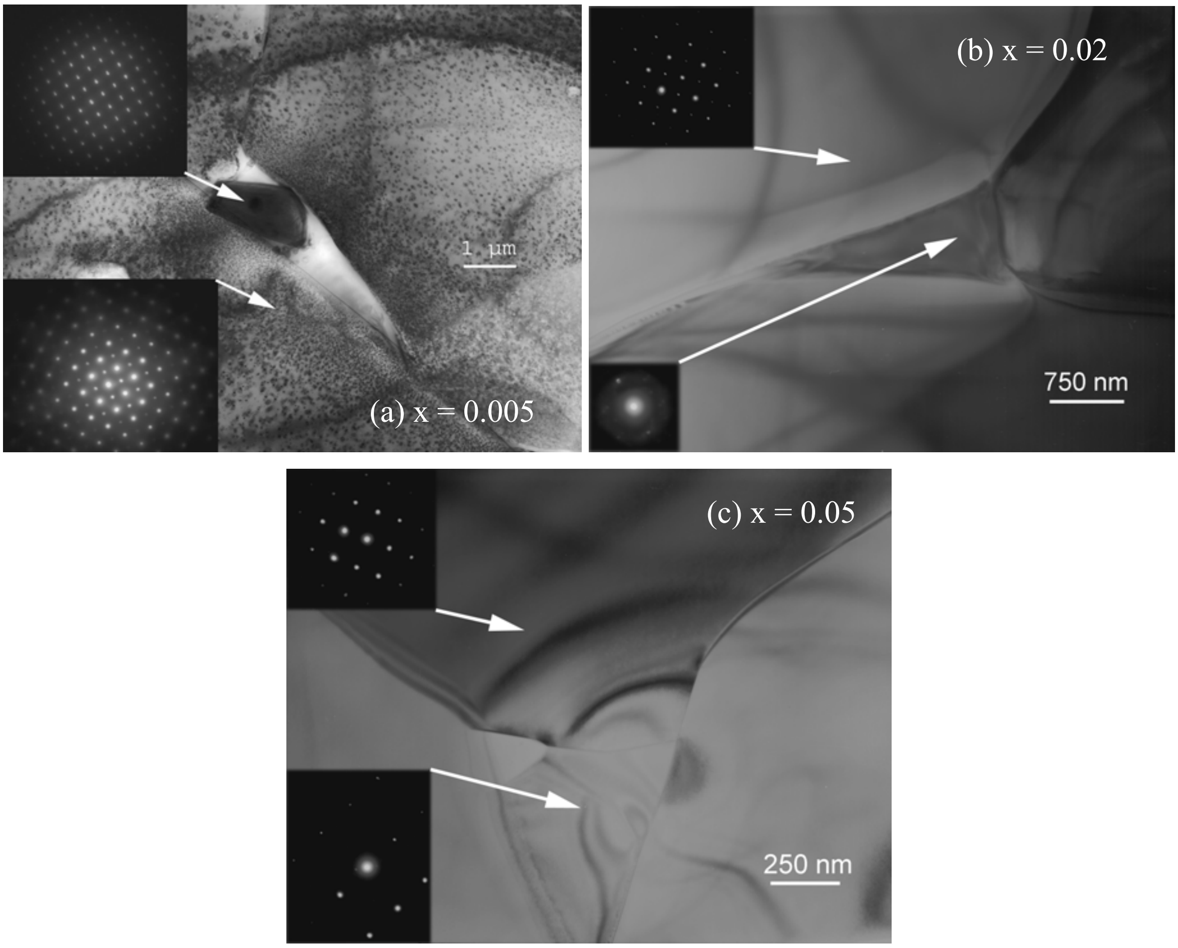

FIGURE 4.12. TEM micrographs of: $Sr_{0.995}Mn_{0.005}TiO_3$ ceramics (**a**) with insets of ED patterns for big and small crystalline perovskite grains (in bottom and top corners respectively); $Sr_{0.98}Mn_{0.02}TiO_3$ ceramics (**b**) with insets of ED patterns for crystalline perovskite grains (in top corner) and for amorphous grain junctions (in bottom corner); $Sr_{0.95}Mn_{0.05}TiO_3$ ceramics (**c**) with inset of ED patterns for crystalline perovskite grains (in top corner) and for crystalline non-perovskite grain (in bottom corner).

TEM images of SMnT ceramics, presented in Figure 4.12 (a-c), reveal sharp grain boundaries, confirming also the predominance of the over-micron-sized grains observed by SEM. ED patterns of such grains reflect the perovskite-type structure, as shown in the insets of Figure 4.12 (a-c). Moreover, their energy dispersive spectra are close to that of $SrTiO_3$ with additional small (but detectable) Mn peak, as presented in Figure 4.14a. In addition, $Sr_{0.995}Mn_{0.005}TiO_3$ ceramics reveals small grains shown in Figure 4.12a with a perovskite structure, as confirmed by ED pattern in the top inset of Figure 4.12a, similarly to undoped ST (see Chapter 3). No second phase was observed for $Sr_{0.995}Mn_{0.005}TiO_3$ and $Sr_{0.98}Mn_{0.02}TiO_3$ ceramic samples, apart from the small amorphous inclusions rich in Sr and Zr with trace amounts of Mn located in few triple points (see Figures 4.14b, 4.12b and bottom inset). Zr contamination might appear during the milling step.

Thus, for $Sr_{1-x}Mn_xTiO_3$ ceramics, TEM equipped with the EDS analysis confirmed the incorporation of Mn into ST grains and the absence of any second crystalline phases for $x \leq 0.02$, as shown in Figures 4.12 (a, b) and 4.14a. In particular, titanium oxide extra-phase, expected if Mn ions would occupy B site of the perovskite lattice, was not detected, supporting the assumption that Mn occupies Sr site.

However, under-micron-sized grains with a non-perovskite structure were clearly detected in SMnT ceramics with $x = 0.03$ and 0.05, as shown in Figure 4.12c and bottom inset for $Sr_{0.95}Mn_{0.05}TiO_3$ sample. Spectra obtained by EDS for this phase shown in Figure 4.14c for $Sr_{0.97}Mn_{0.03}TiO_3$ sample reveal almost equivalent peaks of Mn and Ti, suggesting the presence of $MnTiO_3$ phase, which is known to have an ilmenite-type structure. TEM and the complementary ED and EDS analyses of SMnT ceramics indicate that the formation of $MnTiO_3$ phase starts from $x = 0.03$. This value is thought to be the solid solubility limit of Mn in Sr site of ST, which is lower than the one obtained from XRD data and the value reported by Lemanov et al. (2004).

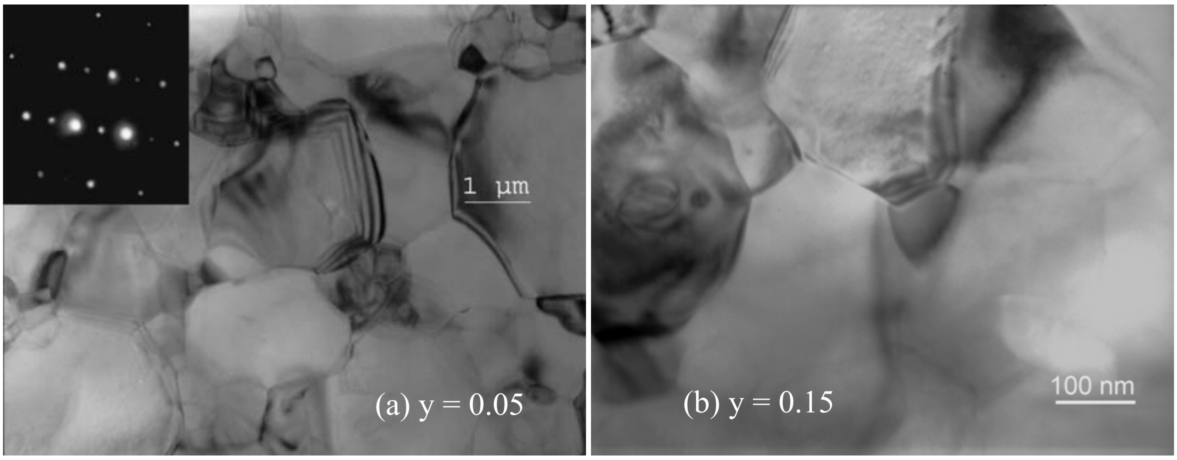

FIGURE 4.12. TEM micrographs of $SrTi_{0.95}Mn_{0.05}O_3$ ceramics (**a**) with inset of ED pattern for crystalline perovskite grains, and of $SrTi_{0.85}Mn_{0.15}O_3$ ceramics (**b**).

Clean grain boundaries and solely perovskite grains of submicron size were observed by TEM in $SrTi_{1-y}Mn_yO_3$ ceramics, whereas Mn incorporation into the lattice was supported by the evident peak in energy dispersive spectra of STMn grains, as shown in Figures 4.13 and 4.15 for $SrTi_{0.95}Mn_{0.05}O_3$ and $SrTi_{0.85}Mn_{0.15}O_3$ samples. Therefore, high solid solubility of Mn in Ti sites of ST, concluded from XRD data, was confirmed by TEM studies.

Thus, in STMn ceramic samples, Mn incorporation into ST grains was evidenced by the absence of Sr-containing second phase and by the energy dispersive spectra of STMn ceramic grains in which Mn peak was clearly observed. This confirms that Mn occupies the Ti site, but not the Sr site of ST.

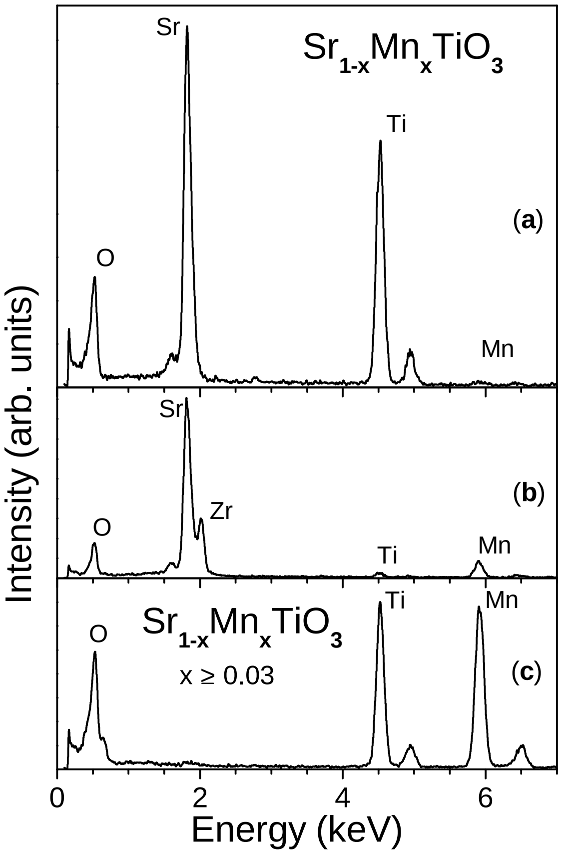

FIGURE 4.14. Typical spectra obtained by TEM-EDS on grains (**a**) and grain-boundary glass phase (**b**) of SMnT ceramics, and on grain-boundary crystalline phase of SMnT ceramics with Mn content ≥ 0.03 (**c**).

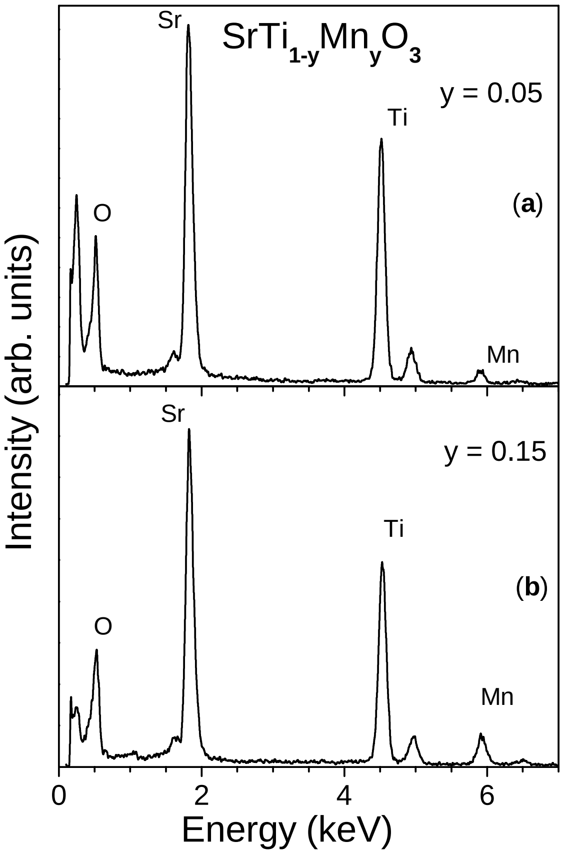

FIGURE 4.15. Spectra obtained by TEM-EDS on crystalline perovskite grains of $SrTi_{1-y}Mn_yO_3$ ceramics with $y = 0.05$ (**a**) and 0.15 (**b**).

In order to deep the structural analysis and to study the effect of Mn doping on the structural phase transition of strontium titanate, in situ cold-stage ED / TEM technique was used on $Sr_{1-x}Mn_xTiO_3$ and $SrTi_{1-y}Mn_yO_3$ ceramics. Figures 4.16 and 4.17 illustrate the electron diffraction patterns with the electron beam parallel to a <110> pseudocubic direction obtained for $Sr_{0.975}Mn_{0.025}TiO_3$ and $SrTi_{0.95}Mn_{0.05}O_3$ samples, respectively. From Figure 4.16, the superlattice reflections at the $<110>_p$ zone axis diffraction patterns, related to the tilting of oxygen octahedra, were detected up to ~200 K for SMnT sample, i.e., the temperature of the structural phase transition is significantly shifted upwards. This observation is in accordance with the Raman result, in which the R mode is observed at 150 K for $Sr_{0.95}Mn_{0.05}TiO_3$ sample (Figure 4.4b). The Mn content of $x = 0.025$ is very close to the solid solubility limit for $Sr_{1-x}Mn_xTiO_3$ system and consequently reveals a maximum effect of the A-site Mn doping on the behaviour of ST.

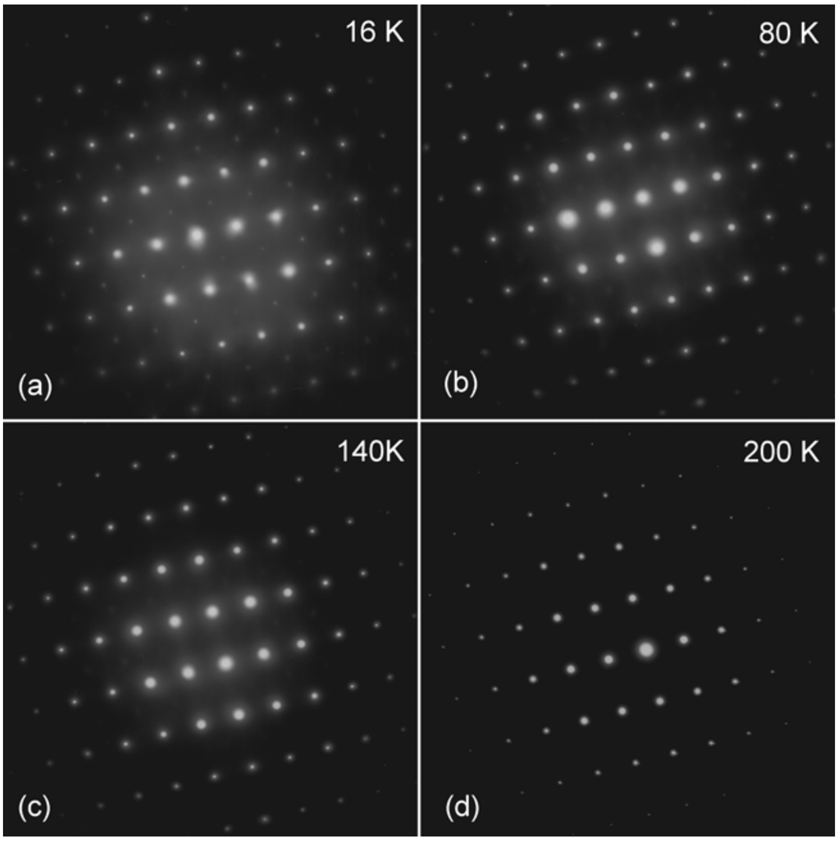

FIGURE 4.16. $<110>_p$ zone axis electron diffraction patterns of $Sr_{0.975}Mn_{0.025}TiO_3$ ceramics at 16 (**a**), 80 (**b**) 140 (**c**) and 200 K (**d**).

On the other hand, for nominal Mn content of $x = 0.05$, which is above the solid solubility limit, the real Mn content in the SMnT ceramic grains is also above solubility limit value. Hence, the temperature dependence of the electron diffraction patterns for

$Sr_{0.975}Mn_{0.025}TiO_3$ ceramics can be compared with ST-related features of Raman spectra of $Sr_{0.95}Mn_{0.05}TiO_3$. For $SrTi_{0.95}Mn_{0.05}O_3$ sample, the superlattice reflections at the $<110>_p$ zone axis electron diffraction patterns were detected only up to T ~80 K, as shown in Figure 4.17, in agreement with the Raman spectroscopy results (Figure 4.4d). This indicates that the oxygen octahedral tilting was suppressed at low temperatures for the B-site doped samples. Thus, the TEM-ED results, obtained at cold stage, are consistent with those of Raman spectroscopy for both A-site and B-site doped samples.

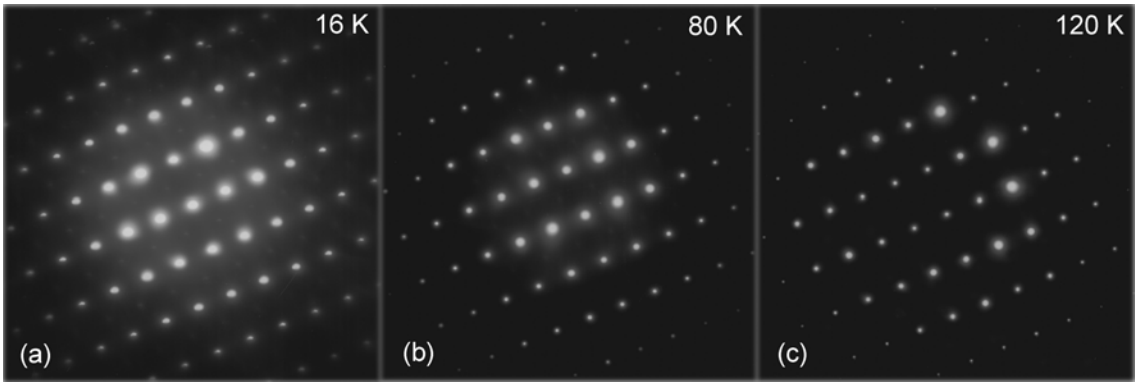

FIGURE 4.17. $<110>_p$ zone axis electron diffraction patterns of $SrTi_{0.95}Mn_{0.05}O_3$ ceramics at 16 (**a**), 80 (**b**) and 120 K (**c**).

Thus, the temperature of the structural phase transition was found to be influenced by doping with Mn and especially by the site at which Mn doping occurs. The structural phase transition which is directly connected with the lattice dynamics of undoped ST, was found to be dependent on the Mn doping. The increase of T_a for SMnT and the decrease of T_a for STMn ceramics strongly support the assumption of the introduction of Mn into the two different sites of the perovskite lattice in these samples.

$SrTiO_3$ is known to be a very high-packed perovskite structure of general formula ABO_3 with a tolerance factor $t = t_1/t_2 \approx 1$. Fractional tolerance factors t_1 and t_2 describe the degree of packing of A or B ions in the perovskite lattice and are given by the following equations:

$$t_1 = \frac{\sqrt{2}(r_A + r_O)}{a} \quad \text{and} \quad t_2 = \frac{2(r_B + r_O)}{a}, \tag{4.5}$$

where r_A and r_B stand for the average ionic radii at A and B-site respectively, and r_O for the ionic radius of the oxygen and a stands for the lattice parameter. For Mn-doped ST system the ionic radius of Sr^{2+} and Mn^{2+}, estimated for coordination number $N_c = 12$, characteristic for the perovskite A-site is $r_{Sr}{}^{2+} = 1.44$ Å and $r_{Mn}{}^{2+} = 1.27$ Å, while is for $r_{Ti}{}^{4+} = 0.605$ Å and $r_{Mn}{}^{4+} = 0.53$ Å, at $N_c = 6$, characteristic for the B-site (Shannon, 1976). For SMnT, both t_1 and $t = t_1/t_2$ decrease with increasing Mn content x, due to the smaller size of Mn^{2+} ions when compared with the one of Sr^{2+} ions. This means that the average A cation size becomes smaller, making the octahedral tilting more favourable. Hence the temperature of the phase transition increased, as it was observed.

For STMn, Mn^{4+} is smaller than Ti^{4+}, the average B cation size and t_2 decrease, but $t = t_1/t_2$ increases with increasing Mn content y, and thus the octahedra do not tend to tilt, consequently T_a decreases. The differences between the temperature values of T_a for SMnT and STMn systems are reasonably explained from the ionic size consideration, particularly, in the light of the differences in tolerance factors.

4.4. Electron spin resonance results

Mn is a multivalent ion with possible charge states of 2+, 3+, 4+, 6+ and 7+. The most probable states in Mn-doped ST systems are 2+ and 4+. It is also well known that lattice defects created in ST due to charge compensation mechanism may affect markedly the final dielectric response of the material. In order to check it and to determine a dominant charge state of Mn ions in each of the $Sr_{1-x}Mn_xTiO_3$ and $SrTi_{1-y}Mn_yO_3$ systems, ESR measurements have been performed at room temperature on the selected samples. The resulting absorption spectra are shown in Figure 4.18.

Groups of six main hyperfine lines characteristic for Mn are observed in the spectra. Even for undoped ST, a weak spectrum with the hyperfine splitting constant A_{hs} of 75 G or 69.5×10^{-4} cm^{-1} and g-factor of 1.994 is detected. Both these parameters agree in the value with the analogous parameters of the spectrum of $SrTiO_3$ single crystal with the addition of 0.01 weight percent of MnO_2 (Müller, 1959). That spectrum was attributed to Mn^{4+} ions at Ti^{4+} site (Müller, 1959). Similar spectrum, but with much higher intensity was observed for $SrTi_{1-y}Mn_yO_3$ ceramics with $y = 0.01$. Further increase of Mn content to $y = 0.05$ leads to the formation of an additional wide line, attributed to the magnetic interaction of Mn ions.

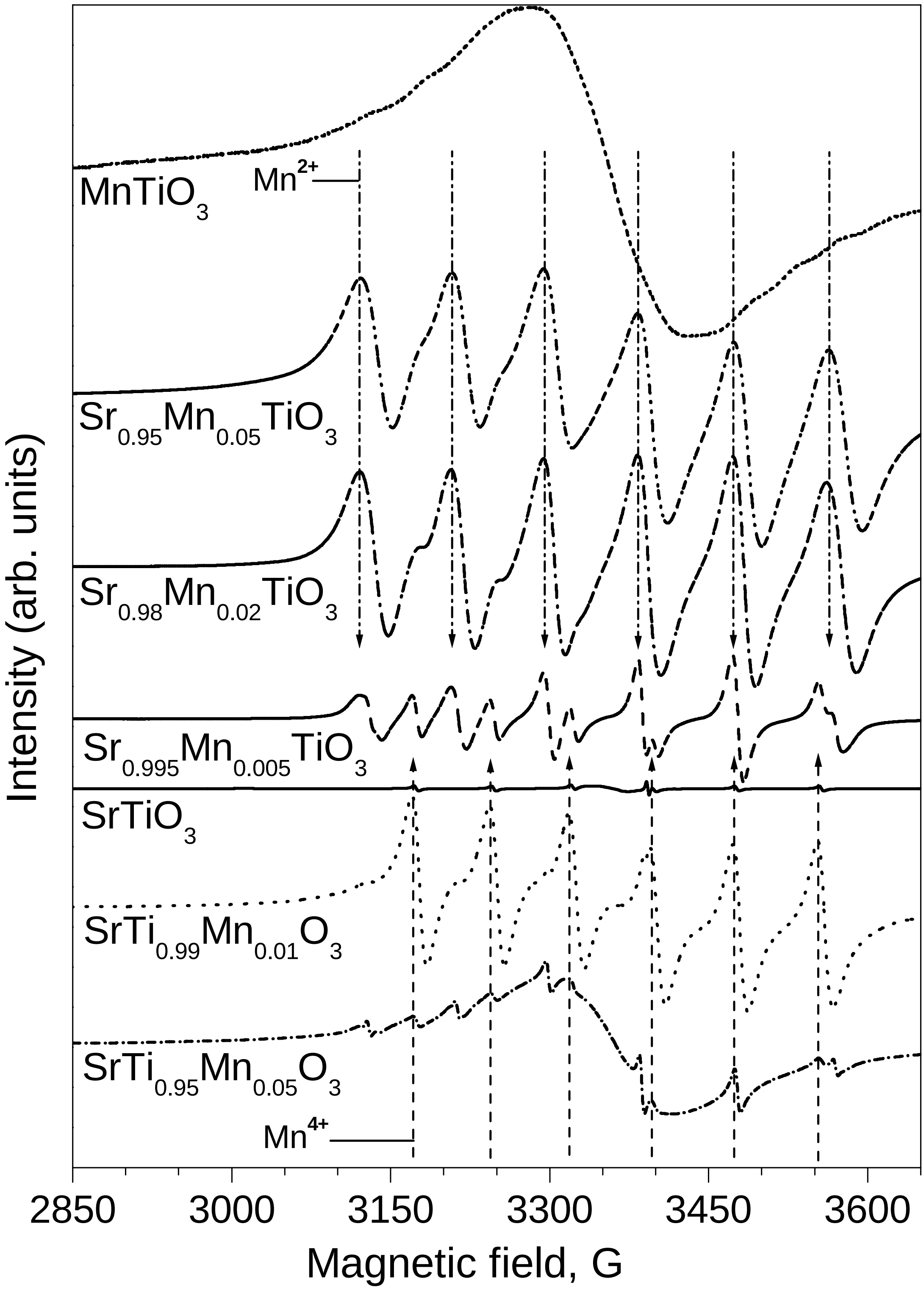

FIGURE 4.17. Room-temperature ESR absorption spectra of MnTiO$_3$, Sr$_{0.95}$Mn$_{0.05}$TiO$_3$, Sr$_{0.98}$Mn$_{0.02}$TiO$_3$, Sr$_{0.995}$Mn$_{0.005}$TiO$_3$, SrTiO$_3$, SrTi$_{0.99}$Mn$_{0.01}$O$_3$ and SrTi$_{0.95}$Mn$_{0.05}$O$_3$ ceramics.

An additional group of six hyperfine lines with g-factor of 2.004 and A_{hs} of 87 G or 81 × 10^{-4} cm^{-1}, which is supposed to be related with Mn^{2+}, is observed for $Sr_{1-x}Mn_xTiO_3$ system, along with the group mentioned above. Therefore, manganese ions of both 2+ and 4+ charge state exist in SMnT system. For $x = 0.005$, the intensity of Mn^{2+}-lines is similar to that of Mn^{4+}-lines, what can be explained by the more favourable occupation of Ti sites than Sr sites for Mn ions. Accordingly, Mn may occupy Ti sites and Sr sites simultaneously. However, the intensity of Mn^{2+}-lines increases with an increase of the concentration x to 0.02, overlapping the Mn^{4+}-lines and implying that the amount of Ti positions occupying by Mn^{4+} is limited. The concentration of Mn^{4+} ions was increased in $Sr_{0.98}Mn_{0.02}TiO_3$ ceramic samples sintered in an oxygen atmosphere, whereas it was decreased in the samples sintered in a nitrogen atmosphere. ESR spectra of these samples are shown in Figure 4.19, in which Mn^{4+}-lines, clearly observed for the samples sintered in oxygen (pointed by thin arrows), transform to just a shoulder for the samples sintered in air and almost disappear for the samples sintered in nitrogen. Colour of the samples was found to vary correspondingly: from dark brawn for oxygen to brawn for a nitrogen sintering atmosphere. This observation demonstrates once again the importance of the processing conditions for the formation of stoichiometric $Sr_{1-x}Mn_xTiO_3$ system.

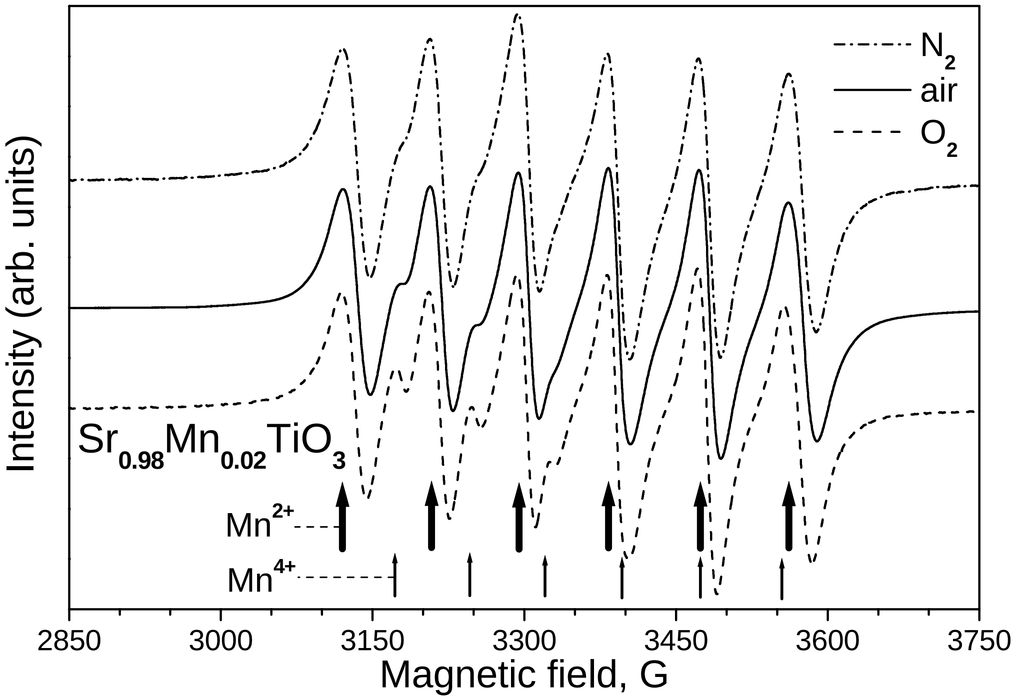

FIGURE 4.19. Room-temperature ESR absorption spectra of $Sr_{0.98}Mn_{0.02}TiO_3$ ceramics, sintered in nitrogen, air and oxygen.

Returning to Figure 4.18, similarly to $SrTi_{1-y}Mn_yO_3$, further increase of Mn content to $x = 0.05$ leads to the formation of an additional wide line, attributed to the magnetic interaction of Mn ions. Finally just this wide line is observed in spectrum of $MnTiO_3$.

4.5. Summary

The systems, $Sr_{1-x}Mn_xTiO_3$ ($0 \leq x \leq 0.15$ and $x = 1$) and $SrTi_{1-y}Mn_yO_3$ ($0 \leq y \leq 0.1$), are synthesised by conventional mixed oxide method. The dominant charge state of Mn ions, microstructure and crystal structure of the sintered samples are studied. The main results obtained are:

1. The density of all the ceramic samples, sintered at 1500 ºC for 5 hours is 4.57-5.00 g/cm^3. The grain size is found to differ markedly for $Sr_{1-x}Mn_xTiO_3$ ceramics, ranging from 20 to 35 μm, and for $SrTi_{1-y}Mn_yO_3$ ceramics, ranging from 0.6 to 0.8 μm, without obvious dependence on Mn content. This difference in the grain growth behavior might be also related to the variations in the Sr/Ti ratio. Precursor type (containing either Mn^{2+} or Mn^{4+}) has not strong effect on final structural and microstructural properties of $Sr_{1-x}Mn_xTiO_3$ ceramics.
2. The solid solubility limit for Mn at Sr site of ST is determined to be about of 2%. Small grains of $MnTiO_3$ are found by TEM / EDS to appear in the grain boundaries of $Sr_{1-x}Mn_xTiO_3$ ceramics for higher Mn concentrations. On the other hand, no second phase and a strong decrease of the lattice parameter with increasing y are observed for $SrTi_{1-y}Mn_yO_3$ ceramics. These facts point to the incorporation of Mn into the perovskite lattice in the whole experimental range of concentrations $0 \leq y \leq 0.15$ used in this work. Consequently the solid solubility limit for Mn in B site of ST is higher than for Mn in A site of ST structure.
3. Based on TEM and Raman spectroscopy with temperature variation, the predicted occupation of Mn at both A and B sites of the ST lattice was confirmed. Also, the relation was established between the temperature T_a of the structural phase transition of Mn-doped ST and the dependence on the Mn site. Mn incorporation at the Sr site was found to increase T_a decreasing the tolerance factor t, while Mn incorporation at the Ti site was found to decrease T_a with raising t. Moreover, additional lines in Raman spectra of SMnT and STMn ceramics imply the formation of additional structural bonds

with their own dynamics, confirming the incorporation of Mn into the Sr- and Ti- sites of the perovskite lattice.

4. The predominance of Mn^{4+} in $SrTi_{1-y}Mn_yO_3$ and of Mn^{2+} in $Sr_{1-x}Mn_xTiO_3$ systems was confirmed by ESR spectroscopy, although features of Mn ions in both charge states were observed in all the Mn-doped ST samples. For $Sr_{1-x}Mn_xTiO_3$ system, the lines attributed to Mn^{2+} increase in intensity with Mn content increase, while those attributed to Mn^{4+} decrease and finally disappear at crossover from an oxidizing to a reducing sintering atmosphere.

5. Low Temperature Dielectric Properties of Manganese-doped Strontium Titanate Ceramics

Dielectric properties of Mg-doped $SrTiO_3$ have been reported in Chapter 3. No dielectric anomaly was found to occur in the case of Sr-site substitution, probably, due to the very restricted solid solubility limit of 1% of Mg in ST lattice. Hence no experimental confirmation of Kvyatkovskii's theoretical predictions could be obtained. On the other hand, the introduction of Mg^{2+} ions into Ti site gives rise to a remarkable decrease of the dielectric constant and loss, driving the system away from ferroelectric instability.

Mn^{2+} ions, having ionic size intermediate between those of Sr^{2+} and of Mg^{2+} and solid solubility limit at Sr site of < 3%, as shown in Chapter 4, may occupy off-centre positions also. In addition, Ti sites may be occupied by Mn^{4+} ions with possible off-centre displacements due to the fact that ionic size of Mn^{4+} is smaller than that of Ti^{4+}. Indeed, the solid solubility of Mn in the ST perovskite lattice in the whole experimental range of concentrations $0 \leq y \leq 0.15$ used in this work was observed. Such doping is expected to change the polar behaviour, to modify the polarisation response of the material and to induce the anomaly in the dielectric response of Mn-doped ST.

Recently, a low-temperature dielectric relaxation with the activation energy $U \approx 30$ meV and the relaxation time $\tau_0 \approx 5 \times 10^{-11}$ s in the $SrTiO_3$:Mn system with Mn concentration up to 0.05 was reported by Lemanov and co-workers (2004). The relaxation was attributed to the reorientation of polarons localized at defects of the $\{Mn^{2+}_{Ti} - O^{-}\}$ type, although the lattice site for the dopant occupancy is not clearly stated in that work. In addition, the relaxation parameters were reported to be insensitive to the post-sintering annealing in an oxygen flow and to the dopant concentration.

In this chapter, the dielectric properties of strontium titanate ceramics, doped with manganese ions at the Sr and Ti sites were studied in a wide frequency range of 10^2-10^{14} Hz, in a temperature range of 10-300 K and in a dc bias field range of 0-20 kV/cm. The dielectric constant and loss, of $Sr_{1-x}Mn_xTiO_3$ (SMnT) and $SrTi_{1-y}Mn_yO_3$ (STMn) systems were examined with radio frequency (rf), microwave (MW), time-domain terahertz (TDT), infrared (IR) dielectric spectroscopy techniques. For the samples revealing diffused peaks of the dielectric permittivity as a function of temperature, relaxation parameters of this anomaly were obtained. The peak dynamics was analysed using Cole-Cole, Arrhenius and Vögel-Fulcher equations. Variations of the dielectric permittivity with a dc bias field and of the hysteresis loops with the temperature were also analysed. The dielectric anomaly behaviour was compared with those of other ST-based systems and the origin of the relaxation was discussed.

5.1. Dielectric properties in low frequency range (100 Hz - 1 MHz)

5.1.1. Complex permittivity as function of manganese concentration, temperature and frequency

The temperature dependence of the real ε' and imaginary ε'' parts of dielectric permittivity of the $Sr_{1-x}Mn_xTiO_3$ (x = 0, 0.0025, 0.005, 0.01, 0.02, 0.03, 0.05, 0.10, 0.15 and 1) ceramic samples at 10 kHz is shown in Figure 5.1.

Figure 5.2 presents also the variation of the dissipation factor $\tan\delta = \varepsilon''/\varepsilon'$ with temperature in the low-T range of 10-110 K.

A typical quantum paraelectric behaviour, i.e., a steep increase of the dielectric constant and levelling-off at high values, as the temperature approaches 0 K, without any dielectric anomaly and frequency dispersion (Müller and Burkard, 1979) was observed for undoped $SrTiO_3$. In contrast, $MnTiO_3$ behaves as an ordinary dielectric: the dielectric constant close to 22 is frequency independent and decreases with temperature decrease with the slope of $d\varepsilon'/dT = 1.1\times10^{-3}$ K^{-1}. However, although neither $SrTiO_3$ nor $MnTiO_3$ exhibit any anomaly of dielectric properties, an anomaly was observed in the temperature dependence of dielectric constant of SMnT samples, starting from $x = 0.005$, as shown in Figure 5.1a. The temperature of the dielectric constant peak $T_{\varepsilon'\mathrm{m}}$ reveals strong dependence on Mn concentration in the range x = 0.005-0.03, weakening in the range x = 0.05-0.15. Such behaviour is accompanied by a monotonous decrease of maximum and low-temperature ε' value with x in all the range of Mn concentrations, as presented in Figure 5.3. The inflection point of $x \approx 0.03$ in $T_{\varepsilon'\mathrm{m}}(x)$ dependence coincide with the value of solid solubility limit, obtained by transmission electron microscopy, as shown in Chapter 4.

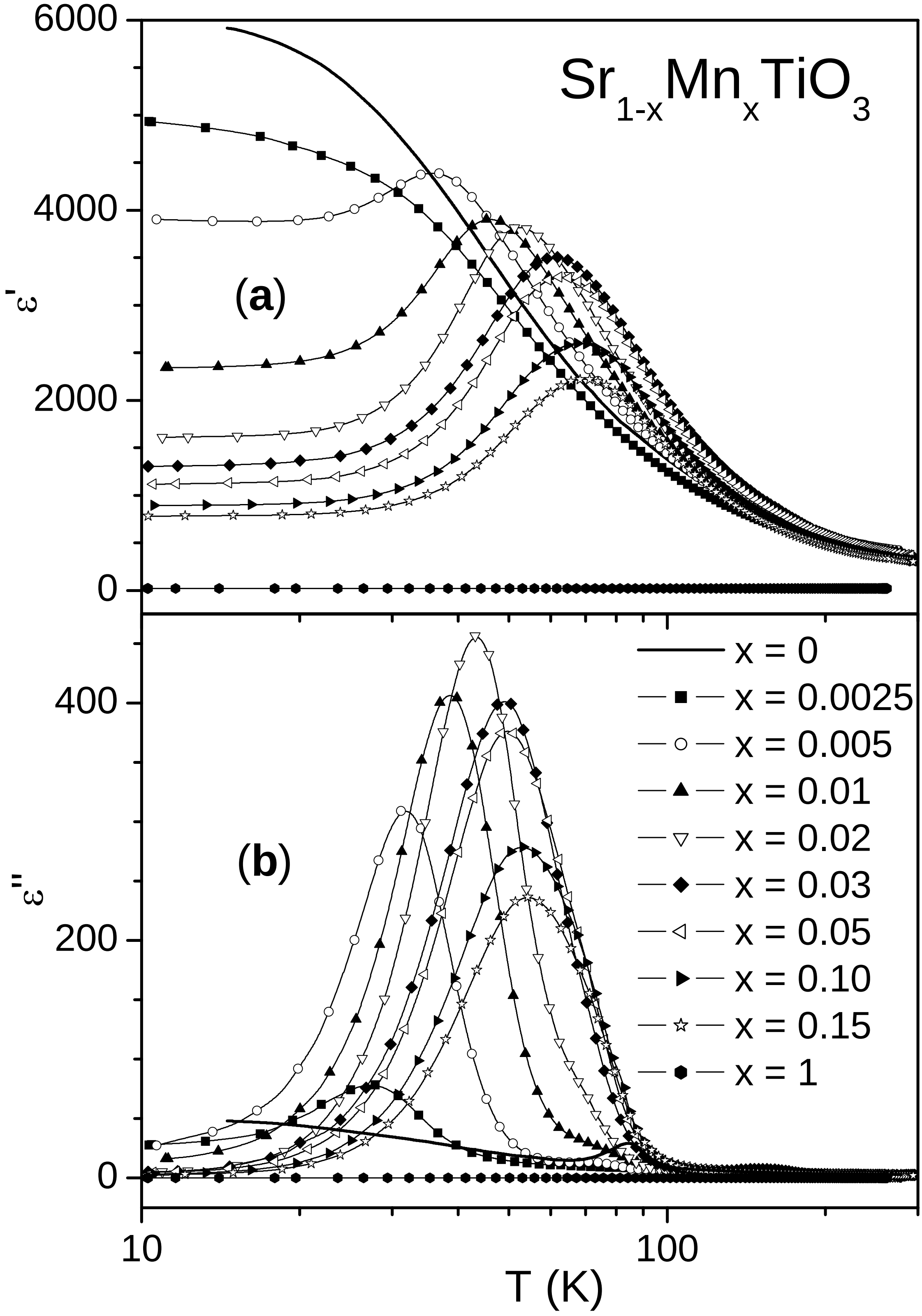

FIGURE 5.1. Temperature dependence of real ε' (**a**) and imaginary ε'' (**b**) parts of dielectric permittivity of $Sr_{1-x}Mn_xTiO_3$ ceramics with x = 0, 0.0025, 0.005, 0.01, 0.02, 0.03, 0.05, 0.10, 0.15 and 1 at 10 kHz.

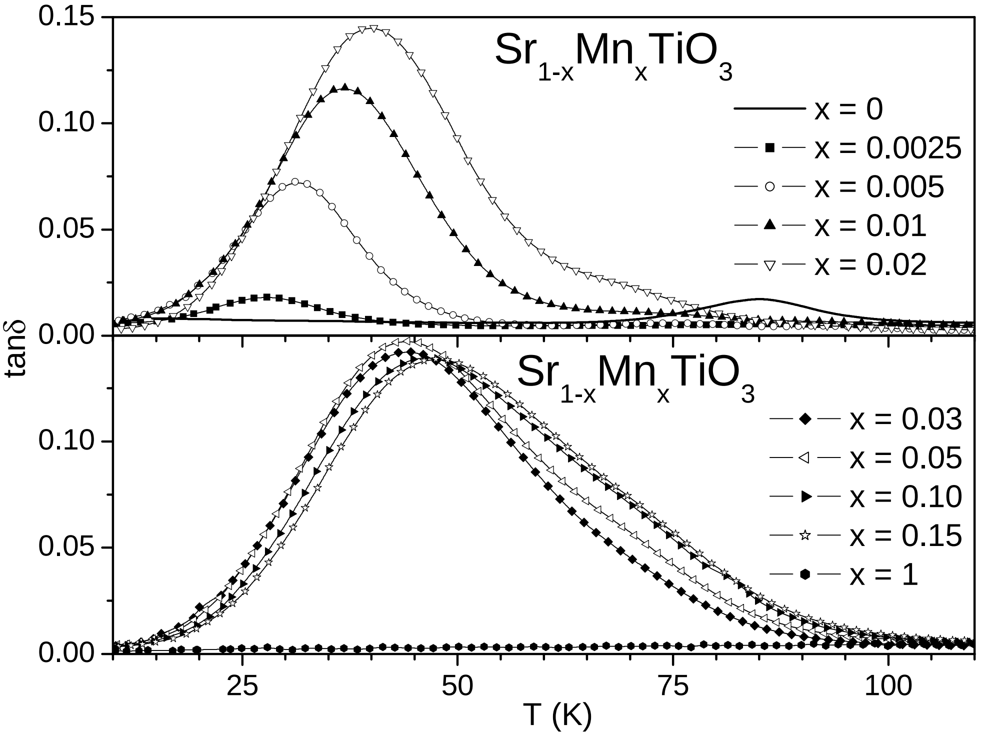

FIGURE 5.2. Temperature dependence of dissipation factor *tanδ* of $Sr_{1-x}Mn_xTiO_3$ ceramics with x = 0, 0.0025, 0.005, 0.01, 0.02, 0.03, 0.05, 0.10, 0.15 and 1 at 10 kHz.

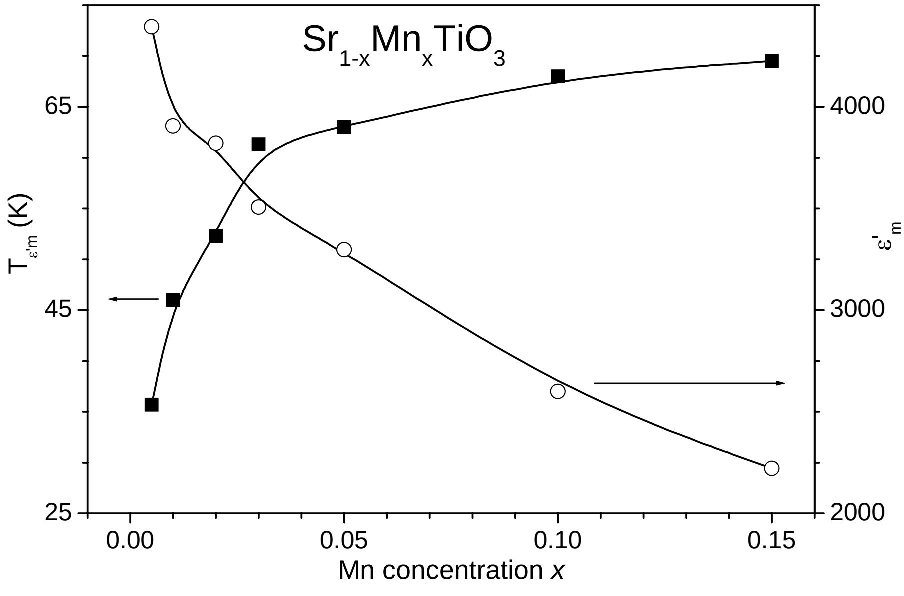

FIGURE 5.3. Variation of maximum dielectric constant temperature $T_{\varepsilon'm}$ (left scale) and of maximum dielectric constant value ε'_m (right scale) at 10 kHz with Mn content in SMnT.

According to the results depicted in Figures 5.1b and 5.2, $MnTiO_3$ exhibits the smallest loss value. The loss of $SrTiO_3$ is slightly higher and characterised by a peak at 70 - 105 K for the frequency range of 10^2 - 10^6 Hz, related to elastic multi-domain state of ST below antiferrodistortive phase transition, as discussed in detail in Chapter 3.

Differently, a low-temperature dielectric loss peak was detected for the rest of the SMnT samples, even for the composition with x = 0.0025, which do not exhibit any dielectric constant anomaly. These peaks are also indicative of the strong dielectric relaxation induced by Mn doping. The temperature of the dielectric loss peak is lower than that of the dielectric constant peak and is consistent with typically observed in relaxor ferroelectrics. On the other hand, for both ε'' and ε', the peak temperature depends on Mn content, strongly in the range of x = 0.0025-0.03, and weakly in the range of x = 0.05-0.15. At the same time, the peak value of $\tan\delta$ increases just in the range of x = 0.0025-0.02 from 1.8% to 14.5%, keeping almost the same (~14.5%) for the compositions with x = 0.03-0.15, as shown in Figure 5.2.

A diffuse maximum at 20-80 K observed in $\varepsilon(T)$ of $Sr_{1-x}Mn_xTiO_3$ system with x = 0.005-0.15 was found to be also frequency-dependent, shifting towards higher temperatures with increasing measurement frequency, as shown in Figures 5.4-5.7.

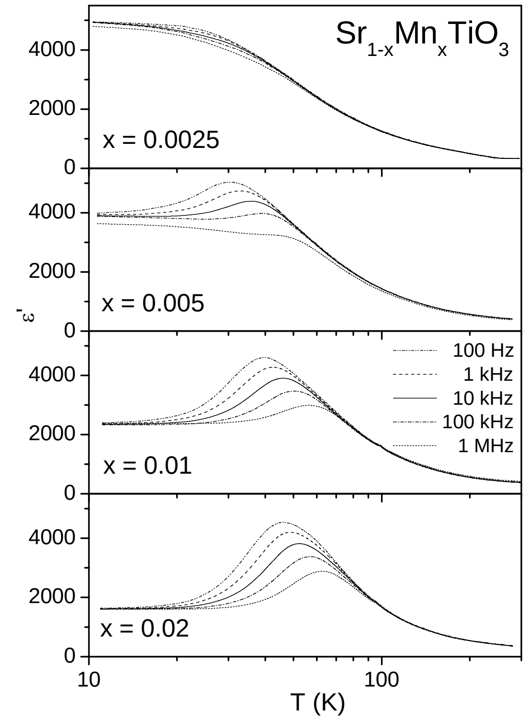

FIGURE 5.4. Temperature dependence of dielectric constant ε' of $Sr_{1-x}Mn_xTiO_3$ ceramics with x = 0.0025, 0.005, 0.01 and 0.02, at 100 Hz, 1 kHz, 10 kHz, 100 kHz and 1 MHz.

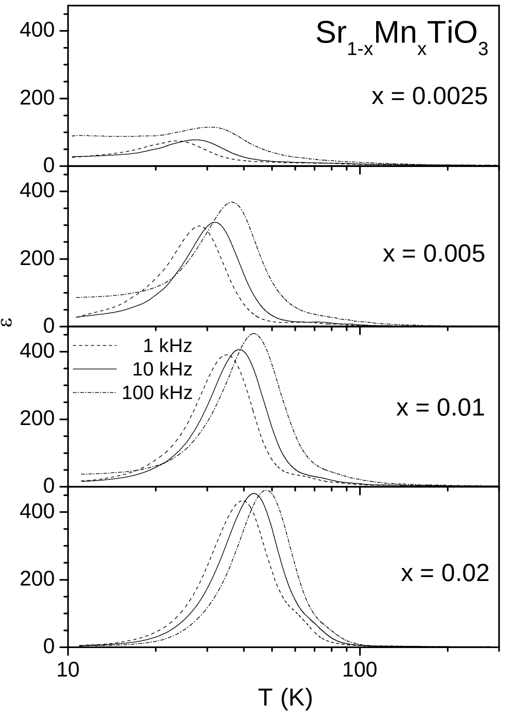

FIGURE 5.5. Temperature dependence of dielectric loss ε'' of $Sr_{1-x}Mn_xTiO_3$ ceramics with x = 0.0025, 0.005, 0.01 and 0.02 at 1, 10 and 100 kHz.

Even though no peak in ε'(*T*) was observed for the composition with $x = 0.0025$, a slight decrease of low-temperature ε' value with increasing frequency can be detected in Figure 5.4. In addition, a small peak appears in ε''(*T*) around 27.5 K for this composition, as shown in Figure 5.5. The loss peak increases in magnitude and shifts towards higher temperature with a frequency increase.

Increasing Mn content to $x = 0.005$, a peak in ε'(*T*) was induced at frequencies ≤ 100 kHz. Meanwhile, the ε'' peak value becomes higher than that of $x = 0.0025$. Further increase of Mn content to $x = 0.01$ and 0.02 makes the frequency-dependent dielectric anomaly stronger and obvious in all measurement frequency range of 100 Hz - 1 MHz. However, for Mn content $x = 0.03$-0.15, the spectra do not markedly change, revealing just simultaneous decrease of ε' and ε'' peak values, as shown in Figure 5.6 and 5.7.

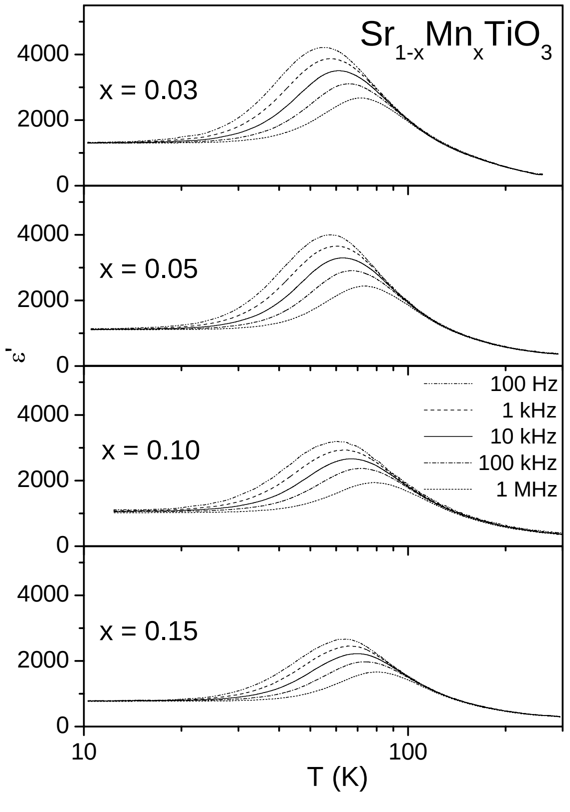

FIGURE 5.6. Temperature dependence of dielectric constant ε' of $Sr_{1-x}Mn_xTiO_3$ ceramics with $x = 0.03$, 0.05, 0. 10 and 0.15 at 100 Hz, 1 kHz, 10 kHz, 100 kHz and 1 MHz.

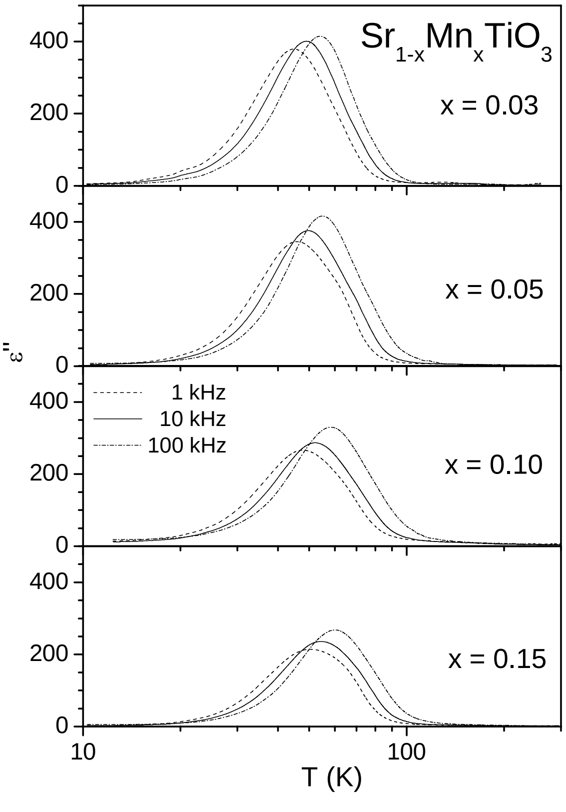

FIGURE 5.7. Temperature dependence of dielectric loss ε'' of $Sr_{1-x}Mn_xTiO_3$ ceramics with $x = 0.03$, 0.05, 0. 10 and 0.15 at 1, 10 and 100 kHz.

Figure 5.8 presents the temperature dependence ε' and ε'' of the $SrTi_{1-y}Mn_yO_3$ ceramics with $y = 0$, 0.01, 0.05, 0.10 and 0.15.

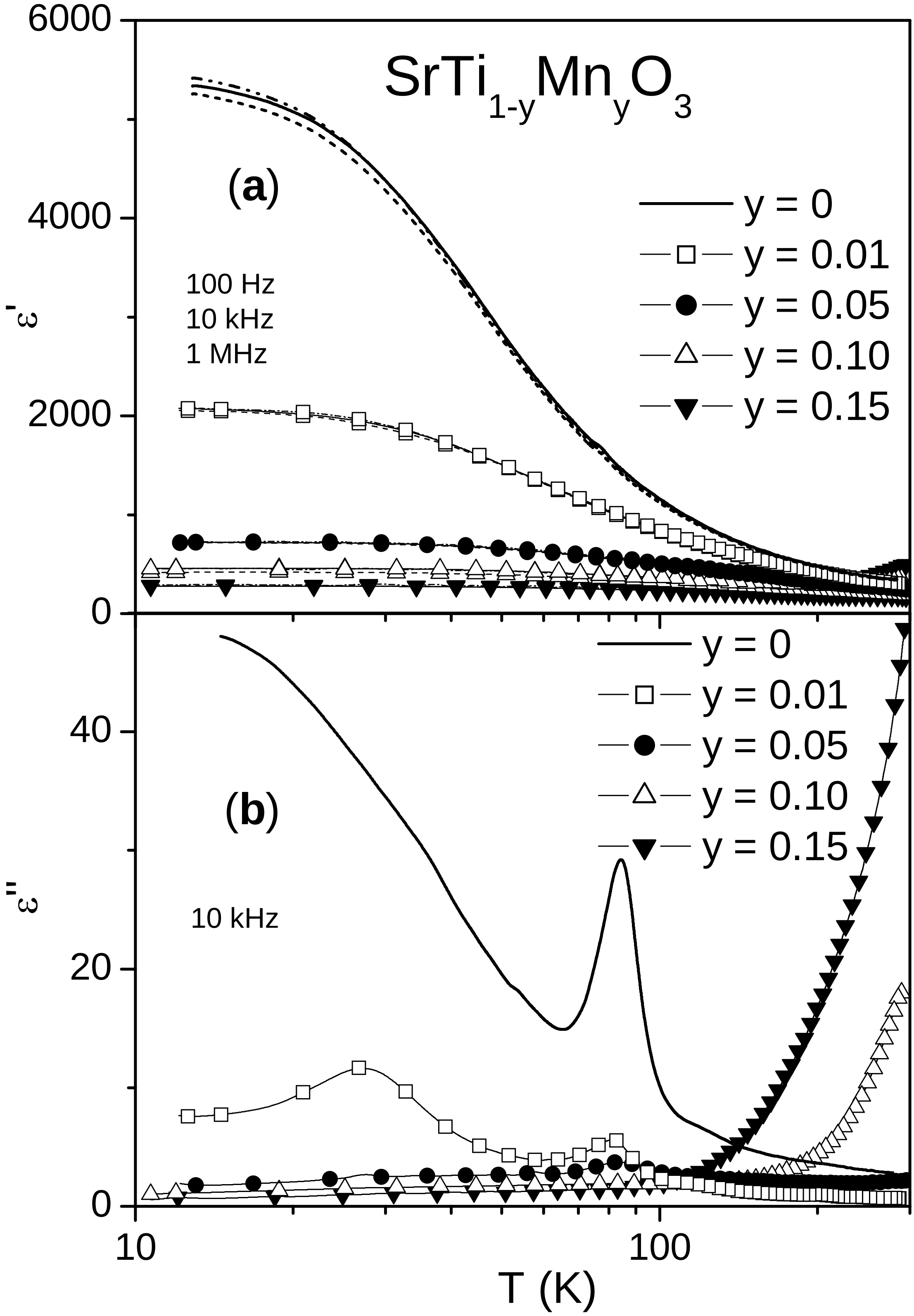

FIGURE 5.8. Temperature dependence of real part of dielectric permittivity ε' at 100 Hz, 10 kHz and 1 MHz (dot, solid and dash lines respectively) (**a**) and of imaginary part of dielectric permittivity ε'' at 10 kHz (**b**) for SrTi$_{1-y}$Mn$_y$O$_3$ ceramics with $y = 0$, 0.01, 0.05, 0.10 and 0.15.

In contradiction to the interpretation of Lemanov et al. (2004), no low-temperature dielectric anomaly or frequency dispersion is observed, but just a marked decrease of the dielectric permittivity with the content of Mn introduced into Ti site may be noticed. Such behaviour of STMn system is similar to that observed in this work for STM and can be explained by the breaking of Ti-Ti long-range interaction by the introduction of less polarisable dopants into oxygen octahedra. Both ε' and ε'' increase near the room temperature with increasing Mn concentration from 0.01 to 0.15 as well as with decreasing frequency from 1 MHz to 100 Hz. Such behaviour corresponds to a gradual crossover from quantum ferroelectric to conductive contribution. Increasing manganese content suggests that some overlap between the Mn 3d wave-functions occurs through the oxygen ions as in cubic $SrMnO_3$ and other antiferromagnetic oxides (Lee and Iguchi, 1995). Then, an enhancement of electronic conduction can be expected due to electrons become very mobile. Consequently, the polar effects of these mobile carriers under the action of alternating electric field yield remarkable increases in the dielectric permittivity.

5.1.2. Fitting to Curie-Weiss law and Barrett relation

The Curie-Weiss law and Barrett relation were used to analyse the temperature dependence of the dielectric constant of $Sr_{1-x}Mn_xTiO_3$ and $SrTi_{1-y}Mn_yO_3$ ceramics. As shown in Figures 5.9 and 5.10, the inverse dielectric constant of SMnT and STMn samples, measured at 10 kHz, was calculated, plotted versus temperature and fitted in the temperature range of 100-200 K to the Curie-Weiss law relation:

$$1/\varepsilon' = (T-T_0)/C \qquad (5.1)$$

Curie-Weiss temperature T_0 and Curie constant C, obtained from the straight line parameters, are tabulated in Table 5.1. The most of the fitting parameters in this thesis were obtained with the maximum error below 3%. For $SrTi_{1-y}Mn_yO_3$ composition with y = 0.15 the influence of conductivity on the dielectric response becomes too strong and does not allow for accurate determination of the Curie-Weiss law parameters.

For $Sr_{1-x}Mn_xTiO_3$ samples, T_0 tends to increase monotonically from 30 K for undoped ST to about of 60 K for x = 0.03, saturating around this value with further increase of Mn content x up to 0.15.

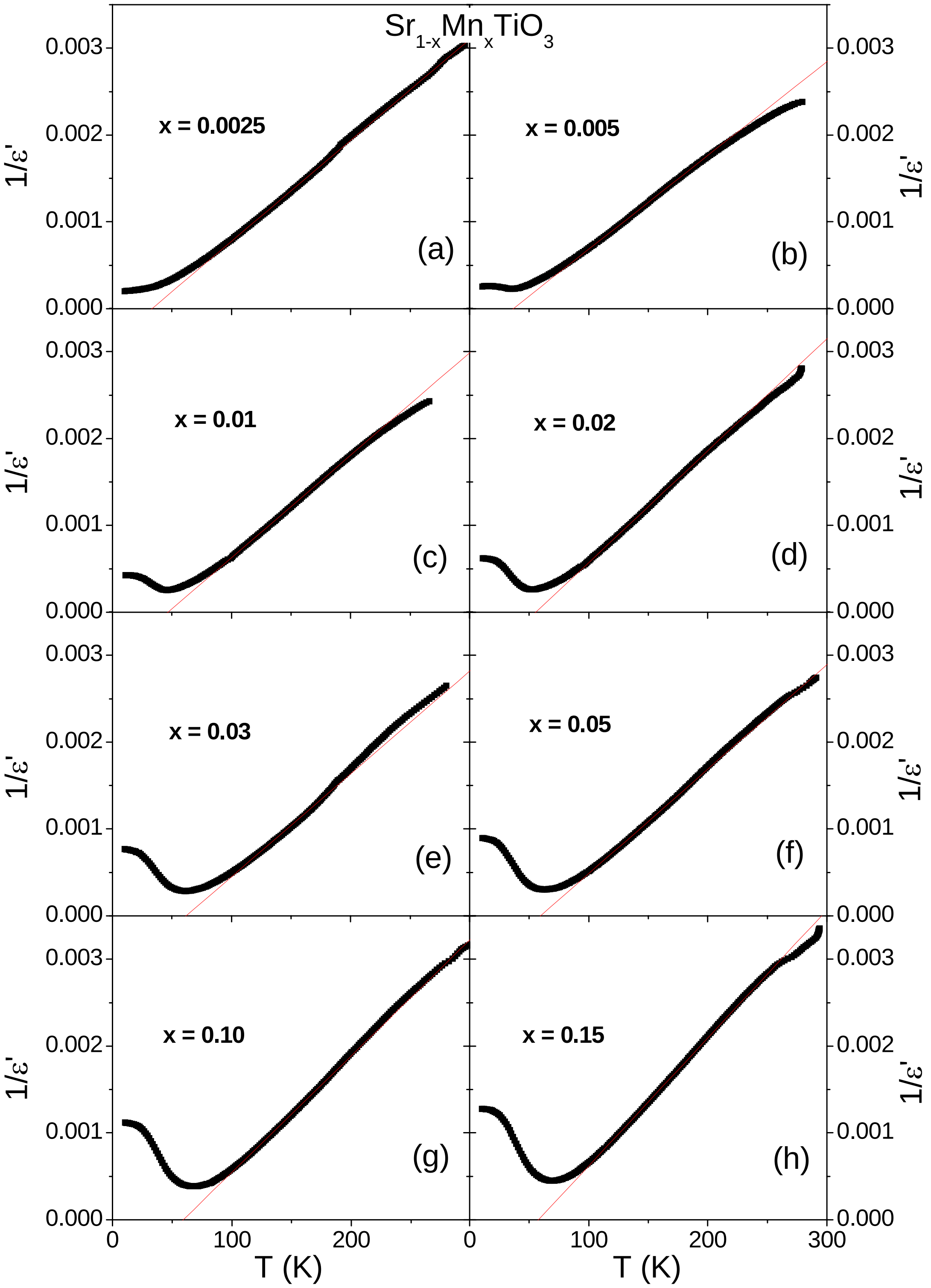

FIGURE 5.9. Temperature dependence of inverse dielectric constant 1/*ε*' at 10 kHz (solid squares) and fits to the Curie-Weiss law (solid lines) for $Sr_{1-x}Mn_xTiO_3$ ceramics with $x = 0.0025$ (**a**), 0.005 (**b**), 0.01 (**c**), 0.02 (**d**), 0.03 (**e**), 0.05 (**f**), 0.10 (**g**) and 0.15 (**h**).

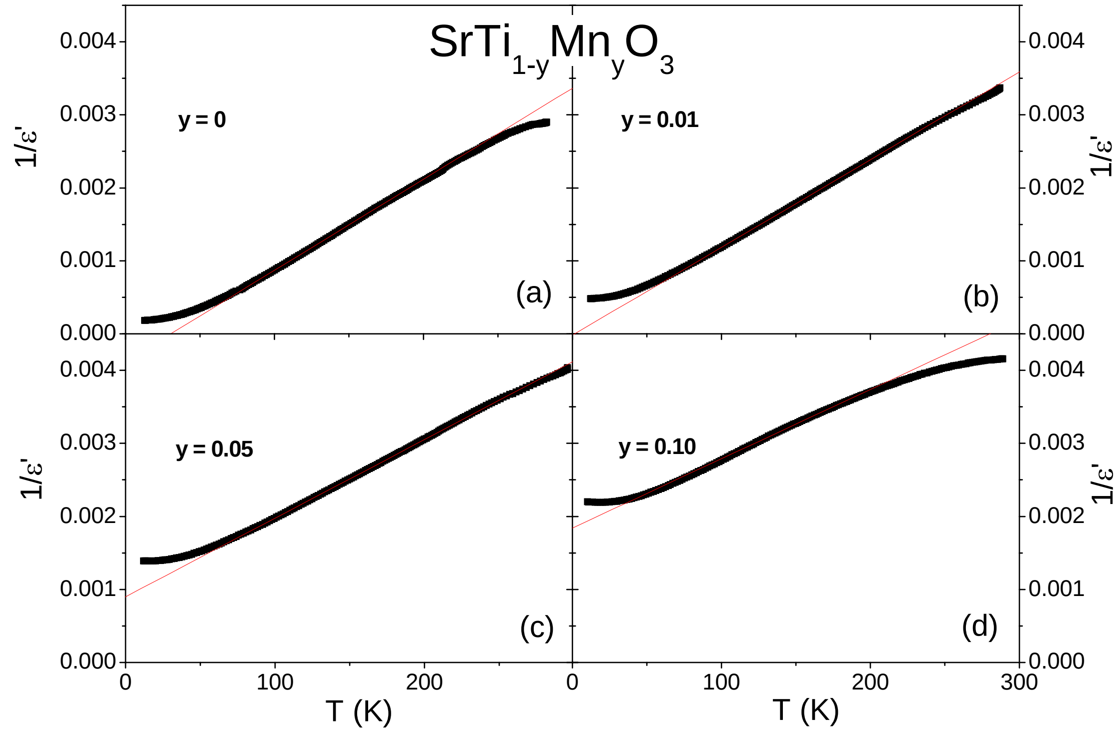

FIGURE 5.10. Temperature dependence of inverse dielectric constant 1/ε' at 10 kHz (solid squares) and fits to the Curie-Weiss law (solid lines) of SrTi$_{1-y}$Mn$_y$O$_3$ ceramics with $y = 0$ (**a**), 0.01 (**b**), 0.05 (**c**), and 0.10 (**d**).

For SrTi$_{1-y}$Mn$_y$O$_3$ ceramics, the Curie-Weiss temperature decreases monotonically with Mn concentration y up to 0.10. Such a decrease of the Curie-Weiss temperature is similar to that of SrTi$_{1-y}$Mg$_y$O$_{3-\delta}$, just lower T_0 values were observed for STM for the same dopant content, as shown in Chapter 3.

The Barrett relation:

$$\varepsilon' = C/[(T_1/2)\coth(T_1/2T)-T_0], \tag{5.2}$$

where T_1 is the temperature of the crossover between classical and quantum behaviour, T_0 is the temperature at which the phase transition would occur in the absence of quantum fluctuations, and C is the Curie constant (Barrett, 1952), was also applied to fit the raw experimental data of $\varepsilon'(T)$ at 10 kHz (see Figures 5.1 and 5.4) in the whole measurement temperature range for STMn and on the high-temperature side of the permittivity peak for SMnT. Values of C, T_1, and T_0 are also presented in Table 5.1. Ti-site Mn doping monotonically reduces T_0 value and raises (T_1 - 2T_0) value, i.e., drives the system away from the ferroelectric instability similarly to STM. In the case of Sr-site Mn doping, the transition temperature T_0 increases with x with a further stabilisation at ~100 K for x = 0.03-0.15. At the same time, the value T_1-2T_0, considering as signature of ferroelectricity, is decreased, comparing with undoped ST, reaching a minimum of 12.6 K at x = 0.02, as shown in Table 5.1. A decrease of the (T_1 - 2T_0) towards 0 for the $Sr_{1-x}Mn_xTiO_3$ compositions indicates an approximation to the ferroelectric behaviour (Bianchi et al., 1995), i.e., ferroelectric ordering become stronger in respect to quantum fluctuations.

Table 5.1. Curie-Weiss law and Barrett relation parameters deduced from $\varepsilon'(T)$ of SMnT and STMn ceramics at 10 kHz.

COMPOSITION	$T_{\varepsilon'm}$	CURIE-WEISS LAW		BARRETT RELATION			
		C, 10^3 K	**T_0, K**	**C, 10^3 K**	**T_1, K**	**T_0, K**	**T_1-2T_0, K**
$SrTi_{0.90}Mn_{0.10}O_3$	-	98.5	-175.3	100.7	110.6	-175.5	461.6
$SrTi_{0.95}Mn_{0.05}O_3$	-	89.1	-69.9	84.0	135.4	-49.1	233.6
$SrTi_{0.99}Mn_{0.01}O_3$	-	81.9	6.8	79.9	110.5	16.6	77.3
$SrTiO_3$	-	80.2	30.0	102.0	105.0	35.0	35.0
$SrTi_{0.9975}Mn_{0.0025}O_3$	-	86.1	33.1	95.0	112.9	39.4	34.1
$SrTi_{0.995}Mn_{0.005}O_3$	35.8	92.6	36.5	86.6	126.9	53.0	20.9
$SrTi_{0.99}Mn_{0.01}O_3$	45.9	84.8	46.7	76.5	132.2	56.4	19.4
$SrTi_{0.98}Mn_{0.02}O_3$	52.4	77.6	55.5	67.5	187.2	87.3	12.6
$SrTi_{0.97}Mn_{0.03}O_3$	61.2	84.4	62.0	65.2	267.5	121.0	25.5
$SrTi_{0.95}Mn_{0.05}O_3$	62.9	83.1	59.6	69.5	211.9	99.2	13.5
$SrTi_{0.90}Mn_{0.10}O_3$	67.9	74.5	59.3	61.2	221.9	102.4	17.1
$SrTi_{0.85}Mn_{0.15}O_3$	69.5	67.9	57.8	56.6	213.1	98.1	16.9

5.1.3. Characterisation of the relaxor behaviour of $Sr_{1-x}Mn_xTiO_3$ system

The dielectric response of $Sr_{1-x}Mn_xTiO_3$ ceramics shows a diffuse dielectric peak, typical for relaxors. A departure from the Curie-Weiss law was also observed for the SMnT samples in the vicinity of the temperature of the dielectric constant maximum $T_{\varepsilon'm}$.

Curie-Weiss law describes the dielectric behaviour on the high temperature side of T_m for classical ferroelectrics. For relaxor systems, a quadratic equation:

$$1/\varepsilon' - 1/\varepsilon'_{\mathrm{m}} = (T - T_{\mathrm{m}})^2/C \tag{5.3}$$

was proposed by Smolenskii (1970). However, the relation:

$$1/\varepsilon' - 1/\varepsilon'_{\mathrm{m}} = (T - T_{\mathrm{m}})^\gamma/C \tag{5.4}$$

with an effective exponent γ that reflects the diffuseness of the permittivity peak, ranging between 1 and 2, is usually used to describe the dielectric behaviour on the high temperature side of T_{m} for relaxor-like ferroelectrics (Bednorz and Müller, 1984; Wang and Itoh, 2001).

Thus, $\varepsilon'(T)$ data on the high temperature side of $T_{\varepsilon'\mathrm{m}}$ at 10 kHz were recalculated to $1/\varepsilon'$ - $1/\varepsilon'_{\mathrm{m}}$, plotted in a log-log scale versus T - $T_{\varepsilon'\mathrm{m}}$ and fitted with Eq. (5.4), as demonstrated in Figure 5.11. For these fittings, the $\varepsilon'_{\mathrm{m}}$ and $T_{\varepsilon'\mathrm{m}}$ values, shown in Figure 5.3, were used. In such a way, an effective exponent γ (the slope of the straight line) was obtained for all the SMnT compositions, which revealed a peak in $\varepsilon'(T)$, and are presented in Table 5.2. The effective exponent γ was found to deviate from the unity and increase from 1.40 to 1.67 with Mn content x, increasing from 0.005 to 0.05. The approximation to the value of 2 is indicative of a typical relaxor behaviour (Smolenskii, 1970).

Relaxor systems are also characterized by diffuse permittivity peaks and frequency dispersion in the radio frequency range (Cross, 1987). The diffuseness can be described by the temperature width of the dielectric constant peak, determined as $\Delta T_\varepsilon = T_{0.9\varepsilon'\mathrm{m(10kHz)}}$ - $T_{\varepsilon'\mathrm{m(10kHz)}}$, i.e., the difference between the temperature corresponding to 90% of the ε' maximum on the high-temperature side and $T_{\varepsilon'\mathrm{m}}$ at 10 kHz. The frequency dispersion of the dielectric constant can be quantified by the difference of $T_{\varepsilon'\mathrm{m}}$ at higher and lower frequencies: $\Delta T_{\mathrm{f}} = T_{\varepsilon'\mathrm{m(100kHz)}} - T_{\varepsilon'\mathrm{m(100Hz)}}$. ΔT_ε increases monotonously from 9.6 K for x = 0.005 to 14.8 K for x = 0.10, implying that the system evolves to a relaxor-type behaviour, as the Mn content increased. This indication of a relaxor-type behaviour corroborates the variation of exponent γ. The increase of ΔT_{f} is not so obvious, but can be seen for the Mn concentration x from 0.005 to 0.02 (Table 5.2).

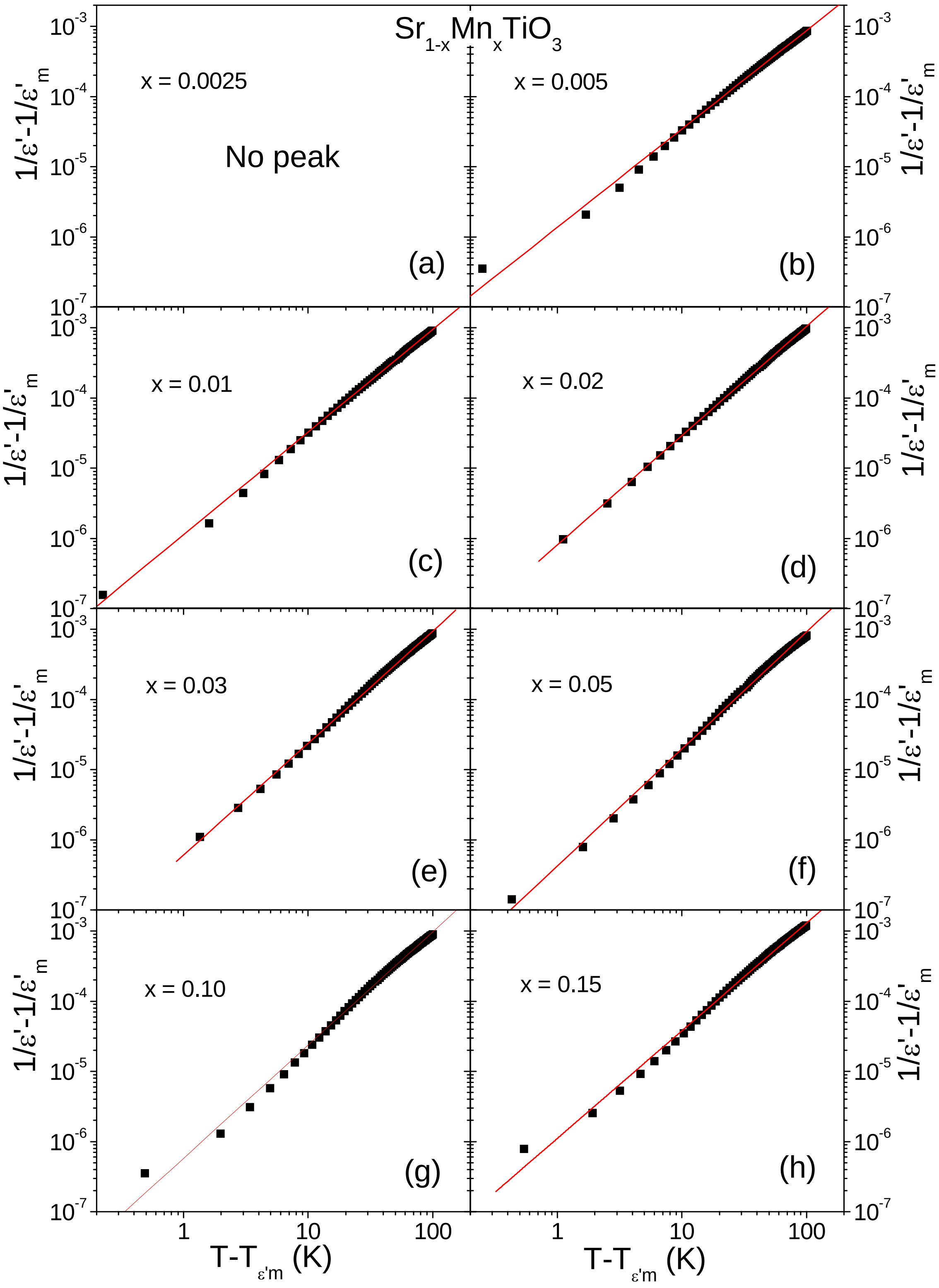

FIGURE 5.11. Plots of $1/\varepsilon'$-$1/\varepsilon'_m$ at 10 kHz versus T-$T_{\varepsilon'm}$ in logarithmic scale (solid squares) and fits to the Eq. (5.4) (solid lines) for $Sr_{1-x}Mn_xTiO_3$ ceramics with $x = 0.0025$ (**a**), 0.005 (**b**), 0.01 (**c**), 0.02 (**d**), 0.03 (**e**), 0.05, (**f**), 0.10 (**g**) and 0.15 (**h**).

Table 5.2. Relaxor parameters deduced from $\varepsilon'(T)$ of $Sr_{1-x}Mn_xTiO_3$ compositions at 10 kHz.

x	γ	**ΔT_{ε}, K**	**ΔT_f, K**
0.005	1.40	9.6	8.8
0.01	1.46	10.0	10.4
0.02	1.56	11.6	10.9
0.03	1.60	12.9	10.4
0.05	1.67	13.5	9.2
0.10	1.61	14.8	10.9
0.15	1.53	13.5	9.8

5.1.4. Relaxation dynamics of $Sr_{1-x}Mn_xTiO_3$ system

The general effect of the measurement frequency on the dielectric response of SMnT ceramics has been shown in Figures 5.4-5.7, which present $\varepsilon'(T)$ and $\varepsilon''(T)$ curves at different frequencies. For more detail consideration, frequency dependence of the dielectric constant $\varepsilon'(f)$ and loss $\varepsilon''(f)$ of SMnT samples with $x = 0.0025$-0.15 at different temperatures are shown in Figure 5.12 (a-h) in a semi logarithmic scale. The relaxation-type dispersion of the dielectric permittivity is evident. The dielectric constant shows continuous decrease with frequency, while the loss exhibits a diffused peak. The peak frequency increases with temperature, what indicate that the microscopic process which leads to the dielectric anomaly is a thermally activated polar motion.

It is known that many dielectric relaxation processes can be described by the modified Debye model, i.e., the Cole-Cole equation:

$$\varepsilon^*(\omega) = \varepsilon_\infty + [\varepsilon_{dc} - \varepsilon_\infty]/[1+(i\omega\tau)^{1-\alpha}],\ 0 < \alpha < 1 \tag{5.5}$$

with a simple Arrhenius expression for the relaxation time τ:

$$\tau = \tau_0 \exp(U/k_B T) \tag{5.6}$$

Here, $\varepsilon^* = \varepsilon' - i\varepsilon''$, ε_{dc} is the permittivity at zero frequency, ε_∞ is the permittivity at infinite frequency, $\omega = 2\pi f$ is the angular frequency, α is the angle of the semicircular arc, an empirical parameter describing diffuseness of the spectrum, τ_0 is the pre-exponential term or inverse attempt frequency, *U* is the activation energy, k_B is the Boltzmann constant, *T* is the temperature. The α value represents the deviation from the ideal Debye model.

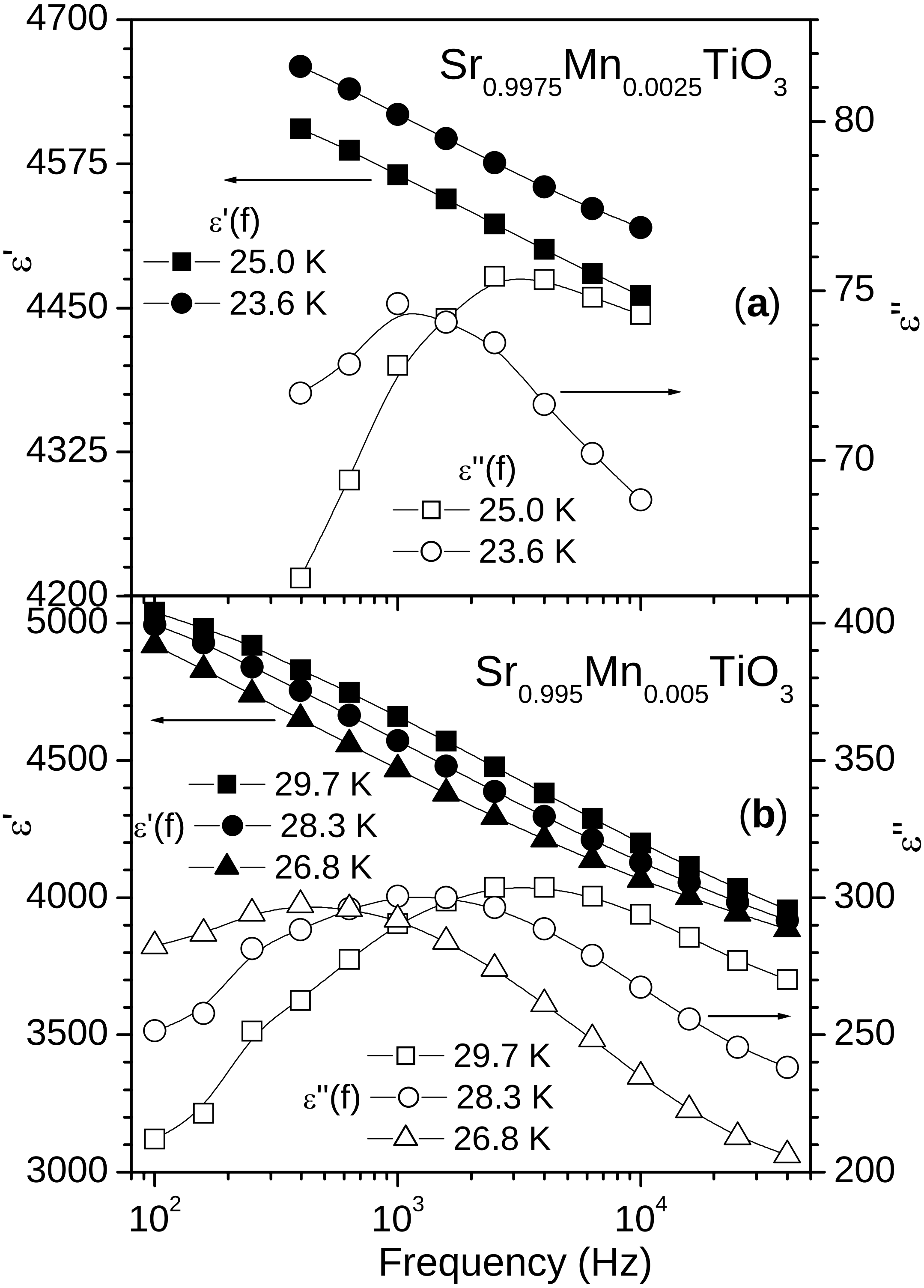

FIGURE 5.12. Frequency dependence of real ε' (left side scale) and imaginary ε'' (right side scale) parts of the dielectric permittivity measured at different temperatures for $Sr_{1-x}Mn_xTiO_3$ ceramics with x = 0.0025 (**a**) and 0.005 (**b**).

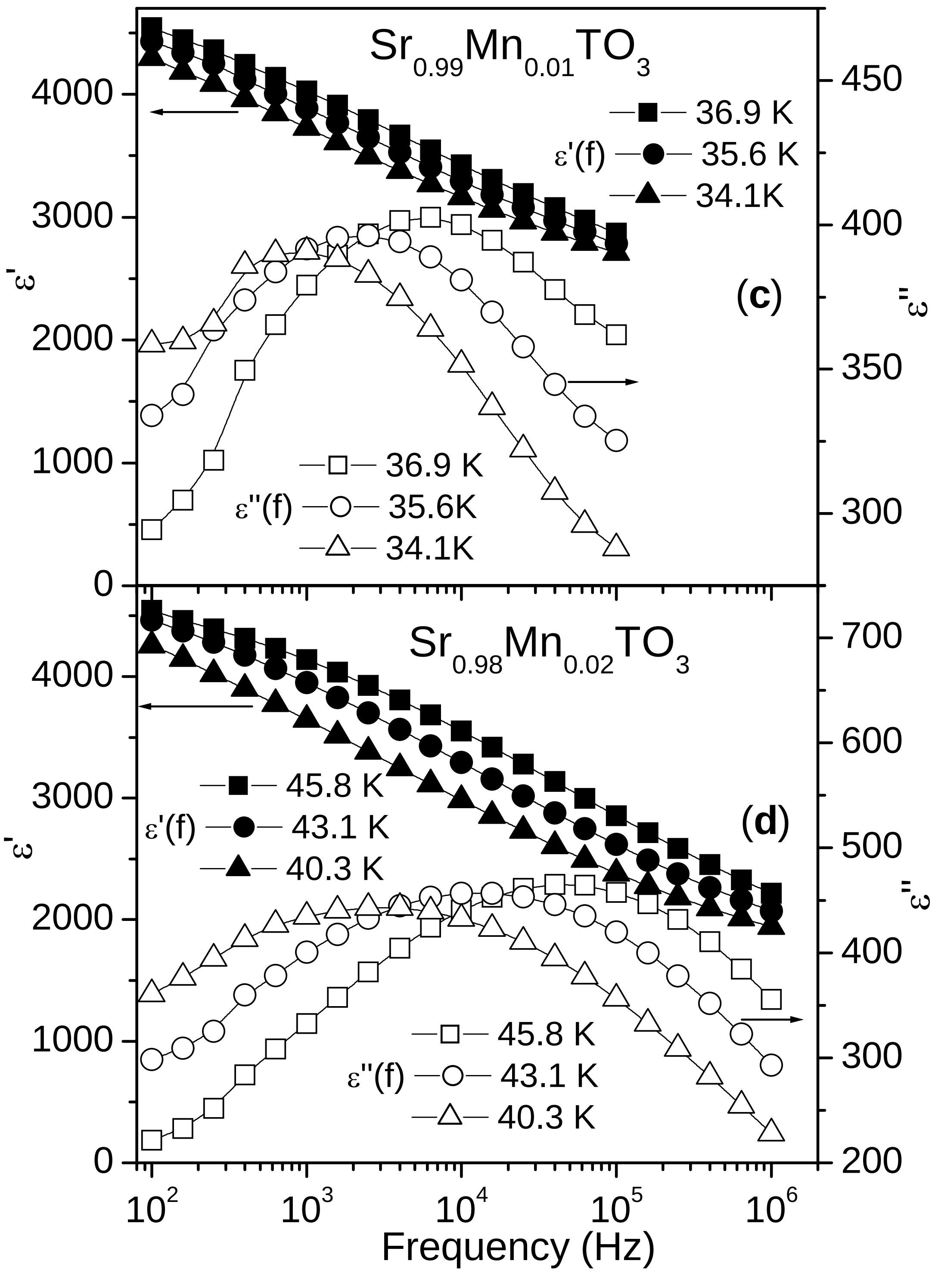

FIGURE 5.12. Frequency dependence of real ε' (left side scale) and imaginary ε" (right side scale) parts of the dielectric permittivity measured at different temperatures for $Sr_{1-x}Mn_xTiO_3$ ceramics with $x = 0.01$ (**c**) and 0.02 (**d**).

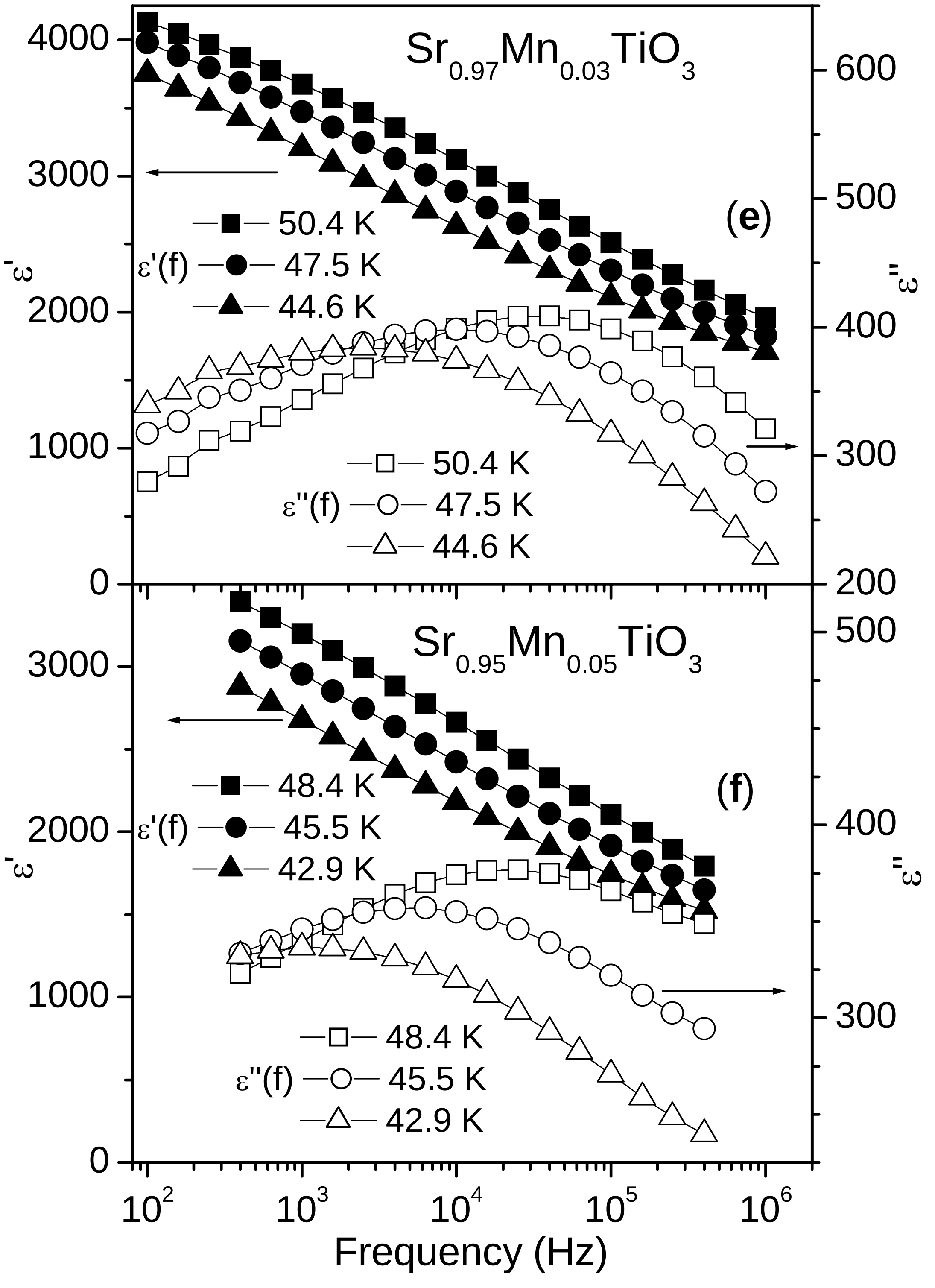

FIGURE 5.12. Frequency dependence of real *ε*' (left side scale) and imaginary *ε*'' (right side scale) parts of the dielectric permittivity measured at different temperatures for $Sr_{1-x}Mn_xTiO_3$ ceramics with $x = 0.03$ (**e**) and 0.05 (**f**).

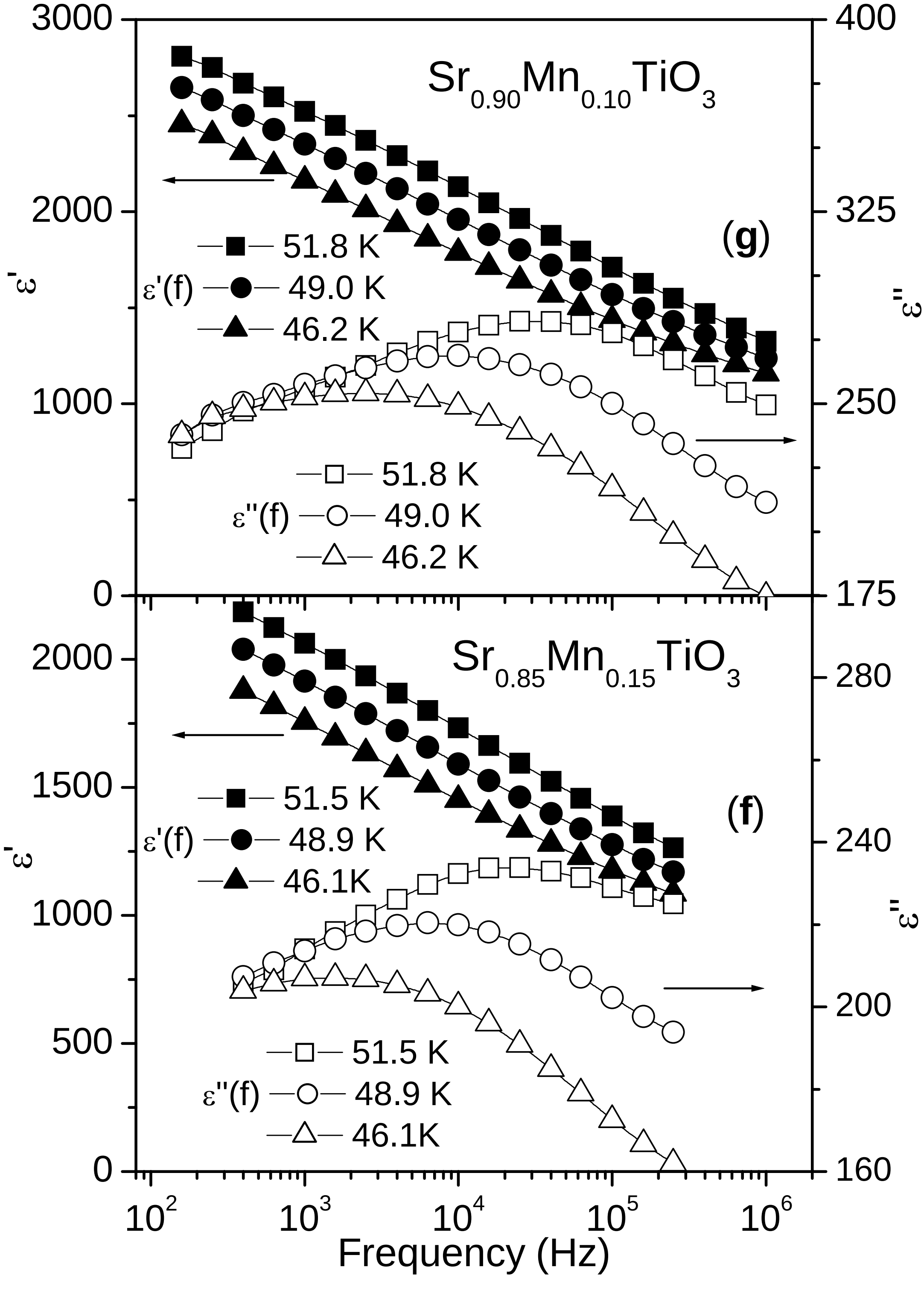

FIGURE 5.12. Frequency dependence of real *ε*' (left side scale) and imaginary *ε*'' (right side scale) parts of the dielectric permittivity measured at different temperatures for $Sr_{1-x}Mn_xTiO_3$ ceramics with $x = 0.10$ (**g**) and 0.15 (**h**).

The Cole-Cole plots (ε'' versus ε' semicircles) are presented in Figure 5.13 (a-h) for SMnT ceramics with $x = 0.0025$-0.15 at different temperatures, corresponding to Figure 5.12 (a-h). The values of the diffuseness parameter α were obtained by the fitting using Eq. (5.5). As shown in Table 5.3, α was found to be about of 0.70±0.03 for $x = 0.0025$-0.02, further increasing trough 0.76 for $x = 0.03$ to 0.81±0.01 for $x = 0.05$-0.15, Such high α values correspond to a high diffusivity of dielectric spectra $\varepsilon(f)$, or in other words, to a wide range distribution of relaxation times, increasing in range $x = 0.03$-0.15.

Parameters of the relaxation dynamics of SMnT ceramics were deduced from the frequency f and temperature T values of ε'' peak. In a dielectric material, if the dielectric relaxation process is governed by a thermally activated motion, the temperature dependence of the relaxation time follows the Arrhenius law [Eq. (5.6)]. For SMnT samples with $x = 0.0025$-0.15, the Arrhenius plots $\ln(\tau) = \ln(\omega^{-1})$ versus $1000/T_{\varepsilon''\mathrm{m}}$ are presented in Figure 5.14 (a-h). It is found that for all the SMnT samples the relaxation times of the relaxation processes follow the Arrhenius relation in the frequency window of 10^2 - 10^6 Hz, monotonously varying at $x = 0.0025$-0.02 and being almost congruent at $x = 0.03$-0.15.

The activation energy U and the pre-exponential term τ_0 values, obtained by fitting to the Arrhenius law are presented in Table 5.3. In the case of $x = 0.005$-0.02, Arrhenius law parameters $U = 52$-73 meV and $\tau_0 \sim (1\text{-}7) \times 10^{-14}$ s were obtained. Such parameters can be related to a relaxation of non-interacting off-centre dopant dipoles in $Sr_{1-x}Mn_xTiO_3$ by analogy with $Sr_{1-1.5x}Bi_xTiO_3$ and $K_{1-x}Li_xTaO_3$, in whose close values for identical parameters were obtained (Bovtun et al., 2004). The deviation of τ_0 and U parameters for $Sr_{0.9975}Mn_{0.025}TiO_3$ composition can be explained both by the difficulty of precise quantitative description of loss peak, due to its weakness, and by the possible overlapping between the thermally activated and quantum tunnelling regimes of the off-centre ions motion at low temperatures (Viana et. al., 1994), included in overall picture of relaxation dynamics.

In the case of $x = 0.03$-0.15, the activation energy $U = 85$-107 meV and pre-exponential term $\tau_0 = (0.2\text{-}16)\cdot\times 10^{-15}$ s were obtained by fitting to Arrhenius law. However, τ_0 values $\sim 10^{-15}$ s are close to the electronic reciprocal collision time and seem to be physically unreasonable. Therefore, the data for such compositions were fitted using an alternative empirical description of relaxation, that is, the Vögel-Fulcher relation:

$$\tau = \tau_0 \exp[U/k_B(T_m - T_f)] \tag{5.7}$$

This relation includes one additional fitting parameter, compared to Arrhenius law, the so called freezing temperature T_f, and usually is used to describe the behaviour of relaxor polar clusters. In SMnT system, polar clusters can be formed by "agglomeration" of the dipoles, created by the off-centre Mn dopant, for Mn contents higher than a certain value. Fitting to Vögel-Fulcher relation, the activation energy U and the relaxation time τ_0 equal to 71±7 meV and $(7.8\pm3.8) \times 10^{-14}$ s were obtained, what seems to be more realistic, than those of Arrhenius law. The obtained values are also listed in Table 5.3, revealing that the freezing temperature T_f increases with Mn content. It is worthwhile to mention here that fitting the data of $Sr_{1-x}Mn_xTiO_3$ ceramics with $x < 0.03$ to Vögel-Fulcher relation had no stable solution. Based on this observation, a crossover at $x = 0.03$ from hopping of individual off-centre Mn^{2+} ions to a polar clusters reversal dominant mechanism of relaxational dynamics is proposed. This idea is supported by a sudden increase of value α at $x = 0.03$ (see Table 5.3), corresponding to a broader distribution of relaxation time.

Several types of dielectric relaxations were reported in ST-based systems (Bianchi et al., 1995; Johnson et al., 1970; Ang and Yu, 2002; Neumann and Artl, 1986; Sotnikov et al., 1999; Kleemann et al., 1997; Ang et al., 2000c; Lemanov et al., 2000). Some of them are listed in Table 5.4 together with correspondent values of the parameters U and τ_0, obtained by fitting with the Arrhenius law.

Table 5.3. Parameters of the Arrhenius law and Vögel-Fulcher relation describing relaxational dynamics in SMnT ceramics.

		ARRHENIUS LAW		**VÖGEL-FULCHER RELATION**		
x	**α**	U**, meV**	τ_0**, s**	U**, meV**	τ_0**, s**	T_f**, K**
0.0025	~0.68	34	8.8×10^{-12}	-	-	-
0.005	~0.68	52	6.6×10^{-14}	-	-	-
0.01	~0.73	69	1.3×10^{-14}	-	-	-
0.02	~0.70	73	3.8×10^{-14}	-	-	-
0.03	~0.76	85	1.6×10^{-14}	78	4.0×10^{-14}	2.2
0.05	~0.80	91	4.4×10^{-15}	71	5.0×10^{-14}	5.8
0.10	~0.81	99	1.1×10^{-15}	73	7.8×10^{-14}	5.0
0.15	~0.81	107	2.1×10^{-16}	64	11.6×10^{-13}	10.1

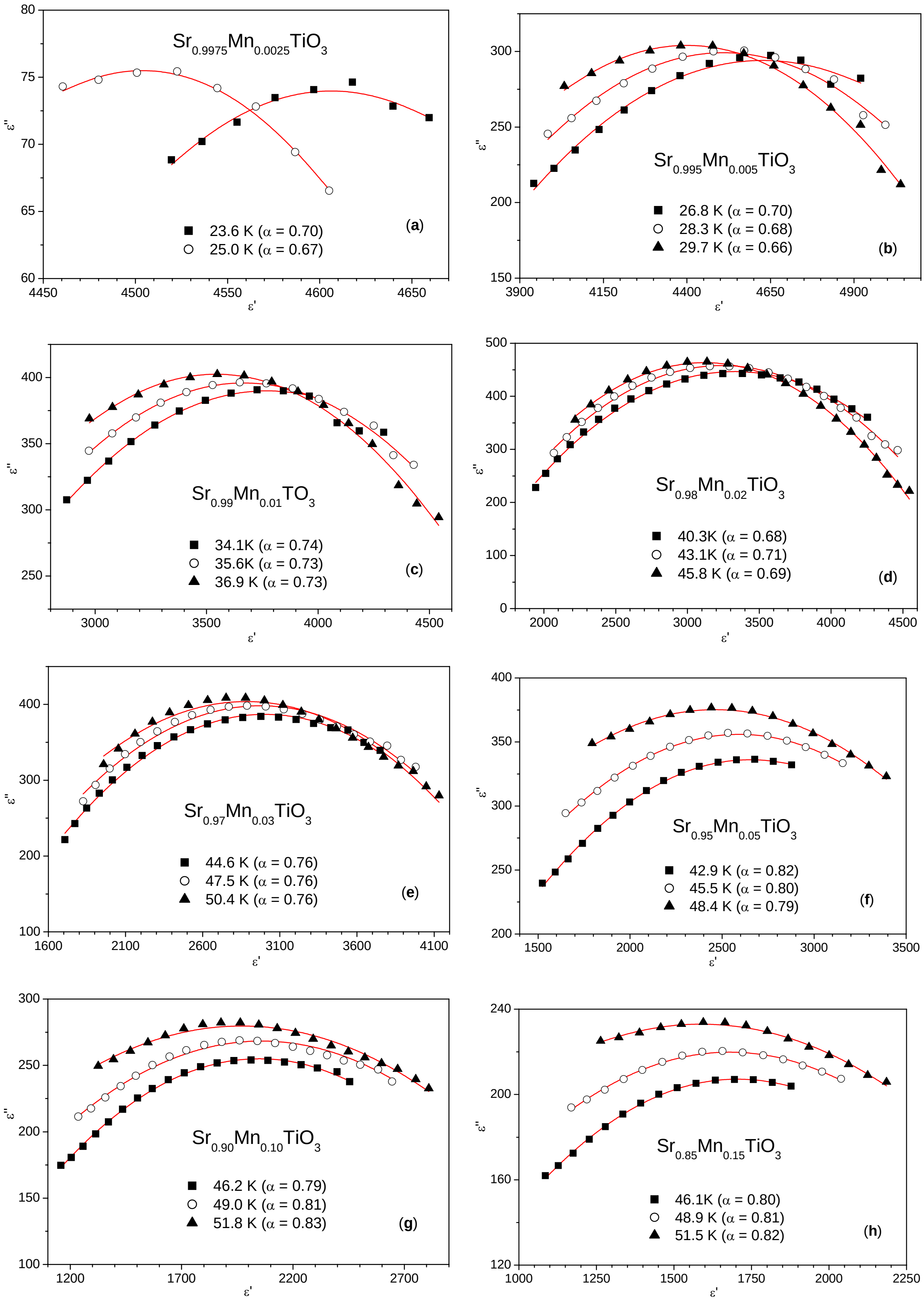

FIGURE 5.13. Cole-Cole plots ε'' versus ε' (solid squares) and fits (solid lines) for the relaxation mode of $Sr_{1-x}Mn_xTiO_3$ ceramics with $x = 0.0025$ (**a**), 0.005 (**b**), 0.01 (**c**), 0.02 (**d**), 0.03 (**e**), 0.05 (**f**), 0.10 (**g**) and 0.15 (**h**) at different temperatures.

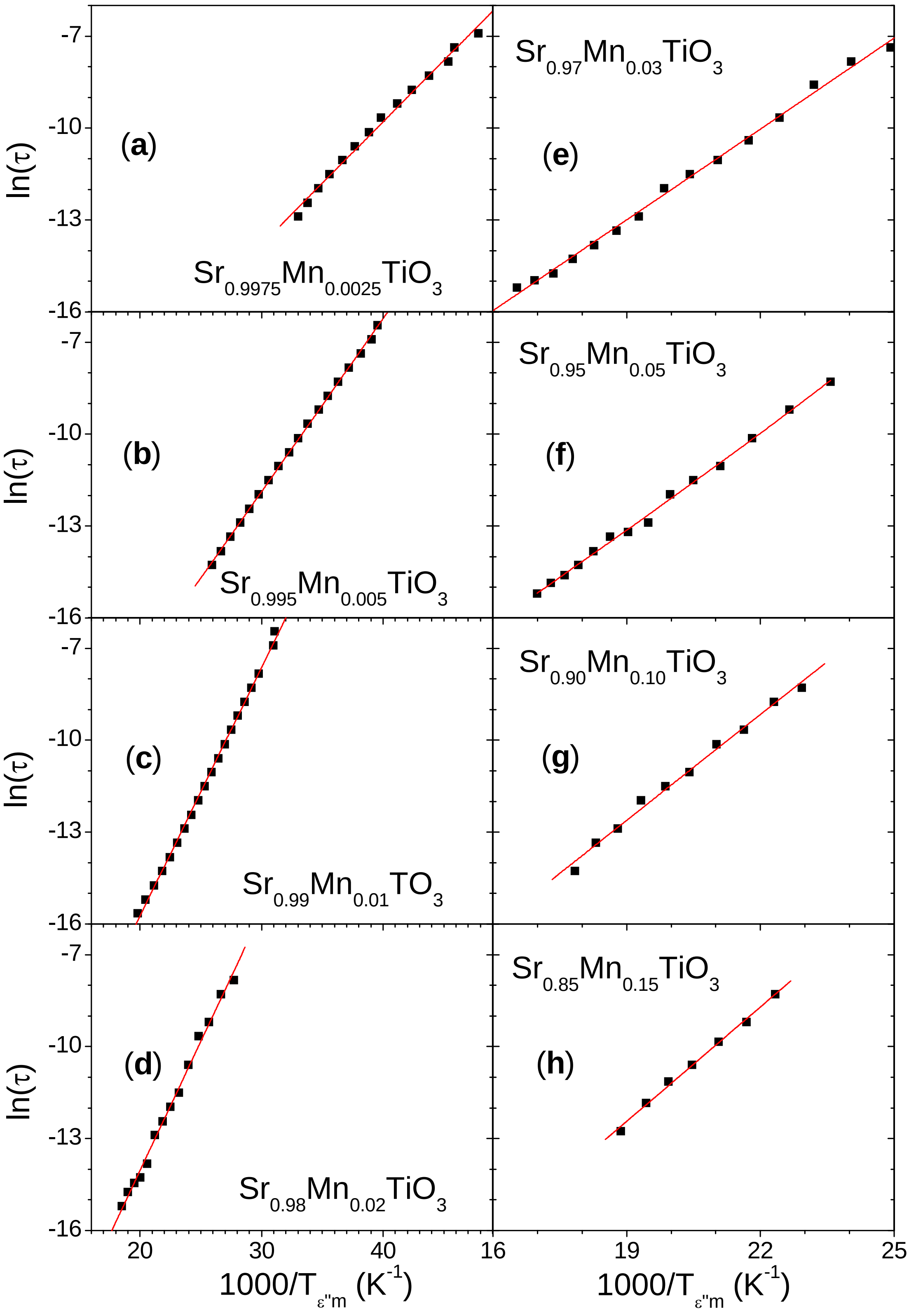

FIGURE 5.14. Arrhenius plots ln(τ) versus 1000/$T_{\varepsilon''\mathrm{m}}$ ($T_{\varepsilon''\mathrm{m}}$ is the temperature at which maximum of ε'' occurs at the angular frequency $w = 2\pi f$; $\tau = w^{-1}$) for $Sr_{1-x}Mn_xTiO_3$ samples with x = 0.0025 (**a**), 0.005 (**b**), 0.01 (**c**) 0.02 (**d**), 0.03 (**e**), 0.05 (**f**), 0.10 (**g**) and 0.15 (**h**).

Interfacial polarisation of the Maxwell-Wagner type could be observed in $Sr_{1-x}Mn_xTiO_3$ system also, as in any ceramics with grains and grain boundaries, possessing different electric properties. However, the Maxwell-Wagner type relaxation usually is ~10 orders slower and its activation energy is ~10 times higher (Neumann and Artl, 1986). Much higher activation energy is also reported for low-frequency dielectric relaxations attributed to oxygen vacancies (Ang et al., 2000c; Lemanov et al., 2000) and to ionic polarisation of Skanavi model (Johnson et al., 1970). The latter model postulates the appearance of more than one off-centre equilibrium position for Ti ion due to the distortions, introduced by rare-earth ions with charge state of 3+ and associated Sr-site vacancies. And thermally activated motion between these equivalent minima leads to the observed relaxation. According to the Skanavi model, activation energy is expected to increase with increasing dopant concentration, which in turns promotes an increase of distortion. However, this model, as all models above, is not applicable to SMnT system, because contrary to the case of all rare-earth containing ST compositions, ln(τ) versus 1000/$T_{\varepsilon''m}$ plots undergo a crossover from Arrhenius law to Vögel-Fulcher relation.

Thus, the relaxation dynamics of SMnT system is very similar to that of $Sr_{1-1.5x}Bi_xTiO_3$, in which Vögel-Fulcher relation, related to the relaxation of dynamic polar nanoclusters, created by the off-centred dopant ions interacting via crystal lattice, i.e., correlated motion of the off-centred dopant ions (Bovtun et al., 2004), can be applicable starting from x = 0.04 (Ang and Yu, 2002). Below that concentration, dispersion in Bi-doped ST, corresponding to the relaxation process, attributed to reorientation of individual dopant dipoles, is better described by Arrhenius law with parameters very close to those of SMnT system (Ang and Yu, 2002). Moreover, the origin of this relaxation in $Sr_{1-1.5x}Bi_xTiO_3$, and consequently in $Sr_{1-x}Mn_xTiO_3$, is similar to that in $K_{1-x}Li_xTaO_3$ (Bovtun et al., 2004), i.e., off-centre dopant relaxation at Sr site of highly polarisable ST lattice.

In addition, a low-temperature relaxation with U = 75 meV and τ_0 ~10^{-14} s, independently on the impurity of substitution and its concentration, was observed in many perovskite crystals and ceramics and was proposed to be due to a polaronic mechanism (Bidault et al., 1995). However, undoped and Ca-doped ST, for which the dielectric loss peaks appeared around 10-13 K, could not be described by the Arrhenius law with such parameters. Regarding SMnT system present in this work, several misfits between the observed behaviour and polaronic model are evident. Arrhenius law is well applicable for

Mn content $x < 0.03$, but with activation energy increasing with x, what is in contradiction to almost invariant values of U and τ_0 obtained by Bidault et al. (1995). On the other hand, U and τ_0 close to 75 meV and $\tau_0 \sim 10^{-14}$ s, respectively, were obtained for $x \geq 0.03$, but by fitting with Vögel-Fulcher relation and not with Arrhenius law.

Table 5.4. Relaxation processes observed in ST-based systems and their Arrhenius law parameters.

SYSTEM	U, meV	τ_0, s	PROPOSED MECHANISM	REF.
$SrTiO_3$, $BaTiO_3$	700	$(2\text{-}6) \times 10^{-2}$	Interfacial polarisation of the Maxwell-Wagner type	Neumann and Artl, 1986
Ba:$SrTiO_3$	40-45	5×10^{-12} - 5×10^{-10}	Electronic process of unknown nature	Sotnikov et al., 1999
	100-120	10^{-11} - 10^{-10}	Off-centre ion hopping between symmetry equivalent position	Sotnikov et al., 1999
Ca:$SrTiO_3$	11-15	$(1.4\text{-}2.3) \times 10^{-10}$	Nanoregions around dilute off-centre dopant dipoles	Bianchi et al., 1995; Kleemann et al., 1997
Bi:$SrTiO_3$	32-34 60-64	$(0.4\text{-}2) \times 10^{-13}$ $(0.4\text{-}1) \times 10^{-13}$	Non-interacting polar clusters formed by off-centre dopant ions with and without Sr vacancy nearby	Ang and Yu, 2002
	300-900	$(0.5\text{-}7) \times 10^{-12}$	Oxygen-vacancy-related low-frequency dielectric relaxation	Ang et al., 2000c
$SrTiO_3$-$SrMg_{1/3}Nb_{2/3}O_3$, $SrTiO_3$-$SrSc_{1/2}Ta_{1/2}O_3$	210-300	$(0.2\text{-}5) \times 10^{-11}$	Oxygen-vacancy-related low-frequency dielectric relaxation	Lemanov et al., 2000
	10-20	$(0.2\text{-}15) \times 10^{-9}$	Polaronic relaxation	Lemanov et al., 2000
ST doped with rare-earth ions	212-496	7×10^{-14} - 9×10^{-10}	Ionic polarisation of Skanavi model	Johnson et al., 1970

5.2. Hysteresis loops of $Sr_{1-x}Mn_xTiO_3$ system

The polar nature of the dielectric anomaly observed in SMnT ceramic samples was further confirmed by the measurements of the $P = f(E)$ curves. Figures 5.15 and 5.16 display the P versus E hysteresis loops measured at 50 Hz, under applied ac fields up to

~15 kV/cm and at different temperatures for $Sr_{0.995}Mn_{0.005}TiO_3$ and $Sr_{0.98}Mn_{0.02}TiO_3$ samples, respectively. Slim S-shaped loops, observed at low temperatures, suggest the appearance of a polar state with non-zero remnant polarization P_r. Further Mn addition apparently results in the increase of the loop area with the concurrent increase of P_r. The hysteresis response slowly degenerates into just non-linearity as the temperature increases to ~40 K for $Sr_{0.995}Mn_{0.005}TiO_3$ and to ~70 K for $Sr_{0.98}Mn_{0.02}TiO_3$, as shown in Figures 5.15 and 5.16. Figure 5.17 presents detailed evolution of P_r that gradually vanishes with increasing temperature. This behaviour is typical for ferroelectric relaxors (Smolenski, 1970).

The appearance of a strong dielectric peak, the increase of the parameter T_0 in both Curie-Weiss and Barrett fits, and the decrease of $(T_1 - 2T_0)$ with Mn addition, as well as the observation of distinct hysteresis suggest ferroelectric-type ordering induced by polar defects. Mn^{2+} ions located at off-centre position at Sr sites are very probable polar defect candidates due to their smaller ionic radii, when compared to Sr^{2+} (Shannon, 1976).

On the other hand, a rounded permittivity peak, a frequency dispersion, a departure from the Curie-Weiss law and a slim shape of the loops are all indicative of a relaxor-type system. This may happen due to appearance of local electric and/or strain fields induced by random Mn^{2+} distribution. In this context, the $Sr_{1-x}Mn_xTiO_3$ system should be similar to the $Sr_{1-x}Ca_xTiO_3$ one.

In 1961, Mitsui and Westphal (1961) reported the dielectric anomaly in $\varepsilon'(T)$ of $Sr_{1-x}Ca_xTiO_3$ ceramic samples with Ca content up to $x = 0.20$, although slim hysteresis loops were observed at 4.3 K for $x \leq 0.10$ only. The field-dependent remnant polarization tailed off to zero well above T_m similarly to SMnT samples (Figures 5.15 and 5.16). The ferroelectric phase produced by the small Ca addition was ascribed to the occupation of off-centre positions at Sr sites and consequently to the enlarged ionic polarisability of Ca^{2+} in the ST lattice (Mitsui and Westphal; 1961). Later, the dielectric behaviour of $Sr_{1-x}Ca_xTiO_3$ system for $x < 0.12$ was studied in detail (Bednorz and Müller; 1984) and attributed to an impurity-induced second order phase transition disrupted by the random electric and strain fields. In addition, Ca^{2+} ions are close to the Mn^{2+} ones in terms of ionic size (Shannon, 1976) and electronic polarisability (Shannon, 1993) (see Figure 1.46).

Thus, there is a number of similar features in the behaviour of Sr-site Mn- and Ca-doped ST systems that makes one believe that the nature of polar behaviour is due to off-centre ions forming dipoles randomly distributed in the highly polarisable host lattice with a concurrent effect of local electric and/or strain fields.

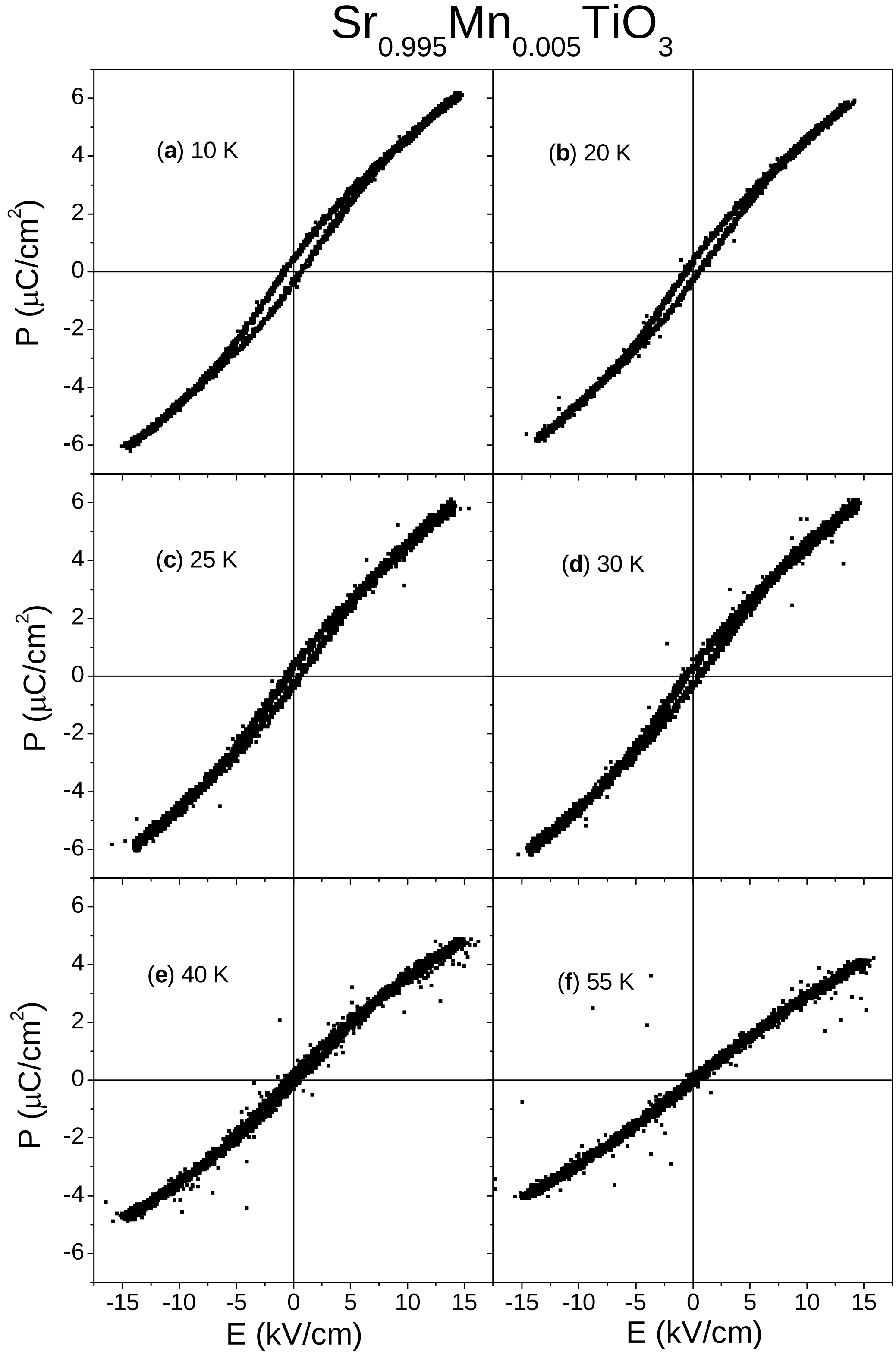

FIGURE 5.15. Hysteresis loops *P*(*E*) at 50 Hz of $Sr_{0.995}Mn_{0.005}TiO_3$ ceramics at 10 (**a**), 20 (**b**), 25 (**c**), 30 (**d**), 40 (**e**) and 55 K (**f**).

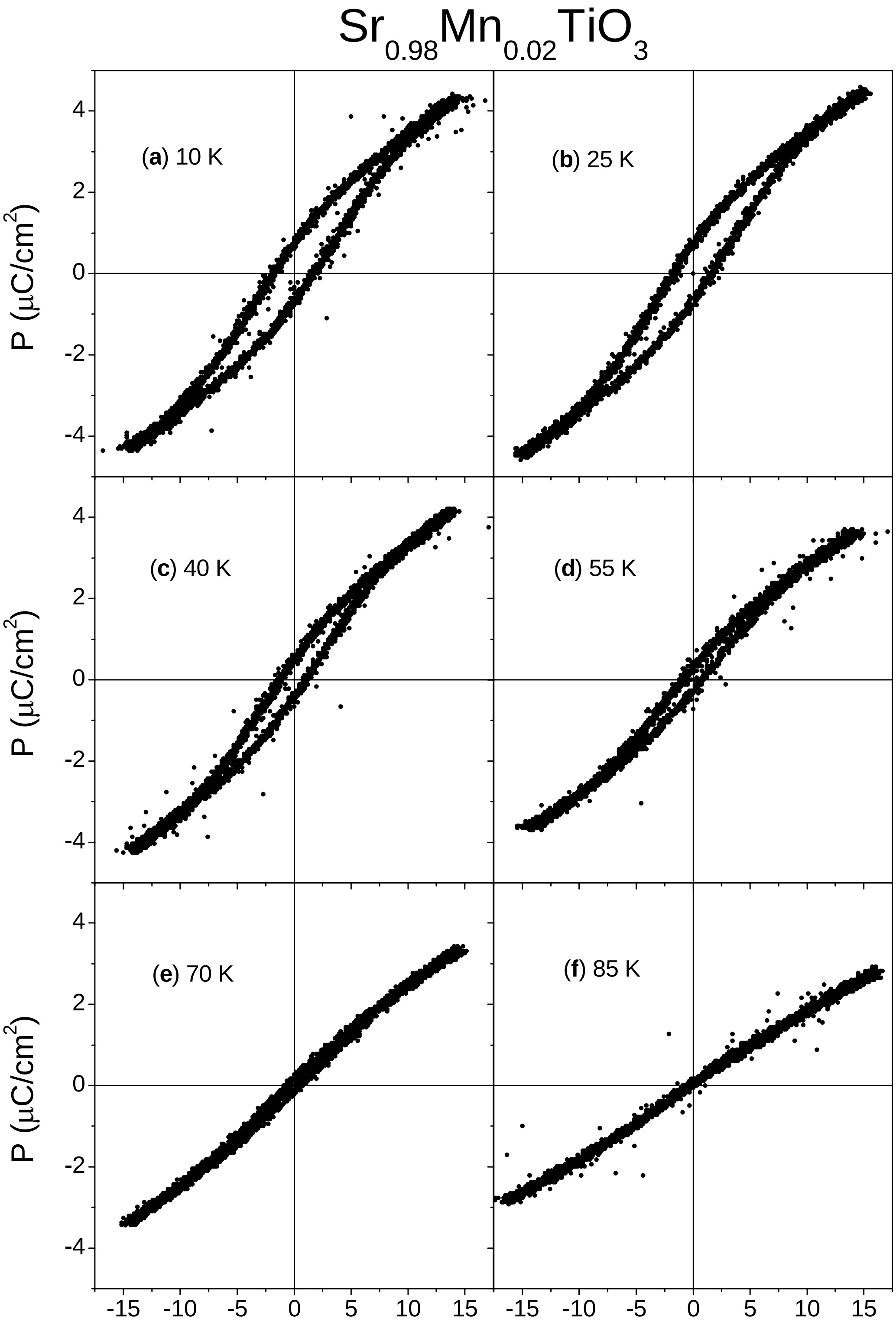

FIGURE 5.16. Hysteresis loops *P*(*E*) at 50 Hz of $Sr_{0.98}Mn_{0.02}TiO_3$ ceramics at 10 (**a**), 25 (**b**), 40 (**c**), 55 (**d**), 70 (**e**) and 85 K (**f**).

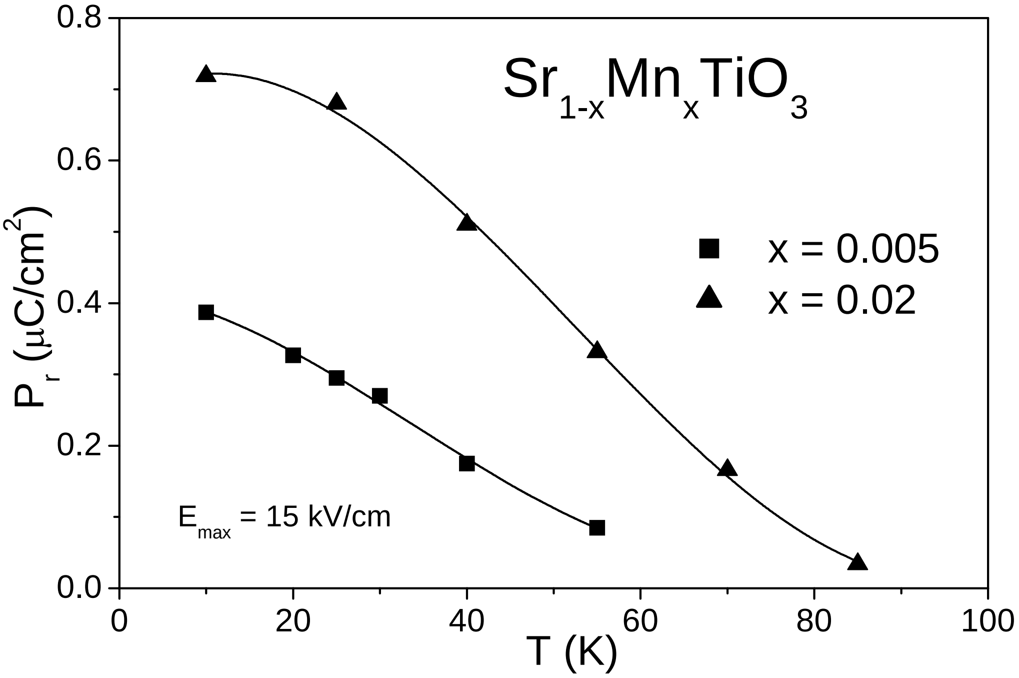

FIGURE 5.17. Remnant polarisation of $Sr_{1-x}Mn_xTiO_3$ ceramics with $x = 0.005$ (squares) and $x = 0.02$ (triangles), obtained from hysteresis loops measured at 50 Hz, as a function of temperature.

However, there are several differences between these two systems. The solid solubility of Mn at Sr site of ST is strongly restricted, whereas $Sr_{1-x}Ca_xTiO_3$ solid solution can be obtained in the whole composition range (Ranjan et al., 2000). Another major difference is related to the behaviour of maximum dielectric permittivity value with dopant content. For $Sr_{1-x}Ca_xTiO_3$, ε'_m increases with x increasing up to 0.0107 and further decreases, as shown in Figure 1.26 (Bednorz and Müller, 1984), while for $Sr_{1-x}Mn_xTiO_3$ that just continuously decrease with increasing x, as shown in Figure 5.3. In addition, a frequency dispersion observed in $Sr_{1-x}Ca_xTiO_3$ single crystals in the limit of small x (Bianchi et al., 1995), is much smaller than that in $Sr_{1-x}Mn_xTiO_3$ system.

5.3. Dielectric properties at high frequency

5.3.1. Dielectric properties in microwave range (1 MHz - 1.8 GHz)

Dielectric spectra in microwave range were obtained for $Sr_{0.95}Mn_{0.05}TiO_3$ and $SrTi_{0.95}Mn_{0.05}O_3$ ceramic samples, as examples for the SMnT and STMn systems respectively. The spectra of $Sr_{0.95}Mn_{0.05}TiO_3$ are presented in Figure 5.18 and those of $SrTi_{0.95}Mn_{0.05}O_3$ are shown in Figure 5.19.

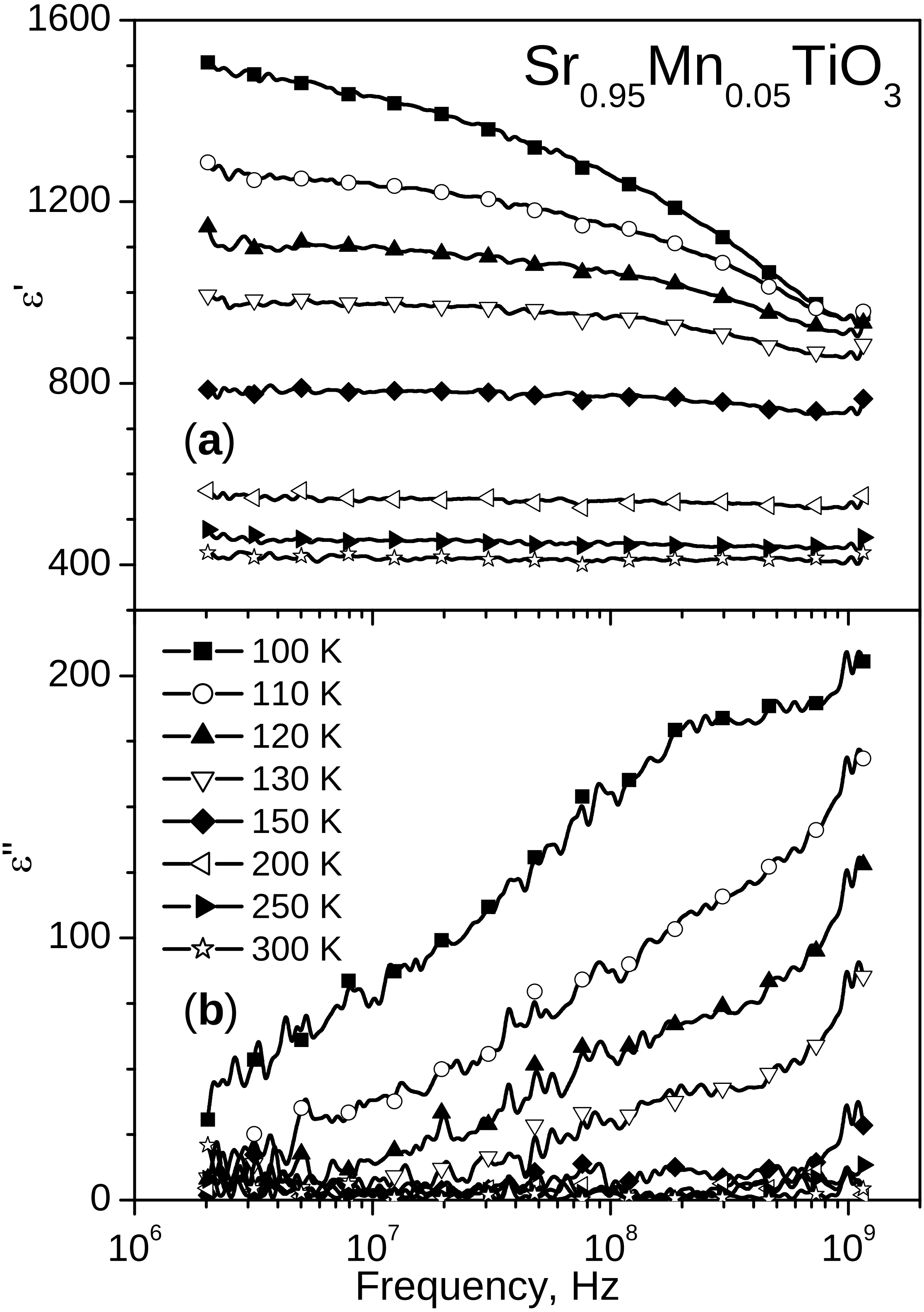

FIGURE 5.18. Frequency dependence of real ε' (**a**) and imaginary ε'' (**b**) parts of dielectric permittivity of $Sr_{0.95}Mn_{0.05}TiO_3$ ceramics in microwave range at 100, 110, 120, 130, 150, 200, 250 and 300 K.

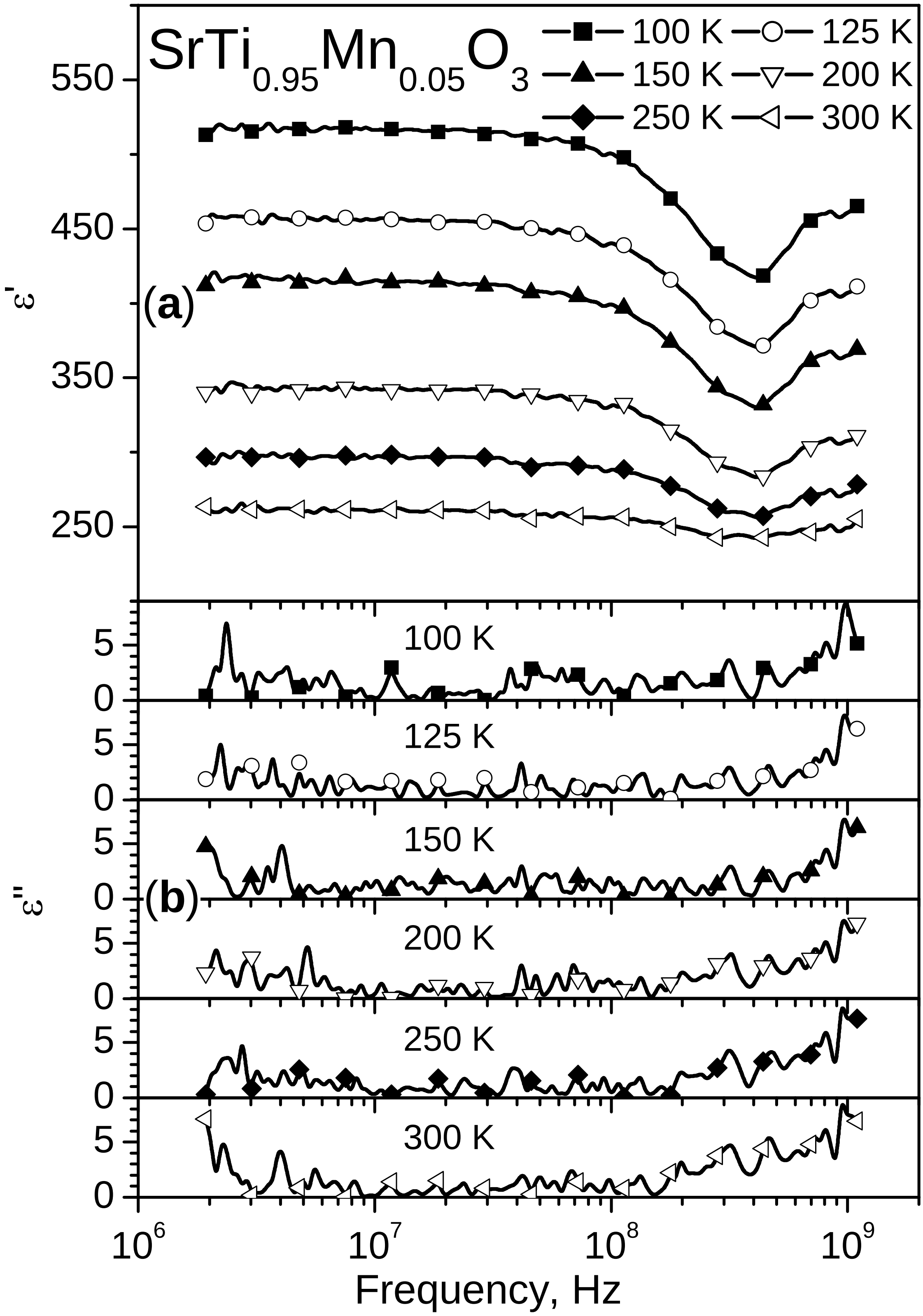

FIGURE 5.19. Frequency dependence of real ε' (**a**) and imaginary ε'' (**b**) parts of dielectric permittivity of $SrTi_{0.95}Mn_{0.05}O_3$ ceramics in microwave range at 100, 125, 150, 200, 250 and 300 K.

A dielectric relaxation in microwave range is clearly observed for SMnT sample at temperatures of 100-150 K, where ε' decreases and ε'' increases with frequency. Such dielectric behaviour is evidently enhanced with a temperature decrease and/or frequency increase. As the temperature rises to 200-300 K, the relaxation is weakened and/or moved to higher frequencies. The dielectric constant ε' gradually decreases and dielectric loss ε'' keeps almost constant with the temperature increasing in this range, being almost invariant with the frequency at constant temperature and revealing a mean $tan\delta = \varepsilon''/\varepsilon'$ value ~0.0085.

Figure 5.19 presents the microwave spectra for $SrTi_{0.95}Mn_{0.05}O_{3-\delta}$ ceramics. ε' almost does not vary with frequency at constant temperature, except in the vicinity of 0.4 GHz, where some minimum of unknown origin appear. ε'' keeps almost constant in the entire frequency and temperature range of experiment, including the in vicinity of 0.4 GHz. An average value of $tan\delta = \varepsilon''/\varepsilon'$ at 1 GHz was found to be of 0.0216 ± 0.0062 for $SrTi_{0.95}Mn_{0.05}O_{3-\delta}$ ceramics.

5.3.2. Time domain terahertz and infrared spectroscopy results

Time domain terahertz (TDT) transmittance and infrared (IR) reflectivity measurements were performed at room temperature for some SMnT ($Sr_{0.995}Mn_{0.005}TiO_3$ and $Sr_{0.95}Mn_{0.05}TiO_3$) and STMn ($SrTi_{0.99}Mn_{0.01}O_3$ and $SrTi_{0.95}Mn_{0.05}O_3$) compositions. The obtained results are presented in Figure 5.20.

Room-temperature IR reflectivity spectra normalised using THz data were fitted using the generalized four-parameter damped oscillator model of the dielectric function:

$$\varepsilon^*(\omega) = \varepsilon_\infty \prod_j \frac{\omega_{LOj}^2 - \omega^2 + i\omega\gamma_{LOj}}{\omega_{TOj}^2 - \omega^2 + i\omega\gamma_{TOj}} + \frac{f_0}{\omega_0^2 - \omega^2 + i\omega\gamma_0} \tag{5.8}$$

where $\varepsilon_\infty$is the optical permittivity, ω_{LOj} and ω_{TOj} denote the longitudinal and transverse eigen-frequencies of the j-th polar mode, and γ_{LOj} and γ_{TOj} designate the respective damping constants. Additional three-parameter overdamped oscillator mode with frequency ω_0, damping constant γ_0 and strength f_0 was added to take into account the relaxational dispersion below phonon frequencies in $Sr_{0.95}Mn_{0.05}TiO_3$ ceramics (Pashkin, 2004). The fitting curves (solid lines in Figure 5.20) are in rather good agreement with the experimental data (dot lines in Figure 5.20). Corresponding dielectric constant and loss spectra are shown in 5.21.

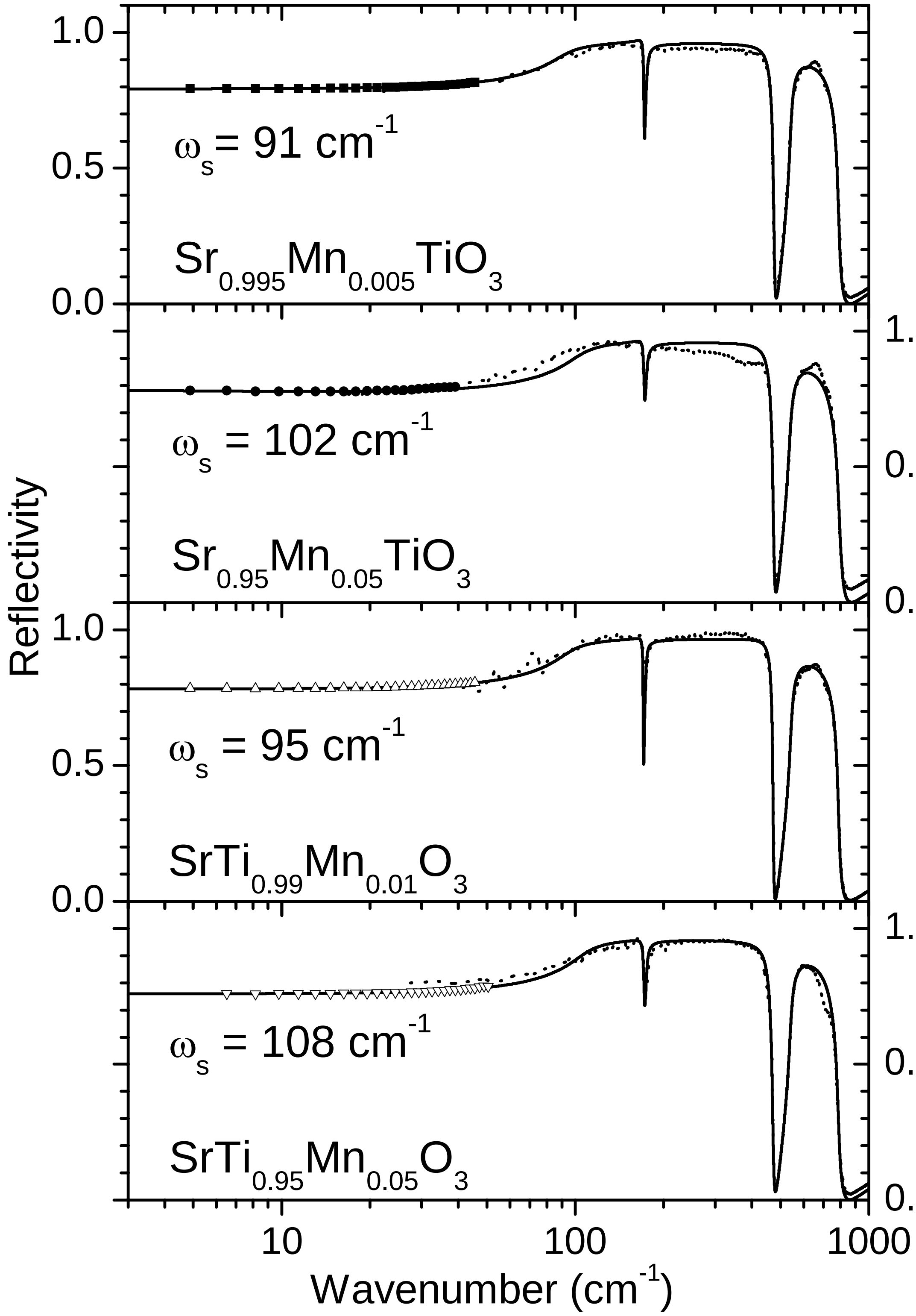

FIGURE 5.20. Room-temperature IR reflectivity spectra (dot lines) of $Sr_{0.995}Mn_{0.005}TiO_3$, $Sr_{0.95}Mn_{0.05}TiO_3$, $SrTi_{0.99}Mn_{0.01}O_3$ and $SrTi_{0.95}Mn_{0.05}O_3$ ceramics and their fits (solid lines) together with TDT data (solid and open symbols). Calculated values of soft mode frequency ω_s are pointed for each composition.

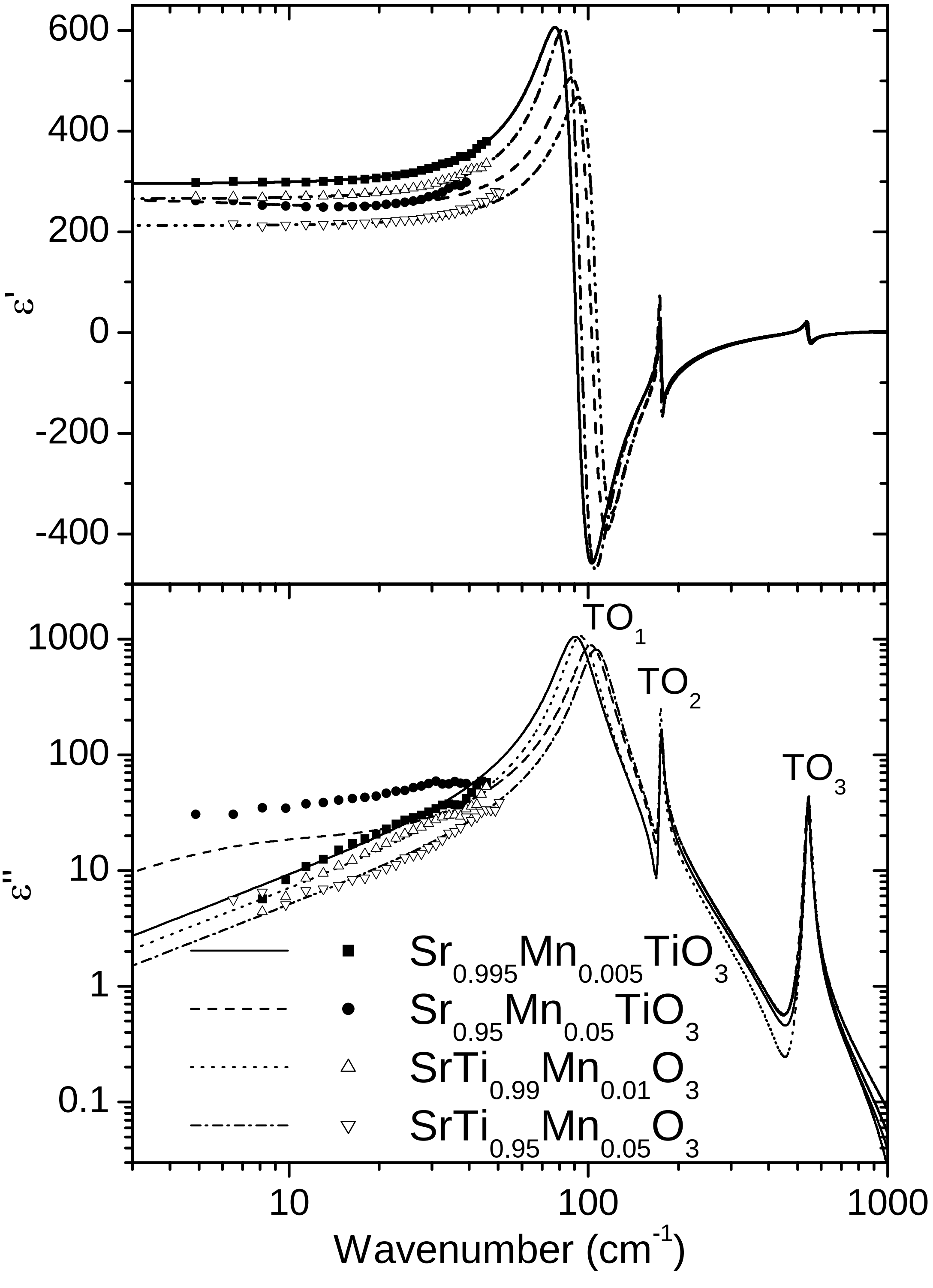

FIGURE 5.21. Room-temperature spectra of real ε' and imaginary ε'' parts of dielectric permittivity in IR range, deduced from the reflectivity fits of $Sr_{0.995}Mn_{0.005}TiO_3$, $Sr_{0.95}Mn_{0.05}TiO_3$, $SrTi_{0.99}Mn_{0.01}O_3$ and $SrTi_{0.95}Mn_{0.05}O_3$ ceramics together with data, obtained by TDT transmission spectroscopy.

As has been shown in Chapter 3, three transverse optic phonon modes TO_1 (soft mode), TO_2 (174 cm^{-1}) and TO_4 (545 cm^{-1}) are observed in undoped $SrTiO_3$ with the cubic phase.

Mn-doping both in Sr- and Ti-sites causes appreciable changes in far IR spectra. The soft mode monotonously hardens with increasing Mn content: from 90 cm^{-1} for $SrTiO_3$ trough 91 cm^{-1} for $Sr_{0.995}Mn_{0.005}TiO_3$ to 102 cm^{-1} for $Sr_{0.95}Mn_{0.05}TiO_3$ in the case of SMnT and from 90 cm^{-1} for $SrTiO_3$ trough 95 cm^{-1} for $SrTi_{0.99}Mn_{0.01}O_3$ to 108 cm^{-1} for $SrTi_{0.95}Mn_{0.05}O_3$ in the case of STMn. The stiffening of the soft mode, accompanied by the corresponding lowering of the dielectric constant value in the terahertz range is stronger for STMn samples. Thus, the phonon contribution to the dielectric constant at room temperature decreases monotonously: from 302 for $SrTiO_3$ trough 298 for $Sr_{0.995}Mn_{0.005}TiO_3$ to 249 for $Sr_{0.95}Mn_{0.05}TiO_3$ in the case of SMnT and from 302 for $SrTiO_3$ trough 268 for $SrTi_{0.99}Mn_{0.01}O_3$ to 212 for $SrTi_{0.95}Mn_{0.05}O_3$ in the case of STMn.

The decreasing phonon contribution can be explained for STMn system by the substitution of more polarisable Ti ions for less polarisable Mn ions. For SMnT system, phonon contribution can be suppressed by the interaction with off-centred ions and polar clusters, by analogy with $Sr_{1-1.5x}Bi_xTiO_3$ and $Ka_{1-x}Li_xTaO_3$ (Bovtun, 2004).

On the other hand, a stepwise decrease of the dielectric constant with the frequency and higher loss are revealed for $Sr_{0.95}Mn_{0.05}TiO_3$ sample in the THz range, as can be seen from Figure 5.21. Thus, the relaxation-like dispersion observed in SMnT over a wide frequency range, reaches a submillimeter range. Therefore, the origin of this dispersion can be attributed to the relaxational hopping of individual (uncorrelated) manganese ions between the off-centre equilibrium positions as the fastest possible polarization process below the optical phonon frequencies.

In addition, $Sr_{0.95}Mn_{0.05}TiO_3$, representing the SMnT system, was examined in THz range down to liquid helium temperature (see Figure 5.22), while $SrTi_{0.95}Mn_{0.05}O_3$, representing STMn, was studied down to liquid nitrogen temperature (see Figure 5.23).

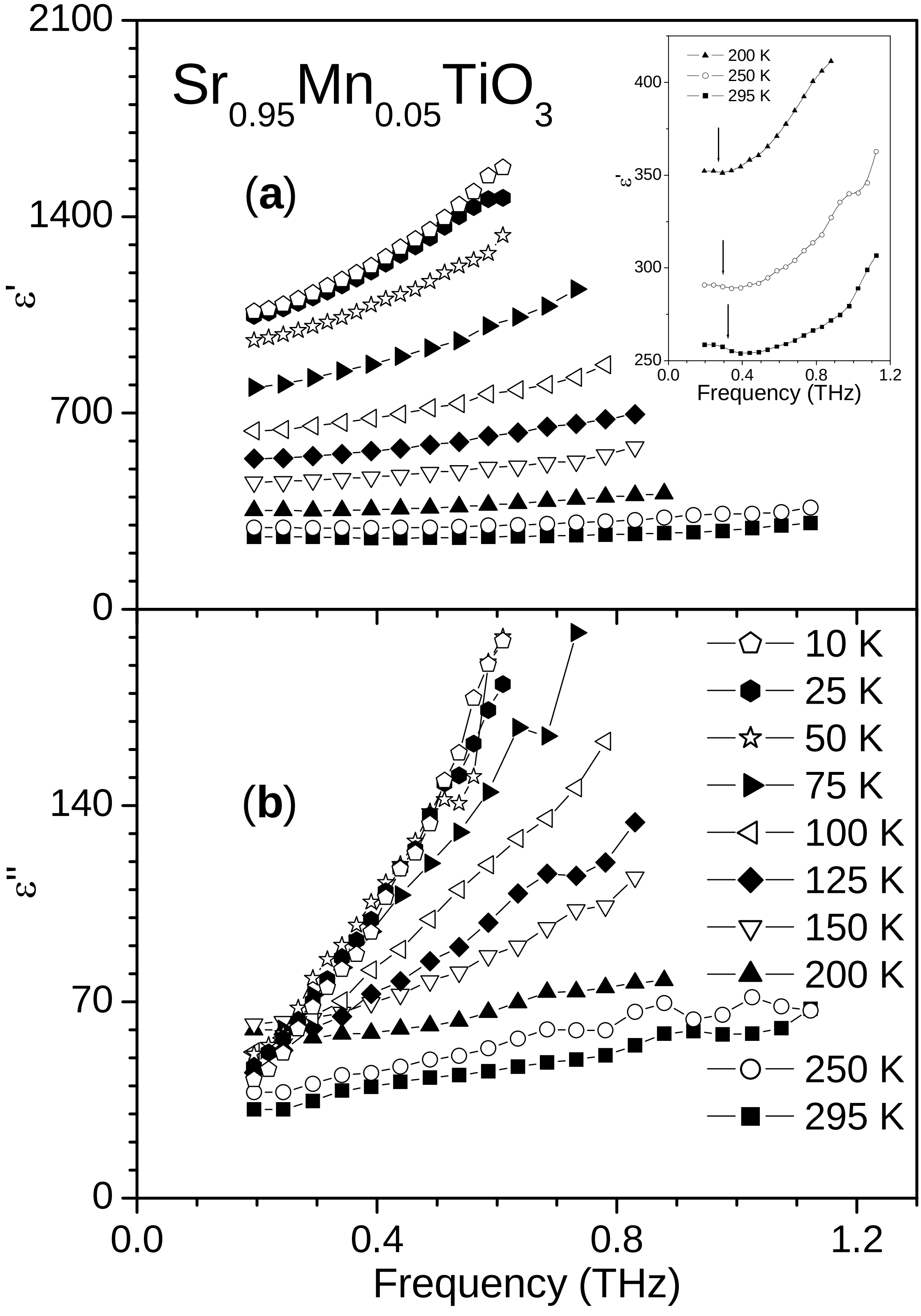

FIGURE 5.22. Frequency dependence of real ε' (**a**) and imaginary ε'' (**b**) parts of dielectric permittivity of $Sr_{0.95}Mn_{0.05}TiO_3$ ceramics in terahertz range at 10, 25, 50, 75, 100, 125, 150, 200, 250 and 295 K. Inset shows ε' as a function of *T* at 200, 250 and 295 K in bigger scale.

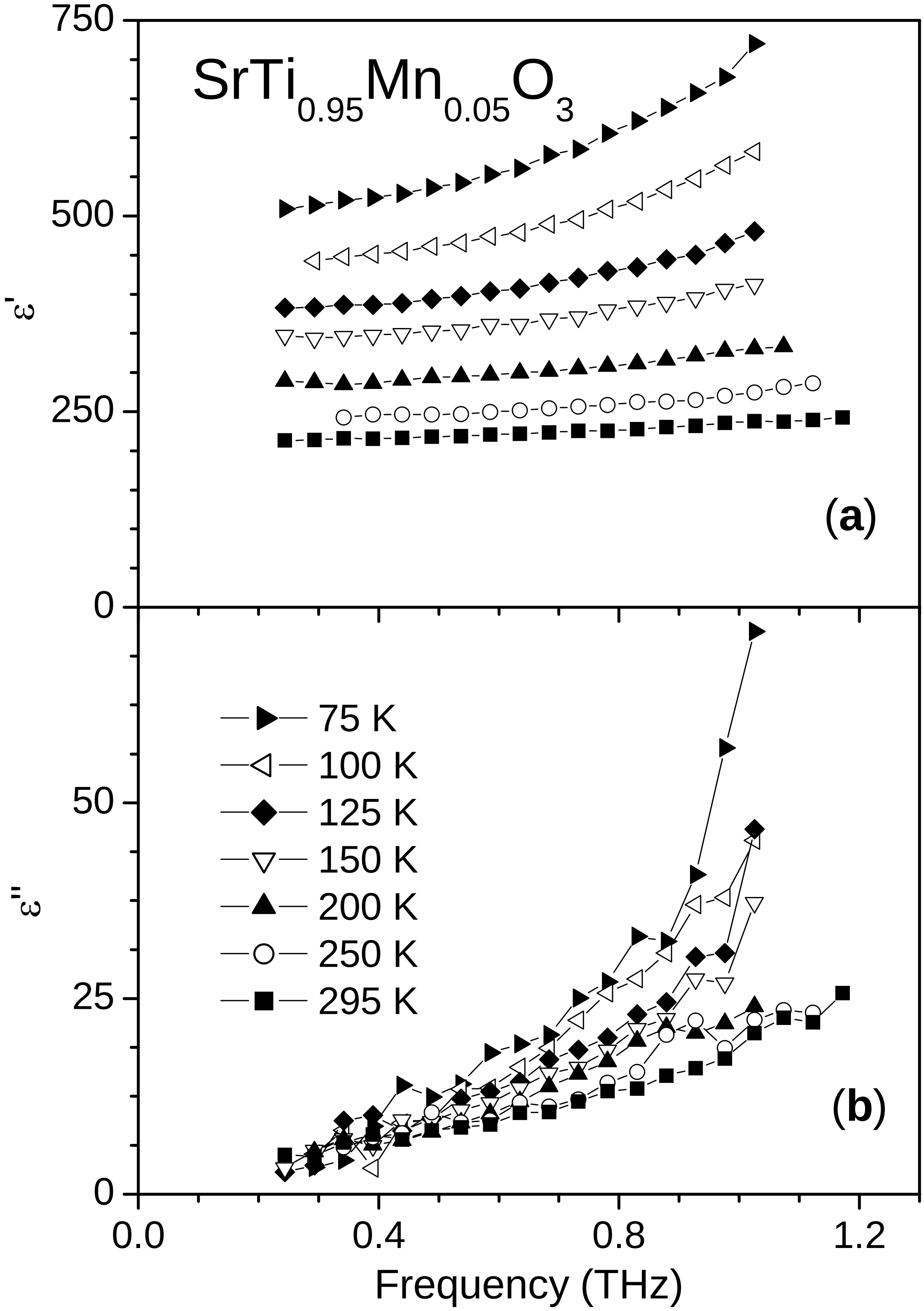

FIGURE 5.23. Frequency dependence of real ε' (**a**) and imaginary ε'' (**b**) parts of dielectric permittivity of SrTi$_{0.95}$Mn$_{0.05}$O$_3$ ceramics in terahertz range at 75, 100, 125, 150, 200, 250 and 295 K.

More considerable variation of dielectric constant and loss values with temperature is observed for $Sr_{0.95}Mn_{0.05}TiO_3$ than for $SrTi_{0.95}Mn_{0.05}O_3$. Hence, TO_1 mode of $Sr_{0.95}Mn_{0.05}TiO_3$ is supposed to soften faster with the temperature decrease than that of $SrTi_{0.95}Mn_{0.05}O_3$. In addition, a stepwise decrease of the dielectric constant in the low frequency side of THz range, corresponding to the relaxation-like dispersion, was observed in $Sr_{0.95}Mn_{0.05}TiO_3$ sample using TDT spectroscopy down to 200 K, as shown in detail in inset of Figure 5.22. At lower temperatures, the relaxation shifts out THz towards MW frequency range. The temperature dependence of both real ε' and imaginary ε'' parts of the dielectric permittivity at the low frequency edge of THz range (at 0.2 THz) is presented in Figure 5.24 (a, b). A rounded maximum in $\varepsilon''(T)$ around 170 K correlate well with the dispersion of the dielectric constant, shown in inset of Figure 5.22.

Figure 5.24 summarises the temperature dependences of both real and imaginary parts of dielectric permittivity ε' and ε'' for $Sr_{0.95}Mn_{0.05}TiO_3$ and $SrTi_{0.95}Mn_{0.05}O_3$ compositions trough all the measurement frequency ranges. The shift of the dielectric permittivity peak for SMnT sample from ~45 K at 100 Hz, trough ~100 K at 1 GHz to ~170 K at 0.2 THz, shown in Figure 5.24 (a, b), unambiguously reveals the evolution of the dielectric relaxation. On the other hand, Figure 5.24 (c, d) demonstrates that values of both real and imaginary parts of dielectric permittivity are close for different frequencies (10 kHz, 1.64 GHz and 0.3 THz) in the error range of the measurements, confirming the absence of any dielectric relaxation for STMn system.

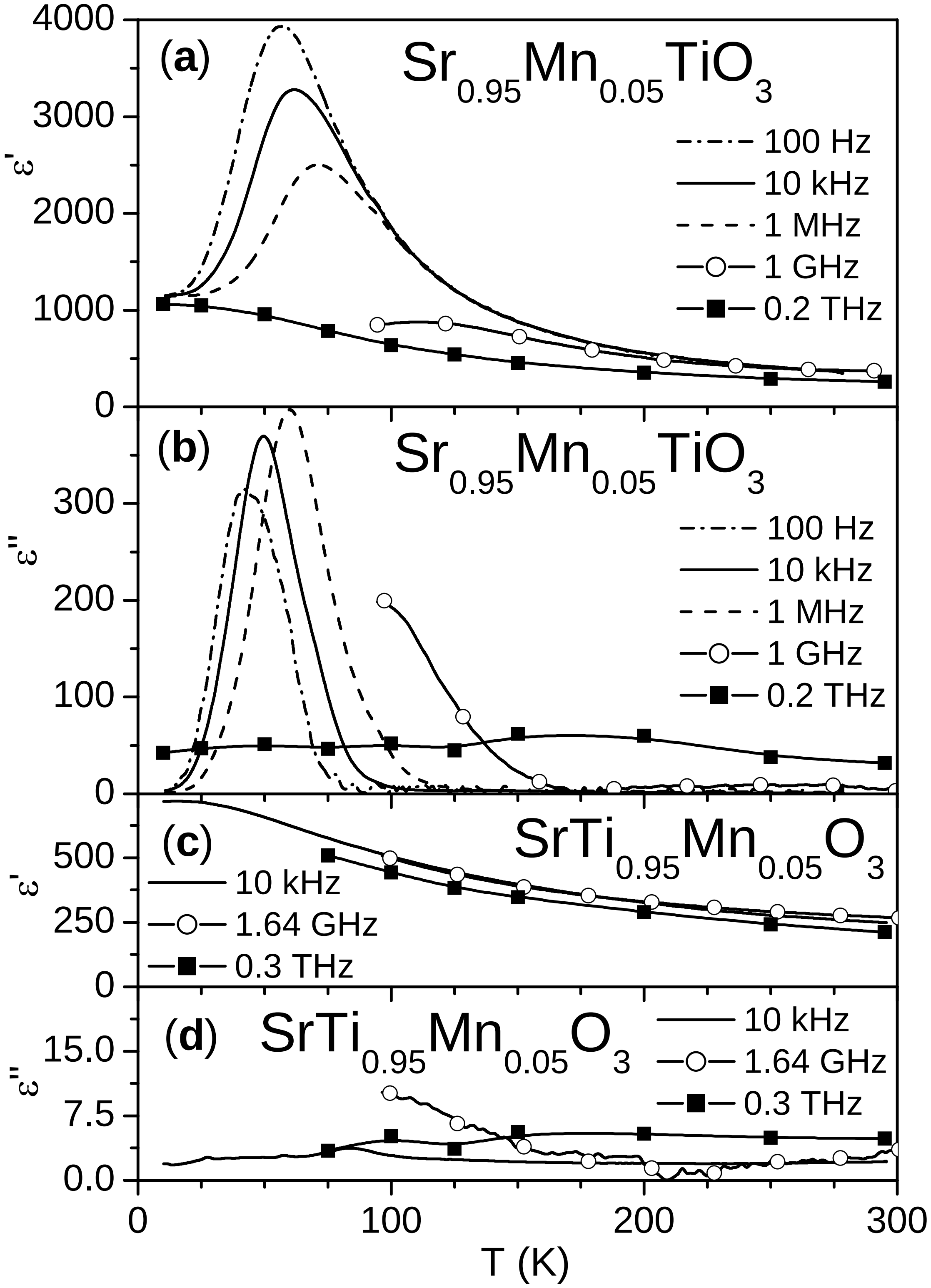

FIGURE 5.24. Temperature dependence of real ε' (**a**) and imaginary ε" (**b**) parts of dielectric permittivity of $Sr_{0.95}Mn_{0.05}TiO_3$ and $SrTi_{0.95}Mn_{0.05}O_3$ ceramics at different frequencies in a wide frequency range.

5.4. Dielectric tunability in the temperature range of 10-300 K

Temperature dependences of the real ε' and imaginary ε'' parts of the dielectric permittivity and of the dissipation factor $tan\delta = \varepsilon''/\varepsilon'$ at 10 kHz under dc electric field up to 22 kV/cm are shown in Figures 5.25-5.28 for SMnT ceramics with Mn content $x = 0$, 0.01, 0.03 and 0.05, respectively.

As presented in Figure 5.25, undoped ST has an adequate tunability (change in the permittivity induced by a dc field) only below ~80 K, what is in agreement with the literature results for single-crystal strontium titanate (Saifi and Cross, 1970; Hemberger et al., 1995). The maximum value of the loss peak, observed at ~75 K at 10 kHz and characteristic for undoped ST, does not reveal strong dependence on the field. This fact confirms the non-polar origin of this loss peak.

Considering the SMnT, the ε' is most field dependent (or tunable) at $T_{\varepsilon'm}$, as shown in Figures 5.26a, 5.27a and 5.28a. The peak of the real part gradually decreases in value, broadens and shifts for ~20 K towards higher temperature with the increase of the bias field. Such behaviour is of a ferroelectric relaxor nature. Thus, the decrease of the ε' can be explained by the stabilization of the local potential wells of the off-centre Mn^{2+} dipoles under applying external electric fields.

Due to the dielectric relaxation, induced by Sr-site Mn-doping in ST, the upper bound of the temperature range, in which ε' is tunable, is expanded from ~80 K for undoped ST to ~150 K for SMnT. There is also a significant influence of bias field on the imaginary part ε'' in temperature range of 10-100 K, as shown in Figures 5.26b, 5.27b and 5.28b. ε'' decrease with the field and such vanishing loss can also be explained by the alignment and stabilisation of off-centre Mn^{2+} dipoles by applied field, reducing the contribution of domain wall dynamics into loss.

The bias field effect on the dielectric response of $SrTi_{1-y}Mn_yO_3$ ceramic system, represented by samples with $y = 0.01$ and 0.05, is depicted in Figures 5.29 and 5.30. Dependences of both real ε' and imaginary ε'' parts of the dielectric permittivity on a applied bias electric field are progressively weakened with increasing Mn content y, as shown in Figures 5.29 (a, b) and 5.30 (a, b). Moreover, $tan\delta$ for $SrTi_{0.95}Mn_{0.05}O_3$ sample, presented in Figure 5.30c, is rather insensitive to the bias field. In contrast, $tan\delta$ for $SrTi_{0.99}Mn_{0.01}O_3$ sample reveal field dependence at low temperature dielectric loss peak.

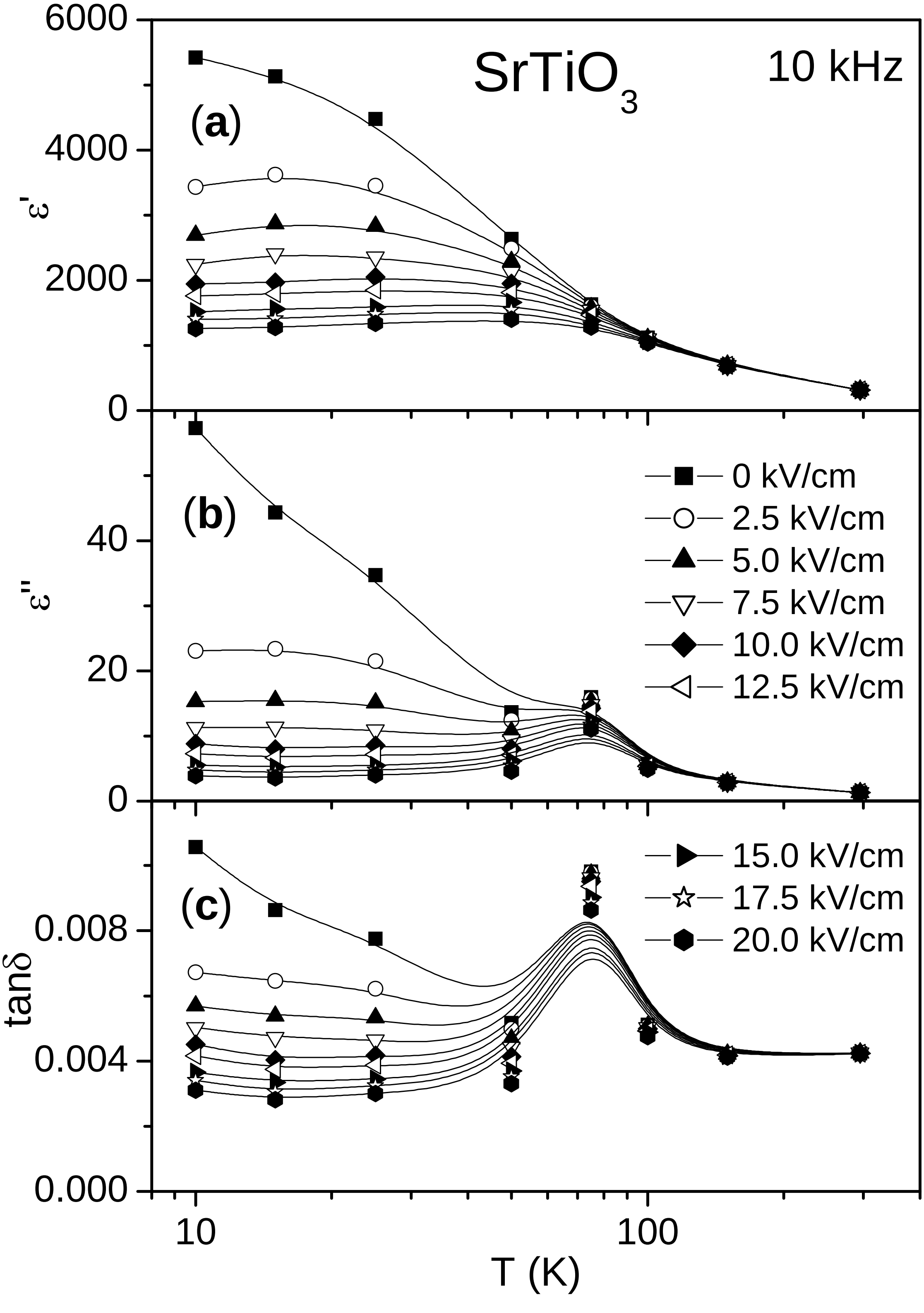

FIGURE 5.25. Variation of real ε' and imaginary ε'' parts of dielectric permittivity and of dissipation factor $tan\delta = \varepsilon''/\varepsilon'$ at 10 kHz with temperature for SrTiO$_3$ ceramics under different dc bias fields.

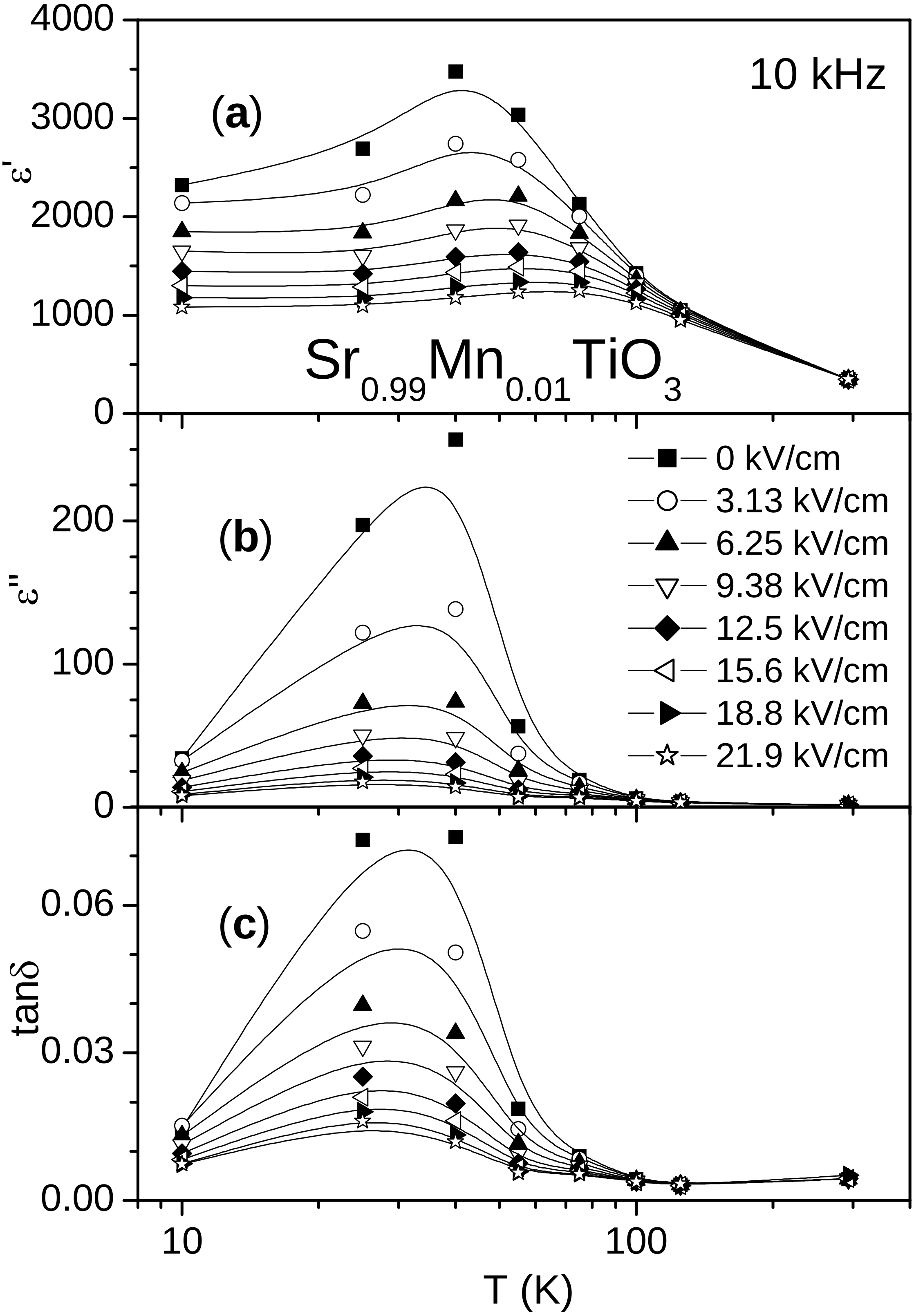

FIGURE 5.26. Variation of real ε' and imaginary ε'' parts of dielectric permittivity and of dissipation factor *tanδ* = ε''/ε' at 10 kHz with temperature for $Sr_{0.99}Mn_{0.01}TiO_3$ ceramics under different dc bias fields.

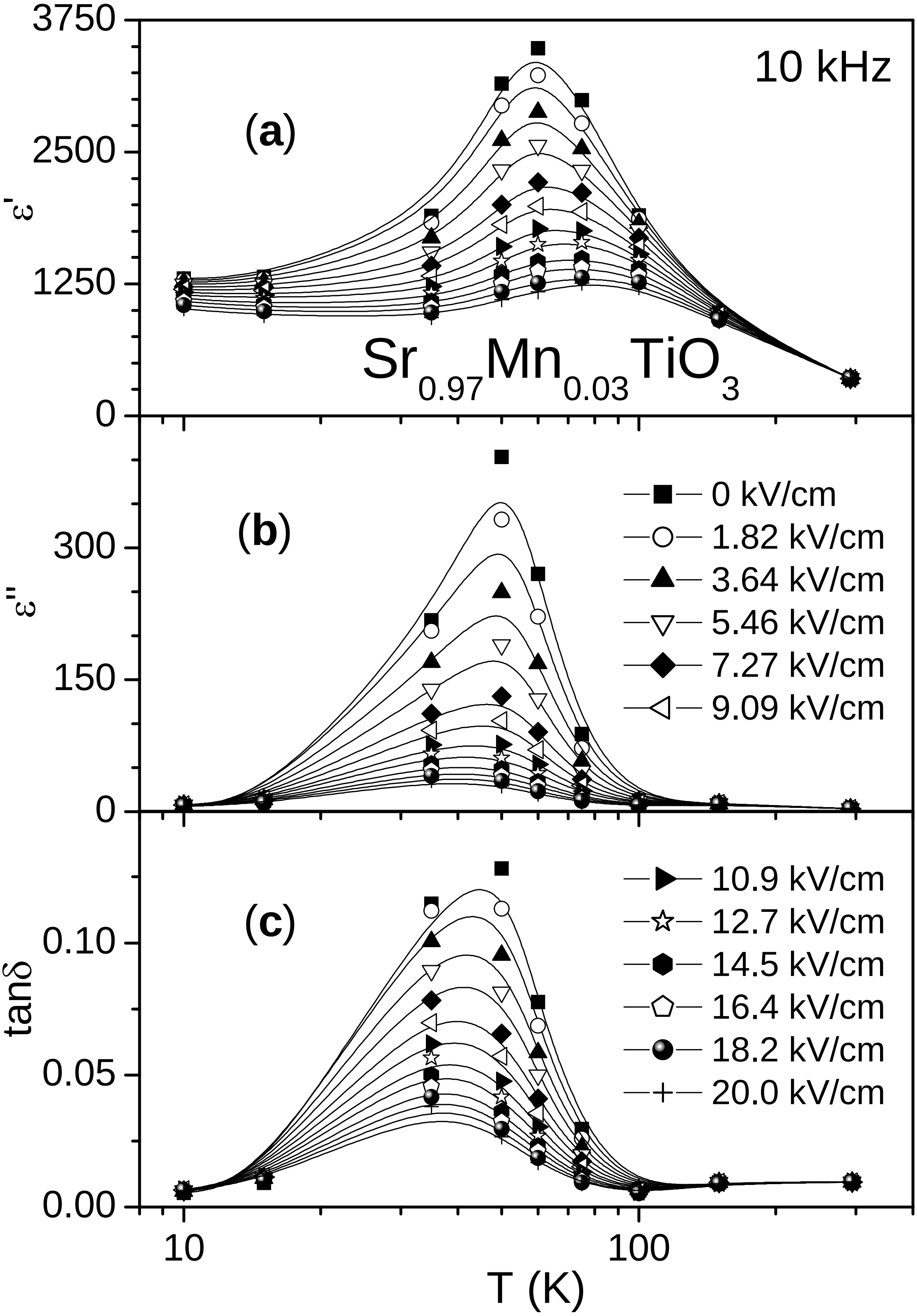

FIGURE 5.27. Variation of real ε' and imaginary ε'' parts of dielectric permittivity and of dissipation factor $tan\delta = \varepsilon''/\varepsilon'$ at 10 kHz with temperature for $Sr_{0.97}Mn_{0.03}TiO_3$ ceramics under different dc bias fields.

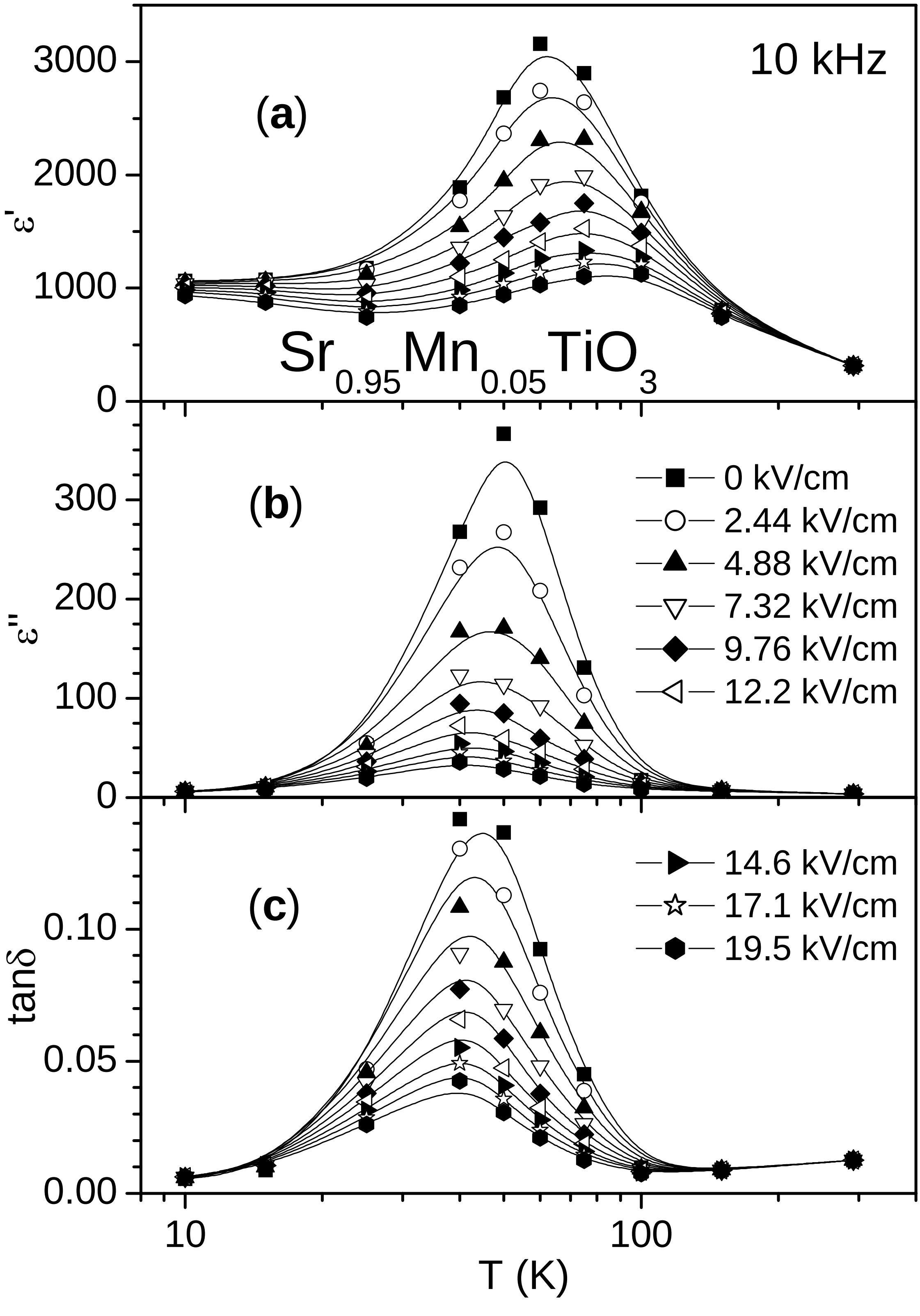

FIGURE 5.28. Variation of real ε' and imaginary ε" parts of dielectric permittivity and of dissipation factor *tanδ* = ε"/ε' at 10 kHz with temperature for $Sr_{0.95}Mn_{0.05}TiO_3$ ceramics under different dc bias fields.

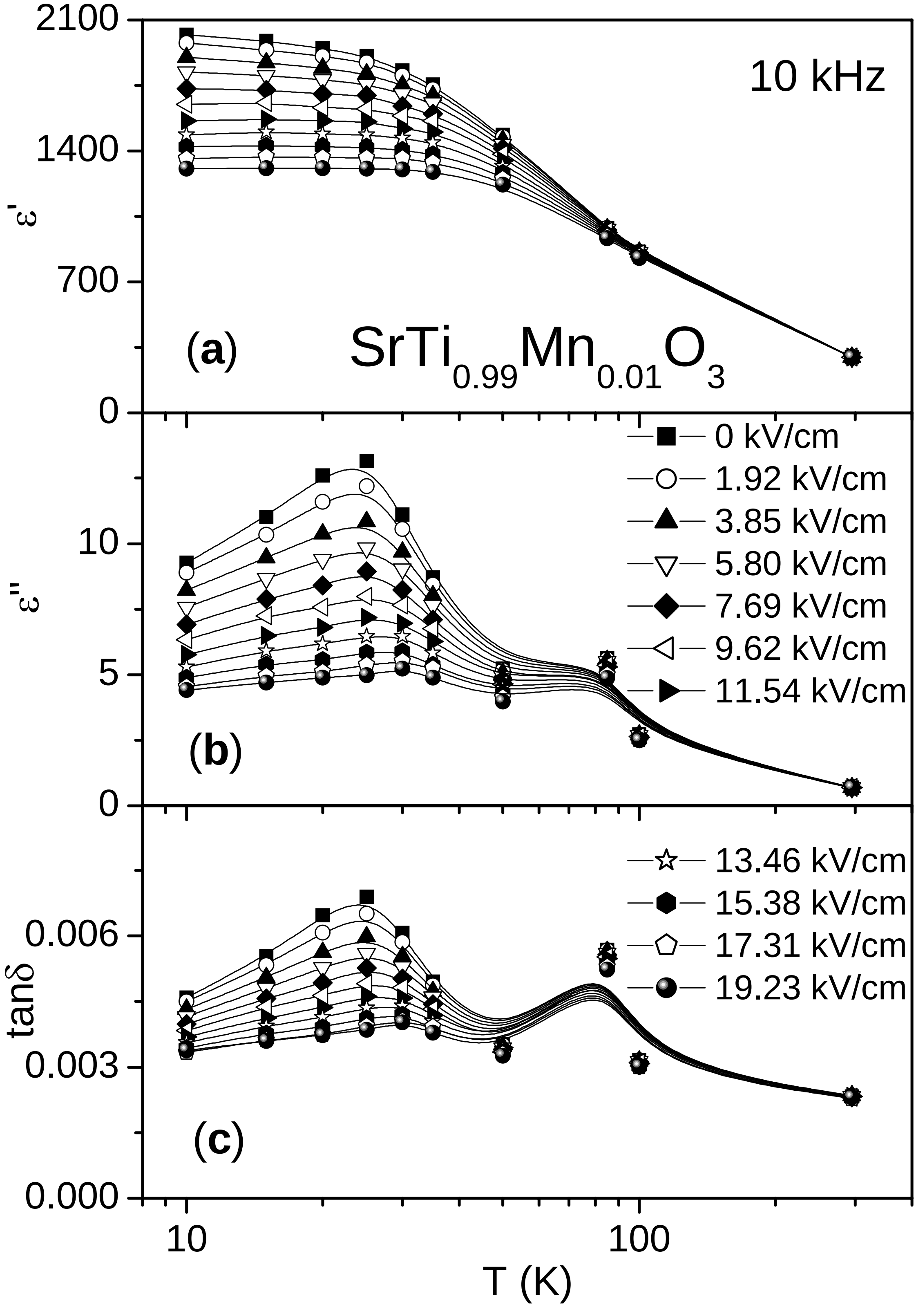

FIGURE 5.29. Variation of real ε' and imaginary ε'' parts of dielectric permittivity and of dissipation factor *tanδ* = ε''/ε' at 10 kHz with temperature for $SrTi_{0.99}Mn_{0.01}O_3$ ceramics under different dc bias fields.

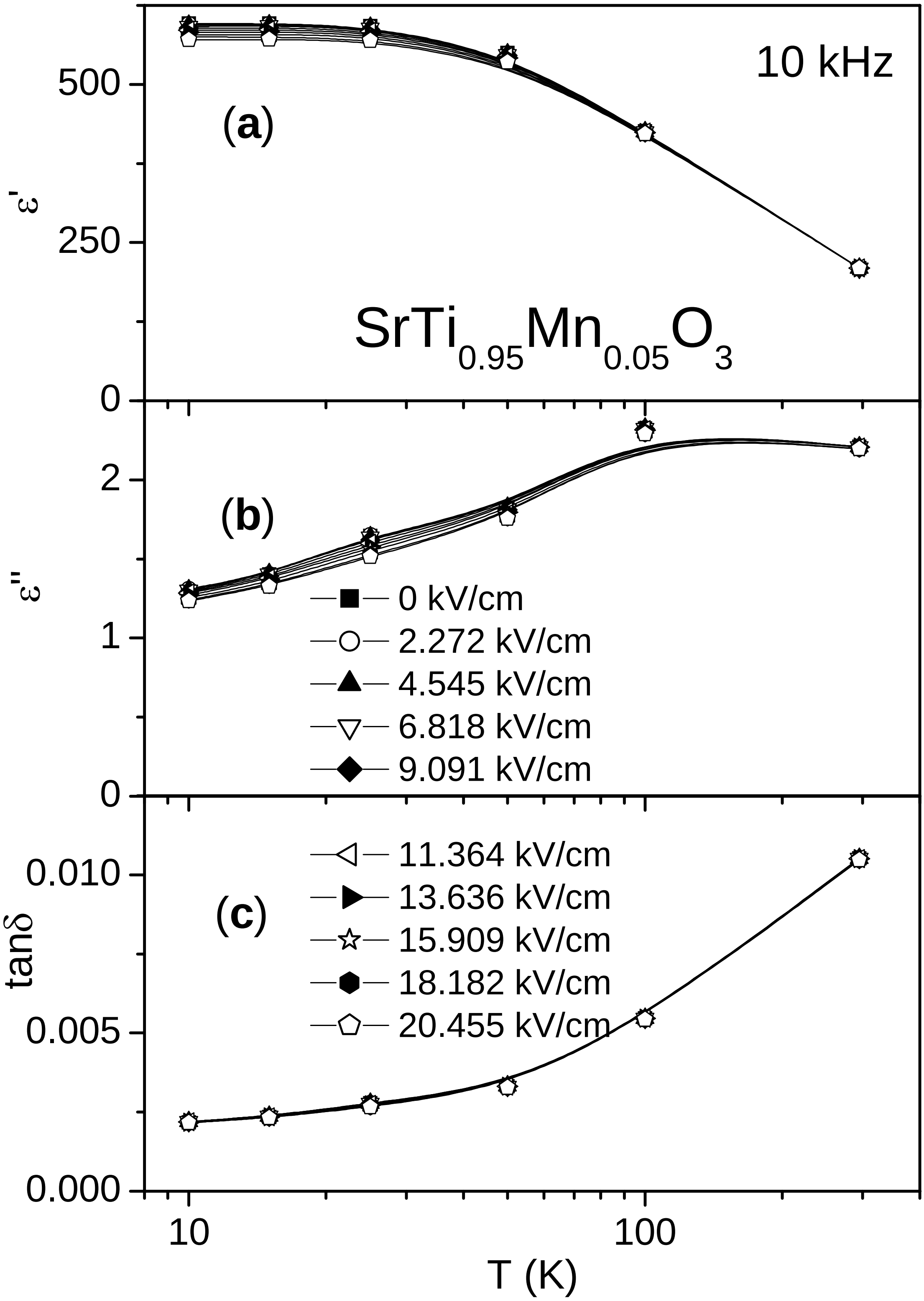

FIGURE 5.30. Variation of real ε' and imaginary ε'' parts of dielectric permittivity and of dissipation factor *tanδ* = ε''/ε' at 10 kHz with temperature for SrTi$_{0.95}$Mn$_{0.05}$O$_3$ ceramics under different dc bias fields.

Dependences of the relative tunability n_r of both $Sr_{1-x}Mn_xTiO_3$ (x = 0, 0.01, 0.03 and 0.05) and $SrTi_{1-y}Mn_yO_3$ (y = 0.01 and 0.05) ceramics on the bias field at fixed temperatures are presented in Figure 5.31 (a-f). The relative tunability is calculated as: $n_r(E) = [\varepsilon'(0) - \varepsilon'(E)]/\varepsilon'(0)$, where $\varepsilon'(0)$ is the dielectric permittivity at zero field and $\varepsilon'(E)$ is the dielectric permittivity under applied bias field E. Evidently non-linear dielectric response on the electric field is observed. The maximum effect of an applied bias field on the relative tunability is observed near the temperature of the peak in the $\varepsilon'(T)$, as seen from Figure 5.31 (a-d) together with Figures 5.25-5.30.

For better consideration, relative tunability under maximum electric field of ~20 kV/cm n_{max} is presented in Figure 5.32a as functions of temperature. For $Sr_{0.99}Mn_{0.01}TiO_3$ ceramics, peak in $n_{max}(T)$ curve appears at ~40 K, while for $Sr_{0.97}Mn_{0.03}TiO_3$ and $Sr_{0.95}Mn_{0.05}TiO_3$ ceramics, peaks in $n_{max}(T)$ curves appears at ~60 K, corresponding to peak in $\varepsilon'(T)$. The n_{max} peak values are of 66.0-67.5%. Thus, it is worthwhile to notice, that maximum tunability value at 60 K for $Sr_{0.97}Mn_{0.03}TiO_3$ and $Sr_{0.95}Mn_{0.05}TiO_3$ is more than 20% higher than that of undoped ST ceramics.

On the other hand, the maximum relative tunability for $SrTi_{1-y}Mn_yO_3$ samples was obtained under electric field of ~20 kV/cm at 10 K, being about of 35% for y = 0.01 and lower than 5% for y = 0.05, as can be seen from Figure 5.31 (e, f).

Low dielectric loss in the temperature range of high tunability is an additional important factor for device application. To evaluate, if a ferroelectric component is suitable for practical applications in microwave engineering, quality factor of a tunable component (QFTC) has to be know. QFTC has been defined as a generalized parameter of a tunable component which can combine the characteristics of tunability and loss factor, and it is given by the following equation

$$K = (n - 1)^2/(n\, tan\delta(0)\, tan\delta(E_{max})) \qquad (5.9)$$

where $n = \varepsilon'(0)/\varepsilon'(E_{max})$ is the tunability of the component (Vendik, 1999). The value of the loss factor under zero $tan\delta(0)$ and maximum bias field $tan\delta(E_{max})$ are used. QFTC was calculated for SMnT samples, as shown in Figure 5.32 together with the maximum relative tunability n_{max}, and compared with the corresponding parameters of undoped ST.

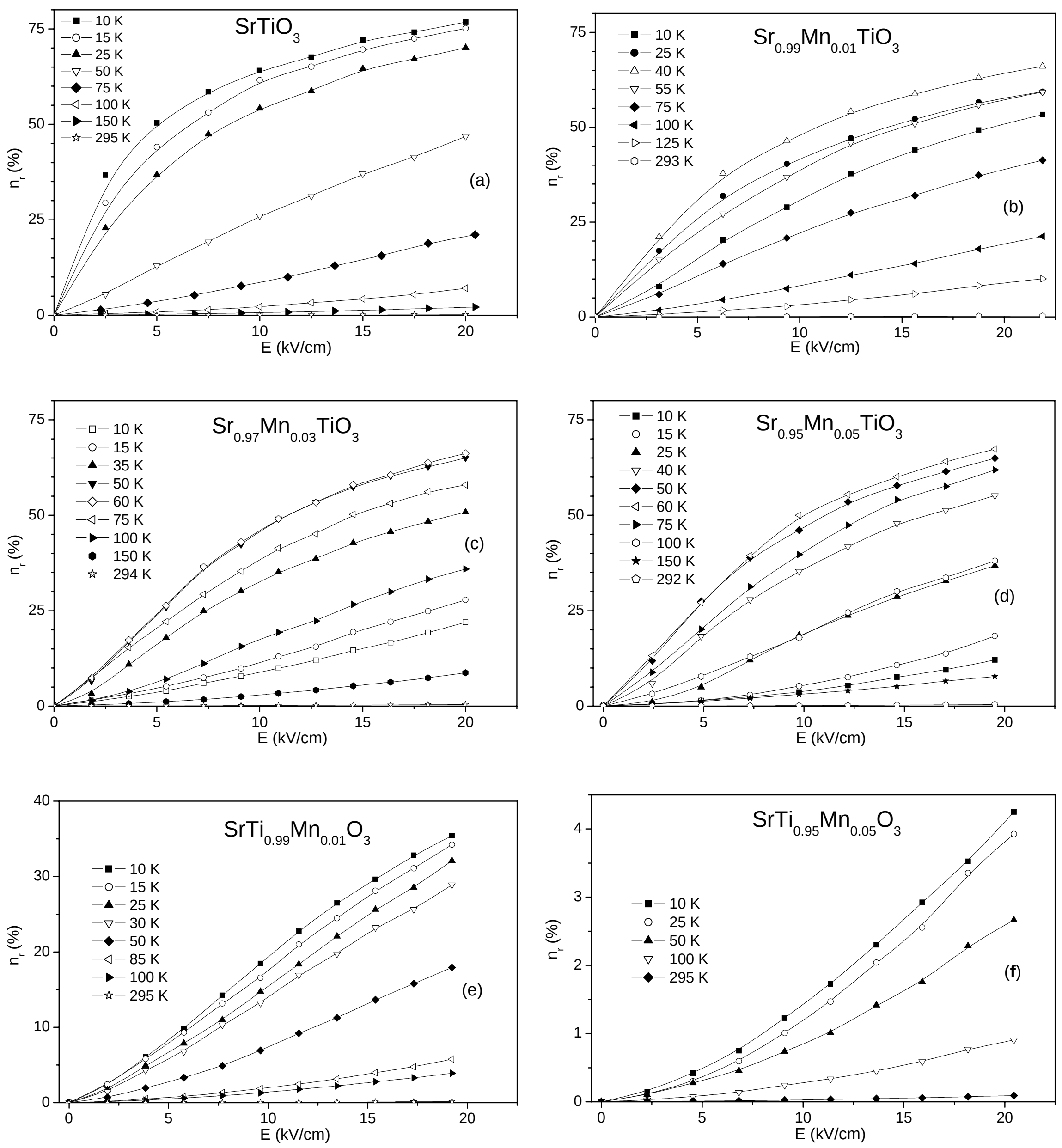

FIGURE 5.31. Variation of relative tunability n_r at 10 kHz, calculated as $n_r(E) = [\varepsilon'(0) - \varepsilon'(E)]/\varepsilon'(0)$, with bias field for SrTiO$_3$ (**a**), Sr$_{0.99}$Mn$_{0.01}$TiO$_3$ (**b**), Sr$_{0.97}$Mn$_{0.03}$TiO$_3$ (**c**), Sr$_{0.95}$Mn$_{0.05}$TiO$_3$ (**d**), SrTi$_{0.99}$Mn$_{0.01}$O$_3$ (**e**) and SrTi$_{0.95}$Mn$_{0.05}$O$_3$ (**f**) ceramics at different temperatures.

Comparison of the obtained results for these samples rises up that QFTC is one and a half order higher for undoped ST than for Mn-doped ST at temperatures lower ~70 K, but the opposite situation is observed for the temperature range 75-125 K. This fact can allow the application of Mn-doped ST ceramics around liquid nitrogen temperature, where high temperature superconductors can applicable as electrodes.

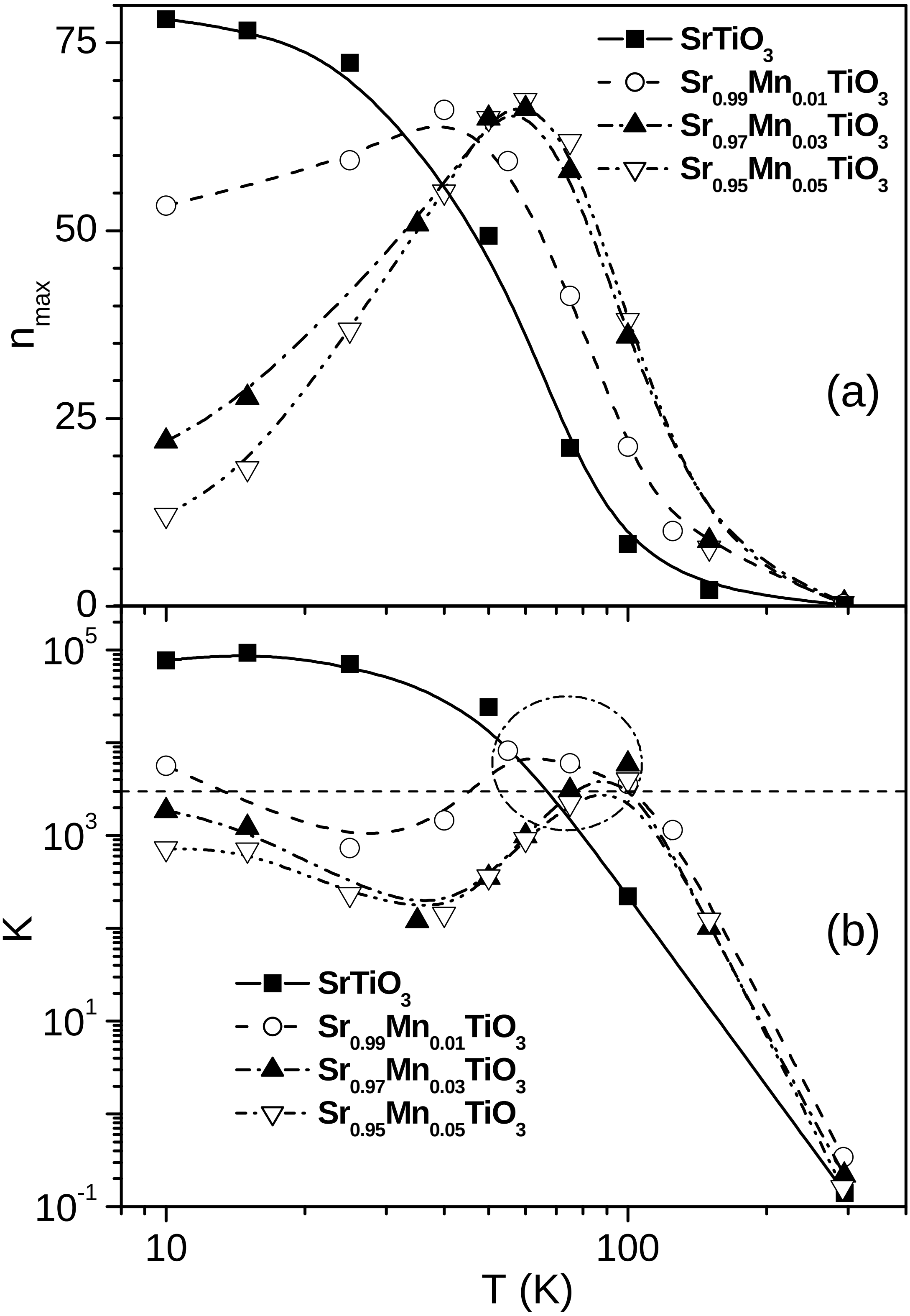

FIGURE 5.32. Maximum relative tunability n_{max} and quality factor of a tunable component K, obtained at bias field E_{max} = 20 kV/cm for $SrTiO_3$, $Sr_{0.99}Mn_{0.01}TiO_3$, $Sr_{0.97}Mn_{0.03}TiO_3$ and $Sr_{0.95}Mn_{0.05}TiO_3$ ceramics.

Moreover, the figure of merit of a phase shifter is determined as the ratio of the phase shift in degrees $\Delta\varphi_{\mathrm{degree}}$ to the insertion loss in dB L_{dB} and is closely connected with the QFTC of the ferroelectric component used in the phase shifter. The figure of merit is given by the following equation (Vendik, 1999):

$$\Delta\varphi_{\mathrm{degree}}/L_{\mathrm{dB}} = 6.6 \times \sqrt{K} \tag{5.10}$$

Accordingly, one can obtain a phase shift more than 360° per 1 dB, if the ferroelectric component is characterized by $K > 3000$ (Vendik, 1999). The values obtained for SMnT ceramics around 80 K satisfy well this condition, as marked in Figure 5.32. This could be expected from data shown in Figures 5.25-5.28, where around 80 K the dielectric constant is still well tunable, but the *tanδ* is already low and rather insensitive to the bias field.

Moreover, using high temperature superconducting electrodes, very well compatible with ST-based materials due to similar crystalline structure, one can obtain a high quality factor for the entire device. On the other hand, a high thermal stability can be obtained in ferroelectrics with diffused phase transitions or relaxors. Thus, SMnT ceramics is a very promising material for possible application as phase shifters.

5.5. Influence of sintering atmosphere on the dielectric properties of manganese-doped strontium titanate ceramics

In order to study the effect of sintering atmosphere on SMnT and STMn ceramics, two compositions with $x = 0.02$ and $y = 0.05$ were sintered at 1500 ºC for 5 hours in oxygen and nitrogen atmospheres.

Temperature dependences of their real ε' and imaginary ε'' parts of the dielectric permittivity and of the dissipation factor *tanδ* at 10 kHz are shown in Figures 5.33 and 5.34 for SMnT and STMn ceramics, respectively. Temperature dependences for $Sr_{0.98}Mn_{0.02}TiO_3$ and $SrTi_{0.95}Mn_{0.05}O_3$ ceramic samples sintered at air are also shown in Figures 5.33 and 5.34 for comparison.

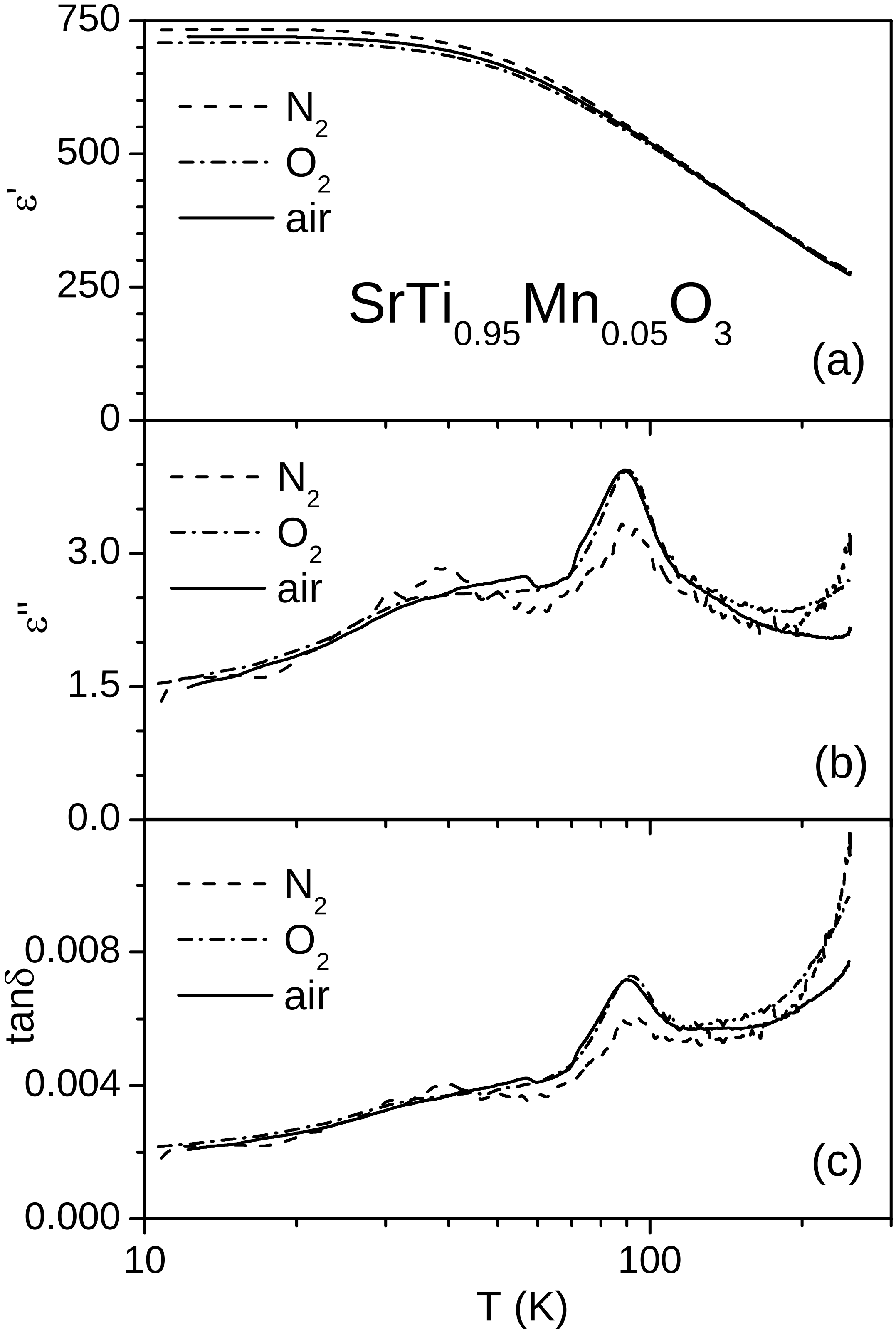

FIGURE 5.33. Temperature dependence of the real *ε*' (**a**) and imaginary *ε*'' (**b**) parts of dielectric permittivity and of the dissipation factor *tanδ* at 10 kHz of $SrTi_{0.95}Mn_{0.05}O_3$ ceramics sintered in oxygen, air and nitrogen.

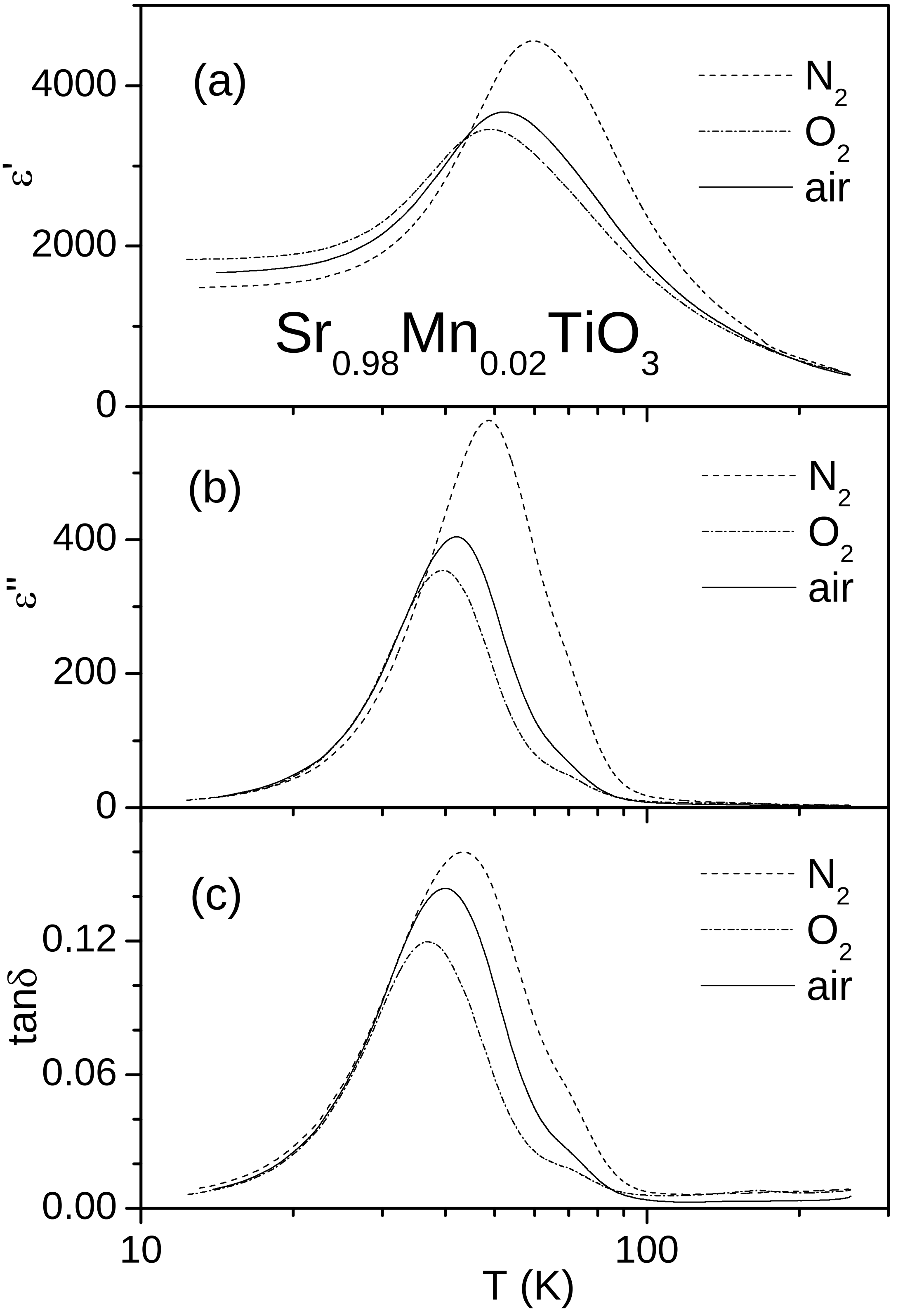

FIGURE 5.34. Temperature dependence of the real *ε*' (**a**) and imaginary *ε*'' (**b**) parts of dielectric permittivity and of the dissipation factor *tanδ* at 10 kHz of $Sr_{0.98}Mn_{0.02}TiO_3$ ceramics sintered in oxygen, air and nitrogen.

While no considerable effect of the sintering atmosphere is observed for STMn ceramics, SMnT samples reveal a marked variation of dielectric anomaly temperature and peak value with a reduction degree of the sintering atmosphere. An increase of the peak value at 10 kHz in ~1.3 times is evident for both ε' and $\tan\delta$ for $Sr_{0.98}Mn_{0.02}TiO_3$ sintered nitrogen, compared with those for $Sr_{0.98}Mn_{0.02}TiO_3$ sintered in oxygen. At the same time, the temperature of the peak in the $\varepsilon'(T)$ shifts for ~10.6 K, while that in the $\tan\delta(T)$ shifts for ~6.5 K. The detailed values of the peak real ε' and imaginary ε'' parts of the dielectric permittivity and dissipation factor $\tan\delta$ of $Sr_{0.98}Mn_{0.02}TiO_3$ are tabulated in Table 5.5.

Table 5.5. Dielectric anomaly temperature and peak value of ε', ε'' and $\tan\delta$ of $Sr_{0.98}Mn_{0.02}TiO_3$ ceramics sintered at 1500 ºC for 5 hours in oxygen, air and nitrogen atmospheres.

		PEAK TEMPERATURE (K)			PEAK VALUE		
Sintering atmosphere		O_2	air	N_2	O_2	air	N_2
Property	ε'	49.0	52.3	59.6	3461	3677	4564
	ε''	39.5	42.0	48.7	355	405	579
	$\tan\delta$	36.9	39.9	43.4	0.120	0.144	0.160

Such behaviour is in complete agreement with the ESR spectra presented in Chapter 4 (see Figure 4.18), that reveals a strong correlation between the relaxation strength and the concentration of Mn^{2+} ions. In addition, it is confirmed that due to a large difference in the ionic size between Mn^{2+} and Sr^{2+}, Mn^{2+} ions require special processing conditions to occupy the 12-coordination Sr site. One of the conditions seems to be the nitrogen (reducing) atmosphere, which strengthens the reduction of Mn^{4+} precursor to Mn^{2+} and promotes the following occupation of Sr sites by Mn^{2+} ions. Such a way an amount of polar dipoles increases, and therefore, increase the intensity of the peak in the $\varepsilon'(T)$. A degree of correlation of the polar dipoles increases as well, what is responsible for a higher temperature of the observed anomaly.

On the other hand, oxygen atmosphere should prevent the reduction of Mn^{4+} precursor to Mn^{2+} and promote the oxidation of Mn^{2+} to Mn^{4+}, such a way decreasing an amount of polar dipoles within some limits.

5.6. Summary

Dielectric properties of Mn-doped ST ceramic samples prepared by conventional mixed oxide method are examined in wide frequency (10^2-10^{14} Hz), temperature (10-300 K) and bias field (0-20 kV/cm) ranges.

A low-temperature dielectric relaxation is observed in SMnT system from low frequency to the optic phonon frequencies in THz range, presenting this system as a model system for moderately doped insipient ferroelectrics, besides $Sr_{1-x}Ca_xTiO_3$. Thus:

1. A diffused dielectric permittivity peak shifting to higher temperature with increasing frequency and/or amount of Mn is observed in $Sr_{1-x}Mn_xTiO_3$ ceramic samples;
2. A fitting both to Curie-Weiss law and to Barrett relation reveals the increase of T_0 with Mn content x indicating the approximation to a ferroelectric behaviour;
3. The low-temperature hysteresis loops are observed implying the transition to polar state;
4. Remnant polarization tails off to zero beyond the dielectric maximum that is indicative of a relaxor state;
5. The relaxation parameters γ, ΔT_ε, ΔT_f and α all tend to increase with increasing x indicating an approaching to classical relaxor behaviour.

The relaxor-type dielectric behaviour is attributed to the off-centre shifts of Mn^{2+} ions at Sr site of highly polarisable $SrTiO_3$ lattice. The contribution of individual off-centre Mn^{2+} ions dominates in dielectric spectra at lower concentrations $x < 0.03$ and can be described by Arrhenius law with the activation energy U ~52-73 meV and the relaxation time τ_0 ~(1-7) × 10^{-14} s, while the contributions of the polar clusters prevail at the higher Mn concentrations in the dielectric spectra and can be described by Vögel-Fulcher relation with the U ~64-78 meV, τ_0 ~(4-12) × 10^{-14} s and freezing temperature T_f ~2-10 K. This correlates well with a scheme of the dielectric behaviour of moderately doped incipient ferroelectrics, constructed from the analysis of dielectric spectra of $K_{1-x}Li_xTaO_3$ and $Sr_{1-1.5x}Bi_xTiO_3$ by Bovtun et al. (2004), presented in part 1.4. Moreover, time domain terahertz and infrared spectra reveal that the soft mode shifts to higher frequency and the soft mode phonon contribution to the dielectric response becomes smaller with increasing concentration of the off-centred Mn^{2+} ions, being suppressed by the interaction with off-centred ions and polar clusters in full agreement with work of Bovtun et al. (2004).

It is considered also, that due to the formation of polar microregions, related to the introduction of Mn^{2+} into the Sr site, the temperature range, where the dielectric constant is tunable, is enlarged up to ~150 K, comparing with undoped ST (~80 K). As well, a higher tunability (~70%) and quality factor of a tunable component (~6000) in the vicinity of liquid nitrogen temperature are obtained for SMnT ceramics.

In spite of that all these parameters are obtained at 10 kHz, a dielectric anomaly is observed in the microwave range also, i.e., in the phase shifter working range. Moreover, the dielectric relaxation still can be detected in THz range. Hence, $Sr_{1-x}Mn_xTiO_3$ is a promising material for possible application as a microwave phase shifter.

In addition, sintering in nitrogen atmosphere is found to increase the relaxation strength and to shift the observed anomaly towards higher temperature.

In contrary, $SrTi_{1-y}Mn_yO_3$ ceramics prepared by conventional mixed oxide method, reveal just a sharp reduction of the dielectric response, without any dielectric anomaly. Although incorporation of Mn^{4+} into ST lattice, decreasing fractional tolerance factor t_2, indicates smaller B-site packing degree and supposedly more favourable off-centre positions of these ions, the quantum fluctuations become more stable and the system is driven away from ferroelectricity accompanied by a decrease of the critical temperature T_0 to negative values. This observation together with a soft mode stiffening and a lowering of the soft mode phonon contribution to the dielectric response corroborates the fact that less polarisable Mn^{4+} ions substitutes more polarisable Ti^{4+} ions, breaking also Ti-Ti long-range interaction.

The absence of the Mn^{4+} relaxation and of the corresponding peak of dielectric permittivity can be explained as follows. The cell parameter of STMn system decreases with increasing Mn content with a high rate, as shown in Chapter 4, implying that such sharp compression of the cell does not allow the Mn^{4+} ions to occupy the off-centre position at Ti site. On the other hand, even more sharp decrease of the cell parameter could be expected for $Sr_{1-x}Mn_xTiO_3$ system from the ionic size consideration, but the cell parameter of SMnT was found to decrease with increasing Mn concentration 3.7 times slower than that of STMn indeed. Thus, a low-temperature dielectric relaxation related to Mn ions off-centre relaxation was observed in $Sr_{1-x}Mn_xTiO_3$ system in contrast to $SrTi_{1-y}Mn_yO_3$ system.

6. Conclusions

As was shown in introduction, $SrTiO_3$-based materials attracted a great interest not only from the fundamental but also from the application point of view, particularly as tunable electronic components. For this particular application, the problem is to shift the temperature range of high tunability towards room temperature that can be solved by the formation of a dielectric anomaly in $SrTiO_3$-based solid solutions. However, for the solid solutions of $SrTiO_3$ and ferroelectrics (such as $BaTiO_3$), where ferroelectric phase transition is formed, insertion loss and temperature coefficient of the dielectric constant increase together with the temperature of the dielectric anomaly. Hence the appearance of dielectric anomalies of a different physical nature is required.

Another mechanism proposed for a formation of the dielectric anomaly in ST-based compounds is related with the off-centre displacements of small dopant ions in the large Sr site (as in $Sr_{1-x}Ca_xTiO_3$). Small Mg and Mn ions were supposed to be suitable to induce the dielectric anomaly in strontium titanate, forming $Sr_{1-x}Mg_xTiO_3$ and $Sr_{1-x}Mn_xTiO_3$ solid solutions. Moreover, the smaller the dopant ion the higher stress is induced in the perovskite lattice, that can promote the diffuseness of the dielectric anomaly on the one hand, but the low solid solubility limit on the other hand. In addition, Mg^{2+} and Mn^{4+} ions may occupy Ti site of ST perovskite lattice, forming $SrTi_{1-y}Mg_yO_{3-\delta}$ and $SrTi_{1-y}Mn_yO_3$ solid solutions, that were rarely studied in past.

This work was a systematic study of four strontium titanate based ceramic systems, namely $Sr_{1-x}Mg_xTiO_3$, $Sr_{1-x}Mn_xTiO_3$, $SrTi_{1-y}Mg_yO_{3-\delta}$ and $SrTi_{1-y}Mn_yO_3$, and the following conclusions were attained.

6.1. Synthesis of strontium titanate ceramics doped with Mg and Mn

Four series of samples with the nominal compositions $Sr_{1-x}Mg_xTiO_3$ (SMT, $x = 0$, 0.01, 0.02, 0.03, 0.08, 0.15), $Sr_{1-x}Mn_xTiO_3$ (SMnT, $x = 0.0025$, 0.005, 0.01, 0.02, 0.025, 0.03, 0.05, 0.10, 0.15), $SrTi_{1-y}Mg_yO_{3-\delta}$ (STM, $y = 0.01$, 0.02, 0.05, 0.10, 0.15) and $SrTi_{1-y}Mn_yO_3$ (STMn, $y = 0.01$, 0.05, 0.10, 0.15) were synthesised by the mixed oxide method.

The optimal sintering conditions for both Mg- and Mn-doped strontium titanate ceramic samples were 1500 °C for 5 h. Single phase ceramics with relative densities higher than 95.6% were obtained.

The grain size was found to vary from 9 to 31 μm for $Sr_{1-x}Mg_xTiO_3$, from 20 to 35 μm for $Sr_{1-x}Mn_xTiO_3$, from 0.2 to 1.5 μm for $SrTi_{1-y}Mg_yO_{3-\delta}$ and from 0.6 to 0.8 μm for $SrTi_{1-y}Mn_yO_3$ systems, without obvious dependence on the dopant content. This one-order difference in the grain size of Sr-site and Ti-site doped ST ceramics might be related to the variations of the Sr/Ti ratio.

TEM and XRD results showed that the solid solubility limits are $x \approx 0.01$ for $Sr_{1-x}Mg_xTiO_3$, $x \approx 0.02$ for $Sr_{1-x}Mn_xTiO_3$, $y \approx 0.10$ for $SrTi_{1-y}Mg_yO_{3-\delta}$ and $y > 0.15$ for $SrTi_{1-y}Mn_yO_3$. The results indicated that solid solubility limit of manganese is higher than that of magnesium both at Sr sites and at Ti sites of ST. For Sr-site occupation, it can be explained by bigger ionic size of Mn^{2+} comparing with Mg^{2+} and hence less probable segregation into the ilmenite-type structure. For Ti-site occupation, ionic size misfit seems to be lower or less important for both Mg^{2+} and Mn^{4+}, however, formation of the oxygen vacancies as a charge compensation mechanism might be an additional parameter for the restricted solid solubility of magnesium in Ti site.

For all the single phase samples, the crystal symmetry was indexed to be preferably cubic at room temperature. No obvious variation of the lattice parameter with Mg content was observed for $Sr_{1-x}Mg_xTiO_3$ system, confirming the very low solubility limit. For $Sr_{1-x}Mn_xTiO_3$ system, a slight decrease of the lattice parameter with increasing Mn concentration was observed. More considerable variation of the lattice parameter was observed for Ti-site doped systems: for $SrTi_{1-y}Mn_yO_3$, the lattice parameter markedly decreased with increasing y, while for $SrTi_{1-y}Mg_yO_{3-\delta}$, the lattice parameter increased with increasing Mg concentration.

In addition, low-temperature Raman spectra of $SrTi_{1-y}Mg_yO_{3-\delta}$ indicated a decrease of the intensity and finally disappearance of R-point modes with increasing y that implies the vanishing of the ST structural phase transition or its shift to lower temperatures.

Based on transmission electron microscopy and ESR and Raman spectroscopy analysis, the predicted occupation of Mn at both Sr and Ti sites of the ST lattice was confirmed. For $Sr_{1-x}Mn_xTiO_3$ system, the lines in ESR spectra attributed to Mn^{2+} increase in intensity with Mn content increase, while those attributed to Mn^{4+} decrease and finally disappear at crossover from oxidizing to reducing sintering atmosphere. Also, the relation between the temperature T_a of the structural phase transition of Mn doped ST and the dependence on the Mn site was established. Mn incorporation at the Sr site increased T_a, decreasing the tolerance factor of the perovskite structure, while Mn incorporation at the Ti site, supposed to increase the tolerance factor, was found to decrease T_a. Moreover, additional lines in Raman spectra of SMnT and STMn ceramics implied formation of the additional structural bonds with their own dynamics.

6.2. Dielectric properties of strontium titanate ceramics doped with Mg and Mn

Dielectric properties of Mg and Mn-doped ST ceramic samples prepared by conventional mixed oxide method were examined in a wide frequency (10^2-10^{14} Hz), temperature (10-300 K) and bias field (0-20 kV/cm) ranges.

From the four studied systems only one ($Sr_{1-x}Mn_xTiO_3$) revealed the formation of a dielectric anomaly, while just a monotonous reduction of the dielectric constant with increasing dopant concentration was observed for the rest three systems.

The reduction of the dielectric constant became stronger in the sequence: $Sr_{1-x}Mg_xTiO_3$, $SrTi_{1-y}Mn_yO_3$, $SrTi_{1-y}Mg_yO_{3-\delta}$. Such behaviour observed for SMT system was explained by the very restricted solid solubility limit of Mg^{2+} ions at the Sr sites, associated with the formation of a second phase of $MgTiO_3$, possessing low dielectric constant. Therefore, although theoretically predicted, no ferroelectric or relaxor-type anomaly was induced. Instead just an additional peak in temperature dependence of the dielectric loss with dynamics described by Arrhenius law with $\tau_0 = (1.8\text{-}5.0) \times 10^{-12}$ s and $U = 28\text{-}34$ meV was observed for $Sr_{1-x}Mg_xTiO_3$. The lattice vibration behaviour and dielectric responses in a wide range of frequency, temperature and dc bias field for ST and SMT samples were found to be similar.

For $SrTi_{1-y}Mn_yO_3$ and $SrTi_{1-y}Mg_yO_{3-\delta}$ ceramics, along with the dielectric constant, the relative tunability in the rf range was found to progressively decrease with increasing dopant content. Such behaviour was explained by the substitution of more polarisable Ti^{4+} ions by less polarisable Mn^{4+} and Mg^{2+} ions, respectively, which may break Ti-Ti long-range interaction.

In addition, $SrTi_{1-y}Mg_yO_{3-\delta}$ system was characterised by the reduced dielectric constant and loss values in the microwave and terahertz ranges with very weak temperature dependence, accompanied with the stiffening of the soft mode in IR frequency range. Therefore, STM ceramics, showing low loss and satisfactory thermostability in microwave range, might be applied as waveguides or resonators.

ST serves as a resonator for radio-frequency superconducting quantum interference device (SQUID) operations, improving the stability of the operating point at 77 K (Zhang et al., 2002c). However, cooling down to this temperature, ST is known to undergo a structural phase transition (Shirane and Yamada, 1969), which can imply the structural twin formation and this may affect the properties of the resonator. The gradual disappearance of the dielectric loss peak, characteristic for multidomain ST, with increasing dopant content together with low-temperature Raman results point to the "cancellation" of the structural phase transition in STM and STMn system. Therefore, $SrTi_{1-y}Mg_yO_{3-\delta}$ and $SrTi_{1-y}Mn_yO_3$ might be used as substrates for the SQUID applications instead of $SrTiO_3$.

$Sr_{1-x}Mn_xTiO_3$ system revealed a diffused dielectric permittivity peak shifting to higher temperatures with increasing frequency and/or amount of Mn. Low-temperature hysteresis loops were observed implying the transition to a polar state, and remnant polarization tailed off to zero beyond the dielectric maximum that is indicative of relaxor state. Such dielectric behaviour was attributed to the off-centre displacements of Mn^{2+} ions at the Sr sites of highly polarisable $SrTiO_3$ lattice. The contribution of individual off-centre Mn^{2+} ions dominates in the dielectric spectra at lower concentrations $x < 0.03$ and can be described by Arrhenius law with the activation energy U ~52-73 meV and the relaxation time $\tau_0 \sim (1\text{-}7) \times 10^{-14}$ s, while the contributions of the polar clusters prevail at the higher Mn concentrations in the dielectric spectra and can be described by the Vögel-Fulcher relation with U ~64-78 meV, $\tau_0 \sim (4\text{-}12) \times 10^{-14}$ s and freezing temperature T_f ~2-10 K. Moreover, time domain terahertz and infrared spectra reveal that the soft mode shifts to higher frequency and the soft mode phonon contribution to the dielectric response becomes smaller with increasing concentration of the off-centred Mn^{2+} ions, being suppressed by the interaction with off-centred ions and polar clusters in complete agreement with a scheme of the dielectric behaviour of moderately doped incipient ferroelectrics, constructed from the analysis of dielectric spectra of $Ka_{1-x}Li_xTaO_3$ and $Sr_{1-1.5x}Bi_xTiO_3$ by Bovtun et al. (2004).

It is considered also, that due to the formation of polar microregions, related to the introduction of Mn^{2+} into the Sr site, the temperature range, where the dielectric constant is tunable, was enlarged up to ~150 K, comparing with undoped ST (~80 K). As well, a higher tunability (~70%) and quality factor of a tunable component (~6000) were obtained for SMnT ceramics in the vicinity of liquid nitrogen temperature. Hence $Sr_{1-x}Mn_xTiO_3$ is a promising material for possible application as a microwave phase shifter.

In addition, sintering in nitrogen atmosphere was found to increase the intensity of the peak in the $\varepsilon'(T)$ and shift the observed anomaly towards higher temperature. This is in agreement with the complete transformation of Mn^{4+} ions into Mn^{2+} ions, indicated by ESR, confirming the dominant role of Mn^{2+} in the relaxation process.

Although incorporation of Mn^{4+} into Ti site of ST lattice (decreasing the fractional tolerance factor t_2) indicates smaller B-site packing degree and supposedly more favourable off-centre positions of these ions, the quantum fluctuations became more stable and the system was driven away from ferroelectricity. This is in accordance with the observed compression of the unit cell of STMn system with increasing Mn content that might not allow Mn^{4+} ions to occupy the off-centre position at Ti site.

6.3. Suggestions for further work

This thesis is a systematic but not complete study of the dielectric polarisation and relaxation in magnesium- and manganese-doped strontium titanate. Interesting physical phenomena were found, and possible physical mechanisms were discussed in these systems, especially in the case of $Sr_{1-x}Mn_xTiO_3$. However, a better understanding of the polarisation mechanism, that will allow a further practical application of the materials, requires the following work to be carried out:

- Measurement of the dielectric tunability at microwave frequencies.
- Further examination of the dielectric permittivity, hysteresis loops and pyroelectricity under zero-field cooling, field heating, field cooling and zero-field heating.
- Measurement of the hysteresis loops at different frequencies.

- Additional experimental evidences of off-centre Mn ions by extended X-ray-absorption fine structure spectroscopy (EXAFS), nuclear magnetic resonance (NMR) and EPR at different temperatures.
- Study of the effect of magnetic field on the dielectric properties of strontium titanate doped with magnetoactive manganese ions, in view of multiferroic state, widely studied nowadays.

References

1. Almeida A., Teles P., Chaves M.R., Vilarinho P.M. and Baptista J.L. (2003) *Ferroelectrics* **294**, 49.
2. Amoss J.W., Donaldson M.R., Lavedan L.J., Stanford A.L., and Pippin J.E. (1965) *IEEE T. Microw. Theory* **13**, 789
3. Ang C., Yu Z., Vilarinho P.M., Baptista J.L. (1998) *Phys. Rev. B* **57**, 7403
4. Ang C., Scott J.F., Yu Z., Ledbetter H., Baptista J.L. (1999) *Phys. Rev. B* **59**, 6661; Ang C., Yu Z., Hemberger J., Lunkenheimer P. and Loidl A. (1999) *ibid.*, 6665; Ang C., Yu Z., Lunkenheimer P., Hemberger J. and Loidl A. (1999) *ibid.*, 6670
5. Ang C., Guo R., Bhalla A.S. and Cross L.E. (2000a) *J. Appl. Phys.* **87**, 3937
6. Ang C., Bhalla A.S., Guo R. and Cross L.E. (2000b) *Appl. Phys. Lett.* **76**, 1929
7. Ang C., Yu Z. and Cross L.E. (2000c) *Phys. Rev. B* **62**, 228
8. Ang C., Yu Z. and Jing Z. (2000d) *Phys. Rev. B* **61**, 957
9. Ang C. and Yu Z. (2000) *Phys. Rev. B* **61**, 11363
10. Ang C. and Yu Z. (2002) *J. Appl. Phys.* **91**, 1487
11. Aseev A.L. and Fedina L.I. (1992) *Electron Microscopy* **2**, 81; Laanab L., Faye M.M., Beauvillain J. et al. (1992) *ibid.*, 137; Lhermitte-Sebire I., Chermant J.L., Levalois M., Paumier E. and Vicens J. (1992) *ibid.*, 425; Fourlaris G.N. and Baker A.J. (1992) *ibid.*, 251, Guilemany J.M., Fernandez J. and Nutting J. (1992) *ibid.*, 259
12. Azzoni C.B., Mozzati M.C., Paleari A., Massarotti V., Bini M. and Capsoni D. (2000a) *Solid State Commun.* **114**, 617
13. Azzoni C.B., Mozzati M.C., Galinetto P., Paleari A., Massarotti V., Bini M. and Capsoni D. (2000b) *Solid State Commun.* **116**, 303
14. Babbit R.W., Koscica T.E., Drach W.C. (1992) *Microwave J.* **35**, 63
15. Barker A.S. and Tinkham M. (1962) *Phys. Rev.* **125**, 1527
16. Barrett J.H. (1952) *Phys. Rev.* **86**, 118
17. Bednorz J.G. and Müller K.A. (1984) *Phys. Rev. Lett.* **52**, 2289
18. Bell R.O. and Rupprecht G. (1963) *Phys. Rev.* **129**, 90
19. Benguigui L. and Bethe K. (1976) *J. Appl. Phys.* **47**, 2787
20. Bhalla A.S., Guo R., Roy R. (2000) *Mat. Res. Innovat.* **4**, 3
21. Bianchi U., Kleemann W. and Bednorz J.G. (1994) *J. Phys.: Condens. Matter.* **6**, 1229

22. Bianchi U., Dec J., Kleemann W. and Bednorz J.G. (1995) *Phys. Rev. B* **51**, 8737
23. Bidault O., Maglione M., Actis M., Kchikech M., Salce B. (1995) *Phys. Rev. B* **52**, 4191
24. Blinc R. and Zeks B. (1974) *Soft modes in Ferroelectrics and Antiferroelectrics*, North-Holland, Amsterdam
25. Blinc, R., Dolinsek, J., Gregorovic, A., Zalar, B., Filipic, C., Kutnjak , Z., and Levstik, A. (2000) *J. Phys. Chem. Sol.* **61**, 177
26. Blinc, R., Zalar, B., Laguta V., and Itoh M. (2005) *Phys. Rev. Lett.* **94**, 147601
27. Bovtun V., Petzelt J., Porokhonskyy V., Kamba S., Yakimenko Y. (2001) *J. Eur. Ceram. Soc.* **21**, 1307
28. Bovtun V., Porokhonskyy V., Savinov M., Pashkin A., Zelezny V., Petzelt J. (2004) *J. Eur. Ceram. Soc.* **24**, 1545
29. Buchanan R.C. (1991) *Ceramic Materials for Electronics - Processing, Properties and Applications*, Marcel Dekker, New York
30. Burns G. and Dacol F.H. (1983) *Phys. Rev. B* **28**, 2527
31. Chang W. and Sengupta L. (2002) *J. Appl. Phys.* **92**, 3941
32. Christen H.-M., Mannhart J., Williams E.J., and Gerber Ch. (1994) *Phys. Rev. B* **49**, 12095
33. Cowley R.A. (1962) *Phys. Rev. Lett.* **9**, 159
34. Cross, L.E. (1987) *Ferroelectrics* **76**, 241
35. Cross, L.E. (1994) *Ferroelectrics* **151**, 305
36. De Flaviis F., Alexopoulos N.G. and Stafsudd O.M. (1997) *IEEE T. Microw. Theory* **45**, 963
37. Dec J., Kleemann W. and Westwanski B. (1999) *J. Phys.: Condens. Matter.* **11**, L379
38. Dec J., Kleemann W. and Itoh M. (2005) *Phys. Rev.* **71**, 144113
39. Eriksson A., Deleniv A. and Gevorgian S. (2003) *J. Appl. Phys.* **93**, 2848
40. Fernandez J.F., Duran P., Moure C. (1992) *Ferroelectrics* **127**, 53
41. Fleury P.A., Scott J.F., and Worlock J.M. (1968) *Phys. Rev. Lett.* **21**, 16
42. Fleury P.A. and Worlock J.M. (1968) *Phys. Rev.* **174**, 613
43. Frederikse H.P.R., Thurber W.R. and Hosler W.R. (1964) *Phys. Rev.* **134**, A442
44. Fujimoto M., Suzuki T., Nishi Y. and Arai K. (1998) *J. Am. Ceram. Soc.* **81**, 33

45. Galasso F.S. (1969): *Structure properties and preparation of perovskite-type compounds* Pergamon, Oxford, UK
46. Gevorgian S., Eriksson A., Linner P., Kollberg E., Vendik O. and Wikborg E. (1996) *IEEE T. Microw. Theory* **44**, 1738
47. Gevorgian S. (2001) *IEEE T. Microw. Theory* **49**, 2117 (and references therein)
48. Gevorgian S., Eriksson A., Deleniv A. and Pandey D. (2002) *J. Appl. Phys.* **92**, 6165
49. Goldstein J.I. (1992) *Scanning electron microscopy and X-ray microanalysis*, Plenum, New York
50. Guzhva M.E., Lemanov V.V., Markovin P.A. (2001) *Fiz. Tverd. Tela* **43**, 2058 (in Russian). English translation: *Phys. Solid State* **43**, 2146
51. Halasyamani P.S. (2004) *Chem. Mater.* **16**, 3586
52. Halasyamani P.S. and Poeppelmeier K.R. (1998) *Chem. Mater.* **10**, 2753
53. Hasebe H., Tsujimi Y., Wang R., Itoh M. and Yagi T. (2003) *Phys. Rev. B* **68**, 014109
54. Hashimoto S. and Iwahara H. (2000) *J. Electroceram.* **4**, 225
55. Hemberger J., Lunkenheimer P., Viana R., Bohmer R. and Loidl A. (1995) *Phys. Rev. B* **52**, 13159
56. von Hippel A., Breckenridge R.C., Chesley F.G. and Tisza L. (1946) *Ind. Eng. Chem.* **38**, 1097
57. Hirata T., Ishioka K. and Kitajima M. (1996) *J. Solid State Chem.* **124**, 353
58. Ibach H. and Lüth H. (1996) *Solid-State Physics*, Springer, Berlin
59. Iguchi E. and Lee K.J. (1993) *J. Mater. Sci.* **28**, 5809
60. Inoue T., Noriaki S., Kamimae J., Eguchi K. and Arai H. (1991) *Solid State Ionics* **48**, 283
61. Itoh M., Wang R., Inaguma Y., Yamaguchi T., Shan Y.J., Nakumura T. (1999) *Phys. Rev. Lett.* **82**, 3540
62. Itoh M. and Wang R. (2000) *Appl. Phys. Lett.* **76**, 221
63. Jaffe B., Cook Jr. W.R. and Jaffe H. (1971) *Piezoelectric ceramics*, Academic Press, London
64. Jang Y.-I. and Chiang Y.-M. (2000) *Solid State Ionics* **130**, 53
65. Jenkins R. and Snyder R.L. (1996) *Introduction to X-ray Powder Diffractometry*, John Wiley and Sons, New York
66. Johnson D.W., Cross L.E. and Hummel F.A. (1970) *J. Appl. Phys.* **31**, 2828

67. Kawada Y. and Fujimoto M. (1990) *Jpn. J. Appl. Phys.* **29**, L126
68. Kennedy B.J., Howard C.J. and Chakoumakos B.C. (1999) *J. Phys.: Condens. Matter.* **11**, 1479
69. Kim B.-J., Park T.-G., Kim M.-H. (1998) *J. Kor. Phys. Soc.* **32**, S289
70. Kleemann W. and Schremmer H. (1989) *Phys. Rev. B* **40**, 7428
71. Kleemann W. and Klossner, A. (1993) *Ferroelectrics* **150**, 35
72. Kleemann W., Albertini A., Chamberlin R.V. and Bednorz J.G. (1997) *Europhys. Lett.* **37**, 145
73. Kleemann W., Dec J. and Westwanski B. (1998) *Phys. Rev. B* **58**, 8985
74. Kleemann W., Dec J., Wang Y.G., Lehnen P., Prosandeev S.A. (2000) *J. Phys. Chem. Solids* **61**, 167
75. Kleemann W., Dec J., Wang R. and Itoh M. (2003) *Phys. Rev. B* **67**, 092107
76. Ko J. and Prewitt C.T. (1988) *Phys. Chem. Minerals* **15**, 355
77. Kolev N., Chen C.L., Gospodinov M., Bontchev R.P., Popov V.N., Litvinchuk A.P., Abrashev M.V., Hadjiev V.G., and Iliev M.N. (2002) *Phys. Rev. B* **66**, 014101
78. Kulagin N., Dojcilovic J. and Popovic D. (2001) *Cryogenics* **41**, 745
79. Kunz M. and Brown I.D. (1995) *J. Solid State Chem.* **115**, 395
80. Kvyatkovskii O.E. (2001) *Solid State Commun.* **117**, 455
81. Kvyatkovskii O.E. (2002) *Fiz. Tverd. Tela* **44**, 1087 (in Russian). English translation: *Phys. Solid State* **44**, 1135
82. Lacerda-Arôso M.T., Ribeiro J.L., Chaves M.R., Almeida B.G. and Almeida A. (2001) *J. Phys.: Condens. Matter.* **13**, 2615
83. Last J.T. (1957) *Phys. Rev.* **105**, 1740
84. Lee K.J. and Iguchi E. (1995) *J. Solid State Chem.* **114**, 242
85. Lemanov V.V. (1999) *Ferroelectrics* **226**, 133
86. Lemanov V.V., Smirnova E.P., Syrnikov P.P. and Tarakanov E.A. (1996) *Phys. Rev. B* **54**, 3151
87. Lemanov V.V., Smirnova E.P. and Tarakanov E.A. (1997a) *Fiz. Tverd. Tela* **39**, 714 (in Russian). English translation: *Phys. Solid State* **39**, 628
88. Lemanov V.V., Trepakov V.A., Syrnikov P.P., Savinov M., Jastrabik L. (1997b) *Fiz. Tverd. Tela* **39**, 1838 (in Russian). English translation: *Phys. Solid State* **39,** 1642

89. Lemanov V.V., Sotnikov A.V., Smirnova E.P., Weihnacht M., Kunze R. (1999) *Solid State Commun.* **110**, 611
90. Lemanov V.V., Smirnova E.P., Sotnikov A.V. and Weihnacht M. (2000) *Appl. Phys. Lett.* 77, 4205
91. Lemanov V.V., Sotnikov A.V., Smirnova E.P. and Weihnacht M. (2002) *Fiz. Tverd. Tela* **44**, 1948. English translation: *Phys. Solid State* **44**, 2039
92. Lemanov V.V., Smirnova E.P., Sotnikov A.V. and Weihnacht M. (2004) *Fiz. Tverd. Tela* **46**, 1402. English translation: *Phys. Solid State* **46**, 1442
93. Lin J.N. and Wu T.B. (1990) *J. Appl. Phys.* **68**, 985
94. Lines, M.E. and Glass, A.M. (1977) *Principles and Applications of Ferroelectric and Related Materials*, Clarendon Press, Oxford
95. Linz A. (1953) *Phys. Rev.* **91**, 753
96. Lytle F.W. (1964) *J. Appl. Phys.* **35**, 2212
97. Lyddane R.H., Sachs R.G. and Teller E. (1941) *Phys. Rev.* **59**, 673
98. Marjanovic S.S. and Popovic Z.V. (1998) *Solid State Phenom.* **61-62**, 309
99. Merz W.J. (1950) *Phys. Rev.* **77**, 52
100. Misra M., Murakami H. and Tonouchi M. (2003) *Electron. Lett.* **39**, 990
101. Mishra S.K., Ranjan R. and Pandey D. (2001) *Phys. Rev. B* **64**, 092302
102. Mitsui T. and Westphal W.B. (1961) *Phys. Rev.* **124**, 1354
103. Mizaras R. and Loidl A. (1997) *Phys. Rev. B* **56**, 10726
104. Müller K.A. (1959) *Phys. Rev. Lett.* **2**, 341
105. Müller K.A., Berlinger W. and Waldner F. (1968) *Phys. Rev. Lett.* **21**, 814
106. Müller K.A. and Berlinger W. (1971) *Phys. Rev. Lett.* **26**, 13
107. Müller K.A. and Burkhard H. (1979) *Phys. Rev. B* **19**, 3593
108. Neumann H. and Artl G. (1986) *Ferroelectrics* **69**, 179
109. Neville R.C., Hoeneisen B. and Mead C.A. (1972) *J. Appl. Phys.* **43**, 2124
110. Newnham R.E. (1983) *J. Mater. Education* **5**, 940
111. Pashkin A. (2004) *Ph.D. thesis*, Institute of Physics, Academy of Sciences of the Czech Republic
112. Petzelt J., Ostapchuk T., Gregora I., Rychetský I., Hoffmann-Eifert S., Pronin A.V., Yuzyuk Y., Gorshunov B.P., Kamba S., Bovtun V., Pokorný J., Savinov M.,

Porokhonskyy V., Rafaja D., Vaněk P., Almeida A., Chaves M.R., Volkov A.A., Dressel M., and Waser R. (2001) *Phys. Rev. B* **64**, 184111

113. Popovic D., Sarvan M., Dojcilovic J. and Kulagin N. (1998) *Solid State Phenom.* **61-62**, 183
114. Porokhonskyy V., Pashkin A., Bovtun V., Petzelt J., Savinov M., Samoukhina P., Ostapchuk T., Pokorny J., Avdeev M., Kholkin A. and Vilarinho P. (2004) *Phys. Rev. B* **69**, 144104
115. Randall C.A., Bhalla A.S., Shrout T.R. and Cross L.E. (1990) *J. Mater. Res.* **5**, 829
116. Ranjan R. and Pandey D. (1999) *J. Phys.: Condens. Matter.* **11**, 2247
117. Ranjan R., Pandey D. and Lalla N.P. (2000) *Phys. Rev. Lett.* **84**, 3726
118. Ranjan R. and Pandey D. (2001) *J. Phys.: Condens. Matter.* **13**, 4239
119. Redfern S.A.T. (1996) *J. Phys.: Condens. Matter.* **8**, 8267
120. Rimai L. and deMars G.A. (1962) *Phys. Rev.* **127**, 702
121. Ross N.L., Ko J. and Prewitt C.T. (1989) *Phys. Chem. Minerals* **16**, 621
122. Rupprecht G. and Bell R.O. (1962) *Phys. Rev.* **125**, 1915
123. Rupprecht G. and Winter W.H. (1967) *Phys. Rev.* **155**, 1019
124. Saifi M.A. and Cross L.E. (1970) *Phys. Rev. B* **2**, 677
125. Sakudo T. and Unoki H. (1971) *Phys. Rev. Lett.* **26**, 851
126. Scott A.W. (1993) *Understanding Microwaves*, Wiley, New York
127. Schooley J.F., Hosler, W.R. and Cohen M.L. (1964) *Phys. Rev. Lett.* **12**, 474
128. Sengupta L.C. and Sengupta S. (1999) *Mat. Res. Innovat.* **2**, 278
129. Serway R.A., Berlinger W., Müller K.A. and Collins R.W. (1977) *Phys. Rev. B* **16**, 4761
130. Shannon R.D. (1976) *Acta Crystallogr. A* **32**, 751
131. Shannon R.D. (1993) *J. Appl. Phys.* **73**, 348
132. Shirane G. and Yamada Y. (1969) *Phys. Rev.* **177**, 858
133. Sivasubramanian V., Murthy V.R.K. and Viswanathan B. (1997) *Jpn. J. Appl. Phys.* **36**, 194
134. Slater J.C. (1950) *Phys. Rev.* **78**, 748
135. Smirnova E.P., Sotnikov A.V., Kunze R., Weihnacht M., Kvyatkovskii O.E. and Lemanov V.V. (2005) *Solid State Commun.* **133**, 421
136. Smolenskii G.A. (1970) *J. Phys. Soc. Japan* **28**, 26

137. Smolenskii G.A. (1984), editor, *Ferroelectrics and Related Materials*, Gordon and Breach Science Publishers, New York

138. Sohn J.-H., Inaguma Y., Yoon S.-O., Itoh M., Nakamura T., Yoon S.-J. and Kim H.-J. (1994) *Jpn. J. Appl. Phys.* **33**, 5466

139. Somiya Y., Bhalla A.S., Cross L.E. (2001) *Int. J. Inorg. Mater.* **3**, 709

140. Somiya Y., Bhalla A.S., Cross L.E. (2004) *Mater. Lett.* **58**, 290

141. Sotnikov A.V., Lemanov V.V., Smirnova E.P., Weihnacht M. and Kunze R. (1999) *Ferroelectrics* **223**, 113

142. Spitzer W.G., Miller R.C., Kleinman D.A. and Howarth L.E. (1962) *Phys. Rev.* **126**, 1710

143. Sung C., Wei G.C., Ostreicher K.J., Rhodes W.H. (1992) *J. Amer. Cer. Soc.* **75**, 1796

144. Tagantsev A.K., Sherman V.O., Astafiev K.F., Venkatesh J. and Setter N. (2003) *J. Electroceram.* **11**, 5

145. Thomas H. and Müller K.A. (1968) *Phys. Rev. Lett.* **21**, 1256

146. Trepakov V.A., Vikhnin V.S., Syrnikov P.P. Smutnyj F., Savinov M., Jastrabik L. (1997) *Fiz. Tverd. Tela* **39**, 2040 (in Russian). English translation: *Phys. Solid State* **39**, 1825

147. Unoki H. and Sakudo T. (1967) *J. Phys. Soc. Japan* **23**, 546

148. Uwe H. and Sakudo T. (1976) *Phys. Rev. B* **13**, 271

149. Varadan V.K., Ghodgaonkar D.K., Varadan V.V., Kelly J.F., Gilkerdas P. (1992) *Microwave J.* **35**, 116

150. Vendik O.G., Kollberg E., Gevorgian S.S., Kozyrev A.B. and Soldatenkov O.I. (1995) *Electron. Lett.* **31**, 654

151. Vendik O.G. and Zubko S.P. (1997) *J. Appl. Phys.* **82**, 4475

152. Vendik O.G., Hollmann E.K., Kozyrev A.B. and Prudan A.M. (1999) *J. Supercond.* **12**, 325

153. Venevtsev Iu.N., Politova E.D., Ivanov S.A. (1985) *Ferro- and Antiferroelectrics of Barium Titanate Family*, Chemistry, Moscow (in Russian).

154. Venturini E.L., Samara G.A. and Kleemann W. (2003) *Phys. Rev. B* **67**, 214102

155. Venturini E.L., Samara G.A., Wang R. and Itoh M. (2004) *Phys. Rev. B* **69**, 184105

156. Viana R., Lunkenheimer P., Hemberger J., Bohmer R. and Loidl A. (1994) *Phys. Rev. B* **50**, 601

157. Viehland, D., Lang, S.J., Cross, L.E., Wuttig, M. (1990) *J. Appl. Phys.* **68**, 2916

158. Viehland, D., Li, J.F., Jang, S.J., Cross, L.E., and Wuttig, M. (1991) *Phys. Rev. B* **43**, 8316

159. Viehland, D., Jang, S.J., Cross, L.E., and Wuttig, M. (1992a) *Phys. Rev. B* **46**, 8003

160. Viehland, D., Li, J.F., Jang, S.J., Cross, L.E., and Wuttig, M. (1992b) *Phys. Rev. B* **46**, 8013

161. Vugmeister B.E. and Glinchuk M.D. (1990) *Rev. Mod. Phys.* **62**, 993

162. Wang R., Inaguma Y., Itoh M. (2000a) *Physica B* **284-288**, 1141

163. Wang R., Sakamoto N. and Itoh M. (2000b) *Phys. Rev. B* **62**, R3577

164. Wang R. and Itoh M. (2000) *Phys. Rev. B* **62**, R731

165. Wang R. and Itoh M. (2001) *Phys. Rev. B* **64**, 174104

166. Wang R. and Itoh M. (2002) *Appl. Phys. Lett.* **80**, 2964

167. Weil J.A., Bolton J.R., Wertz J.E. (1993) *Electron paramagnetic resonance: elementary theory and practical applications*, Wiley, New York

168. Williams D.B. and Carter C.B. (1996) *Transmission electron microscopy: a textbook for materials science* **Vol. 1: Basics**, Plenum, New York

169. Wooldridge I., Turner C.W., Warburton P.A. and Romans E.J. (1999) *IEEE T. Appl. Supercond.* **9**, 3220

170. Worlock J.M. and Fleury P.A. (1967) *Phys. Rev. Lett.* **19**, 1176

171. Wu H.-D., Zhang Z., Barnes F., Jackson C.M., A. Kain and Cuchiaro J.D. (1994) *IEEE T. Appl. Supercond.* **4**, 156

172. Wu L., Chen Y.-C., Chou Y.-P., Tsai Y.-T. And Chu S.-Y. (1999) *Jpn. J. Appl. Phys.* **38**, 5154

173. Wu L., Wu S., Chang F.-C., Shen Y.-T., Chen Y.-C. (2000) *J. Mater. Sci.* **35**, 5945

174. Yagi T., Kasahara M., Tsujimi Y., Ymaguchi M., Hasebe H., Wang R., Itoh M. (2002): *Physica B* **316-317**, 596

175. Yamaguchi M., Yagi T., Wang R. and Itoh M. (2001) *Phys. Rev. B* **63**, 172102

176. Yamanaka A., Kataoka M., Inaba Y., Inoue K., Hehlen B. and Courtens E. (2000) *Europhys. Lett.* **50**, 688

177. Yang C.-F. and Lo S.-H. (1997) *Mat. Res. Bull.* **32**, 1713

178. Yoo Y.-S., Kim H. and Kim D.-Y. (1997) *J. Eur. Ceram. Soc.* **17**, 805

179. Yu Z. (1997) *Ph.D. thesis*, University of Aveiro, Portugal

180. Zhang L., Kleemann W., Wang R. and Itoh M. (2002a) *Appl. Phys. Lett.* **81**, 3022

181. Zhang L., Kleemann W. and Zhong W.-L. (2002b) *Phys. Rev. B* **66**, 104105

182. Zhang Y., Schubert J., Wolters N., Banzet M., Zander W., Krause H.-J. (2002c) *Physica C* **372**, 282

183. Zheng H. and Sorensen O.T. (1999) *J. Eur. Ceram. Soc.* **19**, 1987

184. Zhong W. and Vanderbilt D. (1995) *Phys. Rev. Lett.* **74**, 2587

185. Zhong W. and Vanderbilt D. (1996) *Phys. Rev. B* **53**, 5047

List of Publications

1. **A. Tkach**, P. M. Vilarinho, M. Avdeev, A. L. Kholkin and J. L. Baptista, “Synthesis by sol-gel and characterization of strontium titanate powder”, *Key Engineering Materials,* Vols. 230-232 (2002), pp. 40-43
2. V. Trepakov, I. Kudyk, S. Kapphan, M. Savinov, A. Pashkin, L. Jastrabik, **A. Tkach**, P. Vilarinho, A. Kholkin, “Critical phonons and impurity Cr^{3+} zero-phonon emission line in quantum paraelectrics: A and B-site Mg doping of $SrTiO_3$”, *Journal of Luminescence,* Vol. 102 (2003), pp. 536-542
3. V. Trepakov, M. Savinov, I. Kudyk, A. Pashkin, S. Kapphan, P. Vilarinho, **A. Tkach**, A. Kholkin, L. Jastrabik, “Dielectric Permittivity and Cr^{3+} Impurity Luminescence Probe of $Sr_{0.99}Mg_{0.01}TiO_3$ and $SrTi_{0.99}Mg_{0.01}O_3$”, *Ferroelectrics,* Vol. 294 (2003), pp. 229-238
4. **A. Tkach**, P.M. Vilarinho, A. Kholkin, I.M. Reaney, J. Petzelt, “Structural and Dielectric Properties of Mg-doped Strontium Titanate Ceramics: Dependence on the Materials Processing”, *Materials Science Forum*, Vols. 455-456 (2004), pp. 40-44.
5. **A. Tkach**, P.M. Vilarinho, A. Kholkin, “Structural and Dielectric Properties of Mn-doped Strontium Titanate Ceramics”, *Ferroelectrics* Vol. 304 (2004), pp. 917-920.
6. **A. Tkach**, P. M. Vilarinho, A. Kholkin, “Effect of Mg Doping on the Structural and Dielectric Properties of Strontium Titanate Ceramics”, *Appl. Phys. A – Mater.* Vol. 79 (2004), pp. 2013-2020.
7. **A. Tkach**, P.M. Vilarinho, A.L. Kholkin, A. Pashkin, P. Samoukhina, J. Pokorny, S. Veljko and J. Petzelt, “Lattice dynamics and dielectric response of Mg-doped $SrTiO_3$ ceramics in a wide frequency range”, *J. Appl. Phys.* Vol. 97 (2005), p. 044104.
8. **A. Tkach**, P.M. Vilarinho, A.L. Kholkin, “Polar Behavior in Mn-Doped $SrTiO_3$ Ceramics”, *Appl. Phys. Lett.* Vol. 86 (2005), p. 172902.
9. **A. Tkach**, P.M. Vilarinho, A.M.R. Senos, A.L. Kholkin, “Effect of Nonstoichiometry on the Microstructure and Dielectric Properties of Strontium Titanate Ceramics”, *J. Eur. Ceram. Soc.* Vol. 25 (2005), pp. 2769-2772.
10. **A. Tkach**, A.B. Araújo, P.M. Vilarinho, “The Influence of dc Bias on the Dielectric Response of $Sr_{1-x}Ca_xTiO_3$ Ceramics”, *Materials Science Forum* [accepted].

11. **A. Tkach**, P.M. Vilarinho, A.L. Kholkin, “Structure-microstructure-dielectric tunability relationship in Mn-doped strontium titanate ceramics”, *Acta Materialia* [accepted].